

Promotion Committee

Prof. dr. C. Hoede, Chairman	University of Twente
Prof. dr. ir. A. Nijmeijer	University of Twente
Dr. H.J.M. Bouwmeester	University of Twente
Prof. dr. ing. M. Wessling	University of Twente
Prof. dr. ir. B. Poelsema	University of Twente
Prof. Dr. H.D. Wiemhöfer	Westfälische Universität Münster
Dr. P.V. Hendriksen	Risø National Laboratory · Technical University of Denmark
Prof. Dr.-Ing. Roland Dittmeyer	DECHEMA e.V. Karl-Winnacker-Institut, Technische Chemie

The research described is the result of a collaboration between Risø National Laboratory·DTU and the University of Twente.

ISBN: 978-90-365-2650-0

Printed by Schultz Grafisk 2008

MEASUREMENT AND MODELLING OF THE DEFECT
CHEMISTRY AND TRANSPORT PROPERTIES OF CERAMIC
OXIDE MIXED IONIC AND ELECTRONIC CONDUCTORS

DISSERTATION

to obtain the degree of doctor

at the University of Twente, under the authority of

the rector magnificus, prof. dr. W.H.M. Zijm ,

on account of the decision of the graduation committee,

to be publicly defended

on Thursday the 3rd of April at 13.15

by

Bjarke Thomas Dalslet

born on 3rd of October 1979

in Frederikssund, Danmark

This thesis is approved by the promotor

Prof. dr. ir. A. Nijmeijer

and the assistant promotors

dr. P.V. Hendriksen
and

dr. H.J.M. Bouwmeester

Contents

1	Introduction	12
1.1	The form of this thesis	12
1.2	Mixed conductors	12
1.3	Oxygen chemical potential and oxide concentration in mixed conductors	13
1.4	Diffusion in mixed conductors	14
1.5	Surface oxygen exchange in mixed conductors	15
1.6	Electrolyte probes, sensors and pumps	17
1.7	Evaluation of precision and accuracy	18
2	Determination of Oxygen Transport Properties from Flux and Driving Force Measurements Using an Oxygen Pump and an Electrolyte Probe	21
2.1	Introduction	21
2.2	Experimental	22
2.2.1	Sample preparation	22
2.2.2	Setup and measurement procedure	23
2.3	Defect chemistry and transport properties of LSCF	24
2.3.1	Defect chemistry	24
2.3.2	Transport properties	25
2.3.3	Steady state model	27
2.3.4	Relaxation model	28
2.4	Measurements using an oxygen pump and an electrolyte probe	29
2.4.1	Oxygen chemical potential measurement	29
2.4.2	The oxygen pump	29
	The area specific conductance, G	29
	Effect of gas diffusion in the closed compartment	30
	Effect of permeation flux on the flow gas	30
2.4.3	The electrolyte probe	31
2.5	Results and discussion	33
2.5.1	Steady state measurements	33
	Low flux measurement	33
	p_{O_2} dependence of G_c and r_s	35
	Temperature dependence of G_c and r_s	35
	Steady state model results	37
2.5.2	Relaxation experiments	38
2.5.3	Measurement verification	39
	Influence of corrections	39
	Influence of gas diffusion	40
	V_{probe} evaluation	41
	Measurement reproducibility	42
2.5.4	Comparison of values from steady state and relaxation experiments	43

2.6	Conclusions	44
3	Characterization of oxygen transport in mixed conductors: A method comparison	45
3.1	Introduction	45
3.2	Experimental	46
3.2.1	Sample preparation	46
3.2.2	Membrane and probe measurement	46
3.2.3	Conductivity relaxation	47
3.3	Theory	47
3.3.1	Steady state membrane experiment (SS)	47
3.3.2	Membrane relaxation experiment (MR)	48
3.3.3	Conductivity Relaxation (CR)	49
	Partial model	49
3.4	Results and discussion	50
3.4.1	Influence of corrections	50
	Influence of p_{O_2} step size and the permeation term	52
	Differences between measured and corrected	53
3.4.2	Comparison of the confidence interval of the methods	55
3.4.3	Relaxation vs. steady state	56
3.4.4	Errors in modelling the probe signal	59
3.4.5	Comparison of values to those in the literature	61
3.5	Conclusion	63
4	Defect Chemistry of $(La_{0.6}Sr_{0.4-x}M_x)_{0.99}Co_{0.2}Fe_{0.8}O_{3-\delta}$ $M = Ca$ ($x = 0.05, 0.1$), Ba ($x = 0.1, 0.2$), Sr.	65
4.1	Introduction	65
4.2	Experimental	66
4.2.1	Sample preparation	66
4.2.2	X-ray diffraction (XRD)	66
4.2.3	Thermogravimetry (TG)	67
4.2.4	Coulometric Titration (CT)	67
4.3	Theory	68
4.3.1	Coulometric titration (CT)	68
4.3.2	Defect chemistry of LSMCF	69
	Model I	71
	Model II	71
4.4	Results and discussion	72
4.4.1	Structure	72
4.4.2	Thermogravimetry (TG)	72
	Total reduction	72
	Measurements in air	74
4.4.3	CT	74
4.4.4	p_{O_2} dependence of δ for all materials.	79
4.4.5	Low p_{O_2} measurement	79
4.4.6	H_{ox} and S_{ox}	81
4.4.7	Model fits	82
4.4.8	Parameter extraction	83
4.5	Conclusions	84

5 Oxygen Transport in $(\text{La}_{0.6}\text{Sr}_{0.4-x}\text{M}_x)_{0.99}\text{Co}_{0.2}\text{Fe}_{0.8}\text{O}_{3-\delta}$ $\text{M} = \text{Ca}$ ($x = 0.05, 0.1$), Ba ($x = 0.1, 0.2$), Sr.	85
5.1 Introduction	85
5.2 Experimental	87
5.2.1 Sample preparation	87
5.2.2 X-ray diffraction	87
5.2.3 Membrane and probe measurement	88
5.3 Defect chemistry and transport properties of LSMCF	88
5.3.1 Defect chemistry	89
5.3.2 Transport properties	89
5.3.3 Steady state model	90
5.4 Measurements using an oxygen pump and an electrochemical probe	90
5.4.1 Oxygen chemical potential measurement	91
5.4.2 The oxygen pump	91
The area specific conductance, G	91
5.4.3 The electrolyte probe	92
5.5 Results and discussion	93
5.5.1 G_c and r_s	94
5.5.2 The reduced diffusion coefficient, D_V^0	100
5.5.3 Parameter importance	103
5.5.4 Large perturbations	105
5.5.5 Evaluation of measurements	107
5.5.6 Comparison with literature	108
5.6 Conclusions	110
6 Defect chemistry of $(\text{Ba}_{0.5}\text{Sr}_{0.5})_{0.99}\text{Co}_{0.8}\text{Fe}_{0.2}\text{O}_{3-\delta}$	111
6.1 Introduction	111
6.2 Experimental	112
6.2.1 Sample preparation	112
6.2.2 Thermogravimetry and coulometric titration	112
6.2.3 XANES	112
6.3 Theory	113
6.3.1 Coulometric Titration (CT)	113
6.4 Results and Discussion	114
6.4.1 Coulometric Titration (CT)	114
6.4.2 Thermogravimetry (TG)	115
6.4.3 Comparison with literature	117
6.4.4 XANES	118
6.5 Conclusion	119
7 Assesment of doped Ceria as electrolyte	121
7.1 Introduction	121
7.2 Theory and model description	122
7.2.1 Defect chemistry of $\text{Ce}_{0.9}\text{Gd}_{0.1}\text{O}_{1.95-x}$ (CG10)	122
7.2.2 Ambipolar transport model	123
Overview	123
Transport in the electrolyte	123
Electrode polarization resistance	124
7.2.3 Power density and efficiency	124
7.2.4 Reference cell	125
7.3 Experimental	126

7.3.1	Total conductivity measurements	126
7.3.2	Oxygen permeation experiments	126
7.4	Model validation	126
7.4.1	CG10 conductivity	126
7.4.2	Leak current through a CG10 disk	129
7.4.3	Cell characteristics	130
7.5	Modelling results and discussion	131
7.5.1	Ionic and electronic conductivity	131
7.5.2	p_{O_2} profile through the cell under open circuit and loaded conditions . . .	132
7.5.3	The coupling of leak current density and efficiency	133
7.5.4	Temperature dependence of performance	134
7.5.5	Effects of anode polarization	135
7.5.6	Effects of cathode polarization	136
7.5.7	Effects of the electrode polarization distribution	137
7.5.8	Thickness dependence	137
7.5.9	Nanocrystalline CG10 electrolytes and the importance of the vacancy formation enthalpy	139
7.5.10	Comparison with state of the art zirconia based electrolytes.	140
7.6	Discussion	141
7.6.1	Possibilities of improving cells based on CG10 electrolytes	141
	Case 1: High power density applications	141
	Case 2: High efficiency applications	142
	Case 3: low temperature	142
7.6.2	Considerations of CG10 or zirconia	142
	Future situation	143
7.7	Conclusions	143
8	Model study of a gadolinia doped ceria membrane	144
8.1	Introduction	144
8.2	Gas equilibria	145
8.3	Ceria and the alternatives	145
8.4	Electronic or ionic conductivity.	147
8.5	Effect of membrane thickness	147
8.6	Thin films with small grain size	148
8.7	Pr doped Ceria	149
8.8	Conclusions	151
9	Recommendations for further work.	152
A	Chemical Potential of Oxygen in the Gas Phase	161
B	Derivation of the average driving force above the membrane	162
C	Correlation of D_V^0 with structural parameters	162

Nederlandse samenvatting

Dit proefschrift beschrijft gemengde keramische stoffen met ionische en elektronische geleiding (MIECs). MIECs hebben potentiële toepassingen zoals selectieve zuurstof doorlatende membranen, katalysatoren en als componenten in brandstofcellen. De MIECs in dit proefschrift zijn allemaal oxide geleidende materialen. De defectchemische, en transport eigenschappen van een aantal MIECs en de meetmethoden, die zijn gebruikt om deze eigenschappen te bepalen.

Meetmethoden

- Er werd een meettechniek ontwikkeld, die bestond uit een zuurstofpomp en een elektrolyet probe. De combinatie werd gebruikt om de ionische oppervlakteweerstand en de bulk diffusie coëfficiënt van een aantal verschillende MIECs te bepalen. Deze methode werd bekrachtigd door: 1) een vergelijking met literatuurwaarden van bekende materialen 2) bevestiging van de interne consistentie tussen hoog en laag stroommetingen en 3) succesvolle modelstudies van kleine verschillen van veranderingen in de zuurstof chemische potentiaal. Met deze methode was het mogelijk om met hoge betrouwbaarheid te meten in gebieden waar conventionele methoden niet nauwkeurig zijn.
- Stoichiometrische metingen aan een aantal verschillende MIECs werden uitgevoerd door middel van thermografimetrie en coulometrische titratie in een gesloten electrochemische cel. De metingen werden bekrachtigd door een vergelijking met literatuurwaarden. De resultaten van de coulometrische titraties waren goed te reproduceren en bijna ruisvrij.
- X-ray Absorption Near Edge Structure (XANES) metingen werden uitgevoerd aan de MIEC $\text{Ba}_{0.5}\text{Sr}_{0.5})_{0.99}\text{Co}_{0.8}\text{Fe}_{0.2}\text{O}_{3-\delta}$. XANES werd gebruikt om een onderscheid te maken tussen de veranderingen van de valentie staat van Co en Fe ionen in de MIEC.

Specifieke materiaal eigenschappen

- Het materiaalsysteem $\text{La}_{0.6}\text{Sr}_{0.4x}\text{M}_x)_{0.99}\text{Co}_{0.2}\text{Fe}_{0.8}\text{O}_{3-\delta}$, $M = \text{Sr}, \text{Ca}$ ($x = 0.05, 0.1$), Ba ($x = 0.1, 0.2$) (LSMFC) werd gekarakteriseerd door zuurstof doorlaatbaarheid metingen, oppervlakteweerstand metingen en stoichiometrische metingen. $(\text{La}_{0.6}\text{Sr}_{0.3}\text{Ca}_{0.1})_{0.99}\text{Co}_{0.2}\text{Fe}_{0.8}\text{O}_{3-\delta}$ had de hoogste zuurstof doorlaatbaarheid van de materialen in het systeem. $(\text{La}_{0.6}\text{Sr}_{0.2}\text{Ba}_{0.2})_{0.99}\text{Co}_{0.2}\text{Fe}_{0.8}\text{O}_{3-\delta}$ was in de meeste gevallen het materiaal met de laagste zuurstofstoichiometri waarde, $3 - \delta$. $(\text{La}_{0.6}\text{Sr}_{0.2}\text{Ba}_{0.2})_{0.99}\text{Co}_{0.2}\text{Fe}_{0.8}\text{O}_{3-\delta}$ had ook de laagste ionische oppervlakteweerstand. Helaas had $(\text{La}_{0.6}\text{Sr}_{0.2}\text{Ba}_{0.2})_{0.99}\text{Co}_{0.2}\text{Fe}_{0.8}\text{O}_{3-\delta}$ ook de laagste bulk diffusie coëfficiënten en waren er aanwijzingen voor een lage chemische stabiliteit. $(\text{La}_{0.6}\text{Sr}_{0.4})_{0.99}\text{Co}_{0.2}\text{Fe}_{0.8}\text{O}_{3-\delta}$ had de hoogste zuurstofstoichiometri waarde.
- $(\text{Ba}_{0.5}\text{Sr}_{0.5})_{0.99}\text{Co}_{0.8}\text{Fe}_{0.2}\text{O}_{3-\delta}$ werd geanalyseerd met behulp van XANES. Bij een verhoging van de temperatuur, van 295 K naar 773 K onder een He atmosfeer, werd alleen het cation Co gereduceerd. Stoichiometrische metingen aan hetzelfde materiaal kwamen niet overeen met de literatuurwaarden. Maar bevestigden de waarden van $\delta > 0,5$ bij $T > 973$ K onder condities zoals het materiaal in de literatuur is beschreven met een perovskite structuur.
- Model berekeningen onderzochten een brandstofcel met een elektrolyet membraan van gadolinea gedoopt ceria, $\text{Ce}_{0.9}\text{Gd}_{0.1}\text{O}_{1.95}$ (CG10). CG10 is, hoewel het niet een perfect elektrolyet is (geen elektronische geleiding), een MIEC met een zeer lage elektronische geleiding bij 873 K. Bij deze temperatuur voorspellen de model berekeningen dat bij veel condities CG10 beter presteert dan de conventionele elektrolyet membranen, gebaseerd op

zirconium, zeker wanneer hoge spanningsdichtheden nodig zijn. De verbeterde prestatie is vooral te danken aan de beschikbaarheid van beter cathode materiaal met CG10, in vergelijking met materiaal compatible met elektrolieten gebaseerd op zirconium. De iets hogere ionische geleiding in CG10 werkte ook in het voordeel.

- Een modelstudie bij 873 K toont aan dat de elektronische geleiding van gadolinea gedoopt ceria voldoende verhoogt om het een interessant materiaal te maken voor zuurstofscheidende membranen. Gadolinea gedoopte ceria membranen, met een dikte van minder dan 10 μm , zouden prima kandidaten kunnen zijn voor syngas productie bij temperaturen van 973 K en hoger.

Gemeenschappelijke waarnemingen van de materialen

- De experimenten leiden tot de volgende algemene conclusies: Elektroliet geprobete metingen laten zien dat de oppervlakte reactieconstanten van zuurstof dat het membraan verlaat (reductie) en zuurstof dat het membraan inkomt (oxidatie) van alle onderzochte MIECs hetzelfde zijn. Bij hoge temperatuur is de oppervlakte reactie gelimiteerd door absorptie, terwijl het bij lage temperatuur gelimiteerd is door de incorporatie reactie. De gemeten activeringsenergie van de oppervlakte reactie, verkregen door de gepulseerde isotoop uitwisseling en de elektroliet geprobete metingen, zijn hiermee in overeenstemming.
- Het ionentransport wordt gecontroleerd door zowel de gereduceerde diffusie coefficient, analoog aan de mobiliteit van een enkel vrije ionplaats, en de concentratie van vrije ionplaatsen. De gereduceerde diffusiecoefficient was afhankelijk van de chemische potentiaal van zuurstof en de temperatuur. Hetzelfde gold voor de concentratie van vrije ionplaatsen. Hierdoor moet het gedrag van zowel de gereduceerde diffusiecoefficient, als de concentratie van vrije ionplaatsen bekend zijn, om de afhankelijkheid van het bulk transport op de chemische potentiaal van zuurstof en de temperatuur te bepalen.
- Langzame overgangen in de MIEC samples kunnen de transport parameters dramatisch veranderen binnen dagen of weken. Er moet dus goed overwogen worden in welke mate twee verschillende metingen vergelijkbaar zijn, wanneer deze met elkaar worden vergeleken.

English summary

The subject of this thesis is ceramic mixed ionic and electronic conductors (MIECs). MIECs have potential uses, such as solid oxygen permeation membranes, as catalysts, and as components in fuel cells. The MIECs examined in this thesis are all oxide ion conducting materials. This thesis describes the defect chemistry and transport properties of a number of MIECs, and the measurement methods used to determine these properties.

Measurement methods

- A measurement technique was developed based on an oxygen pump and an electrolyte probe. This combination was used to extract values of the ionic surface resistance and the bulk diffusion coefficient of several different MIECs. The setup was validated: 1) by comparison with literature values of known substances; 2) by confirming internal consistency between high and low current measurements; and 3) by successful modelling of transient responses to changes in the oxygen chemical potential. The method was shown to be able to measure with high confidence in regimes where conventional methods are unprecise.
- Stoichiometry measurements were carried out, on several different MIECs, using thermogravimetry and coulometric titration in a closed electrochemical cell. The measurements were validated by comparison with literature values. The coulometric titration measurements were highly reproducible, and almost noise free.
- X-ray Absorption Near Edge Structure (XANES) measurements were carried out on the MIEC $(\text{Ba}_{0.5}\text{Sr}_{0.5})_{0.99}\text{Co}_{0.8}\text{Fe}_{0.2}\text{O}_{3-\delta}$. XANES was used to distinguish between valence state changes of Co and Fe ions in the MIEC.

Specific material properties

- The materials system $(\text{La}_{0.6}\text{Sr}_{0.4-x}\text{M}_x)_{0.99}\text{Co}_{0.2}\text{Fe}_{0.8}\text{O}_{3-\delta}$, $M = \text{Sr}, \text{Ca}$ ($x = 0.05, 0.1$), Ba ($x = 0.1, 0.2$) (LSMFC) was characterized by oxygen permeation measurements, surface resistance measurements and stoichiometry measurements. $(\text{La}_{0.6}\text{Sr}_{0.3}\text{Ca}_{0.1})_{0.99}\text{Co}_{0.2}\text{Fe}_{0.8}\text{O}_{3-\delta}$ showed the highest oxygen permeability of the materials in the system. $(\text{La}_{0.6}\text{Sr}_{0.2}\text{Ba}_{0.2})_{0.99}\text{Co}_{0.2}\text{Fe}_{0.8}\text{O}_{3-\delta}$ was the material with the highest value of δ in most circumstances. $(\text{La}_{0.6}\text{Sr}_{0.2}\text{Ba}_{0.2})_{0.99}\text{Co}_{0.2}\text{Fe}_{0.8}\text{O}_{3-\delta}$ also had the lowest ionic surface resistance. Unfortunately, $(\text{La}_{0.6}\text{Sr}_{0.2}\text{Ba}_{0.2})_{0.99}\text{Co}_{0.2}\text{Fe}_{0.8}\text{O}_{3-\delta}$ also had the lowest bulk diffusion coefficients, and showed signs of low chemical stability. $(\text{La}_{0.6}\text{Sr}_{0.4})_{0.99}\text{Co}_{0.2}\text{Fe}_{0.8}\text{O}_{3-\delta}$ was the material with the lowest δ .
- $(\text{Ba}_{0.5}\text{Sr}_{0.5})_{0.99}\text{Co}_{0.8}\text{Fe}_{0.2}\text{O}_{3-\delta}$ was investigated using X-ray Absorption Near Edge Structure (XANES) measurements. When increasing the temperature, T , from 295 K to 773 K in a He atmosphere, it was found that Co was the only B-site cation being reduced. Stoichiometry studies on the same material disagreed with literature. Values of $\delta > 0.5$ was found at $T > 973$ K under conditions where the material is reported to have perovskite structure in the literature.
- Model calculations investigated a fuel cell with an electrolyte membrane made from gadolinia doped ceria, $\text{Ce}_{0.9}\text{Gd}_{0.1}\text{O}_{1.95}$ (CG10). While not a perfect electrolyte (with no electronic conductivity), CG10 is a MIEC with a very low electronic conductivity at $T \leq 873$ K. At $T \leq 873$ K the model calculations predicted that CG10, in many conditions, performs better than conventional electrolyte membranes based on zirconia, especially when high power densities are required. The better performance is mainly due to the availability of better cathode materials compatible with $\text{Ce}_{0.9}\text{Gd}_{0.1}\text{O}_{1.95}$, compared to

those compatible with electrolytes based on zirconia. The slightly higher ionic conductivity in $\text{Ce}_{0.9}\text{Gd}_{0.1}\text{O}_{1.95}$ was also beneficial.

- Modelling at $T > 873$ K revealed that the electronic conductivity of gadolinia doped ceria increases enough for it to become an interesting material for oxygen separation membranes. It was thus found from the model studies, that gadolinia doped ceria membranes with thicknesses less than $10\ \mu\text{m}$ could be excellent candidates for syngas production membranes at $T > 973$ K.

Observations common to the materials

- Electrolyte probe measurements revealed that the surface reaction rate constants of oxygen leaving a membrane (reduction) and oxygen entering the membrane (oxidation) of the investigated MIECs are the same.
- The bulk transport of oxide ions is controlled by both the reduced diffusion coefficient, analogous to the mobility of a single ion vacancy, and the oxide site vacancy concentration. The oxide site reduced diffusion coefficient was dependent on the chemical potential of oxygen and the temperature. Also the oxide site vacancy concentration was dependent on the chemical potential of oxygen and the temperature. Consequently, the behavior of both the oxide site reduced diffusion coefficient and the oxide site vacancy concentration must be known in order to determine the dependence of the bulk transport on the chemical potential of oxygen and the temperature.
- Slow transients in the MIEC samples can alter the transport parameters dramatically over the course of days or weeks. Special care had to be taken to ensure that measurements were not performed during a slow transient but at true equilibrium.

Dansk resumé

I denne afhandling vil keramiske stoffer med blandet elektronisk og ionisk ledningsevne (MIEC'er) blive behandlet. MIEC'er kan potentielt gøre nytte som selektive iltpermeable membraner, som katalysatorer og som dele af faststofoxidbrændselsceller. Afhandlingen vil beskrive defektkemien og transportegenskaberne for en række MIEC'er, og de målemetoder der bliver brugt til at undersøge dem. MIEC'erne der bliver undersøgt i denne afhandling er alle oxidionledere.

Målemetoder

- En målemetode baseret på kombinationen af en iltpumpe og en elektrolytprobe blev udviklet. Denne metode blev brugt til at fastslå værdier af den ioniske overflademodstand og diffusionskoefficienten i det indre af membraner lavet af flere forskellige typer MIEC'er. Teknikkens gyldighed blev bekræftet ved: 1) sammenligning med litteraturværdier for de undersøgte stoffer, 2) ved observation af intern konsistens imellem høj- og lavstrømsmålinger, og 3) ved overensstemmelse med modellerede stofovergange efter gasskifte i måleopstillingen. Metoden var i stand til at måle med lille usikkerhed under forhold hvor konventionelle metoder er upræcise.
- En række MIEC'er fik målt deres støkiometrimålinger ved brug af termogravimetri og coulometrisk titrering i en lukket elektrokemisk celle. Metodens gyldighed blev bekræftet ved sammenligning med litteraturværdier. Coulometrisk titrering udmærkede sig ved at være meget reproducérbart og næsten fri for støj.
- Røngtenabsorptionskantstrukturer (XANES) blev målt på MIEC'en $(\text{Ba}_{0.5}\text{Sr}_{0.5})_{0.99}\text{Co}_{0.8}\text{Fe}_{0.2}\text{O}_{3-\delta}$. Disse målinger kunne bruges til at skelne mellem ændringer i valens af Co og Fe.

Specifikke materialeegenskaber

- Iltpermeationsmålinger, overflademodstandsmålinger og støkiometrimålinger blev udført på materialesystemet $(\text{La}_{0.6}\text{Sr}_{0.4-x}\text{M}_x)_{0.99}\text{Co}_{0.2}\text{Fe}_{0.8}\text{O}_{3-\delta}$, $M = \text{Sr}, \text{Ca}$ ($x = 0.05, 0.1$), Ba ($x = 0.1, 0.2$) (LSMFC). $(\text{La}_{0.6}\text{Sr}_{0.3}\text{Ca}_{0.1})_{0.99}\text{Co}_{0.2}\text{Fe}_{0.8}\text{O}_{3-\delta}$ havde den højeste iltpermeabilitet i systemet. $(\text{La}_{0.6}\text{Sr}_{0.2}\text{Ba}_{0.2})_{0.99}\text{Co}_{0.2}\text{Fe}_{0.8}\text{O}_{3-\delta}$ havde den laveste iltstøkiometri, $3 - \delta$, af materialerne under de fleste forhold. $(\text{La}_{0.6}\text{Sr}_{0.2}\text{Ba}_{0.2})_{0.99}\text{Co}_{0.2}\text{Fe}_{0.8}\text{O}_{3-\delta}$ havde også den laveste ioniske overflademodstand. Desværre havde $(\text{La}_{0.6}\text{Sr}_{0.2}\text{Ba}_{0.2})_{0.99}\text{Co}_{0.2}\text{Fe}_{0.8}\text{O}_{3-\delta}$ også den laveste indre diffusionskoefficient ligesom materialet udviste tegn på lav kemisk stabilitet. $(\text{La}_{0.6}\text{Sr}_{0.4})_{0.99}\text{Co}_{0.2}\text{Fe}_{0.8}\text{O}_{3-\delta}$ havde den højeste iltstøkiometri af materialerne.
- $(\text{Ba}_{0.5}\text{Sr}_{0.5})_{0.99}\text{Co}_{0.8}\text{Fe}_{0.2}\text{O}_{3-\delta}$ blev undersøgt ved hjælp af røngtenabsorptionskantstrukturmålinger (XANES). Under en temperaturforøgelse fra 295 K til 773 K i en heliumatmosfære blev alene materialets Co kationer reduceret. Støkiometrimålinger på samme materiale kunne ikke bekræftes af litteraturen. Der blev dog fundet værdier af δ over 0.5 under forhold hvor materialet ifølge litteraturen bibeholder sin perovskitstruktur.
- Brændselsceller med elektrolytmembraner af gadoliniumdoteret ceria, $\text{Ce}_{0.9}\text{Gd}_{0.1}\text{O}_{1.95}$ (CG10), blev undersøgt via et modelstudie. Selv om CG10 ikke er en perfekt elektrolyt (dvs. CG10 har en målbar elektronledningsevne) er elektronledningsevnen lav nok til at CG10 kan konkurrere med traditionelle zirconiabaserede elektrolytter, især når høje effekttætheder er ønsket. Den bedre præstationsevne skyldes tilgængeligheden af bedre katodematerialer der er kompatible med CG10, end de katodematerialer der er kompatible

med zirconiabaserede elektrolytter. CG10 har også en smule højere ionledningsevne end zirconia baserede elektrolytter.

- Et modelstudie ved temperaturer over 873 K afslørede at den elektriske ledningsevne af CG10 her bliver høj nok til at CG10 bliver et interessant materiale for membraner til brug i syntesegasproduktion. Gadolina doterede ceriamembraner tyndere end 10 μm kan potentielt være udmærkede i syntesegasproduktion ved temperaturer over 973 K.

Fælles observationer for materialerne

- Elektrolytprobemålingerne afslørede at overfladereaktionsratekonstanten var den samme uanset om nettostrømmen af ilt skete ind i en membran eller ud af membranen i alle de undersøgte materialer.
- Iontransporten inde i de undersøgte MIEC'er er styret både af den reducerede diffusion-skoefficient, der er analog til den enkelte ionvakancess mobilitet, og koncentrationen af ionvakancesser. Den reducerede diffusionskoefficient er afhængig af det kemiske potential af ilt og af temperaturen. Ligeledes er koncentrationen af ionvakancesser afhængig af det kemiske potential af ilt og af temperaturen. A denne grund må både den reducerede diffusionskoefficient og koncentrationen af ionvakancesser afhængighed af det kemiske potential af ilt og temperaturen kortlægges præcist hvis man ønsker at karakterisere iontransporten fyldestgørende.
- Langsomme overgange kan ændre transportparametrene dramatisk i sintrede prøver af MIEC'er. Disse overgange sker typisk over dage eller uger. Man må derfor grundigt overveje hvor vidt to forskellige målinger virkeligt er ækvivalente, når man sammenligner dem.

The scope of this thesis

The scope of this thesis incorporates the characterization of a new measurement setup, experimental investigation and comparison of several different materials, and modelling of fuel cells and membranes based on material properties reported in the literature.

A measurement setup consisting of an oxygen pump and an electrolyte probe was developed. A detailed description of this setup is given in Chapter 2 and compared with other measurement methods in Chapter 3. Measurements using this setup on a material series consisting of five different materials are presented in Chapter 5.

The perovskites $(\text{La}_{0.6}\text{Sr}_{0.4-x}\text{M}_x)_{0.99}\text{Co}_{0.2}\text{Fe}_{0.8}\text{O}_{3-\delta}$, $M = \text{Ca, Ba, Sr}$ (LSMCF) were investigated. In Chapter 4, measurements of the concentration of oxygen vacancies in LSMCF are presented and in Chapter 5 measurements of the transport parameters of LSMCF are presented.

Data of measurements of the defect chemistry are presented for another perovskite, $(\text{Ba}_{0.5}\text{Sr}_{0.5})_{0.99}\text{Co}_{0.8}\text{Fe}_{0.2}\text{O}_{3-\delta}$ (BSCF), in Chapter 6.

The fluorite MIEC $\text{Ce}_{0.9}\text{Gd}_{0.1}\text{O}_{1.95}$ (CG10) is assessed as a fuel cell electrolyte, in Chapter 7, based on properties of that material reported in the literature. In Chapter 8 this material is further assessed for use as an oxygen separation membrane.

Chapter 1

Introduction

1.1 The form of this thesis

This thesis consists of a series of Chapters. Apart from the introduction Chapter and the recommendations Chapter, each Chapter is formulated as an independent paper. The intent of this form is to present the thesis as a series of self contained essays, each with their individual focus, to improve readability.

The choice of making the Chapters self contained will inevitably lead to some repetitions, especially in the theory sections. This is intentional, as it allows the theory relevant for each Chapter to be on the forefront of the readers mind.

1.2 Mixed conductors

The topic of this thesis is the subgroup of mixed ion and electronic conductors (MIECs) consisting of ceramic oxides exhibiting selective oxygen permeability at temperatures, $T > 873$ K. Such materials have a wide range of potential uses in the chemical industry, especially as catalysts and oxygen separation membranes in the oil and gas refining industries, but also as components in fuel cells used for compact, mobile, auxiliary power units and decentralized domestic heat and power installations [1–3].

In traditional solid oxide fuel cells (SOFCs), the transformation between gaseous O_2 and O^{2-} in the solid phase is facilitated by a catalyst. Traditional catalysts, like $La_{0.5}Sr_{0.5}MnO_3$ or Pt, have very little ionic conductivity, thus confining the effective reaction area to the triple phase (ideally one dimensional) boundary between catalyst, electrolyte and gas. MIECs have been investigated for electrode materials in solid oxide fuel cells [4–6] as their ability to transport oxygen ions can expand the effective reaction area, to the larger dual phase (i.e. two dimensional) boundary between the MIEC catalyst and the gas.

A dense MIEC membrane can provide a pure oxygen supply from any gas mixture containing oxygen, due to its highly selective permeability. MIECs are thus useful as membranes for oxygen production, or reactors for partial oxidation of methane to synthesis gas [1, 7, 8].

When the chemical potential of oxygen in the MIEC, $\mu_{O_2}^{MIEC}$ is changed either by heating the MIEC or by exposing it to a reducing atmosphere, the MIEC will begin to expel oxygen, creating oxide ion vacancies in the crystal structure. Many bulk properties of MIECs, and in particular the ones in this study, depend on the oxygen chemical potential in the MIEC, $\mu_{O_2}^{MIEC}$. The MIECs can thus be used as oxygen sensors [9].

The oxide ion vacancy creation results in chemical expansion of the crystal structure, and is therefore the cause of extraordinarily large apparent thermal expansion coefficients (TEC). It may thus be difficult to assemble systems combining MIECs with components of other materials, if these are to work at varying temperatures and $\mu_{O_2}^{MIEC}$; the interfacial strains can cause the

systems to fail mechanically as the MIEC expands. For some of the materials, particularly the Co containing perovskites, a low $\mu_{\text{O}_2}^{\text{MIEC}}$ can cause a decomposition into various oxides, destroying the membrane material.

The primary topic of this study, however, is not the mechanical properties, but rather the transport properties and their dependency on $\mu_{\text{O}_2}^{\text{MIEC}}$ and the associated concentration of oxygen vacancies. The ambition is to determine the MIEC properties and mechanisms responsible for their performance in fuel cells and as oxygen separation membranes. In particular, the relative importance of the number of oxygen vacancies, their mobility, the electronic conductance and the surface exchange reaction are addressed.

We have chosen to investigate the perovskites $(\text{La}_{0.6}\text{Sr}_{0.4-x}\text{M}_x)_{0.99}\text{Co}_{0.2}\text{Fe}_{0.8}\text{O}_{3-\delta}$, $\text{M}=\text{Sr}, \text{Ca}$ ($x = 0.05, 0.1$), Ba ($x = 0.1, 0.2$) (LSMFC) and $(\text{Ba}_{0.5}\text{Sr}_{0.5})_{0.99}\text{Co}_{0.8}\text{Fe}_{0.2}\text{O}_{3-\delta}$ (BSCF), due to their good transport properties, both regarding bulk transport of ions, and in terms of high catalytic surface activity when exchanging oxygen with the surrounding atmosphere.

Ceria based fluorites have been investigated on the basis of materials data reported in the literature. A model study of the defect chemistry and transport properties of $\text{Ce}_{0.9}\text{Gd}_{0.1}\text{O}_{1.95-x}$ (CG10) was also performed, as this material has high stability, and good transport properties at intermediate temperature.

1.3 Oxygen chemical potential and oxide concentration in mixed conductors

The oxygen vacancy concentration in a MIEC can be changed by altering $\mu_{\text{O}_2}^{\text{MIEC}}$; If the oxygen is exchanged by a gas, the exchange reaction is, in the Kröger-Vink notation, written as:



The oxide ion vacancy concentration in MIECS can be several percent of the total oxide site concentration. As the MIECs studied in this thesis transport the oxygen via oxide ion vacancies in the crystal structure, the vacancy concentration is one of the most important material parameters of a MIEC. A direct measure of the oxide vacancy concentration is the molar mass, which can be measured using thermogravimetry. The chemical potential of oxygen in a MIEC, $\mu_{\text{O}_2}^{\text{MIEC}}$ is highly dependent on the oxide ion vacancy concentration, and can serve as an indirect measure of the concentration of oxide ion vacancies, when direct measures are not available. If a MIEC is allowed to equilibrate in an unchanging gas, the equilibrium condition in terms of the standard Gibbs energy, $\Delta G_{\text{ox}}^\ominus$ and the chemical potentials of the reaction species, $\mu_{\text{O}_\text{O}^\times}$, $\mu_{\text{V}_\text{O}^{\bullet\bullet}}$, $\mu_{\text{e}'}$ and $\mu_{\text{O}_2}^{\text{gas}}$ are:

$$\Delta G_{\text{ox}}^\ominus = 2 \left(\mu_{\text{O}_\text{O}^\times} - \mu_{\text{V}_\text{O}^{\bullet\bullet}} \right) - 4\mu_{\text{e}'} - \mu_{\text{O}_2}^{\text{gas}} = 0 \quad (1.2)$$

The chemical potential of oxygen, $\mu_{\text{O}_2}^{\text{MIEC}}$, in a MIEC in equilibrium with a gas with a given chemical potential of oxygen $\mu_{\text{O}_2}^{\text{gas}}$ can then be defined as:

$$\mu_{\text{O}_2}^{\text{MIEC}} = 2 \left(\mu_{\text{O}_\text{O}^\times} - \mu_{\text{V}_\text{O}^{\bullet\bullet}} \right) - 4\mu_{\text{e}'} = \mu_{\text{O}_2}^{\text{gas}} \quad (1.3)$$

This allows us to label the state of the MIEC with the state of the gas with which it is in equilibrium (and vice versa). The oxygen chemical potential of a gas, $\mu_{\text{O}_2}^{\text{gas}}$, is a standardized function of the oxygen partial pressure and temperature:

$$\mu_{\text{O}_2}^{\text{gas}} = \mu_{\text{O}_2}^\ominus + RT \ln \left(p_{\text{O}_2}^{\text{gas}} / p_{\text{O}_2}^\ominus \right) \quad (1.4)$$

where R is the gas constant and T is the temperature. $p_{\text{O}_2}^\ominus$ and $p_{\text{O}_2}^{\text{gas}}$ are the oxygen partial pressures of a standard gas and investigated gas, respectively. Calculation of the oxygen chemical potential of the selected standard gas $\mu_{\text{O}_2}^\ominus$ is done using the IUPAC standards [10] (See Appendix A).

Eq. 1.3 points to an advantage of measuring the equilibrium oxide vacancy concentration, along with the μ_{O_2} of the surrounding gas. These data can be used in later measurements to calculate the oxygen vacancy concentration of a MIEC, by measuring the oxygen chemical potential of a gas in equilibrium with the MIEC.

Instead of describing the state of the MIEC by $\mu_{\text{O}_2}^{\text{MIEC}}$ it can be described by the concentration of oxide ions, $C_{\text{O}}^{\text{MIEC}}$. A gradient in $\mu_{\text{O}_2}^{\text{MIEC}}$, $\nabla\mu_{\text{O}_2}^{\text{MIEC}}$, can then (for small differences) be written in terms of a gradient in $C_{\text{O}}^{\text{MIEC}}$, $\nabla C_{\text{O}}^{\text{MIEC}}$ using the relation $\frac{d \ln x}{dx} = \frac{1}{x}$:

$$\nabla\mu_{\text{O}_2}^{\text{MIEC}} = RT\nabla \ln p_{\text{O}_2}^{\text{gas}} \simeq RT \frac{\nabla C_{\text{O}}^{\text{MIEC}}}{C_{\text{O}}^{\text{MIEC}}} \frac{\partial \ln p_{\text{O}_2}^{\text{gas}}}{\partial \ln C_{\text{O}}^{\text{MIEC}}} = 2RT \frac{\gamma}{C_{\text{O}}^{\text{MIEC}}} \nabla C_{\text{O}}^{\text{MIEC}} \quad (1.5)$$

where $\gamma = \frac{\partial \ln p_{\text{O}_2}^{\text{gas}}}{2\partial \ln C_{\text{O}}^{\text{MIEC}}}$ is the thermodynamic factor.

1.4 Diffusion in mixed conductors

As mentioned, the oxygen transport in the bulk of the mixed conductors described in this study, occurs by diffusion of oxide ions between oxide ion vacancy sites. In the literature, different parameters are used to describe the diffusion in the bulk of an MIEC. These parameters, and their relations, are described by Maier [11] and in the textbooks by Tilley [12] or Gellings and Bouwmeester [4]. While the parameters describe the same diffusion phenomena, the parameters assumes different driving forces of diffusion. Common to them all is that the driving force is the gradient of some physical property. In the following the parameters used directly to present data, and indirectly to convert literature data for comparison, in this thesis are listed.

The ambipolar conductivity, Σ

In MIECs the requirement of local electroneutrality causes the transport of electrons (e^-) and oxygen ions (O^{2-}) to be coupled. The ionic current must thus be balanced by a corresponding electronic current in the opposite direction. In the absence of external electrical fields, we are free to define the diffusing species in the material as "oxygen", O_2 , consisting of two oxide ions O^{2-} and four electron holes. The driving force for the transport is the gradient in the chemical potential of oxygen:

$$j_{\text{O}_2} = -\frac{1}{4^2 F^2} \frac{\sigma_e \sigma_{\text{O}}}{\sigma_e + \sigma_{\text{O}}} \nabla\mu_{\text{O}_2}^{\text{MIEC}} = -\frac{1}{4^2 F^2} \Sigma \nabla\mu_{\text{O}_2}^{\text{MIEC}}, \quad \Sigma = \frac{\sigma_e \sigma_{\text{O}}}{\sigma_e + \sigma_{\text{O}}} \quad (1.6)$$

where F is the Faraday constant, j_{O_2} is the oxygen flux, σ_e is the electronic conductivity and σ_{O} is the oxide ion conductivity. Σ is known as the ambipolar conductivity. When $\sigma_{\text{O}} \gg \sigma_e$, $\Sigma \simeq \sigma_e$ and when $\sigma_e \gg \sigma_{\text{O}}$, $\Sigma \simeq \sigma_{\text{O}}$.

Σ is convenient to use when characterizing the permeability of a membrane between two gas phases with a small, known, difference in p_{O_2} . If the surface resistance is ignored and if Σ and the p_{O_2} of the two gas phases, p'_{O_2} and p''_{O_2} , are known, the steady state flux can be calculated as:

$$j_{\text{O}_2} = -\frac{RT}{4^2 F^2} \int_{p'_{\text{O}_2}}^{p''_{\text{O}_2}} \Sigma d \ln p_{\text{O}_2} \quad (1.7)$$

The chemical diffusion coefficient, D_{chem}

When characterizing transients, where the spatial distribution of oxide ions changes with time, such as the transients of a conductivity relaxation measurement, many researchers use the chemical diffusion coefficient, defined using the relation between the flux and the gradient of the oxide ion concentration. To easily compare the measurement results of different authors, we will derive the chemical diffusion coefficient in terms of Σ . Combining Eq. 1.5 with Eq. 1.6 we can describe the transport with $\nabla C_{\text{O}}^{\text{MIEC}}$ as the driving force instead of $\nabla \mu_{\text{O}_2}^{\text{MIEC}}$, and get Ficks first law of diffusion:

$$j_{\text{O}_2} = -\frac{D_{\text{chem}}}{2} \nabla C_{\text{O}}^{\text{MIEC}}, \quad D_{\text{chem}} = \frac{4\gamma RT}{C_{\text{O}}^{\text{MIEC}}} \frac{1}{4^2 F^2} \Sigma \quad (1.8)$$

where D_{chem} is the chemical diffusion coefficient of oxide ions.

The usefulness of using $\nabla C_{\text{O}}^{\text{MIEC}}$ is evident, as mass balance in the MIEC is then especially simple to describe:

$$\frac{\partial C_{\text{O}}^{\text{MIEC}}}{\partial t} = \nabla \cdot \mathbf{j}_{\text{O}} \quad (1.9)$$

The vacancy diffusion coefficient, D_{V}

When most of the oxide ion sites in the structure are occupied, the number of oxide ion vacancy sites available for hopping, rather than the concentration of oxide ions, becomes the limiting factor for the oxygen permeation. The transport of oxide ions is thus proportional to the concentration of oxide ion vacancy sites, rather than the concentration of oxide ions. For small vacancy concentrations the transport equation becomes:

$$j_{\text{O}_2} = \frac{\gamma_{\text{V}}}{2} D_{\text{V}} \nabla C_{\text{V}}, \quad D_{\text{V}} = \frac{4RT}{C_{\text{V}}} \frac{1}{4^2 F^2} \Sigma, \quad \gamma_{\text{V}} = \gamma \frac{C_{\text{V}}}{C_{\text{O}}^{\text{MIEC}}} \quad (1.10)$$

where C_{V} is the vacancy concentration and γ_{V} is the thermodynamic factor associated with the oxygen vacancies.

The reduced diffusion coefficient D_{V}^0

As an oxide ion vacancy cannot move to a site which already contains an oxide ion vacancy (it takes an oxide ion to jump to a vacancy occupied site), the bulk transport is proportional to the factor $\left(1 - \frac{\delta}{3}\right)$ describing the fractional oxide ion occupancy of the oxide ion sites. This leads to the reduced diffusion coefficient, D_{V}^0 , which is independent of C_{V} apart from second order effects (such as C_{V} influencing the crystal structure or immobilization of vacancies due to ordering):

$$j_{\text{O}_2} = \frac{\gamma_{\text{V}}}{2} D_{\text{V}}^0 \left(1 - \frac{\delta}{3}\right) \nabla C_{\text{V}}, \quad D_{\text{V}}^0 = \frac{4RT}{C_{\text{V}} \left(1 - \frac{\delta}{3}\right)} \frac{1}{4^2 F^2} \Sigma \quad (1.11)$$

1.5 Surface oxygen exchange in mixed conductors

Diffusion in the bulk of an MIEC will dominate the oxygen permeation of a MIEC when the sample is thick, or when it is operating at high T where the surface exchange for the MIECs of this study becomes very fast. The permeation of thinner samples, or samples operating at lower T will, conversely, be limited by the processes involved in transforming oxygen molecules to oxide ions, and incorporating them in the lattice. When the permeation flux is sufficiently small, these processes can often be characterized by a linear relationship between driving force and permeation flux. In the following different transport parameters are listed. As in Sec. 1.4,

the parameters are defined assuming different material properties as the driving force for the transport.

The surface rate constant, k_O

A MIEC surface in chemical equilibrium with the surrounding gas phase will have equal amounts of oxygen leaving and entering the surface per unit time (the exchange flux). The surface rate constant, k_O is defined by the exchange flux as.

$$\vec{j}_O = \overleftarrow{j}_O = C_O^{\text{MIEC}} k_O \quad (1.12)$$

Here k_O is defined in relation to the exchange flux of O atoms - not O_2 molecules. This exchange flux can be measured using isotope exchange experiments.

The surface exchange coefficient, k

If the chemical potential of the solid phase, $\mu_{O_2}^{\text{MIEC}}$ is perturbed, while the the chemical potential of the gas phase, $\mu_{O_2}^{\text{gas}}$, is unchanged $\vec{j}_O \neq \overleftarrow{j}_O$, and a net oxygen flux in or out of the material is the result. For small perturbation the flux is proportional to the difference in chemical potential, $\Delta\mu_{O_2} = \mu_{O_2}^{\text{MIEC}} - \mu_{O_2}^{\text{gas}}$, and we can define a surface exchange coefficient, k :

$$j_{O_2} = -k\Delta\mu_{O_2} \quad (1.13)$$

The relation between k and k_O can be derived by a linear expansion [13]. We have:

$$j_{O_2} = \frac{d\vec{j}_{O_2}}{d\mu_{O_2}^{\text{MIEC}}} \Delta\mu_{O_2}^{\text{MIEC}} = \frac{1}{2} \left(\frac{dC_O^{\text{MIEC}}}{d\mu_{O_2}^{\text{MIEC}}} k_O + C_O^{\text{MIEC}} \frac{dk_O}{d\mu_{O_2}^{\text{MIEC}}} \right) \Delta\mu_{O_2} \quad (1.14)$$

The factor of $\frac{1}{2}$ is caused by $j_{O_2} = \frac{1}{2}j_O$. At uniform temperature $\Delta\mu_{O_2}^{\text{MIEC}} = \Delta RT \ln p_{O_2}$. Furthermore, for the MIEC materials in this study, $\frac{d \ln k_O}{d \ln p_{O_2}} = n$ where n is a positive reaction order, usually between 0.5 and 1. We have:

$$j_{O_2} = \frac{k_O C_O^{\text{MIEC}}}{2 RT} \left(\frac{1}{2\gamma} + n \right) \Delta\mu_{O_2} \quad (1.15)$$

As γ is typically > 100 for the perovskites and > 7 for the fluorites in this thesis, the second term is dominating the right side of the equation and we can approximate k_O as:

$$k_O = k \frac{2RT}{C_O^{\text{MIEC}} n} \quad (1.16)$$

The chemical rate constant k_{chem}

For a given T , the $\mu_{O_2}^{\text{gas}}$ of a gas can be uniquely labelled with its "equivalent oxygen concentration", $C_O^{\text{gas}} = C_O^{\text{MIEC}}$, where C_O^{MIEC} is the oxygen concentration of an MIEC in equilibrium with the gas. We stress that C_O^{gas} is *not* the concentration of O atoms in the gas but the concentration of oxide ions in the MIEC when the gas and MIEC are in chemical equilibrium. We can then define a "concentration difference" across the surface $\Delta C_O = C_O^{\text{gas}} - C_O^{\text{MIEC}}$. Combining Eq. 1.5 and 1.13 we then get:

$$j_{O_2} = \frac{k_{\text{chem}}}{2} (C_O^{\text{gas}} - C_O^{\text{MIEC}}), \quad k_{\text{chem}} = \frac{4RT\gamma}{C_O^{\text{MIEC}}} k \quad (1.17)$$

k_{chem} is thus useful when characterizing transients, where the spatial distribution of oxide ions changes with time, such as the transients of a conductivity relaxation measurement. It is thus widely used in the literature.

The surface resistance r_s

The surface exchange of an MIEC can be characterized by the Nernst voltage across its surface, V_{surface} corresponding to the difference in μ_{O_2} across the surface. V_{surface} is, for small ionic currents, proportional to the ionic current through the surface, i , and the surface resistance, r_s is defined as.

$$r_s = \frac{\Delta\mu_{\text{O}_2}}{4Fi} = \frac{V_{\text{surface}}}{i} \quad (1.18)$$

We have:

$$j_{\text{O}_2} = \frac{i}{4F} = \frac{V_{\text{surface}}}{4Fr_s} = k\Delta\mu_{\text{O}_2}, \quad k = \frac{1}{16F^2r_s} \quad (1.19)$$

The relations between the different transport parameters for materials with $\sigma_e \gg \sigma_{\text{O}}$ are summarized in Fig. 1.1.

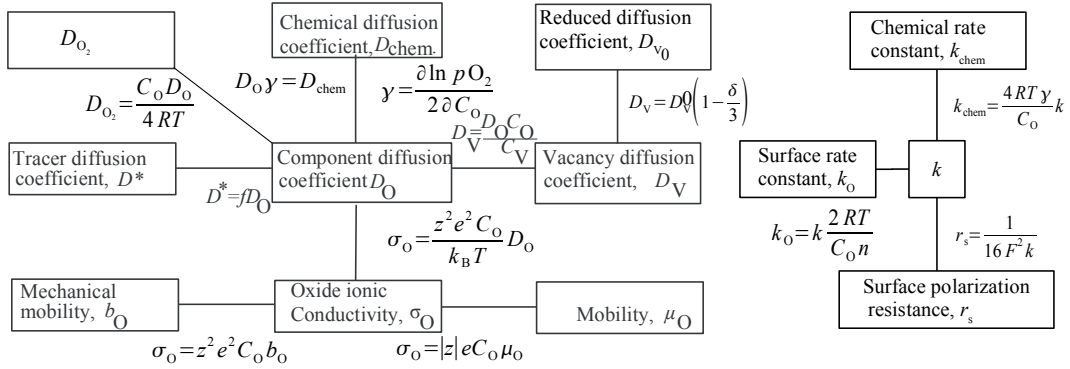


Figure 1.1: Relations between transport parameters. f is the correlation factor (0.69 for perovskites); γ is the thermodynamic enhancement factor; z is the charge number of the ionic species i.e. -2 for O^{2-} ; k_{B} is the Boltzmann constant; e is the electronic charge; δ is the number of vacancies per formula unit; C_{O} is the concentration of oxide ions; C_{V} is the concentration of oxide ion vacancies; R is the gas constant; T is the temperature.

1.6 Electrolyte probes, sensors and pumps

A large part of this study has been devoted to developing electrochemical cell designs used as measurement devices. The basic cell consists of two electrodes separated by an oxide electrolyte. If the electrochemical cell is placed between two external phases with different oxygen chemical potentials, it will approach an equilibrium between the oxygen in the two external phases and the oxide ions in the corresponding electrolyte surfaces. This equilibrium is a balance between the oxygen activity and the Nernst voltage across the cell. The relationship, at equilibrium, between the oxygen activity of the external phases and the cell voltage, as measured between electrodes placed on the two interfaces, is:

$$\mu'_{\text{O}_2} - \mu''_{\text{O}_2} = 4FV_{\text{ele}} \quad (1.20)$$

where μ'_{O_2} and μ''_{O_2} are the oxygen chemical potential in each of the external phases, and V_{ele} is the voltage between electrodes placed at the two external phases. The cell can thus be used as a μ_{O_2} sensor and provide precise information about the μ_{O_2} of the phases with which it is in

contact.

Applying a voltage to an electrochemical cell will turn it into an oxygen pump. As four electrons pumped in the external circuit will correspond to one oxygen molecule passing between the electrodes of the cell the relationship between pumping current and oxygen transfer is:

$$j_{\text{O}_2} = \frac{i_{\text{pump}}}{4F} \quad (1.21)$$

Where i_{pump} is the area specific pumping current. Working as an oxygen pump, the cell provides both control of the μ_{O_2} of the phases with which it is in contact, and a precise measure of the ionic current passing through the cell to maintain this μ_{O_2} . Electrochemical cells have been used for a number of purposes in this thesis, as described in the following.

To map the vacancy concentration of MIEC powder in different temperatures and atmospheres, coulometric titration has been used in combination with thermogravimetry. In coulometric titration the powder to be investigated is placed in a sealed chamber, and oxygen transport in and out of the cell is controlled by an electrochemical cell. This arrangement means that the oxygen content can be measured with high precision. Examples of coulometric titration experiments are presented in Chapter 4 and Chapter 6.

Measuring the oxygen permeation of dense MIEC membranes, shaped as flat cylinders, was done by placing the membranes on top of an electrochemical cell with two sets of electrodes. Application of a voltage between one set of electrodes forces a current passing through the MIEC. The other set of electrodes then provides in-situ measurements of μ_{O_2} . Finally, a cone shaped electrolyte probe - an electrochemical cell with the MIEC membrane acting as one electrode - measures the difference in the chemical potential of the gas above the membrane, $\mu_{\text{O}_2}^{\text{gas}}$ and the chemical potential of the MIEC, $\mu_{\text{O}_2}^{\text{MIEC}}$, providing information about the surface polarization resistance, r_s . The combination of these electrochemical cells is the electrochemical equivalent of a steady state four point resistance measurement. This allows an unmatched precision, which traditional electrochemical methods relying on transient responses have difficulties to mimic [14–19]. A detailed description of this setup is given in Chapter 2 and measurements using this setup are presented in Chapter 5.

1.7 Evaluation of precision and accuracy

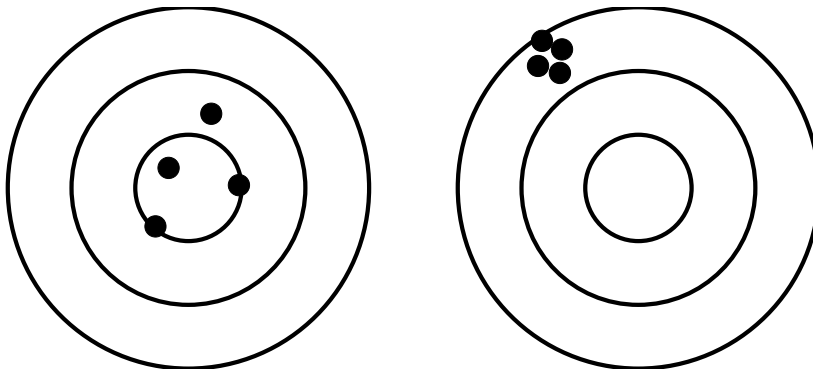


Figure 1.2: *The error of a series of measurements shown as shots on a target - the center represents zero error. Left a measurement with high accuracy and low precision. Right a measurement with low accuracy and high precision.*

Throughout this thesis, results from different measurement methods and models are compared. In order to evaluate the reasons for discrepancies between methods, it is necessary to investigate the confidence interval and error of each data point. Two different types of errors

exist; systematic errors and statistical (random) errors.

Statistical errors are caused by noise and will affect the precision of a measurement. Noise is random, or seemingly random, fluctuations of the measurement signal. Noise can be removed by increasing the number of measurements; the precision is proportional to $\frac{1}{\sqrt{N}}$ where N is the number of measurements. In Fig. 1.2 the left example shows a measurement with large statistical error (i.e. low precision). The average of the measurements is however close to the center.

Systematic errors will affect the accuracy of the measurement. A wrongly set zero point in a voltmeter, or an unwanted thermovoltage in a measurement circuit are examples of systematic errors, which will affect all measurements. This means that the average of a series of measurements is offset from the true value. Increasing the number of measurements will not remove this error. In Fig. 1.2 the right example shows a measurement with small statistical error (i.e. high precision), which is suffering from a large systematic error (i.e. low accuracy).

The statistical error of parameters extracted from a measurement can be estimated by comparing fits of a model to the measured data [20]. Assuming that the model is perfect, the best possible fit will yield the expected value, $E(t_i)$, of each data point, t_i . The standard deviation, σ , of the individual points in a fit, is then estimated as the square root of the mean square deviation (MSD) between these expectation values and the measurements $V(t_i)$:

$$\sigma = \sqrt{\sum_{i=1}^N \left(\frac{(E(t_i) - V(t_i))^2}{N} \right)} \quad (1.22)$$

In that case the χ^2 value of a fit, $F(t)$ can be calculated as:

$$\chi^2 = \sqrt{\sum_{i=1}^N \left(\frac{(F(t_i) - V(t_i))^2}{\sigma^2} \right)} = \frac{\text{MSD}}{\text{MSD}_{\text{Best}}} \quad (1.23)$$

where MSD_{Best} is the mean square deviation of the best possible fit. The error bars assigned to a fitting parameter is then defined as the values of the parameter that will lead to a $\chi^2 < 2$ corresponding to a 68% confidence interval. The width of this interval is referred to as the *Error*, E_x where the subscript x refers to the parameter.

The assumption of a perfect model is not necessarily true. The relaxation measurements of Chapters 2 and 3, for instance, are complex functions of time, where inaccuracies will build up during the relaxation, making perfect modelling impossible. The MSD of the relaxations in this thesis are thus determined by inadequacies of the modelling, rather than statistical scatter of the measured voltages. Using χ^2 to estimate the *precision* is then wrong - it is the *accuracy* that is measured. This accuracy, however, has some of the properties of precision: It is limited by unknown parameters which the model can not account for; and it is possible to quantify its contribution to the error using a χ^2 analysis.

The steady state measurements of Chapters 2, 3 and 5 are simpler. In the steady state measurements, a large number of high precision measurements show that linear relationships exist between the applied driving force and the ionic flux for small fluxes. We therefore believe that a first order polynomial is a perfect model for these measurement. In that case Eq 1.23 will give the error as the confidence interval of the precision.

When doing regression analysis any fits to measured values are defined as within the confidence interval, if the MSD between measured data and the model fit is less than twice the MSD of the best possible fit. A brute force search in the entire parameter space is used to write down all the fits within the confidence interval. If a parameter value is present in one of the fits, it is considered within the confidence interval. For instance, in Figure 2.15b the confidence intervals of D and k are the projections on the horizontal and vertical axis of the round shape marked

with "2", respectively. Although this is a crude and very time consuming method even with fast computers, it takes all correlations into account.

Chapter 2

Determination of Oxygen Transport Properties from Flux and Driving Force Measurements Using an Oxygen Pump and an Electrolyte Probe

Abstract

We demonstrate, that an electrolyte probe can be used to measure the difference in oxygen chemical potential across the surface, when an oxygen flux is forced through an oxygen permeable membrane disc. The oxygen flux as well as the total oxygen chemical potential difference is carefully controlled by an oxygen pump. The developed method is tested on a $(\text{La}_{0.6}\text{Sr}_{0.4})_{0.99}\text{Co}_{0.2}\text{Fe}_{0.8}\text{O}_{3-\delta}$ membrane. An LSM|YSZ|LSM oxygen pump was attached to one side of the membrane. A conical $\text{Ce}_{0.9}\text{Gd}_{0.1}\text{O}_{1.95}$ (CG10) electrolyte probe was pressed against the other side of the membrane. The voltage difference between the base and the tip of the CG10 probe was recorded with an applied oxygen flux through the membrane. This voltage was used to extract precise values of the surface exchange rate constant, k_{O} . Using these values of k_{O} , the reduced diffusion coefficient, D_{V}^0 , could be extracted from data of the flux and the oxygen chemical potential difference across the membrane measured with the oxygen pump. Furthermore, upon a gas change, the transient voltage signals of the oxygen pump and the probe could be fitted to give values of D_{V}^0 and k_{O} .

2.1 Introduction

Mixed ionic and electronic conductors (MIECs) are interesting materials for cathodes in solid oxide fuel cells [4, 5]. Other uses of MIECs exist in the field of controlled oxidation, oxygen production, or reactors for partial oxidation of methane to synthesis gas [7, 8]. Current research focuses on identifying materials combining good mechanical, catalytic and oxygen permeation properties. To rationalize this process, accurate measurement methods and models are needed, to evaluate the catalytic properties and the ionic and electronic transport parameters. Numerous studies using methods like conductivity relaxation [15, 16, 18, 19] and isotopic exchange [14, 17] characterize both the ionic exchange process on the surface of the MIEC and the bulk

transport of ions, based on the fitting of a single transient response. Other studies have investigated the oxygen permeability of membranes positioned between gas flows of different oxygen chemical potential [21–23]. These conventional methods lack precision as the surface exchange process and the bulk transport process can be difficult or impossible to distinguish from each other. Several studies [4, 19, 24, 25] show, for instance, the difficulty in measuring the surface exchange rate of perovskite MIEC samples thicker than 0.1 mm at high temperature and oxygen partial pressure, where the surface exchange reaction is so fast that transport is completely dominated by the bulk. A possible solution is to investigate samples of different geometry (thick membranes to determine the bulk transport, thin films for surface sensitivity). This is, however, a cumbersome and not always satisfactory approach as the relaxations of thin films are very fast at high temperatures. Furthermore, the surface properties of thin films are not necessarily the same as those of bulk samples as they depend heavily on the substrate and preparation method [26].

The objective of this study is to demonstrate a setup with improved measurement precision, combining a surface sensitive electrolyte probe and an oxygen pump. Firstly, the required equipment is detailed; secondly, the basic theory of electrolyte sensors and mixed conductors is treated; thirdly, the models needed to interpret the measurements are described; and finally, details of the data treatment and minor corrections are discussed. The transport properties of the well characterized perovskite MIEC $(\text{La}_{0.6}\text{Sr}_{0.4})_{0.99}\text{Co}_{0.2}\text{Fe}_{0.8}\text{O}_{3-\delta}$ (LSCF) measured by the method are then presented, followed by a discussion of possible misinterpretations and inaccuracies of the models.

Oxygen pumps, i.e. electrically controlled electrochemical cells, have frequently been used to measure oxygen fluxes with high precision in titration and permeation studies [24, 27–30]. In this study, the oxygen pump is used to measure the oxygen flux passing through a membrane; as the flux is directly proportional to the electronic current applied between the pumping electrodes, the oxygen flux can be measured with very high accuracy. Furthermore, a set of reference electrodes on the pump can be used to measure the oxygen chemical potential, μ_{O_2} , in-situ. Electrolyte probes have been used to measure properties of oxygen ion conducting materials by e.g. Foulletier *et al.* [31] and Wiemhöfer *et al.* [32]. Their potential for measuring the surface exchange kinetics was proposed by Bouwmeester [4]. The electrolyte probe in this study measures the difference in chemical potential of oxygen across the membrane surface as a voltage. The combination of a local probe and a precise flux measurement allows the precise determination of both the bulk transport and surface exchange parameters while only applying a small steady state oxygen chemical potential difference across the membrane ensuring an almost homogeneous oxide ion distribution. Furthermore, relaxation measurements are made by application of a stepwise gas composition change on one side of the membrane. This causes a relaxation of the oxide ion distribution in the membrane. The resulting transient response in the driving force gradients provides another experimental route to determine the bulk transport and surface exchange parameters.

2.2 Experimental

2.2.1 Sample preparation

LSCF powder was prepared by the glycine pyrolysis process [33]. The powder was calcined at 900°C for 12 h, and ball milled using 5 mm × 5 mm cylindrical ZrO₂ balls in a 500 ml polyethylene container with ethanol for 24 h at 200 RPM. A flat cylindrical membrane was shaped from this powder using a uniaxial pressure of 70 MPa. This membrane was isostatically compressed in an evacuated latex container suspended in water at a pressure up to 325 MPa. The membrane was sintered at 1300°C for 12 hours. The sintered membrane was polished with SiC polishing sheets and diamond suspensions (particle size down to 1 μm). The sintered and polished membrane had a diameter of 20.3±0.1 mm, a thickness of 2.253±0.005 mm and a density of 5965 kg m⁻³ (95%

of bulk). X-ray diffraction revealed a single phase hexagonal perovskite with cell parameters $a=5.487 \text{ \AA}$ and $c=13.48 \text{ \AA}$.

2.2.2 Setup and measurement procedure

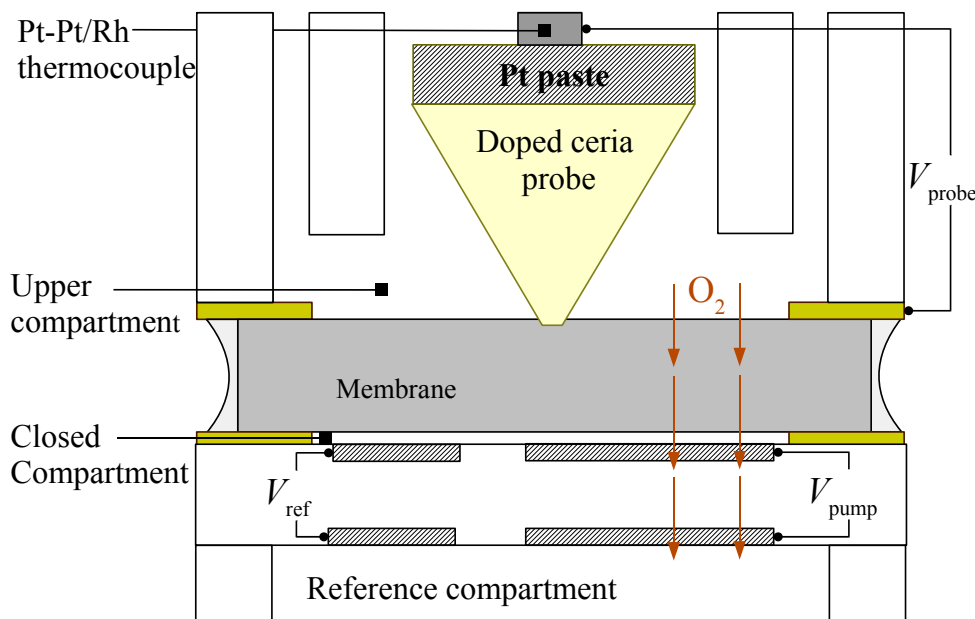


Figure 2.1: *The measurement setup.*

The experimental setup is shown in Fig. 2.1. The MIEC membrane is placed between two $300 \mu\text{m}$ thick gold sealing rings. The inner diameter of the gold rings is 14 mm and defines the perimeter of the active surface of the membrane. The closed compartment is defined by the membrane, the lower gold sealing ring and an $\text{Y}_{0.16}\text{Zr}_{0.84}\text{O}_{1.92}$ (YSZ) oxygen pump. Two pairs of electrodes are painted on the oxygen pump. Each pair has one electrode in the closed compartment, and one electrode in the reference compartment, which is flushed with an air flow ($> 2 \cdot 10^{-6} \text{ m}^3/\text{s}$ or 120 ml/min at ambient conditions). The *pumping* electrode pair is made of a mixture of porous 50% YSZ+50% $\text{La}_{0.75}\text{Sr}_{0.25}\text{MnO}_3$ (YSZ/LSM) with porous Pt as current collector and is used to pump oxygen in and out of the closed compartment. The *reference* electrode pair is made of porous Pt (sintered Ferro Pt paste), and is used to measure the difference in oxygen chemical potential between the closed compartment and the reference compartment. The circumference of the membrane is sealed using a glass seal. Above the membrane an alumina cylinder defines an upper compartment. Two concentric alumina pipes terminate in the upper compartment. The inner pipe feeds gas (the "flow gas") to the upper compartment while the outer pipe transports the exhaust gas to a Pt|YSZ|Pt p_{O_2} sensor. The gas flow through the upper compartment is $1.67 \cdot 10^{-6} \text{ m}^3/\text{s}$ (100 ml/min measured at ambient conditions) of air diluted with N_2 . Inside the inner pipe a spring loaded thermocouple applies an electrical contact and a downward mechanical force to a pointed electrolyte probe in contact with the membrane surface. The pointed probe was made from $\text{Ce}_{0.9}\text{Gd}_{0.1}\text{O}_{1.95}$ (CG10). A cylinder was shaped using an uniaxial pressure of 70 MPa. It was then isostatically compressed in an evacuated latex container suspended in water at a pressure up to 325 MPa. After sintering at 1323 K the CG10 cylinder was mechanically sharpened and resintered at 1873 K. All electrical contacts were made using platinum and gold wires. A Solartron 1250/1286 setup was used as a programmable current source with a Keithley 2700 multimeter/data collector.

2.3 Defect chemistry and transport properties of LSCF

In this section, the defect chemistry and transport properties of the test material - LSCF - are described. Two models for interpretation of steady state and relaxation measurements, respectively, are presented.

2.3.1 Defect chemistry

The release and incorporation of oxygen in LSCF can in the Kröger-Vink notation be written:



At equilibrium the chemical potential of oxygen, μ_{O_2} is the same in the gas and solid phase. This allows us to label the state of the LSCF MIEC with the state of the gas with which it is in equilibrium, and vice versa. The chemical potential of oxygen, $\mu_{\text{O}_2}^{\text{MIEC}}$, in an MIEC in equilibrium with a gas with a given chemical potential of oxygen $\mu_{\text{O}_2}^{\text{eq.gas}}$ can then be defined as:

$$\mu_{\text{O}_2}^{\text{MIEC}} = \mu_{\text{O}_2}^{\text{gas}} = \mu_{\text{O}_2}^{\ominus} + RT \ln \left(p_{\text{O}_2}^{\text{eq.gas}} / p_{\text{O}_2}^{\ominus} \right) \quad (2.2)$$

Where R is the gas constant and T is the temperature. $p_{\text{O}_2}^{\text{eq.gas}}$ and $p_{\text{O}_2}^{\ominus}$ are the oxygen partial pressures of the equilibrium and standard gas, respectively. The oxygen chemical potential of the selected standard gas $\mu_{\text{O}_2}^{\ominus}$ can be calculated using the IUPAC standards [10] (See appendix A). Likewise, the equivalent oxide concentration in the gas, $C_{\text{O}}^{\text{gas}}$, is defined as the oxide concentration $C_{\text{O}}^{\text{MIEC}}$ in the MIEC with which it is in equilibrium. A difference in $\mu_{\text{O}_2}^{\text{MIEC}}$, $\Delta\mu_{\text{O}_2}^{\text{MIEC}}$, can then (for small differences) be written in terms of a difference in $C_{\text{O}}^{\text{MIEC}}$, $\Delta C_{\text{O}}^{\text{MIEC}}$:

$$\Delta\mu_{\text{O}_2}^{\text{MIEC}} = RT \Delta \ln p_{\text{O}_2}^{\text{eq.gas}} \simeq RT \frac{\Delta C_{\text{O}}^{\text{MIEC}}}{C_{\text{O}}^{\text{MIEC}}} \frac{\partial \ln p_{\text{O}_2}^{\text{eq.gas}}}{\partial \ln C_{\text{O}}^{\text{MIEC}}} = 2RT \frac{\Delta C_{\text{O}}^{\text{MIEC}}}{C_{\text{O}}^{\text{MIEC}}} \gamma \quad (2.3)$$

where $\gamma = \frac{\partial \ln p_{\text{O}_2}^{\text{eq.gas}}}{2 \partial \ln C_{\text{O}}^{\text{MIEC}}}$ is the thermodynamical factor.

The relation at equilibrium between μ_{O_2} and $C_{\text{O}}^{\text{MIEC}}$ for a given $p_{\text{O}_2}^{\text{eq.gas}}$ has been determined using thermogravimetry and coulometric titration. A description of these measurements is found in Chapter 4. The values for the thermodynamic factor, γ , and oxygen nonstoichiometry parameter, δ , are reproduced in Fig. 2.2.

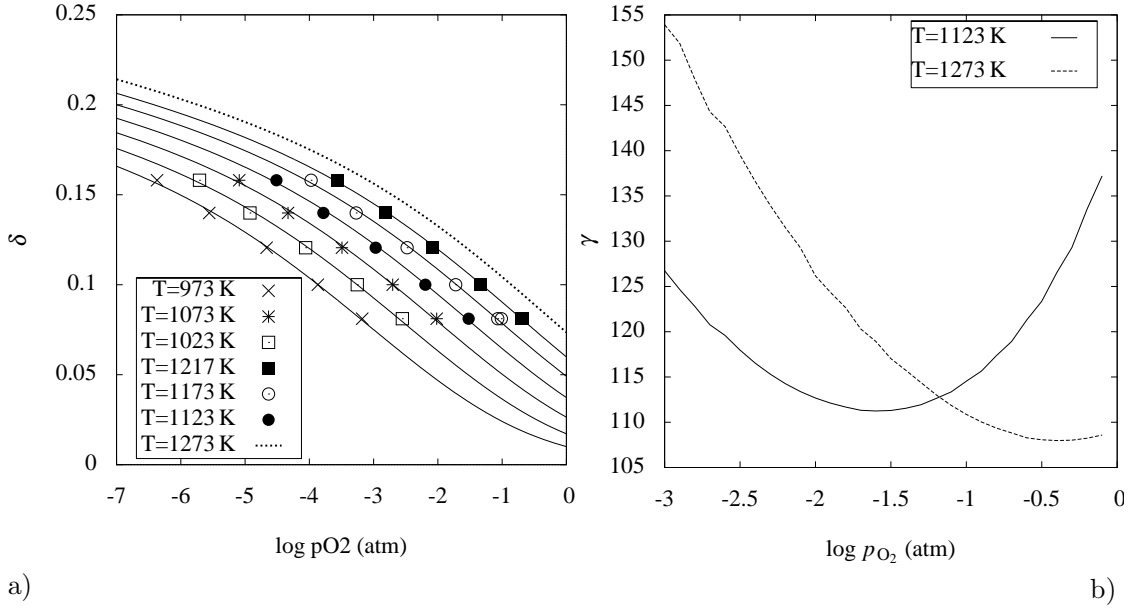


Figure 2.2: a) δ as a function of p_{O_2} . Points are measured values and the lines are from a model fit used to interpolate the data (see Chapter 4). b) The thermodynamic factor, γ , as a function of p_{O_2} derived from the model lines in a).

2.3.2 Transport properties

In this study different parameters are used to describe the oxygen transport in the bulk and across the surface. These parameters are described by Maier [11] and in the textbooks by Tilley [12] or Gellings and Bouwmeester [4]. In LSCF, local electroneutrality causes the transport of electrons (e^-) and oxygen ions (O^{2-}) to be coupled. In LSCF, the ionic conductivity is controlling the transport of both electrons and ions as the electronic conductivity is much larger than the ionic conductivity. In the absence of external electrical fields, we are free to define the diffusing species in the material as "oxygen", O_2 , consisting of two oxide ions O^{2-} and four electron holes. From Gellings and Bouwmeester [4]:

$$j_{O_2} = -\frac{1}{4^2 F^2} \frac{\sigma_e \sigma_O}{\sigma_e + \sigma_O} \nabla \mu_{O_2}^{MIEC} \simeq -D_{O_2} \nabla \mu_{O_2}^{MIEC}, \quad D_{O_2} = \frac{\sigma_O}{4^2 F^2} \quad (2.4)$$

where F is the Faraday constant, j_{O_2} is the oxygen flux, σ_e is the electronic conductivity and σ_O is the oxide ion conductivity. D_{O_2} is the diffusion coefficient and is defined under the assumption (true for LSCF) that $\sigma_O \ll \sigma_e$. Combining Eq. 2.3 with Eq. 2.4 we get Ficks first law of diffusion:

$$j_{O_2} = -\frac{D_{chem}}{2} \nabla C_O^{MIEC}, \quad D_{chem} = \frac{4\gamma RT}{C_O^{MIEC}} D_{O_2} \quad (2.5)$$

where D_{chem} is the chemical diffusion coefficient of oxide ions. From D_{chem} we obtain the oxygen atom self diffusion coefficient D_O as $D_{chem} \gamma^{-1}$. As most of the oxide ion sites in the structure are occupied, the diffusion of oxide ions is controlled by the number of oxide ion vacancy sites available. For small vacancy concentrations the transport equation becomes:

$$j_{O_2} = \frac{\gamma_V}{2} D_V^0 \left(1 - \frac{\delta}{3}\right) \nabla C_V, \quad D_V^0 = \frac{4RT}{C_V \left(1 - \frac{\delta}{3}\right)} D_{O_2}, \quad \gamma_V = \gamma \frac{C_V}{C_O^{MIEC}} \quad (2.6)$$

CHAPTER 2. DETERMINATION OF OXYGEN TRANSPORT PROPERTIES FROM FLUX AND DRIVING FORCE MEASUREMENTS USING AN OXYGEN PUMP AND AN ELECTROLYTE PROBE

where D_V^0 is the reduced diffusion coefficient, C_V is the vacancy concentration and γ_V is the thermodynamic factor associated with the oxygen vacancies. The term $\left(1 - \frac{\delta}{3}\right)$ was proposed by Lankhorst [24] because a vacancy can not diffuse to a vacant oxide site. We expect that D_V^0 is independent of C_V apart from second order effects (such as C_V influencing the crystal structure or immobilization of vacancies due to ordering). When interpreting our measurements, D_V^0 is therefore used as a fitting parameter.

When the surface is brought out of equilibrium with the surrounding atmosphere, a step in μ_{O_2} , $\Delta\mu_{O_2}$, exists at the surface. Assuming a linear response of the flux to the step in μ_{O_2} we can define a surface exchange coefficient, k , and an equivalent surface resistance r_s .

$$j_{O_2} = -k\Delta\mu_{O_2} = -\frac{1}{4^2 F^2 r_s} \Delta\mu_{O_2} \quad (2.7)$$

The relations between the different transport parameters are summarized in Fig. 2.3.

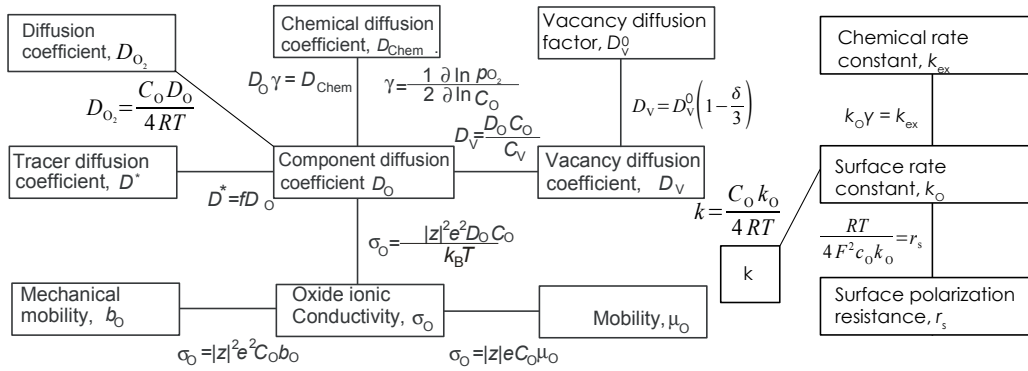


Figure 2.3: Relations between transport parameters in LSCF. f is the correlation factor (0.69 for perovskites as LSCF). γ is the thermodynamic enhancement factor. z is the charge number of the ionic species i.e. -2 for O^{2-} . k_B is the Boltzmann constant. e is the electronic charge and δ is the number of vacancies per formula unit. C_O is the concentration of oxide ions. C_V is the concentration of oxide ion vacancies. R is the gas constant and T is the temperature.

2.3.3 Steady state model

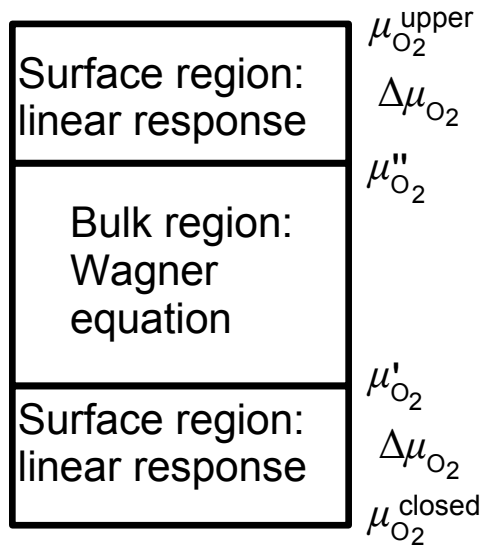


Figure 2.4: Sketch of the model used for analysis of steady state permeation.

To fit data recorded during steady state permeation measurements, a one dimensional numerical model based on the Wagner equation [34] combined with oxygen exchange at the surface is used. The Wagner equation is obtained from integration of Eq. 2.4:

$$j_{O_2} = -\frac{1}{4^2 F^2 L} \int_{\mu_{O_2}^{'}}^{\mu_{O_2}^{''}} \frac{\sigma_e \sigma_O}{\sigma_e + \sigma_O} d\mu_{O_2} \quad (2.8)$$

where $\mu_{O_2}^{'}$ and $\mu_{O_2}^{''}$ are the chemical potentials of oxygen at each interface (just inside the bulk - see Fig. 2.4).

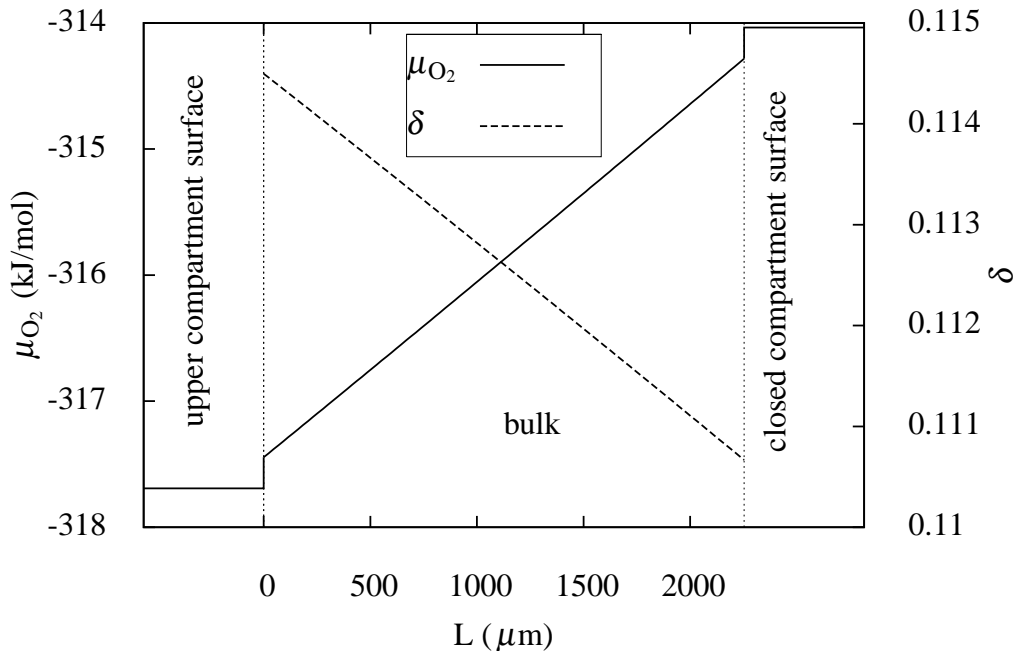


Figure 2.5: An example of the chemical potential profile, and the δ value of the membrane in the experiment shown in Fig. 2.9 calculated using the steady state model.

The μ_{O_2} profile in Fig. 2.5 has been calculated by combination of Eq. 2.7 at the surfaces and Eq. 2.8 in the bulk. The calculation was done with $i_{\text{pump}} = -100 \text{ A/m}^2$ and all material properties as determined for LSCF at $T = 1248 \text{ K}$ and $p_{O_2} = 4 \text{ kPa}$. The vertical parts are the discrete jumps in μ_{O_2} at the surfaces, and the apparently linear part is in the bulk. The linearity is achieved as very small gradients in μ_{O_2} are applied because the oxygen pump allows very precise control of the oxygen flux. The need for a large signal/noise ratio requires a current density of more than 10 A/m^2 , but Fig. 2.5 shows that even at $i_{\text{pump}} = -100 \text{ A/m}^2$ ($I_{\text{pump}} = 15 \text{ mA}$) only a very small variation in δ is imposed, and the transport parameters are therefore almost constant throughout the membrane.

The gold seals act as apertures for the surface exchange (see Fig. 2.1) but the membrane cross-section is wider than these apertures, resulting in an overestimation of D_V^0 . D_V^0 can be corrected by multiplying with a membrane geometry dependent factor f_c (for the membrane of this study it has a value of 0.93) [35].

2.3.4 Relaxation model

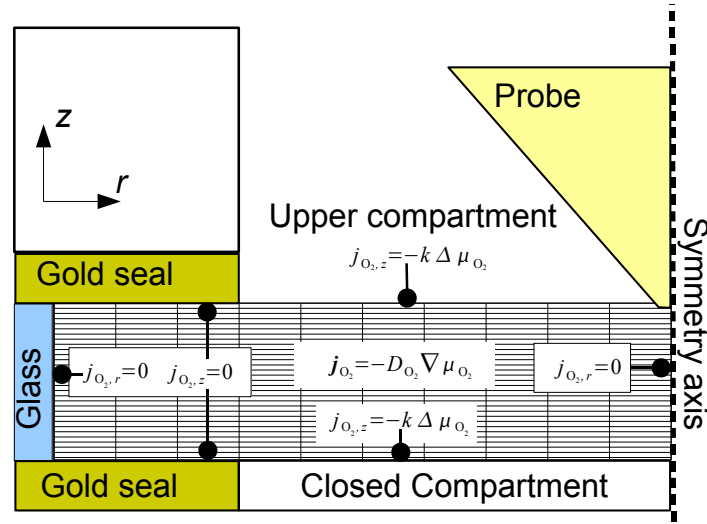


Figure 2.6: Sketch of the model used for analysis of relaxation measurements.

When changing the p_{O_2} of the flow gas in the upper compartment the membrane will adjust its δ value to the value of μ_{O_2} . This relaxation can be fitted with an appropriate model. When the membrane is not in steady state, the time dependence of $\mu_{O_2}^{\text{MIEC}}$ is governed by conservation of mass:

$$\frac{\partial C_O^{\text{MIEC}}}{\partial t} = \nabla \cdot \mathbf{j}_O \quad (2.9)$$

where t is the time. Combining with Eq. 2.3 we get:

$$\frac{\partial \mu_{O_2}^{\text{MIEC}}}{\partial t} = 2 \frac{2RT\gamma}{C_O^{\text{MIEC}}} \nabla \cdot \mathbf{j}_{O_2} \quad (2.10)$$

Equations 2.4, 2.7, and 2.10 are solved using an iterative algorithm in a cylindrical finite element mesh. The finite element mesh consists of 20 segments in the longitudinal dimension and 10 in the radial dimension. Using more segments than the above numbers did not change the results significantly. The model geometry and boundary conditions is outlined in Fig. 2.6.

When fitting the relaxation data, D_V^0 is used as the fitting parameter; D is calculated from D_V^0 for each spatial segment of the membrane. D_V^0 is assumed constant for the entire membrane.

2.4 Measurements using an oxygen pump and an electrolyte probe

In this section the basic principle of using electrolytes to measure chemical potential differences, and the operation principle of the oxygen pump, is described. An area specific conductance of the membrane is introduced and a few necessary corrections are treated. Finally, the same principle is used to give an interpretation of the signal from an electrolyte probe along with a few corrections.

2.4.1 Oxygen chemical potential measurement

The basic principle behind both the probe and the oxygen pump is using oxide conducting electrolytes to measure differences in the chemical potential of oxygen. An oxide conducting electrolyte placed between two external phases with different oxygen chemical potential, will approach an equilibrium between the oxide or oxygen in the two external phases and the oxide in the electrolyte surfaces. The relationship, at equilibrium, between the oxygen activity of the external phases and cell voltage, as measured between electrodes placed on the two interfaces, is:

$$\mu'_{\text{O}_2} - \mu''_{\text{O}_2} = 4FV_{\text{ele}} \quad (2.11)$$

where μ'_{O_2} and μ''_{O_2} are the oxygen chemical potential in each of the external phases, and V_{ele} is the voltage between the two electrolyte|external phase interfaces.

2.4.2 The oxygen pump

The YSZ oxygen pump is an electrochemical cell with an YSZ electrolyte. It is assumed that the following reaction takes place at the pumping and reference electrodes:



Combining Eqs. 2.2 and 2.11, the Nernst equation governing the relationship between oxygen activity and cell voltage becomes:

$$p_{\text{O}_2}^{\text{gas}} = p_{\text{O}_2}^{\text{ref}} \cdot \exp\left(\frac{4FV_{\text{ref}}}{RT}\right) \quad (2.13)$$

$p_{\text{O}_2}^{\text{gas}}$ is the oxygen partial pressure of the gas in the closed compartment, $p_{\text{O}_2}^{\text{ref}}$ is the p_{O_2} of the gas in the reference compartment (air in these measurements) and V_{ref} is the voltage between the reference electrodes. As four electrons pumped in the external circuit will correspond to one oxygen molecule passing between the electrodes of the cup the relationship between pumping current and oxygen transfer is:

$$j_{\text{O}_2} = \frac{I_{\text{pump}}}{4F} \quad (2.14)$$

Where I_{pump} is the pumping current.

The area specific conductance, G

In the setup of Fig. 2.1 the ionic current through the membrane in steady state must equal the ionic current through the pump. In this case an area specific conductance, G , of the membrane can be defined as:

$$G = \frac{i_{\text{pump}}}{\Delta V_{\text{Nernst}}}, \quad i_{\text{pump}} = I_{\text{pump}}/A_{\text{MIEC}} \quad (2.15)$$

$$\Delta V_{\text{Nernst}} = V_{\text{closed}} - V_{\text{upper}} = V_{\text{ref}} - V_{\text{ref}}^0 \quad (2.16)$$

where i_{pump} is the area specific current, and A_{MIEC} is the exposed area of the MIEC membrane. ΔV_{Nernst} is the difference in the Nernst voltages between the gas in the upper compartment, V_{upper} , and the gas in the closed compartment, V_{closed} , with the reference compartment gas as a common reference. $V_{\text{closed}} = V_{\text{ref}}$ are measured by the reference electrodes of the oxygen pump, with the air in the reference compartment providing the reference μ_{O_2} . V_{ref}^0 is measured at zero flux, where the flow gas of the upper compartment is in equilibrium with the gas in the closed compartment (i.e. $V_{\text{upper}} = V_{\text{closed}}$). As the Nernst voltage measures the oxygen chemical potential, which is the driving force of both the bulk (Eq. 2.7) and the surface oxygen ion transport (Eq. 2.8), G can be expected to be independent of the flux if σ_{O} , σ_{e} and the surface resistance, r_s , are independent of the flux; this is only expected true for very small fluxes. G can in this case be extracted with good accuracy as the slope of a plot of steady state values of i_{pump} as a function of ΔV_{Nernst} . If the surface resistance is small, G can be converted to an ionic conductivity:

$$\sigma_{\text{O}} = \frac{Gf_c}{L} \quad (2.17)$$

by dividing with the membrane thickness L and multiplying with the geometric factor f_c .

Effect of gas diffusion in the closed compartment

In the closed compartment V_{ref} is measured using two reference electrodes painted on either side of the pump. As the gas in the compartment is not stirred, an oxygen concentration gradient is present between the reference electrode and the membrane when an ionic current runs through the membrane. The diffusion coefficient of O_2 in N_2 at 1273 K is $2.6 \cdot 10^{-4} \text{ m}^2/\text{s}$ [36]. As the distance between the electrode and the membrane is 0.3 mm, the p_{O_2} difference needed to support a large 130 A/m^2 pumping current would be 5 Pa according to Ficks first law of diffusion. This is much smaller than the difference measured with ΔV_{Nernst} which in this case is more than 100 Pa. The p_{O_2} gradient in the compartment is thus very small and G is not affected by gas diffusion in the compartment.

Effect of permeation flux on the flow gas

When a flow of oxygen, J_{O_2} [mol s^{-1}], passes through the membrane, it will change the p_{O_2} in the upper compartment:

$$p_{\text{O}_2} = p_{\text{O}_2}^{\text{in}} + \frac{J_{\text{O}_2} RT_{\Phi_f}}{P \Phi_f} \quad (2.18)$$

where P is the absolute pressure, Φ_f is the volume flow, and T_{Φ_f} is the T where volume flow is measured.

The gas flow enters the upper compartment above the center of the membrane and moves towards the periphery. The p_{O_2} above the center of the membrane will thus be close to the p_{O_2} of the gas entering the chamber, while the p_{O_2} of the gas at the periphery is close to the gas leaving the chamber. $V_{\text{Nernst}}^{\text{upper}}$ will thus depend on the distance from the center of the membrane, r :

$$V_{\text{Nernst}}^{\text{upper}}(r) = \frac{RT}{4F} \ln \left(\frac{p_{\text{O}_2}^{\text{in}} + \frac{J_{\text{O}_2}(r) RT_{\Phi_f}}{P \Phi_f}}{p_{\text{O}_2}^{\text{ref}}} \right) \quad (2.19)$$

where $J_{\text{O}_2}(r)$ is the amount of oxygen passing through the membrane inside a circle with radius

r . $J_{O_2}(r)$ is a fraction of J_{O_2} :

$$J_{O_2}(r) = \int_0^r J_{O_2} \frac{2\pi r'}{\pi r_0} dr' = \frac{r^2}{r_0^2} J_{O_2} \quad (2.20)$$

where r_0 is the total exposed membrane surface. The average $V_{\text{Nernst}}^{\text{upper}}$ on the surface is:

$$V_{\text{Nernst}}^{\text{upper}} = \frac{1}{\pi r_0^2} \int_0^{r_0} V_{\text{Nernst}}^{\text{upper}}(r) \cdot 2\pi r dr \quad (2.21)$$

which leads to:

$$V_{\text{Nernst}}^{\text{upper}} = \frac{RT}{4F} \left[\ln \left(\frac{p_{O_2}^{\text{in}}}{p_{O_2}^{\text{air}}} \right) + \left(\frac{p_{O_2}^{\text{in}}}{\Delta p_{O_2}} + 1 \right) \left(\ln \left(\frac{\Delta p_{O_2}}{p_{O_2}^{\text{in}}} + 1 \right) - 1 \right) \right] \quad (2.22)$$

$$\Delta p_{O_2} = \frac{I_{\text{pump}} RT \Phi_f}{4F \Phi_f} \quad (\text{Steady state}) \quad (2.23)$$

$$\Delta p_{O_2} = \frac{j_{O_2} RT \Phi_f}{\Phi_f} \quad (\text{Relaxation}) \quad (2.24)$$

where T_{Φ_f} is the temperature at which the volume flow is measured. $p_{O_2}^{\text{in}}$ is the p_{O_2} of the inlet gas, calculated from V_{ref}^0 . The deviation of $V_{\text{Nernst}}^{\text{upper}}$ from V_{ref}^0 results in an underestimation of G in the steady state measurement. Substituting $V_{\text{Nernst}}^{\text{upper}}$ for V_{ref}^0 in Eq. 2.15 gives a corrected area specific conductance G_c . In the relaxation measurements the permeation flux will cause a deviation from the usual step change of μ_{O_2} . If this deviation is not taken into account, k is underestimated.

2.4.3 The electrolyte probe

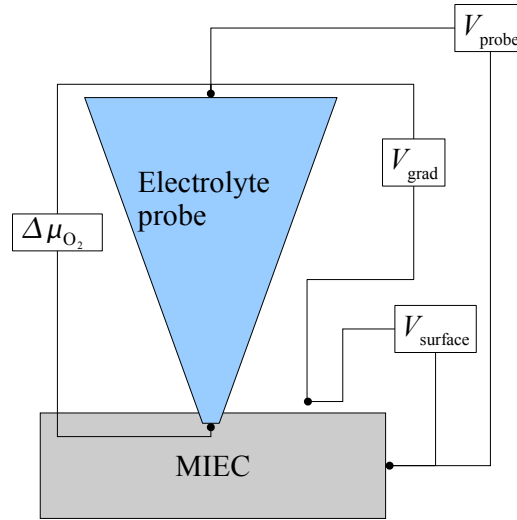


Figure 2.7: A schematic of the origins of the contributions to the probe voltage.

The tip of the electrolyte probe is in ionic and electronic contact with the MIEC membrane; the porous platinum electrode on the other side of the probe sits in the flow gas. Assuming that equilibrium exists between the platinum and the gas and between the probe tip and the MIEC membrane, Eqs. 2.11 and 2.2 state that the probe voltage, V_{probe} , is a direct measure of the

difference in μ_{O_2} between the inlet flow gas and the MIEC membrane surface:

$$\Delta\mu_{\text{O}_2} = \mu_{\text{O}_2}^{\text{in}} - \mu_{\text{O}_2}^{\text{MIEC}} = 4FV_{\text{surface}} \quad (2.25)$$

where $\mu_{\text{O}_2}^{\text{in}}$ and $\mu_{\text{O}_2}^{\text{MIEC}}$ are the oxygen chemical potential, of the inlet flow gas, and just inside the MIEC surface respectively. V_{surface} is the part of the probe voltage, V_{probe} , attributable to the oxygen exchange over the surface.

Apart from V_{surface} , there are other contributions to V_{probe} when there is a flux of oxygen through the membrane surface (see Fig. 2.7). They can be written

$$V_{\text{probe}} = V_{\text{surface}} + V_{\text{grad}} + \Sigma_i V_i, \quad (2.26)$$

where the gas gradient voltage, V_{grad} , is the contribution from differences in the p_{O_2} of the gas at a point just over the membrane, and the gas at the Pt electrode on the back of the probe. $\Sigma_i V_i$ is the sum of any other contributions present, such as thermoelectric voltages. $\Sigma_i V_i$ is assumed to be independent of the ionic current. While $\Sigma_i V_i$ can be the largest contribution to V_{probe} , it can thus be filtered out by measuring V_{probe} at different currents.

The gas gradient voltage V_{grad}

V_{grad} is determined by a number of factors including flow geometry, gas diffusion coefficient, T , etc. In the next section it is shown that V_{probe} is independent of the gas diffusion coefficient. Assuming that the flow geometry is symmetric with respect to a gas flow direction reversal, V_{grad} can be estimated:

The p_{O_2} of the gas close to the probe/MIEC membrane interface, $p_{\text{O}_2}^{\text{tip}}$ is different from the p_{O_2} of the inlet gas, due to the oxygen flux through the membrane. Assuming that the flux distribution over the membrane is independent of the flow rate and p_{O_2} of the gas, $p_{\text{O}_2}^{\text{tip}}$ can be written:

$$p_{\text{O}_2}^{\text{tip}} = p_{\text{O}_2}^{\text{in}} + \beta (p_{\text{O}_2}^{\text{out}} - p_{\text{O}_2}^{\text{in}}) \quad (2.27)$$

where β is a variable depending on the geometry of the setup. If the gas flow direction is reversed such that it enters via the outer pipe and exits via the inner pipe Eq. 2.27 becomes:

$$p_{\text{O}_2}^{\text{tip}} = p_{\text{O}_2}^{\text{in}} + (1 - \beta) (p_{\text{O}_2}^{\text{out}} - p_{\text{O}_2}^{\text{in}}) \quad (2.28)$$

β was extracted using Eq. 2.27 and 2.28 by comparing measurements with the regular and inverted gas flow directions. It was found to be 0.09 ± 0.02 . $p_{\text{O}_2}^{\text{tip}}$ is thus close to $p_{\text{O}_2}^{\text{in}}$.

V_{grad} can then be calculated as:

$$V_{\text{grad}} = \frac{RT}{4F} \ln \left(\frac{p_{\text{O}_2}^{\text{in}} + \beta \frac{i_{\text{pump}} RT \Phi_f}{4F \Phi_f}}{p_{\text{O}_2}^{\text{in}}} \right) \quad (2.29)$$

The polarization resistance, r_s , of the surface is finally calculated as:

$$r_s = \frac{V_{\text{probe}} - V_{\text{grad}} - \Sigma_i V_i}{i_{\text{pump}}} \quad (2.30)$$

In the data analysis, we assume that $\Sigma_i V_i$ is independent of i_{pump} and equal to V_{probe} when $i_{\text{pump}}=0$. V_{mixing} is between 0 and 10 % of V_{probe} in the measurements of this study. This difference is largest when the p_{O_2} is low and when the temperature is high.

2.5 Results and discussion

In this section the transport properties of the $(\text{La}_{0.6}\text{Sr}_{0.4})_{0.99}\text{Co}_{0.2}\text{Fe}_{0.8}\text{O}_{3-\delta}$ (LSCF) as measured by the described method are presented, including discussions of possible misinterpretations of the measured data.

2.5.1 Steady state measurements

Low flux measurement

Steady state experiments are performed by applying various currents to the pump. This creates a gradient in μ_{O_2} . The calculated μ_{O_2} in the membrane in a steady state measurement at $T = 1273 \text{ K}$ in air and with pumping current $i_{\text{pump}} = -65 \text{ A/m}^2$ is shown in Fig. 2.8.

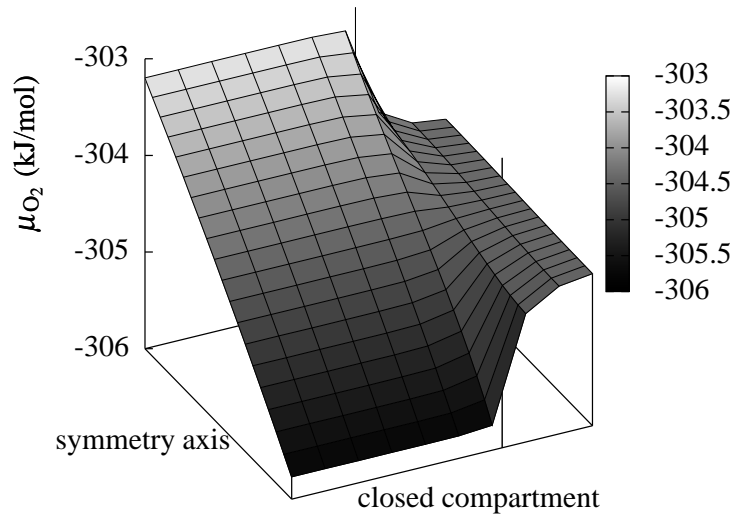


Figure 2.8: μ_{O_2} in the MIEC membrane in a steady state measurement at $T = 1273 \text{ K}$ in air. $i_{\text{pump}} = -65 \text{ A/m}^2$. Two vertical lines mark the edge of the gold seal. The total length along the symmetry axis is 2.253 mm . The total length along the closed compartment edge is 10.15 mm (half the membrane diameter), with the aperture extending 7 mm from the symmetry axis, where the gold seal blocks the flux (see Fig 2.6).

For each value of T and $p_{\text{O}_2}^{\text{in}}$ several different values of i_{pump} were applied. i_{pump} is plotted as a function of the reference voltage at $T = 1248 \text{ K}$ in a 4:1 N_2 :air gas mixture (i.e. p_{O_2} about 4 kPa), in Fig. 2.9a). Negative values of i_{pump} corresponds to oxygen being pumped from the closed compartment to the reference compartment. Negative values of V_{ref} means that the p_{O_2} in the closed compartment is lower than the p_{O_2} in the reference compartment. There is clearly a linear relation between i_{pump} and V_{ref} . $G = 10.11 \pm 0.03 \text{ kS/m}^2$ is extracted as the slope of the linear fit. Note that the standard deviation is less than 0.1% of the measured value. Most of the G measurements in this study were done with standard deviations less than 1% .

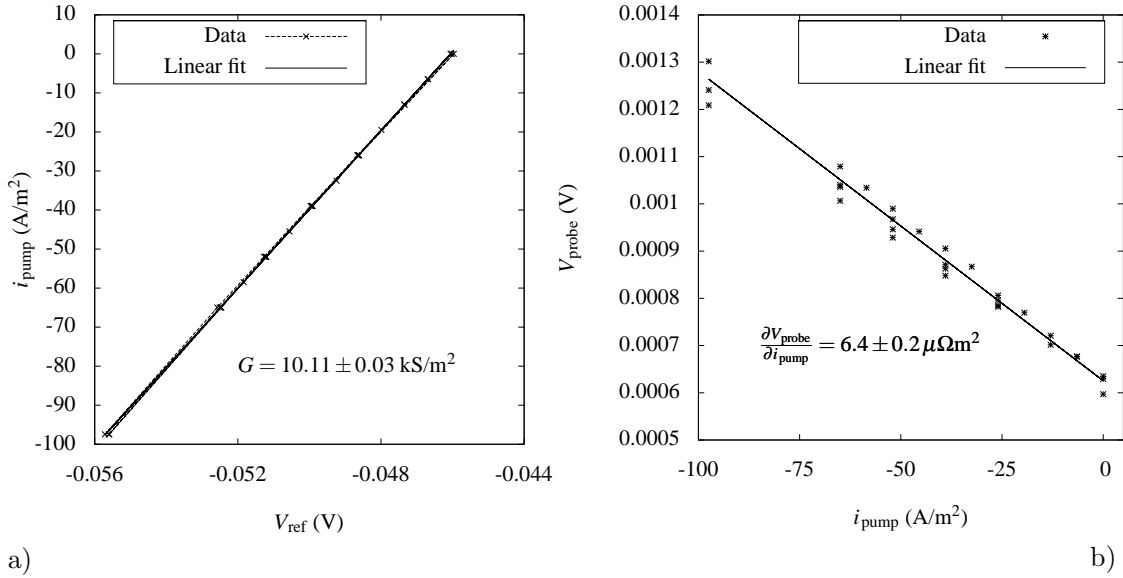


Figure 2.9: *a)* i_{pump} as a function of V_{ref} . $T=1248 \text{ K}$, gas 20% air + 80 % N_2 . *b)* V_{probe} as a function of i_{pump} . $T=1248 \text{ K}$, gas 20% air + 80 % N_2

In the same experiment a linear relationship between V_{probe} and i_{pump} is also found and shown in Fig. 2.9b). Positive values of V_{probe} corresponds to μ_{O_2} being lower at the probe tip than at the platinum electrode at the back of the probe. The deviation of V_{probe} from 0 at $i_{\text{pump}} = 0$ is attributed to thermoelectric voltages in the measuring circuit. $\frac{\partial V_{\text{probe}}}{\partial i_{\text{pump}}}$ was extracted as $6.4 \pm 0.2 \mu\Omega\text{m}^2$. The standard deviation is about 3%. The standard deviation is lower at lower T and lower p_{O_2} and higher at higher T and higher p_{O_2} .

The low standard deviations are a consequence of the oxygen pump which allows very precise measurement of the flux and p_{O_2} difference compared to traditional mass-balance experiments [21–23, 37]. Furthermore, the reliance on steady state allows very long sampling times of the measured voltages resulting in high precision on the individual measurement. The nonlinearities caused by the non-constant σ_{O} of a membrane in a μ_{O_2} gradient are avoided due to the very small μ_{O_2} gradients. This has the added effect that the measured G_{c} and r_{s} values are indeed the values at $p_{\text{O}_2} = p_{\text{O}_2}^{\text{in}}$ and not integrated quantities over a large p_{O_2} interval.

p_{O_2} dependence of G_c and r_s

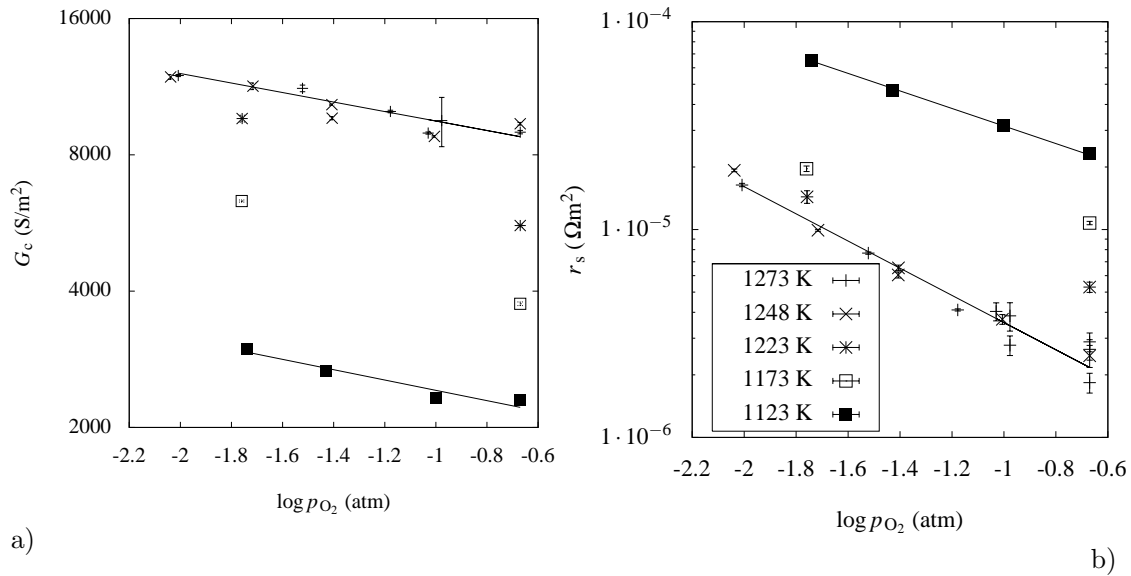


Figure 2.10: **a)** G_c as a function of $p_{O_2}^{\text{in}}$ and temperature. **b)** r_s as a function of $p_{O_2}^{\text{in}}$ and temperature. *a) and b) share legends*

The $p_{O_2}^{\text{in}}$ dependence of G_c for different temperatures is plotted in Fig. 2.10a). An increase in G_c is seen when $p_{O_2}^{\text{in}}$ is lowered. G_c is proportional to $p_{O_2}^{-0.114}$ at $T=1123$ K and $p_{O_2}^{-0.104}$ at $T=1273$ K. The $p_{O_2}^{\text{in}}$ dependence of r_s for different temperatures is plotted in Fig. 2.10b). r_s is proportional to $p_{O_2}^{-0.42}$ at $T=1123$ K and $p_{O_2}^{-0.65}$ at $T=1273$ K. The error bars show the precision of the measurements. It is remarkable that the precision of the measurement of r_s is reasonably small, even when measuring at $T=1273$ K and $p_{O_2}=0.21$ atm. The origin of the scatter is discussed in section 2.5.3.

Temperature dependence of G_c and r_s

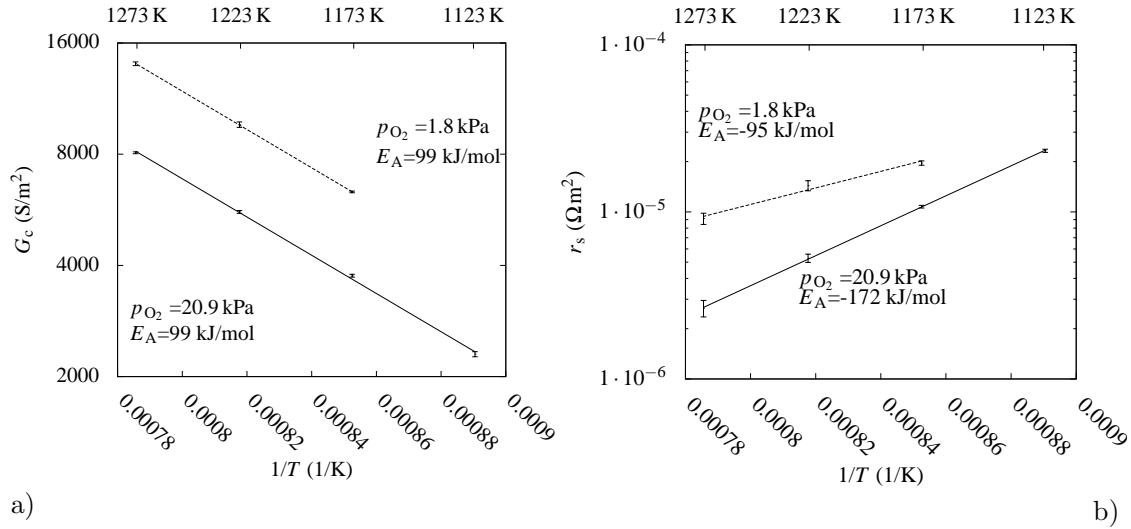


Figure 2.11: **a)** G_c as a function of $1/T$ plotted for air ($p_{O_2} = 20.9$ kPa) and air/N₂ ($p_{O_2}^{in} = 1.8$ kPa) flow gas. The activation energies are $99 \frac{kJ}{mol}$ for both gas compositions. **b)** r_s as a function of $1/T$ plotted for flow gas with $p_{O_2}^{in} = 20.9$ kPa and 1.8 kPa. The activation energies for the surface reaction ($\propto r_s^{-1}$) are $172 \frac{kJ}{mol}$ and $95 \frac{kJ}{mol}$ respectively.

G_c is plotted as a function of $1/T$ for air ($p_{O_2}^{in} = 20.9$ kPa) and an air/N₂ gas mixture ($p_{O_2}^{in} = 1.8$ kPa) in Fig. 2.11a). G_c has an Arrhenius dependence with an activation energy of $E_A = 99 \frac{kJ}{mol}$ for both gasses. r_s is plotted as a function of $1/T$ for flow gas with $p_{O_2}^{in} = 20.9$ kPa and 1.8 kPa in Fig 2.11b). The surface reaction $\propto r_s^{-1}$ has an Arrhenius dependence with an activation energy E_A of $172 \frac{kJ}{mol}$ and $95 \frac{kJ}{mol}$ for each gas mixture respectively.

The diffusion coefficient of O₂ in a gas is proportional to $T^{3/2}$ [36]. Oxygen concentration gradients in the gas phase will thus add terms to G_c and r_s that will cause a deviation from activated behavior. As both G_c and r_s show no deviation from thermally activated behavior, we conclude that oxygen concentration gradients in the gas phase are not influencing our measurements.

Steady state model results

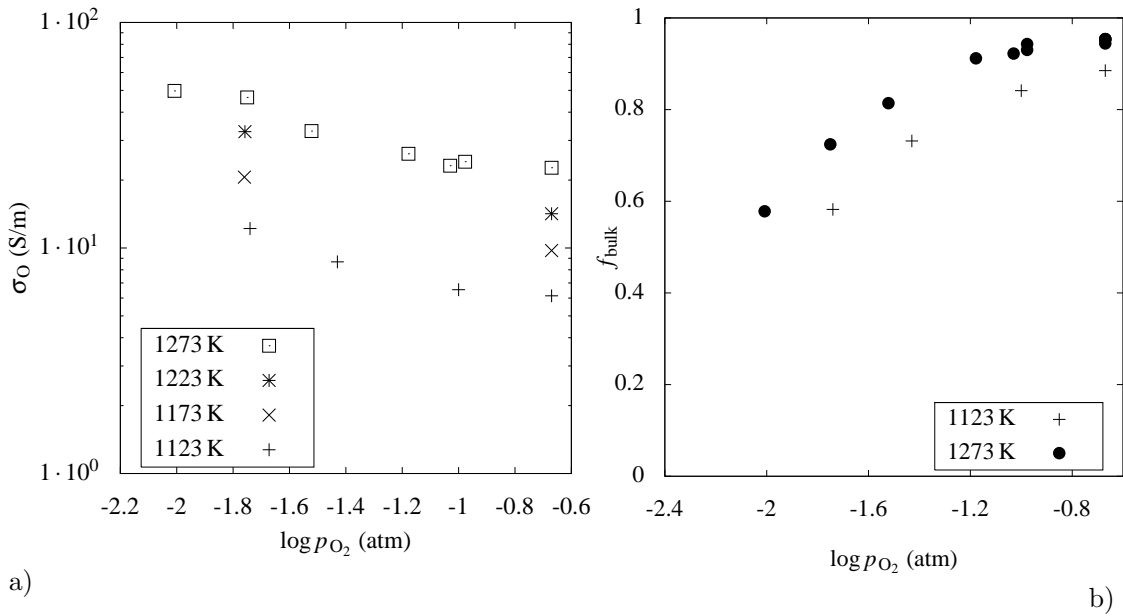


Figure 2.12: a) σ_{O_2} as a function of T and $\log p_{O_2}$. b) f_{bulk} as a function of T and p_{O_2}

The steady state model described in Section 2.3.3 was used to extract D_V^0 from the data of G_c and r_s . This has been converted to σ_{O_2} and plotted in Fig. 2.12a). The fraction of $\Delta\mu_{O_2}$ spent over the bulk part of the membrane, f_{bulk} , is plotted in Fig. 2.12b). As can be seen, the bulk transport limits the transport at high p_{O_2} , while the surface exchange will dominate at low p_{O_2} as r_s is much larger at low p_{O_2} . The large r_s at low p_{O_2} begins to lower G_c at $\log p_{O_2}(\text{atm}) < -2.5$ (see Fig. 2.16a).

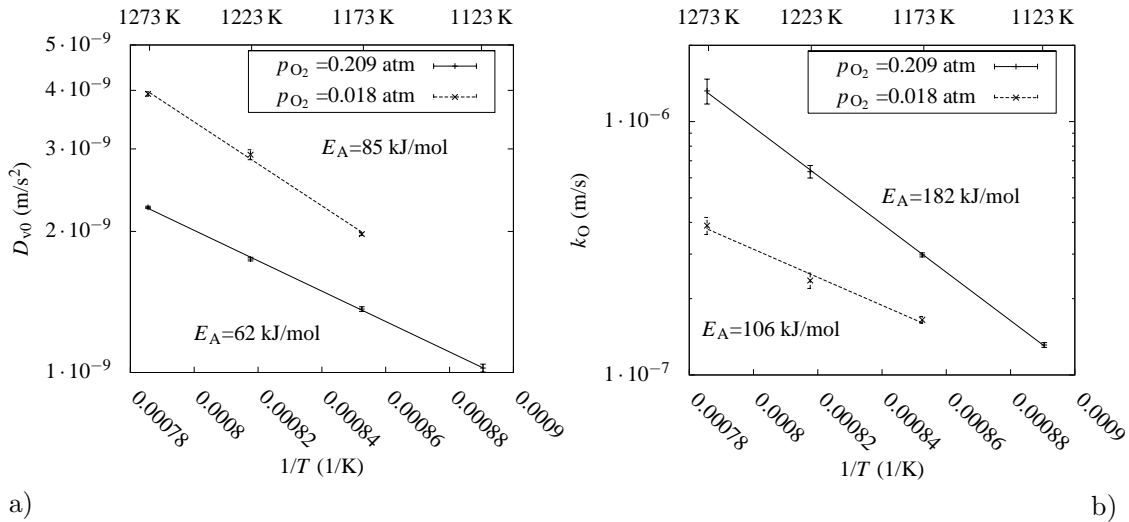


Figure 2.13: a) D_V^0 as a function of $1/T$ plotted for air ($p_{O_2}^{\text{in}} = 20.9$ kPa) and air/N₂ ($p_{O_2}^{\text{in}} = 1.8$ kPa) flow gas. The activation energies are $62 \frac{\text{kJ}}{\text{mol}}$ and $85 \frac{\text{kJ}}{\text{mol}}$ respectively. b) k_O as a function of $1/T$ plotted for flow gases with $p_{O_2}^{\text{in}} = 20.9$ kPa and 1.8 kPa. The activation energies for k_O are $182 \frac{\text{kJ}}{\text{mol}}$ and $106 \frac{\text{kJ}}{\text{mol}}$ respectively.

The temperature dependence of D_V^0 and k_O for air ($p_{O_2}^{\text{in}} = 20.9$ kPa) and air/N₂ ($p_{O_2}^{\text{in}} = 1.8$ kPa)

Table 2.1: Transport and stoichiometry parameters of LSCF in air. k_{chem} is the chemical surface exchange coefficient, analogous to D_{chem}

T (K)	D_V^0 (m ² /s)	D_{chem} (m ² /s)	σ_{O} (S/m)	r_s (Ωm^2)	k_{chem} (m/s)	k_{O} (m/s)	δ	γ
1123	$1.02 \cdot 10^{-9}$	$2.24 \cdot 10^{-9}$	6.14	$2.32 \cdot 10^{-5}$	$1.57 \cdot 10^{-5}$	$1.31 \cdot 10^{-7}$	$5.50 \cdot 10^{-2}$	119
1173	$1.37 \cdot 10^{-9}$	$3.50 \cdot 10^{-9}$	9.74	$1.08 \cdot 10^{-5}$	$3.34 \cdot 10^{-5}$	$2.98 \cdot 10^{-7}$	$6.85 \cdot 10^{-2}$	112
1223	$1.75 \cdot 10^{-9}$	$5.19 \cdot 10^{-9}$	14.2	$5.28 \cdot 10^{-6}$	$6.92 \cdot 10^{-5}$	$6.34 \cdot 10^{-7}$	$8.17 \cdot 10^{-2}$	109
1273	$2.25 \cdot 10^{-9}$	$7.69 \cdot 10^{-9}$	20.2	$2.65 \cdot 10^{-6}$	$1.44 \cdot 10^{-4}$	$1.32 \cdot 10^{-6}$	$9.43 \cdot 10^{-2}$	109

flow gas are shown in Figs 2.13a) and 2.13b), respectively. The activation energies are $62 \frac{\text{kJ}}{\text{mol}}$ and $85 \frac{\text{kJ}}{\text{mol}}$ for D_V^0 in the two gas mixtures. For k_{O} they are $182 \frac{\text{kJ}}{\text{mol}}$ and $106 \frac{\text{kJ}}{\text{mol}}$, respectively. k_{O} was calculated from r_s using the formulas in Fig. 2.3.

Transport parameters of LSCF measured using steady state measurements are summarized in Table 2.1. Values of δ and γ used in the computations are also provided.

2.5.2 Relaxation experiments

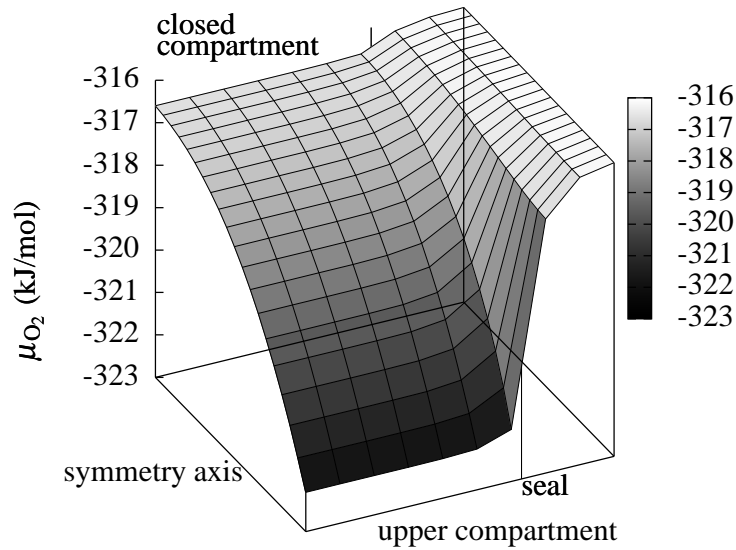


Figure 2.14: μ_{O_2} in the membrane in the relaxation experiment shown in Fig. 2.15a) at time, $t=120$ s. The total length along the symmetry axis is 2.253 mm. The total length along the upper compartment edge is 10.15 mm (half the membrane diameter), with the aperture extending 7 mm from the symmetry axis, where the gold seal blocks the flux (see Fig 2.6).

Relaxation experiments were performed by making sudden changes of the composition, and thus μ_{O_2} , of the flow gas in the upper compartment, while keeping $i_{\text{pump}} = 0$. An example of μ_{O_2} in the membrane in the relaxation experiment shown in Fig. 2.15a) at time, $t=120$ s is shown in Fig. 2.14.

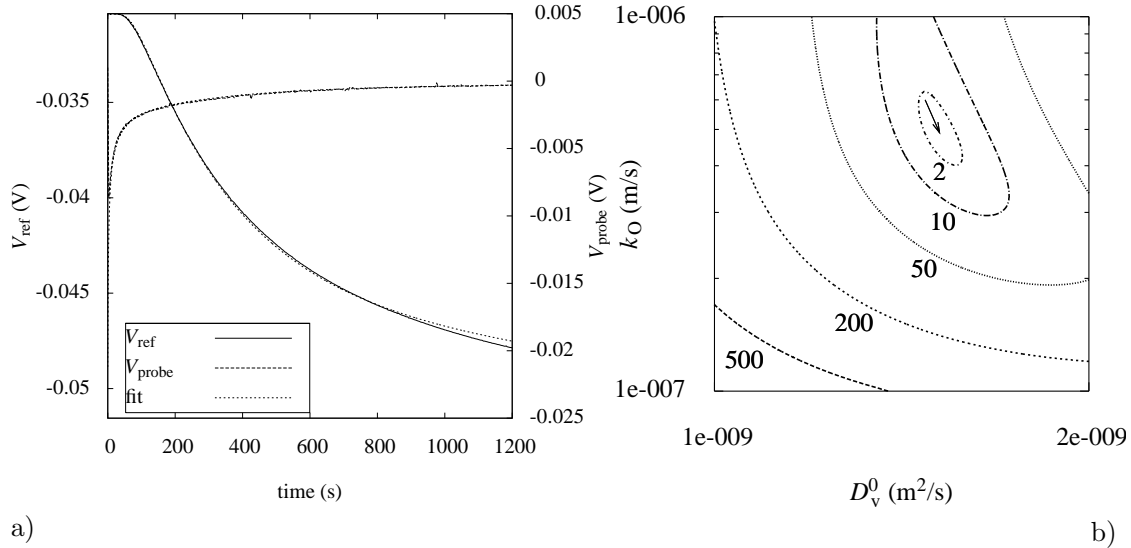


Figure 2.15: *a) Measured V_{probe} and V_{ref} together with calculated values of V_{probe} and V_{ref} for a sudden gas composition change $p_{\text{O}_2}^{\text{in}}$: 7.1 kPa \rightarrow 3.2 kPa at $T = 1273$ K. b) Contour plot of $\text{SSD}/\text{SSD}_{\text{min}}$ as a function of D_{V}^0 and k_{O} .*

Measured and calculated values of V_{probe} and V_{ref} for a sudden change in the gas composition $p_{\text{O}_2}^{\text{in}}$: 7.1 kPa \rightarrow 3.2 kPa at $T = 1273$ K are plotted in Fig. 2.15a). Fitting parameter values of $D_{\text{V}}^0 = 1.5 \cdot 10^{-9} \text{ m}^2/\text{s}$ and $k_{\text{O}} = 4.9 \cdot 10^{-7} \text{ m/s}$ were used. At large times the calculated and measured values of V_{ref} disagrees. As the model uses many input data of finite precision (δ , membrane dimensions, voltages), this disagreement is well within the expected precision. A contour plot of the sum of square differences (SSD) [20] of the measured and calculated values is given in Fig. 2.15 b). SSD is normalized to the best fit (SSD_{min}). The SSD is more sensitive to D_{V}^0 than k_{O} , and thus D_{V}^0 is determined with higher precision than k_{O} .

2.5.3 Measurement verification

In the following we present measurements designed to rule out possible misinterpretations of the measured data.

Influence of corrections

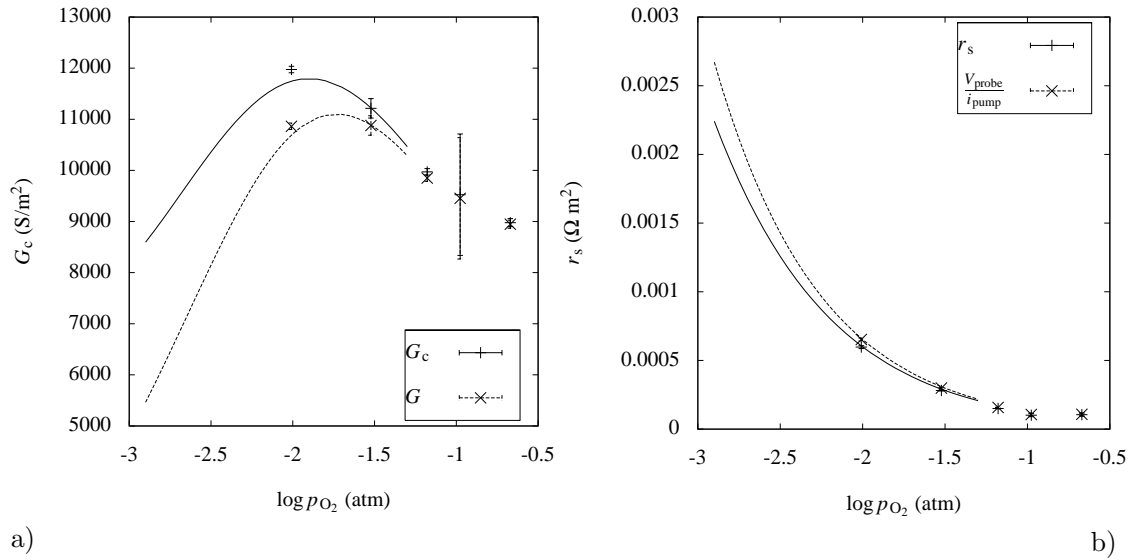


Figure 2.16: a) G_c and G at 1273 K as a function of $\log p_{\text{O}_2}^{\text{in}}$. The lines are model predictions. b) r_s and $\frac{\partial V_{\text{probe}}}{\partial i_{\text{pump}}}$ at 1273 K as a function of $\log p_{\text{O}_2}^{\text{in}}$. The lines are model predictions.

A few corrections were proposed in section 2.4. These corrections are not necessarily specific to this setup, and are equally relevant in e.g. a conductivity relaxation experiment, where the perturbation of $p_{\text{O}_2}^{\text{in}}$ can be considerable. To illustrate the impact of these corrections, G_c and r_s (i.e. corrected values) are compared to G and $\frac{V_{\text{probe}}}{i_{\text{pump}}}$ (i.e. uncorrected values) in Fig. 2.16a) and Fig. 2.16b). To represent extrapolation towards lower $p_{\text{O}_2}^{\text{in}}$, lines illustrating the steady state model prediction values have been added. These lines were calculated using a weakly p_{O_2} dependent D_V^0 and a $\frac{\partial V_{\text{probe}}}{\partial i_{\text{pump}}} \propto p_{\text{O}_2}^{-0.68}$. The corrections to G and $\frac{V_{\text{probe}}}{i_{\text{pump}}}$ in the measured $p_{\text{O}_2}^{\text{in}}$ regime are less than 15%. However, in accordance with equations 2.22 and 2.29 the extrapolations show that these corrections will increase as the $p_{\text{O}_2}^{\text{in}}$ is reduced. Measurements in inert gas with $p_{\text{O}_2}^{\text{in}}$ below 1 kPa should therefore be interpreted with care. In regimes with high r_s (i.e. low temperature and low $p_{\text{O}_2}^{\text{in}}$), it is possible to conduct good measurements using low pumping currents; this reduces the corrections.

Influence of gas diffusion

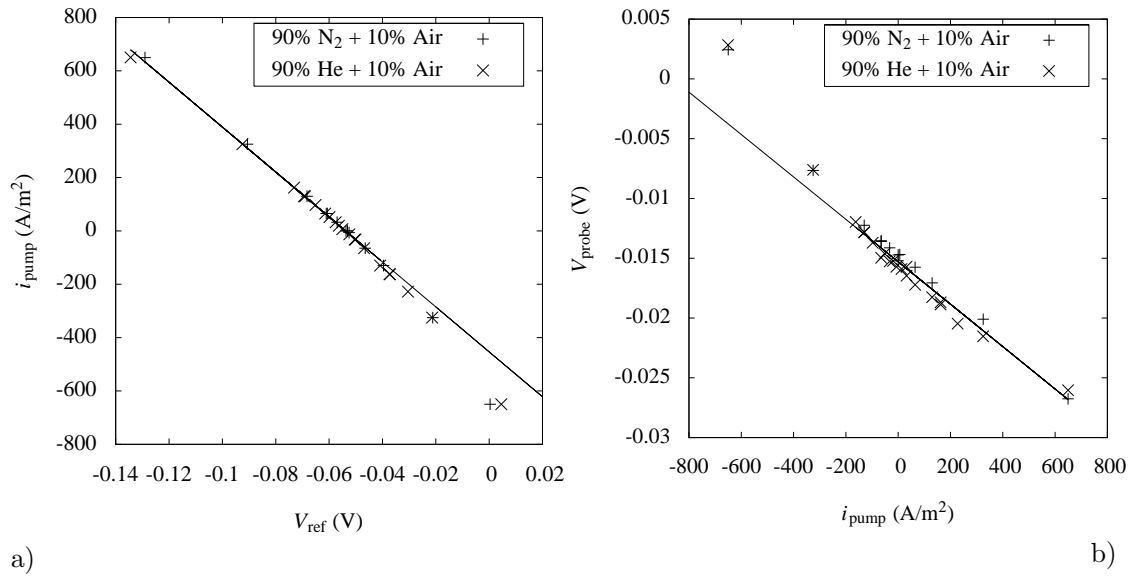


Figure 2.17: Measurements performed in a gas mixture of 90% He + 10 % air (i.e. 2% O₂+8% N₂), and in 90% N₂ + 10 % air. **a)** i_{pump} as a function of V_{ref} at 1273 K. **b)** V_{probe} as a function of i_{pump} at 1273 K.

The diffusion of oxygen molecules in a gas is not infinitely fast; it is therefore important to test whether limitations of gas diffusion will develop gradients in the oxygen concentration, reducing the accuracy of the measurement. i_{pump} is shown as a function of V_{ref} for two experiments in Fig. 2.17a). One experiment is performed in a gas mixture of 90% He + 10% air, and the other in a gas mixture of 90% N₂ + 10% air. The diffusion coefficient of O₂ in He is about four times larger than the diffusion coefficient of O₂ in N₂. Gradients in the gas above the membrane would thus be larger in the 90% N₂ + 10 % air gas mixture than in 90% He + 10% air. Evidently G is independent of the gas diffusion coefficient of oxygen in the upper compartment. V_{probe} is shown in Fig. 2.17b) as a function of i_{pump} at $T=1273$ K in the same two experiments. It can be seen that $\frac{\partial V_{\text{probe}}}{\partial i_{\text{pump}}}$ is also independent of the gas diffusion coefficient.

The measurements shown in Fig. 2.9a) and 2.9b) are cautious measurements in the sense that oxygen is pumped out of the compartment below the membrane (negative values of i_{pump}) and the flux magnitude is kept low; this protects the membrane and glass seal from large mechanical pressure gradients. In the measurements in Fig. 2.17a) and 2.17b) the gradients and fluxes are much larger; this allows us to observe a deviation from the linear regime of G in Fig. 2.17a). This deviation is only seen when pumping oxygen into the closed compartment. We believe that this is caused by leaks in the glass seal being forced open by oxygen overpressure at the membrane perimeter.

$\frac{\partial V_{\text{probe}}}{\partial i_{\text{pump}}}$ shows a nonlinearity when pumping gas out of the closed compartment in Fig. 2.17b); this is attributed to a decrease of $p_{\text{O}_2}^{\text{tip}}$ (i.e. the p_{O_2} in the gas beside the tip of the probe) and the corresponding increase in r_s . Both G and $\frac{\partial V_{\text{probe}}}{\partial i_{\text{pump}}}$ are independent of pumping direction for small fluxes; this shows that the rate limiting step of gas entering and leaving the membrane surface is the same. This independence of the current direction is seen in all measurements for small fluxes.

V_{probe} evaluation

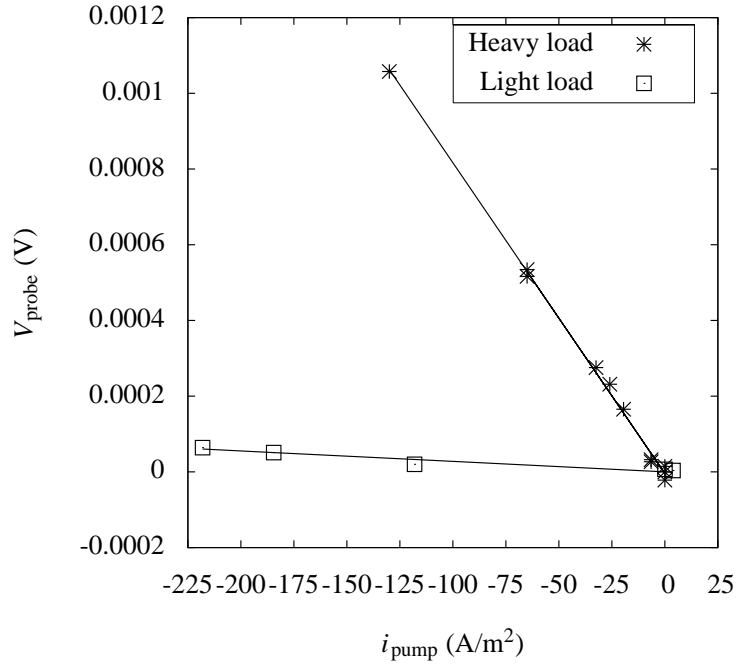


Figure 2.18: Measurement of V_{probe} at $p_{\text{O}_2} = 4 \text{ kPa}$, $T = 1273 \text{ K}$ on $(\text{La}_{0.6}\text{Sr}_{0.4})_{0.99}\text{Co}_{0.2}\text{Fe}_{0.8}\text{O}_{3-\delta}$ (heavy load) and on $(\text{La}_{0.6}\text{Sr}_{0.2}\text{Ba}_{0.2})_{0.99}\text{Fe}_{0.8}\text{Co}_{0.2}\text{O}_{3-\delta}$ (light load).

As mentioned in section 2.4.3, V_{probe} has several contributions apart from V_{surface} . If electronic contact, but no ionic contact between the MIEC membrane and the probe exists, V_{probe} becomes the sum of these extra contributions only. In effect V_{probe} is measuring $p_{\text{O}_2}^{\text{tip}}$, i.e. the p_{O_2} of the gas close to the contact point of the probe and membrane, and possibly some thermoelectric voltages. A measurement of V_{probe} as a function of the pumping current for a membrane of the LSCF derived MIEC material $(\text{La}_{0.6}\text{Sr}_{0.2}\text{Ba}_{0.2})_{0.99}\text{Fe}_{0.8}\text{Co}_{0.2}\text{O}_{3-\delta}$ (LSB20CF) with a light load applied to the probe is compared to a measurement on LSCF with a heavy load applied to the probe, in Fig. 2.18. $\frac{V_{\text{probe}}}{i_{\text{pump}}}$, was about 20 times less for the lightly loaded LSB20CF than for the heavily loaded LSCF (Fig. 2.18)). Except for the load on the probe and the sample composition, all other measurement parameters were equivalent. We interpret the low V_{probe} as a sign of poor ionic contact to the membrane. In conclusion, with good ionic contact to the membrane, V_{grad} is small compared to the contribution from V_{surface} . Our recommendation is to apply a pressure of 10-100 MPa to ensure ionic contact.

Measurement reproducibility

While the precision error bars on the individual measurements in Figs 2.10a), 2.10b), 2.11a) and 2.11b) are smaller than the symbols used to mark the measurements, some scatter still exists. We believe that this is caused by slow relaxation of the membrane surface and microstructure. First, a series with varying $p_{\text{O}_2}^{\text{in}}$ was run at $T = 1273 \text{ K}$. Neither G_c or r_s were reproducible. Another series was then run at $T = 1248 \text{ K}$. This series was reasonably reproducible. After a month of measurements a new series was recorded at $T = 1273 \text{ K}$. The values for G_c or r_s agreed reasonably with the last 8 measurements of the first $T = 1273 \text{ K}$ series. We conclude that more than one week of equilibration is needed before the membrane is stable. This is also seen with other membrane materials in this setup, and we attribute it to relaxation of the microstructure and surface, as well as possible cation diffusion.

2.5.4 Comparison of values from steady state and relaxation experiments

An advantage of having both steady state and relaxation measurements performed in the same setup, is that comparison of the results from each measurement type, can point out discrepancies in the modelling.

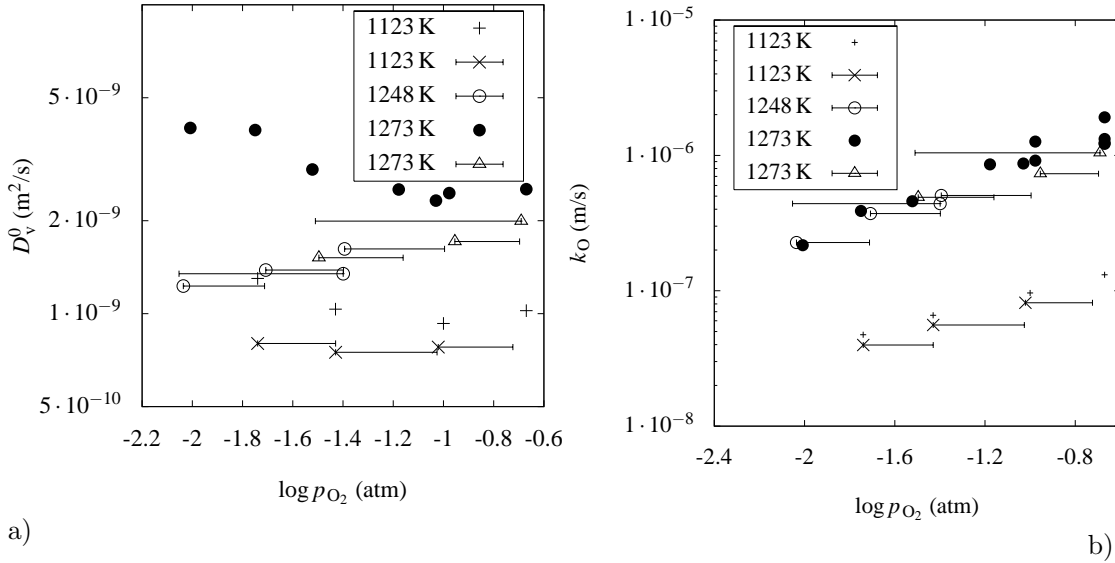


Figure 2.19: a) D_v^0 calculated from steady state and relaxation experiments. The marks connected to lines are relaxation experiments, where the marks signifies the end $p_{O_2}^{\text{in}}$ value of a relaxation and the bar spanning the p_{O_2} variation of the relaxation. b) k_O calculated from the steady state and the relaxation experiments.

D_v^0 as deduced from the steady state measurements and the relaxation experiments are plotted in Fig. 2.19a). As mentioned in section 2.3.2, D_v^0 should not be directly dependent on C_v , and should thus be a measure of the mobility of the vacancies. The values obtained using steady state measurements show an increase in D_v^0 at low p_{O_2} . The values for D_v^0 obtained using relaxation experiments are constant when $p_{O_2}^{\text{in}}$ is reduced at $T = 1123$ K and decreases slightly when $p_{O_2}^{\text{in}}$ is reduced at $T = 1248$ K and $T = 1273$ K. While the D_v^0 values in air are very close and $p_{O_2}^{\text{in}}$ dependencies of the steady state and relaxation values are not too different, the agreement is not complete. The conversion from D_{chem} to D_v^0 makes use of the thermodynamic factor γ as well as δ . Any error in these parameters will accumulate in D_v^0 . While the coulometric titration gives a high precision on $\gamma = \frac{\partial \ln p_{O_2}}{2 \partial \ln c_O}$, the absolute value of δ is difficult to obtain as illustrated by the variation in the values reported in the literature (c.f. Tai [38], Den Otter [39] or Stevenson [22]). Furthermore, D_v^0 and k_O are linearly correlated in a steady state experiment, while the correlation is more complicated in the fit of a relaxation experiment. This could give a systematic difference in the results of steady state measurements and relaxation measurements.

k_O values calculated from the steady state and the relaxation experiments are plotted in Fig. 2.19b). The steady state and relaxation values of k_O are in excellent agreement, if it is assumed that it is the end $p_{O_2}^{\text{in}}$ that determines k_O in the relaxation. This is expected, as the $\mu_{O_2}^{\text{MIEC}}$ just below the surface will adjust its $\mu_{O_2}^{\text{MIEC}}$ to a value close to the $\mu_{O_2}^{\text{MIEC}}$ of the flow gas during the first tenth of the fitted relaxation time. k_O is proportional to $p_{O_2}^{0.41}$ at $T = 1123$ K and $p_{O_2}^{0.52}$ at $T = 1273$ K. It is noteworthy that the precision of the measurement of the steady state values of k_O is on the order of the symbol size or less, even when measuring at $T = 1273$ K and $p_{O_2} = 0.21$ atm. In this regime, high T and high p_{O_2} regime methods such as conductivity relaxation and isotope exchange will have errors spanning an order of magnitude or more.

The increase in D_v^0 with lower $p_{O_2}^{\text{in}}$ in the steady state measurements could be caused by

misinterpretation of the measured data. At low p_{O_2} surface oxygen exchange processes becomes more important in determining the oxygen transport (about 45% of the μ_{O_2} difference is found at the surfaces at $p_{\text{O}_2}^{\text{in}} = 1 \text{ kPa}$ and $T=1123 \text{ K}$), and the increase in D_{V}^0 could be related to an overestimation of r_{s} . As the $(V_{\text{probe}}/i_{\text{pump}})$ plots used to determine r_{s} are close to linear at all measured $p_{\text{O}_2}^{\text{in}}$ values, terms causing an overestimation not accounted for must have the same linearity.

One error term with such a linearity could be caused by the probe penetrating deep into the membrane and probing μ_{O_2} some distance into the bulk. Another term could come from the probe blocking the flux and altering the μ_{O_2} profile through the membrane, resulting in an enhanced V_{probe} . To investigate these possibilities, each of the relaxation measurements were fitted again, but this time with the cone depth as a fitting parameter. No common cone probe depth was, however, found for the relaxations.

Thermovoltages have also been dismissed as an error term. While heat from the oxidation reaction will change the temperature at the probe tip, the enthalpy of oxidation should only be weakly temperature dependent, and as the thermopower of the CG10 probe increases with temperature [40], the thermovoltage would not experience the decrease of r_{s} with temperature seen in Fig. 2.11b). Furthermore, localized ohmic heating in the membrane will scale with $(i_{\text{pump}})^2$ in contrast with the linear relations seen in Fig. 2.9b). Finally, the Seebeck coefficient is less than $20 \mu\text{V/K}$.

2.6 Conclusions

A setup combining an oxygen pump with an electrolyte probe was demonstrated. From this setup the μ_{O_2} difference across the membrane and across an LSCF membrane surface could be determined from the voltage across a pair of reference electrodes on the oxygen pump and from the voltage across the electrolyte probe in contact with the membrane surface. During steady state the voltages had a linear dependence on the oxygen flux. The area specific conductance, G_{c} (a measure of the permeability of the membrane), and the surface resistance, r_{s} , could thus be extracted. G_{c} and r_{s} were found to be independent of the flux direction, showing that the rate limiting step of the oxygen exchange reaction on the surface is the same when oxygen is incorporated into the membrane and when it is released from the membrane. From G_{c} and r_{s} a model was used to extract values of the ionic conductivity, σ_{O} and the concentration independent reduced diffusion coefficient D_{V}^0 . Excellent precision was achieved using small perturbations, illustrating the advantages of 1) measuring at steady state (with very large sampling times) and 2) direct electronic measurement of the oxygen flux and 3) direct electronic measurement of the μ_{O_2} difference across the membrane surface and 4) direct electronic measurement of the total μ_{O_2} difference across the membrane. Furthermore precise determination of r_{s} was not limited to low temperature and low p_{O_2} , where r_{s} is normally dominating the transport, but could also be recorded at high temperature and p_{O_2} , where it is usually too small to be determined accurately. A model based on Ficks law of diffusion was used to fit the measured voltages after stepwise gas composition changes and thus extract D_{V}^0 and k_{O} . The values extracted from steady state and relaxation measurements were reasonably consistent.

Chapter 3

Characterization of oxygen transport in mixed conductors: A method comparison

Abstract

The reduced diffusion coefficient, D_V^0 , and the surface exchange coefficient, k_O , of $(\text{La}_{0.6}\text{Sr}_{0.4})_{0.99}\text{Co}_{0.2}\text{Fe}_{0.8}\text{O}_{3-\delta}$ are evaluated using three types of experiments: Conductivity relaxation; membrane and surface probe relaxation; and steady state surface probe and ionic flux measurements. The precision and accuracy of the methods is discussed. The importance of adequate modelling is analyzed.

3.1 Introduction

The oxygen permeation flux of a mixed electronic and ionic conducting (MIEC) membrane is influenced by both the surface and bulk transport parameters. These parameters will vary several orders of magnitude, depending on the temperature, T , and the oxygen partial pressure, p_{O_2} . Traditional methods for measuring the surface and bulk transport parameters, such as permeation measurements, conductivity relaxation and isotope exchange combined with secondary ion mass spectrometry (SIMS), can be used to measure the surface kinetics and bulk transport in a wide range of parameter values, using different sample geometries. The balance between the surface and bulk transport parameters will however vary, from the completely bulk diffusion controlled regime, exemplified by a thick membrane working at high T in pure, pressurized O_2 , to the completely surface reaction controlled regime, exemplified by a thin film membrane working at low temperature in an oxygen starved N_2 gas. When either the bulk diffusion or the surface reaction is completely controlling the oxygen permeation, the above mentioned methods can be used to resolve the noncontrolling parameters only with great uncertainty. While this is a problem for all measurement methods, the problem is amplified for methods relying on a single signal to extract parameters from both the bulk and the surface.

Several techniques exist for evaluation of the transport properties of MIECs, each with different operation ranges regarding oxygen partial pressure, p_{O_2} , and temperature, T , and each with different accuracy and precision. In this Chapter three techniques are evaluated: conductivity

relaxation (CR) where the conductivity of a MIEC bar is measured during a change in the p_{O_2} of the surrounding gas; membrane and surface probe relaxation (MR) where the oxygen chemical potential of the surfaces of a MIEC membrane is recorded during a change in the p_{O_2} of the gas on one side of the membrane; and steady state surface probe and ionic flux measurements (SS), where the permeation flux is recorded as a function of the surface activity and oxygen chemical potential difference on each side of the membrane. The precision and accuracy of the methods is discussed. The importance of adequate modelling is also analyzed.

3.2 Experimental

3.2.1 Sample preparation

$(La_{0.6}Sr_{0.4})_{0.99}Co_{0.2}Fe_{0.8}O_{3-\delta}$ perovskite powder was prepared by the glycine pyrolysis process [33]. The powders were calcined at $900^\circ C$ for 12 h, and ball milled using ZrO_2 balls in a 500 ml polyethylene container, with ethanol for 24 h at 200 RPM. Shaped samples were pressed from this powder using a uniaxial pressure of 30-70 MPa. Two types of solid MIEC samples were produced for examination; a flat cylindrical membrane for membrane experiments and an oblong bar with a quadratic cross section for conductivity relaxation experiments. The samples were further compressed in an evacuated latex container suspended in water at a pressure up to 325 MPa. The samples were then sintered at $1300^\circ C$ for 12 hours. The sintered samples were polished with SiC polishing sheets and diamond suspensions (particle size down to $1 \mu m$). The sintered and polished membrane sample had a diameter of 20.3 ± 0.1 mm, a thickness of 2.253 ± 0.005 mm and a density of $5965 \frac{kg}{m^3}$ (95% of bulk). The sintered and polished bar sample to be used in conductivity relaxation was $1.3 \text{ mm} \times 1.3 \text{ mm} \times 18 \text{ mm}$ and had a density of 6110 kg/m^2 . X-ray diffraction revealed single phase perovskite structure in all samples.

3.2.2 Membrane and probe measurement

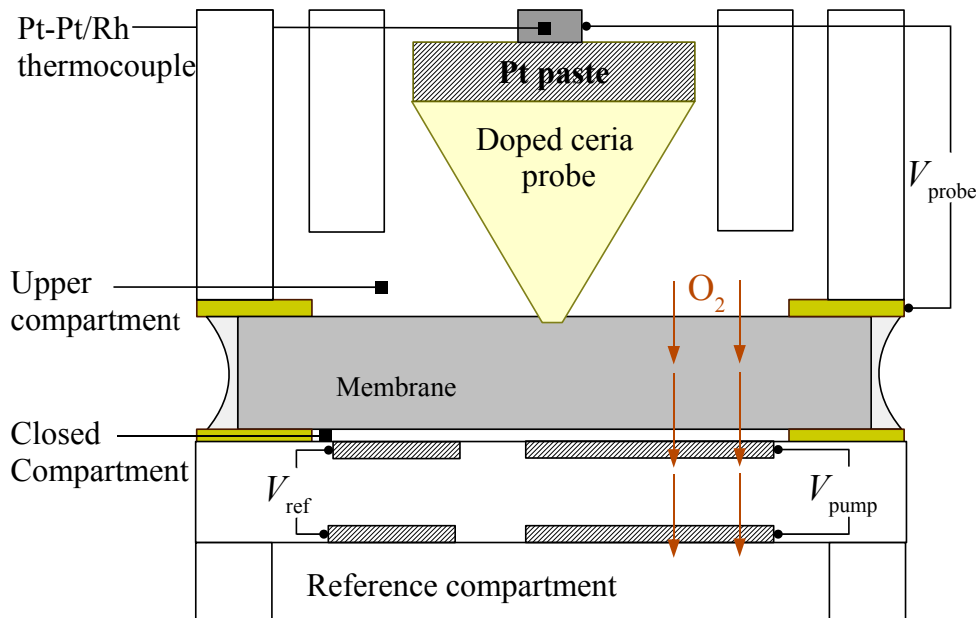


Figure 3.1: The membrane setup used in MR and SS measurements. The electrodes used to obtain the measured voltage signals are marked.

The experimental setup used for the SS and MR measurements is sketched in Figure 3.1. The

membrane is resting on a 0.3 mm gold ring spacer/seal above an $Y_{0.16}Zr_{0.84}O_{1.92}$ (YSZ) oxygen pump, which can simultaneously apply a current through the membrane and monitor the oxygen chemical potential in the closed compartment. On top of the membrane is the upper compartment, where a continuous gas flow of $1.67 \cdot 10^{-6} \text{ m}^3/\text{s}$ (100 mL/min) measured at 295 K is applied. A $Ce_{0.9}Gd_{0.1}O_{1.95}$ solid cone shaped electrolyte probe is probing the difference in oxygen chemical potential of the flow gas and the membrane. Further details of the setup can be found in Chapter 2.

3.2.3 Conductivity relaxation

The electrical conductivity was measured using a standard 4-probe method as illustrated in Fig. 3.2. An electric current is passed through a bar of the sample and the voltage drop is measured across a well defined distance in the middle of the sample. The current was adjusted to keep the voltage difference between the probes less than 25 mV in order to avoid heating effects. The sample was heated in air to the desired temperature followed by changes in the oxygen partial pressure of the nitrogen and air mixture with which the gas was flushed at a rate of $4.17 \cdot 10^{-6} \text{ m}^3/\text{s}$ (250 mL/min) measured at 295 K. The oxygen partial pressure change of the sample chamber took place in a time frame of less than 10 s.

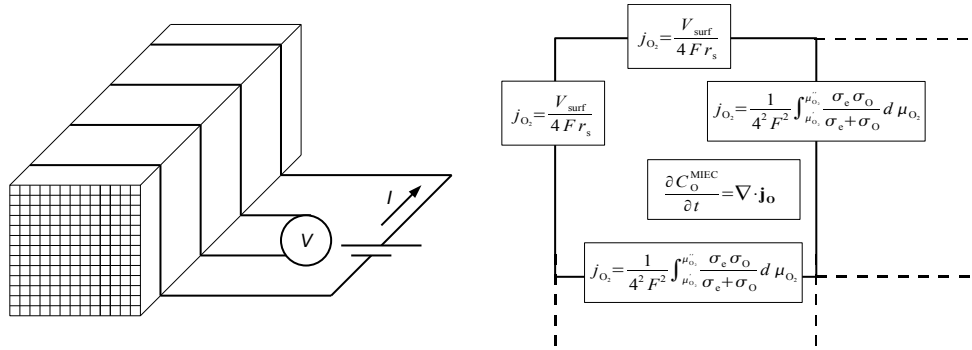


Figure 3.2: Left: Measurement schematic of the four point conductivity relaxation experiment. A current supply applies a current to the outer electrodes, while a voltmeter measures the potential drop between the inner electrodes. The mesh on the end face illustrates the mesh used for modelling of the transient response. right Overview of the transport and mass balance equations used in the SS, MR and CR models. A corner segment of the CR experiment has been used as an example.

3.3 Theory

The theory of the MR and SS experiment, and the data treatment used for interpreting the data is described in detail in Chapter 2. The transport models of SS, MR and CR is illustrated in Fig. 3.2 (right) with a corner segment of the CR experiment as an example. Below the main points are summarized.

3.3.1 Steady state membrane experiment (SS)

In the SS measurement, a steady current is applied to the pumping electrodes of the oxygen pump. The signals of the reference electrodes and the electrolyte probe are then be recorded at steady state. During steady state, the oxygen current pumped through the oxygen pump equals the current through the membrane. The oxygen flux through the membrane j_{O_2} , is described

using the Wagner equation:

$$j_{O_2} = -\frac{1}{4^2 F^2 L} \int_{\mu_{O_2}^{\prime}}^{\mu_{O_2}^{\prime\prime}} \frac{\sigma_e \sigma_O}{\sigma_e + \sigma_O} d\mu_{O_2} \quad (3.1)$$

where $\mu_{O_2}^{\prime}$ and $\mu_{O_2}^{\prime\prime}$ are the chemical potentials of oxygen at each interface, L is the thickness of the membrane, σ_e and σ_O are the electronic and ionic conductivity and F is the Faraday constant. As the diffusion happens by vacancy jumping σ_O is the product of the mobility and concentration of oxide ions. Instead of σ_O we will fit with the reduced diffusion coefficient, D_V^0 :

$$D_V^0 = \frac{4RT}{C_V \left(1 - \frac{\delta}{3}\right)} \frac{1}{4^2 F^2} \frac{\sigma_e \sigma_O}{\sigma_e + \sigma_O} \quad (3.2)$$

For further details of the relations between Eq. 3.1, the reduced diffusion coefficient, D_V^0 and the chemical diffusion coefficient, D_{chem} , widely used in the literature, we refer to Section 1.4.

μ_{O_2} in the closed compartment can be measured using the reference electrodes of the oxygen pump, while μ_{O_2} of the upper compartment can be deduced from the p_{O_2} measured by the reference electrodes when no pumping current is applied, and the flux of oxygen through the membrane:

$$p_{O_2} = p_{O_2}^{I_{pump}=0} + \overbrace{\frac{J_{O_2} RT \Phi_f}{P \Phi_f}}^{\text{permeation term}} \quad (3.3)$$

where $J_{O_2} = I_{pump}/4F$ is the oxygen flux applied by the oxygen pump, I_{pump} is the current applied to the oxygen pump electrodes, R is the gas constant, Φ_f is the volume flow, and T_{Φ_f} is the T where the volume flow is measured. The second term on the right side of Eq. 3.3 originates from the oxygen permeation through the membrane, and will be referred to as the *permeation term* in the following.

The surface resistance is defined as:

$$r_s = \frac{V_{surf}}{i_{pump}}, \quad k_O = \frac{RT}{8C_O^{MIEC} n F^2 r_s} \quad (3.4)$$

where V_{surf} is the Nernst voltage across the MIEC surface, i_{pump} is the area specific pumping current and n the reaction order of the surface reaction. For the details of conversion between the r_s and the chemical surface coefficient k_{chem} , and the surface rate constant k_O we refer to section 1.5.

3.3.2 Membrane relaxation experiment (MR)

When the membrane is in equilibrium with the p_{O_2} in the upper compartment and when no pumping current is applied, a change of the p_{O_2} of the gas in the upper compartment will cause a relaxation of the membrane. This relaxation can be monitored using the oxygen pump and electrolyte probe. The time dependence of the oxygen concentration in a given part of the MIEC, C_O^{MIEC} , is governed by conservation of mass:

$$\frac{\partial C_O^{MIEC}}{\partial t} = \nabla \cdot \mathbf{j}_O \quad (3.5)$$

where t is the time and \mathbf{j}_O is the oxygen flux vector.

At the surface:

$$j_{O_2} = \frac{V_{surf}}{4F r_s} \quad (3.6)$$

In the MR experiment we also take the permeation term into account:

$$p_{O_2} = p_{O_2}^{t>0} + \frac{\overbrace{J_{O_2} RT \Phi_f}^{\text{permeation term}}}{P \Phi_f} \quad (3.7)$$

where $p_{O_2}^{t>0}$ is the p_{O_2} of the gas flow after the gas change and J_{O_2} is the flux of oxygen from the membrane into the upper compartment.

By dividing the membrane into a mesh of sections, and applying Eqs. 3.1, 3.5, 3.6 and 3.7, the time dependence can be fitted.

3.3.3 Conductivity Relaxation (CR)

Full model

Conductivity relaxation is similar to membrane relaxation, except it is the total conductivity of the bar shaped sample which is measured as a function of time, and oxygen leaves the bar from all surfaces. Assuming a C_O^{MIEC} independent electron mobility much larger than the oxide ion mobility, the electronic conductance, G_e of a conductivity relaxation measurement can be written:

$$G_e = \int_A \sigma_{\text{tot}} dA, \quad \sigma_{\text{tot}} \simeq \sigma_e \propto C_O^{\text{MIEC}} \quad (3.8)$$

Equations 3.1, 3.5, 3.7 and 3.8 are solved for a bar sample and fitted to the measured data. The model geometry for the conductivity relaxation setup is shown on the end face of the bar in Fig. 3.2. The number of segments is adjusted for each relaxation as some are surface controlled; some are diffusion controlled and some are in a mixed regime.

Partial model

Conductivity relaxation is a widely used technique for extracting transport parameters of mixed conductors [16, 37, 41, 42]. Instead of applying the full model previously described, it is traditionally modelled using the concentration of oxide ions as the driving force in the bulk, instead of the chemical potential [15]:

$$J_{O_2} = -D_{\text{chem}} \nabla C_O^{\text{MIEC}} \quad (3.9)$$

where D_{chem} is the chemical diffusion coefficient. At the surfaces a linear relationship between concentration is also assumed:

$$J_{O_2} = -k_{\text{chem}} (C_O^{\text{MIEC}} - C_O^{\text{MIEC},t=\infty}) \quad (3.10)$$

where $C_O^{\text{MIEC},t=\infty}$ is the concentration of oxygen ions in the surface when equilibrium is reestablished. The relaxation after a step change in the p_{O_2} at the gas/MIEC interface can be modelled with a simple analytical expression if D_{chem} and k_{chem} is assumed to be constant, and the effect of the permeation term in Eq. 3.3 is neglected. For a bar shaped sample of equal height and width, a , it is [42]:

$$\frac{\sigma - \sigma^{t=0}}{\sigma^{t=\infty} - \sigma^{t=0}} = 1 - \left[\sum_{m=1}^{\infty} \frac{2L^2 \exp\left(\frac{-\beta_m^2 D_{\text{chem}} t}{a^2}\right)}{\beta_m^2 (\beta_m^2 + L^2 + L)} \right]^2 \quad (3.11)$$

where t is the time since the gas change and β_m is given by the positive roots of the equation:

$$\beta \tan \beta = L; \quad L = \frac{ak_{\text{chem}}}{D_{\text{chem}}} \quad (3.12)$$

D_{chem} and k_{chem} are, however, generally not constant as a function of p_{O_2} , and the analytical approach will require that the p_{O_2} step changes are small. The full model which keeps D_{V}^0 and k_{O} constant and calculates the p_{O_2} change in the gas caused by the flux through the sample surface, should not require these small steps. The full model, however, requires knowledge of the oxygen stoichiometry of the sample and takes 400-800 times the time to calculate, so the simple model is preferable when applicable.

3.4 Results and discussion

3.4.1 Influence of corrections

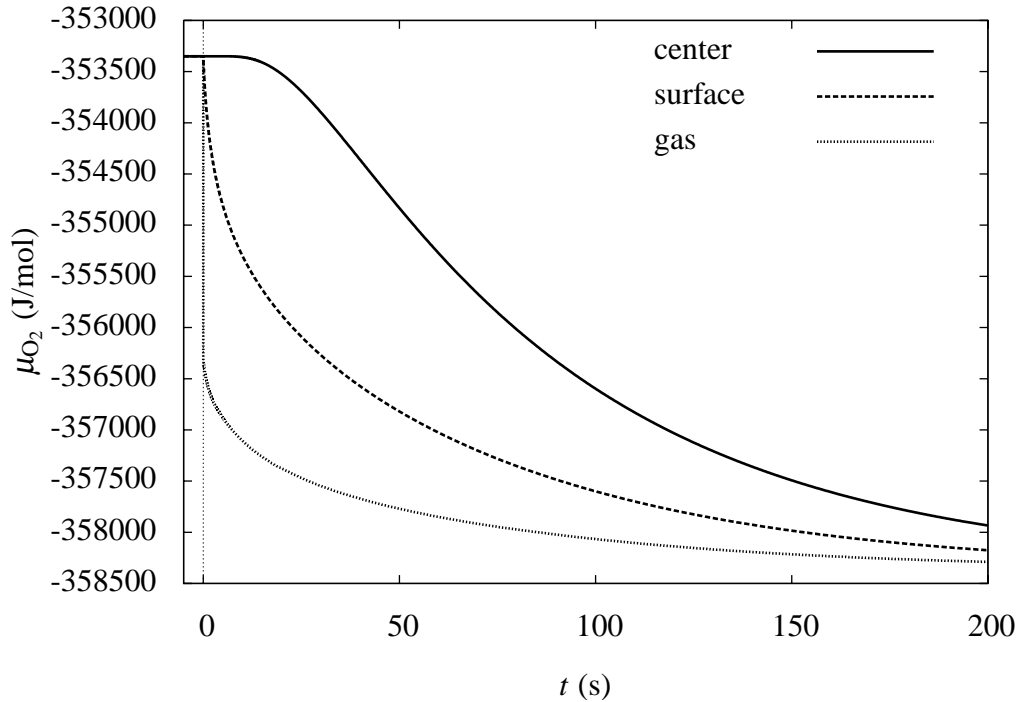


Figure 3.3: Example of the modelling of a conductivity relaxation after a gas change at $t = 0$ s from $p_{\text{O}_2} = 0.0022$ to $p_{\text{O}_2} = 0.00137$. The μ_{O_2} of the center of the sample, the surface of the sample and the gas around the sample is shown as a function of time after a gas change.

In Fig. 3.3, an example of the modelling of a relaxation after a gas change is shown. The μ_{O_2} of the inlet gas is assumed to change immediately to the end value. The "gas" curve is the result of the mixing of the inlet gas with the oxygen permeating out of the bar sample. The "surface" curve is the μ_{O_2} of the surface of the sample. The "center" is the μ_{O_2} of the center of the sample. The center has a delayed response to the gas change as the gradients of μ_{O_2} inside the sample need to be built up.

Table 3.1: Model parameters for the relaxation in Fig. 3.4.

Curve	Model	D_V^0 $10^{-10} \text{ m}^2/\text{s}$	k_O 10^{-8} m/s
Full	Full	3.01	9.76
Partial	Partial	3.03	4.04
Partial B	Partial	3.01	9.76

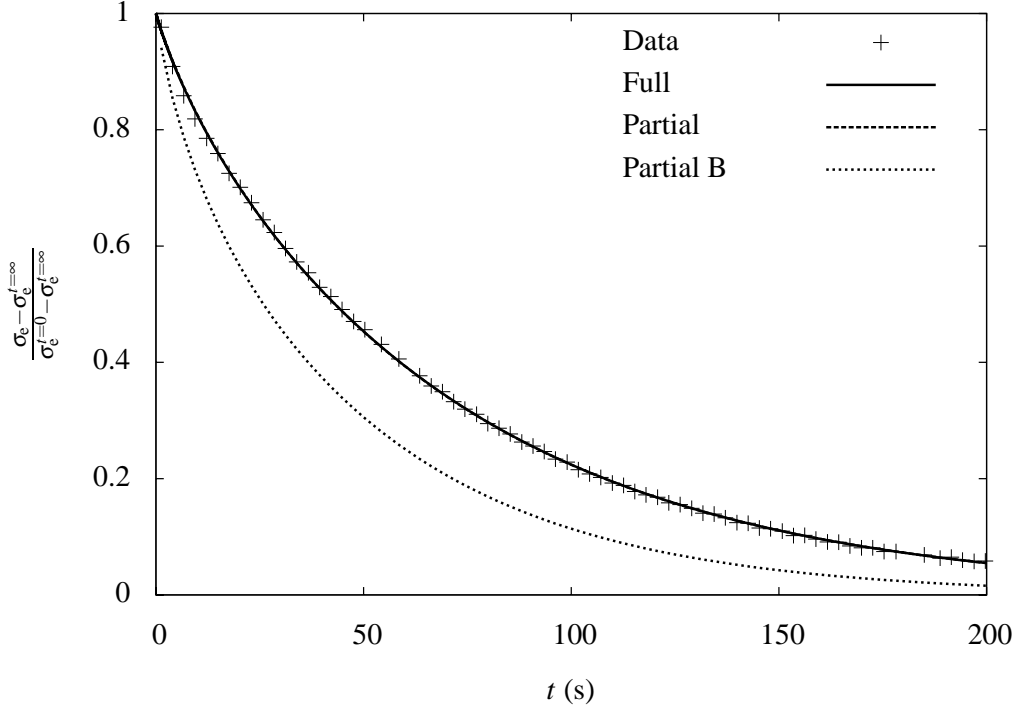


Figure 3.4: Best fits to the normalized CR data using the partial (constant D_{chem} and no perturbation term) and full models. Note that both the models are able to fit the curve and have extensive overlap. The "Partial B" curve is calculated using the partial model, but with the D_V^0 and k_O values of the best fit using the full model. t denotes time. σ_e is the electronic conductivity. $\sigma_e^{t=\infty}$ is the electronic conductivity when the relaxation is finished. $\sigma_e^{t=0}$ is the electronic conductivity at the beginning of the relaxation.

In Figure 3.4 fits using a partial model (constant D_{chem} and no perturbation term) and a full model to normalized conductivity relaxation data are shown. The fits of the two models are indistinguishable and both follow the measured data well. To illustrate the difference between the models, a calculation using the best fitting parameters of the full model has been inserted into the partial model (the "Partial B" curve). The model parameters are shown in table 3.1. While the models provide a similar fit, they use very different values of k_O to obtain that fit.

Influence of p_{O_2} step size and the permeation term

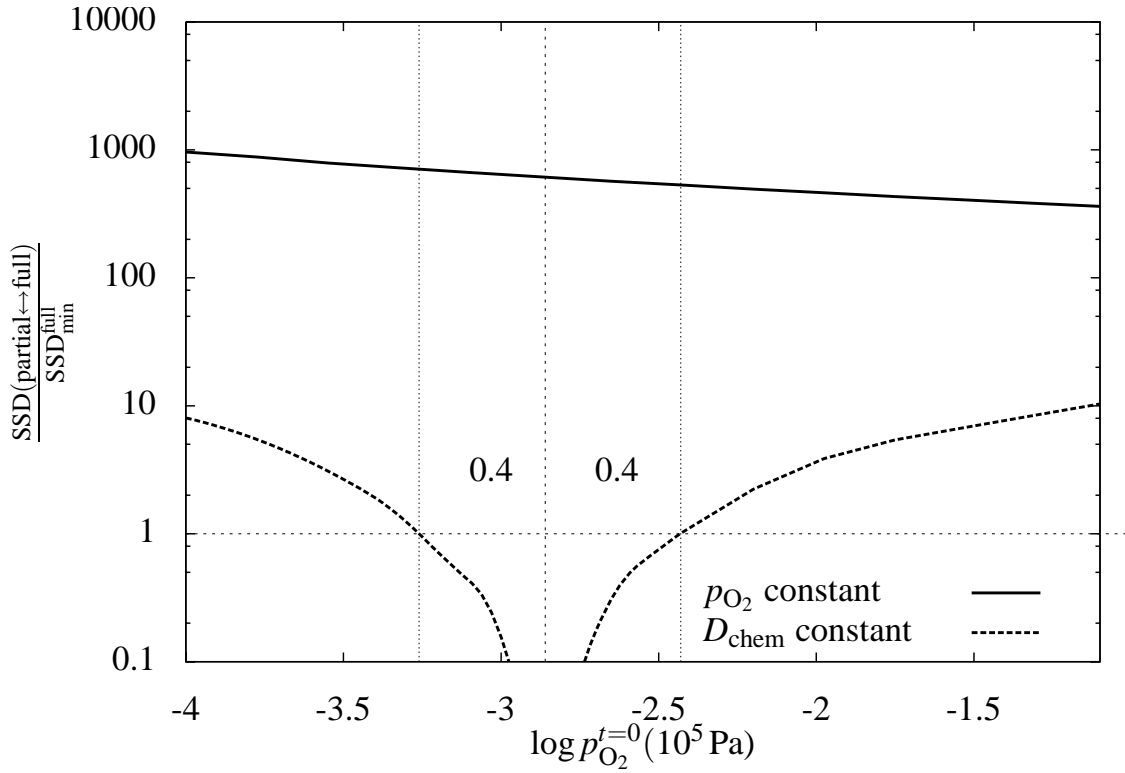


Figure 3.5: Calculated $\frac{SSD(\text{partial} \leftrightarrow \text{full})}{SSD_{\min}^{\text{full}}}$ for relaxation steps $p_{O_2}^{t=0} \rightarrow 1.37 \cdot 10^2 \text{ Pa}$ at 1273 K. A vertical dotted line at $\log p_{O_2} = -2.86$ (atm) marks the end p_{O_2} , while a horizontal dotted line marks the noise limit. The " D_{chem} constant" curve is the full model versus the full model with a constant D_{chem} . The crossing points of the " D_{chem} constant" curve with the noise limit have been marked with vertical dotted lines. The " p_{O_2} constant" curve is the full model, versus the full model where the permeation term is not ignored.

An evaluation of the advantage of the complex models is presented in Fig. 3.5 for CR measurements. The start p_{O_2} is varied while the end p_{O_2} is kept constant. Sum of square differences (SSD) are calculated between the full model, and partial versions of the model (see the "Full" curve and the "Partial B" curve in Fig. 3.4). The sum of square differences are normalized by dividing with the sum of square differences of the best fit of the full simulation to a measured relaxation $17 \cdot 10^2 \text{ Pa} \rightarrow 1.37 \cdot 10^2 \text{ Pa}$, SSD_{\min}^{Full} . A value below the dotted line at $\frac{SSD(\text{partial} \leftrightarrow \text{full})}{SSD_{\min}^{\text{full}}} = 1$, thus signifies the noise limit, i.e., that the difference between the full and partial simulation is smaller than the difference between the full simulation and the measured data.

In the " D_{chem} constant" curve, the partial model is identical to the full model, except that D_{chem} is kept constant through the membrane in the partial simulation. The different values of D_{chem} as a function of $\mu_{O_2}^{\text{MIEC}}$ in the membrane, that are calculated in the full model, have been approximated by a single value in the partial model. The curve crosses the $\frac{SSD(\text{partial} \leftrightarrow \text{full})}{SSD_{\min}^{\text{full}}} = 1$ line at $\log p_{O_2} = -3.26$ and -2.46 - both values about 0.4 from the $\log p_{O_2}$ value of the end p_{O_2} . It shows that if D_{chem} is kept constant, p_{O_2} steps exceeding a factor of $10^{0.4} = 2.5$ should be avoided as the error from not taking the variation of D_{chem} into account will otherwise exceed the noise limit and affect the results. This maximum allowed p_{O_2} step corresponds to a change in δ of 0.01. The absolute value of δ at the end p_{O_2} was 0.153. A p_{O_2} step of a factor of 2.5 is enough for most relaxation experiments, and we conclude that considering D_{chem} constant is a

good approximation for most applications.

In the " p_{O_2} constant" curve, the partial model is identical to the full model, except that in the partial model the permeation term is ignored. As can be deduced from Fig. 3.5, the permeation term shifts the fit significantly. The shift is caused by a reduction in driving force for the surface exchange coefficient by the permeation term. Reducing the step size will not reduce the shift, as the permeation term scales with the driving force. Note that this experiment was done with a gas flow of $4.17 \cdot 10^{-6} \text{ m}^3/\text{s}$ (250 mL/min) and a smaller gas flow would lead to even larger deviation. A gas flow of about $4 \cdot 10^{-3} \text{ m}^3/\text{s}$ (250 L/min) is required to make the permeation term insignificant, which is not practical. A reduction of temperature to reduce k_O and the flux out of the sample is another solution.

Differences between measured and corrected

We will now compare the results of our "full model" of CR experiments with those of a "simple model" which assumes a constant D_{chem} , and ignores the permeation term.

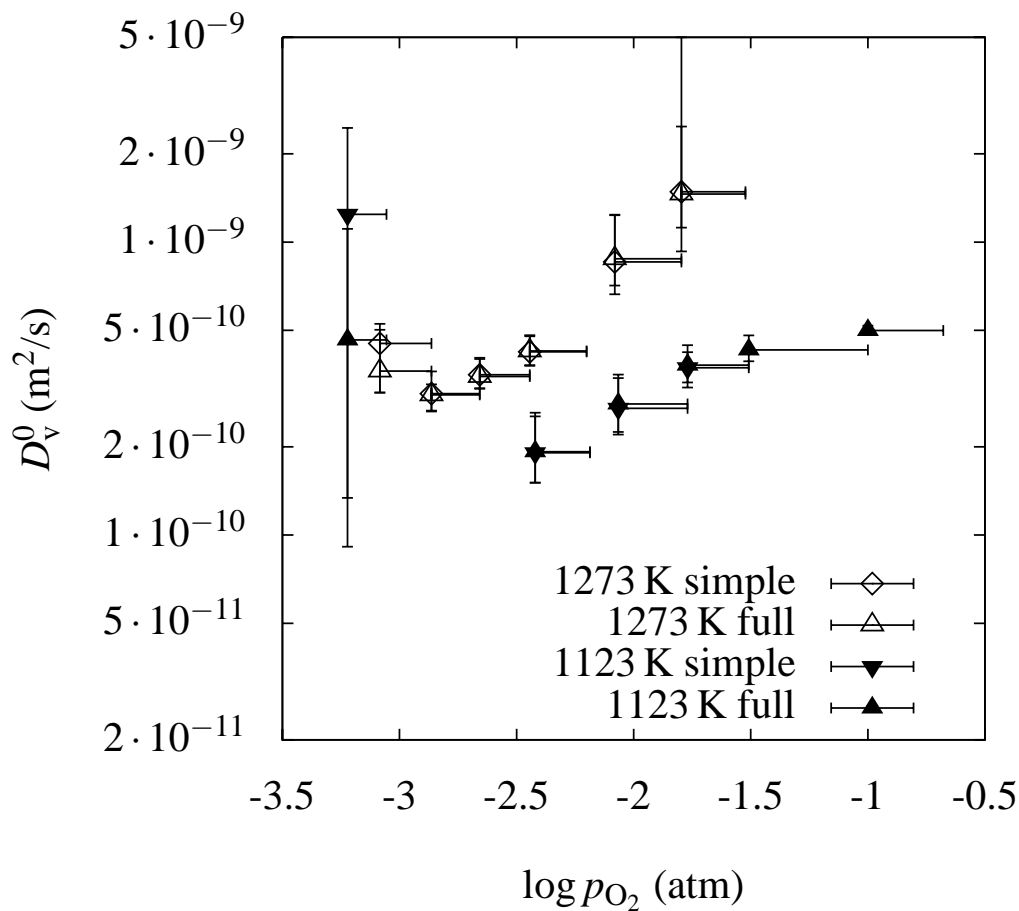


Figure 3.6: Comparison of simple and complex numerical models of a CR experiment. The horizontal error bar denotes the p_{O_2} interval of the relaxation, with the symbol at the end p_{O_2} .

In Fig. 3.6 the D_V^0 of the best fits using the simple and complex models are presented. No deviation exist between the simple and advanced models at either temperature except at very low p_{O_2} . We note that the deviation is within the confidence interval and attribute it to artifacts of the fitting. Thus, for the purpose of establishing D_V^0 , the simple and complex models are equally valid. We note however, that reducing the gas flow in the chamber from 250 mL/min to 100 mL/min or less (both volumes measured at $T = 295 \text{ K}$) will cause deviations at $T = 1273 \text{ K}$

outside the confidence interval.

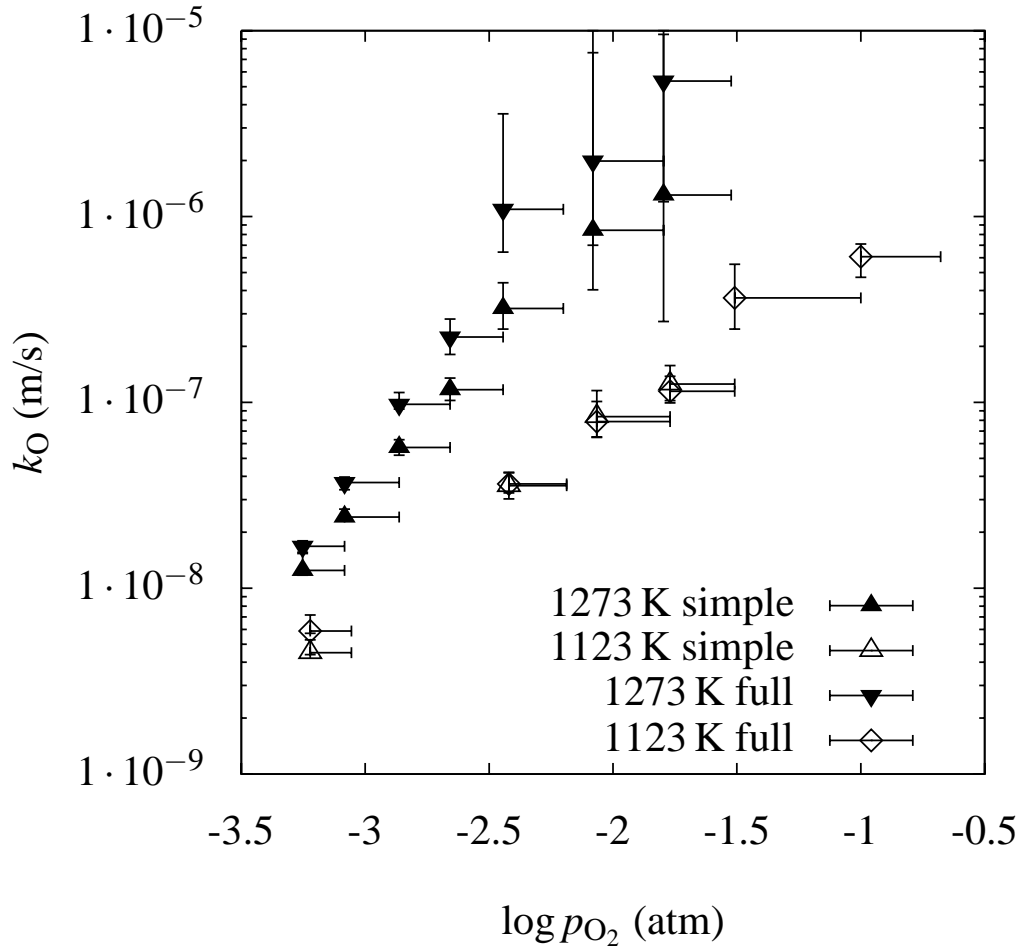


Figure 3.7: Comparison of simple and complex numerical model. The horizontal error bar denotes the p_{O_2} interval of the relaxation, with the symbol at the end p_{O_2} .

The values of k_O for the simple and complex models, plotted in Fig. 3.7 differ by 5-15% at $T=1123$ K (well within the confidence interval) and a factor of 3 to 5 at $T = 1273$ K. The main part of the difference comes from the permeation term. The difference between the values of the complex and the simple model shrinks as the p_{O_2} is reduced. This behavior can be rationalized by noting that k_O , and with it, the flux, is reduced by two orders of magnitude for each order of magnitude the p_{O_2} is reduced. The strong p_{O_2} dependence of k_O causes the difference between the models to shrink as the p_{O_2} is reduced, even though there is less oxygen in the gas to offset the permeation term.

The broader confidence intervals of the complex model reflects that the complex model is less sensitive to k_O than the simple model. In the simple model, the flux and k_O are roughly proportional. In the complex model, the benefit of a larger k_O is less than 1:1; Increasing k_O also increases the flux and thus reduce the available driving force across the surface. This results in the lower sensitivity of the complex model.

In conclusion, the usage of simple models with analytical solutions gives a significant systematic error to the extracted values of k_O , especially at high temperature and when oxygen exchange is fast. The dominant error source is that the simple models fail to take the oxygen exchanged by the membrane into account when evaluating the p_{O_2} of the gas around the sample.

3.4.2 Comparison of the confidence interval of the methods

We will now look at the width of the confidence intervals of SS, MR and CC.

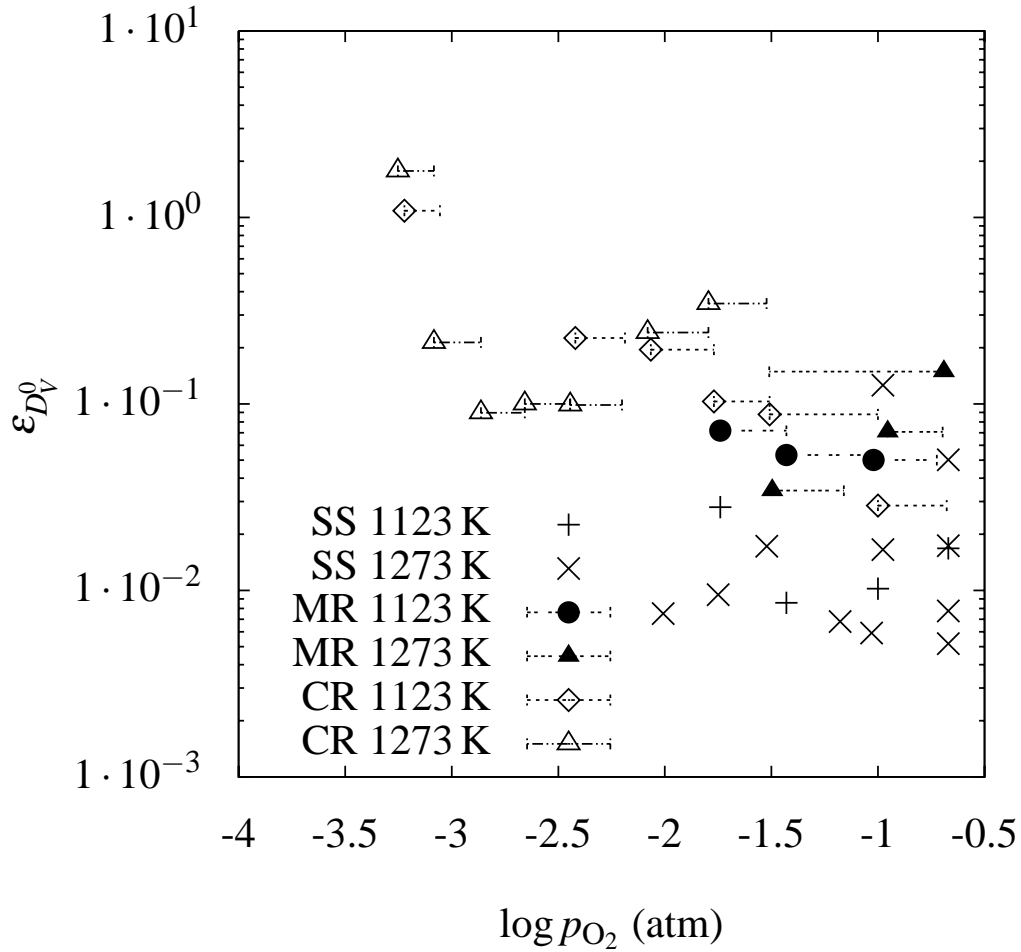


Figure 3.8: $\epsilon_{D_V^0}$ is plotted for the different measurement methods. SS is steady state, MR is membrane relaxation and CR is conductivity relaxation. The horizontal error bar denotes the p_{O_2} interval of the relaxation, with the symbol at the end p_{O_2} .

$\epsilon_{D_V^0} = \frac{\Delta D_V^0}{D_V^0}$ is the normalized width of the confidence interval of the measurements of D_V^0 . $\epsilon_{D_V^0}$ of the different measurements is plotted in Figure 3.8. Values of $\epsilon_{D_V^0}$ larger than 1 mean that only a lower limit of D_V^0 could be established. The steady state measurements have the smallest $\epsilon_{D_V^0}$, membrane relaxations and conductivity relaxation have a 5-10 times larger $\epsilon_{D_V^0}$. $\epsilon_{D_V^0}$ is large when p_{O_2} is low, as the sensitivity of the models to D_V^0 decreases as k_O becomes small enough to dominate the relaxation.

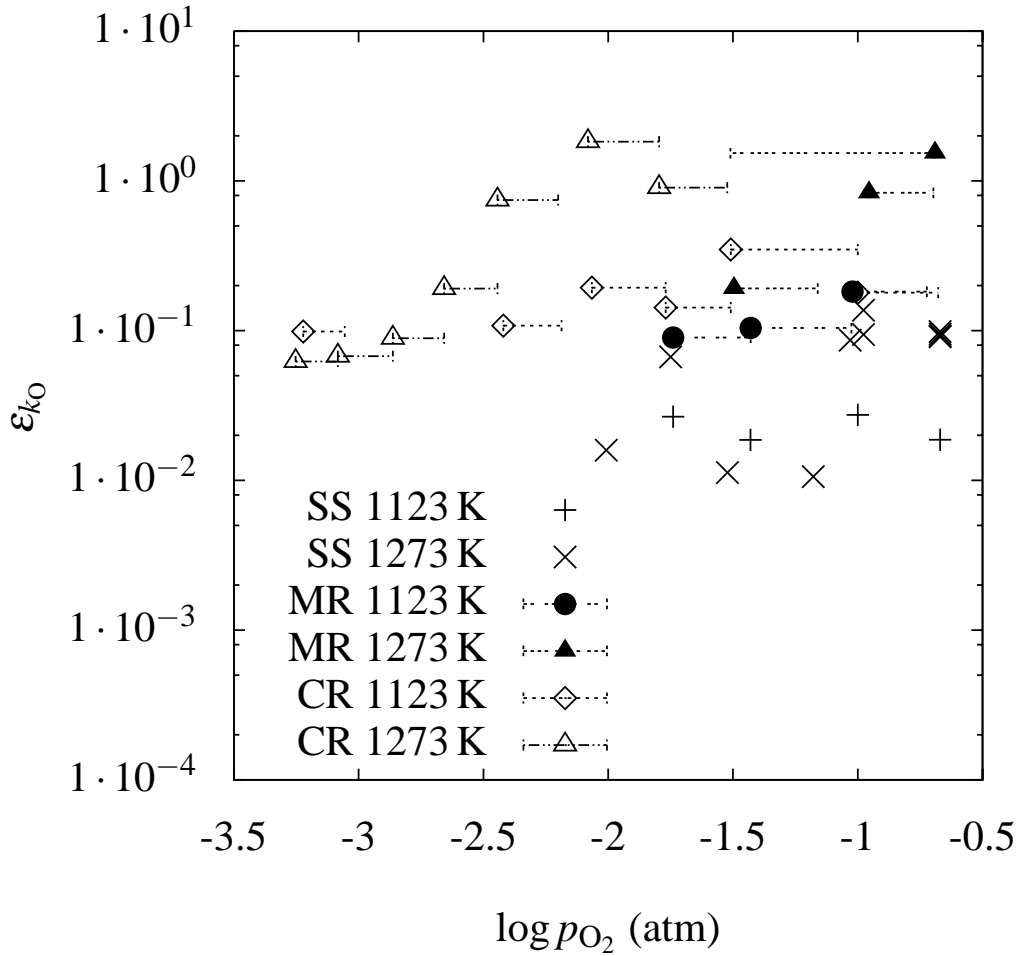


Figure 3.9: Comparison of ϵ_{k_O} of the different measurement methods. SS is steady state, MR is membrane relaxation and CR is conductivity relaxation. The horizontal error bar denotes the p_{O_2} interval of the relaxation, with the symbol at the end p_{O_2} .

$\epsilon_{k_O} = \frac{\Delta k_O}{k_O}$ is the width of the normalized confidence interval of the measurements of k_O . ϵ_{k_O} of the different measurements is plotted in Figure 3.9. Values of ϵ_{k_O} larger than 1 effectively mean that only a lower limit of k_O could be established. Steady state measurements have the smallest ϵ_{k_O} , membrane relaxations have a 5-10 times larger ϵ_{k_O} , and conductivity relaxation has ϵ_{k_O} further 2-5 times larger. The lowest ϵ_{k_O} is found at low temperature and low p_{O_2} , where k_O is small compared to D_V^0 and the models are more sensitive to k_O .

In general, the confidence intervals of the steady state measurements are much narrower than the confidence intervals of the relaxations. The confidence intervals of the steady state measurements are also less dependent on p_{O_2} and T . This is attributed to the simpler task of modelling a steady state compared to a transient relaxation. Furthermore, the confidence intervals on the membrane relaxations seem to be narrower than the confidence intervals of the conductivity relaxations, especially when measuring k_O at high p_{O_2} - this is attributed to the probe signal sensitivity to k_O and the added precision from measuring two signals instead of just one.

3.4.3 Relaxation vs. steady state

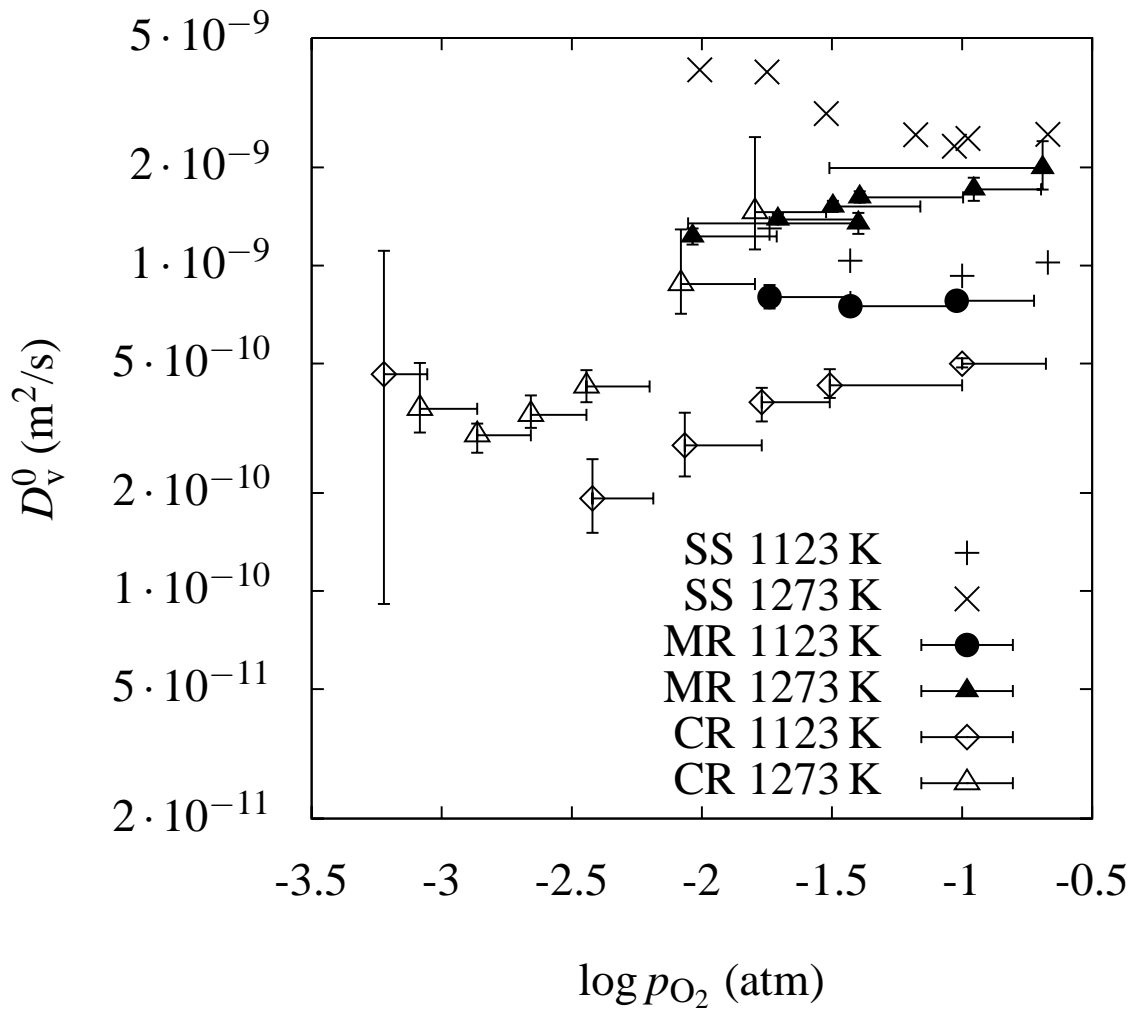


Figure 3.10: D_v^0 calculated from steady state (SS), membrane relaxations (MR) and conductivity relaxation (CR) experiments. The horizontal error bar denotes the p_{O_2} interval of the relaxation, with the symbol at the end p_{O_2} .

D_v^0 obtained from the steady state measurements and the relaxation experiments are plotted in Fig. 3.10. The values obtained using steady state measurements show a small increase in D_v^0 when reducing the p_{O_2} , while the relaxations show a constant or decreasing D_v^0 when reducing the p_{O_2} . Note that the D_v^0 values from CR are lower than the MR and SS values at $T = 1123$ K.

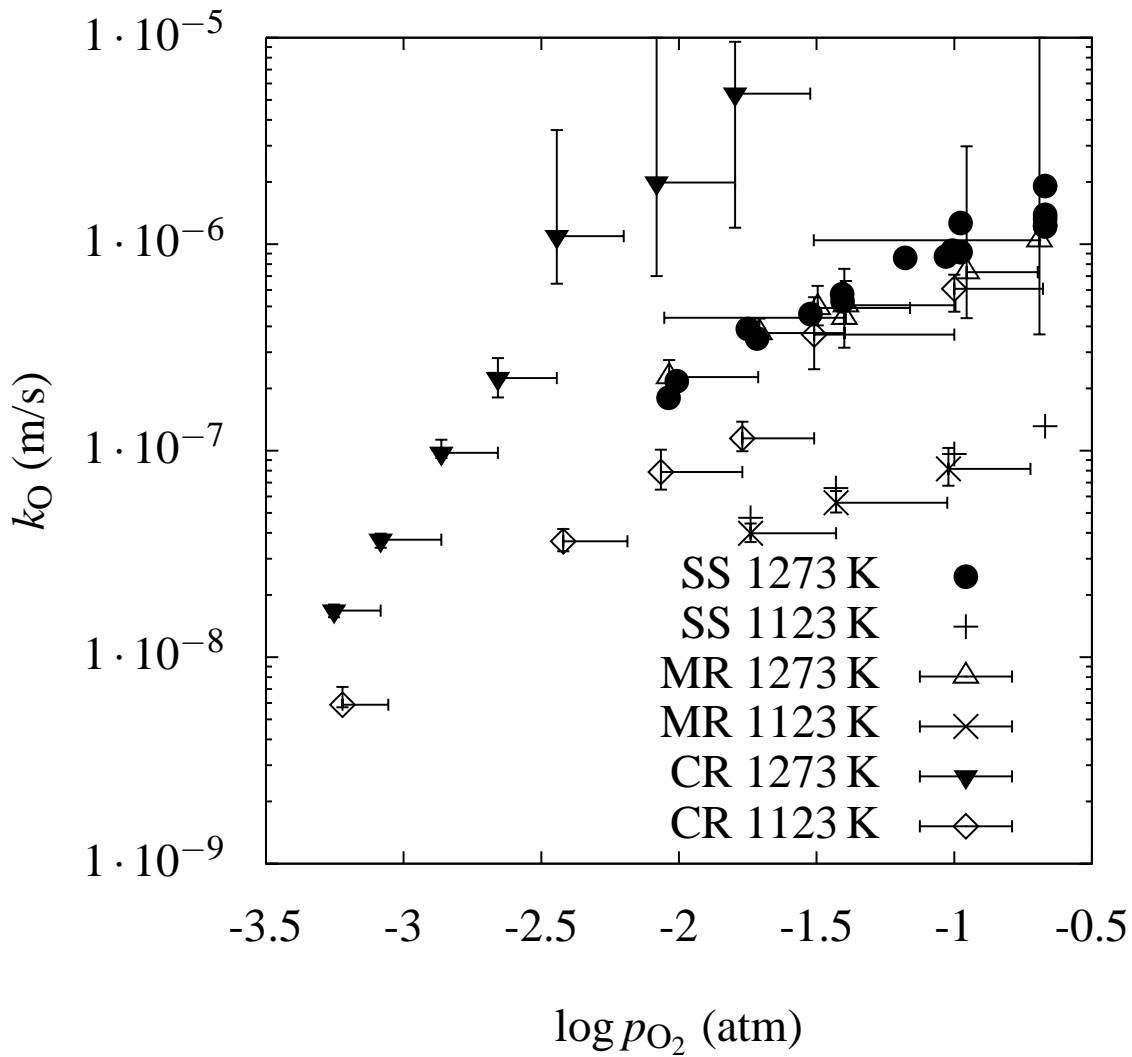


Figure 3.11: k_O calculated from the SS, MR and CR experiments. The horizontal error bar denotes the p_{O_2} interval of the relaxation, with the symbol at the end p_{O_2} .

k_O obtained from the steady state measurements and the relaxation experiments are plotted in Fig. 3.11. The CR values are double that of the MR and SS values. In the SS and MR experiments, k_O is primarily determined by the electrolyte probe.

The correlation between D_V^0 and k_O is evident as the k_O values from CR at $T = 1123$ K are higher than those from MR and SS - while the D_V^0 values from CR are lower than the MR and SS values. Lowering D_V^0 while simultaneously increasing k_O will, to some extent result in much the same transient response for the CR measurements. This is, as mentioned, reflected in the wide confidence intervals. The MR and SS relaxations do not have the same interchangeability as the electrolyte probe narrows the confidence interval of k_O significantly. The systematic deviation between CR and MR/SS can thus originate from two possible causes:

- The interpretation of the cone signal is wrong
- The CR fits are influenced by a systematic tendency to overestimate k_O and underestimate D_V^0 .

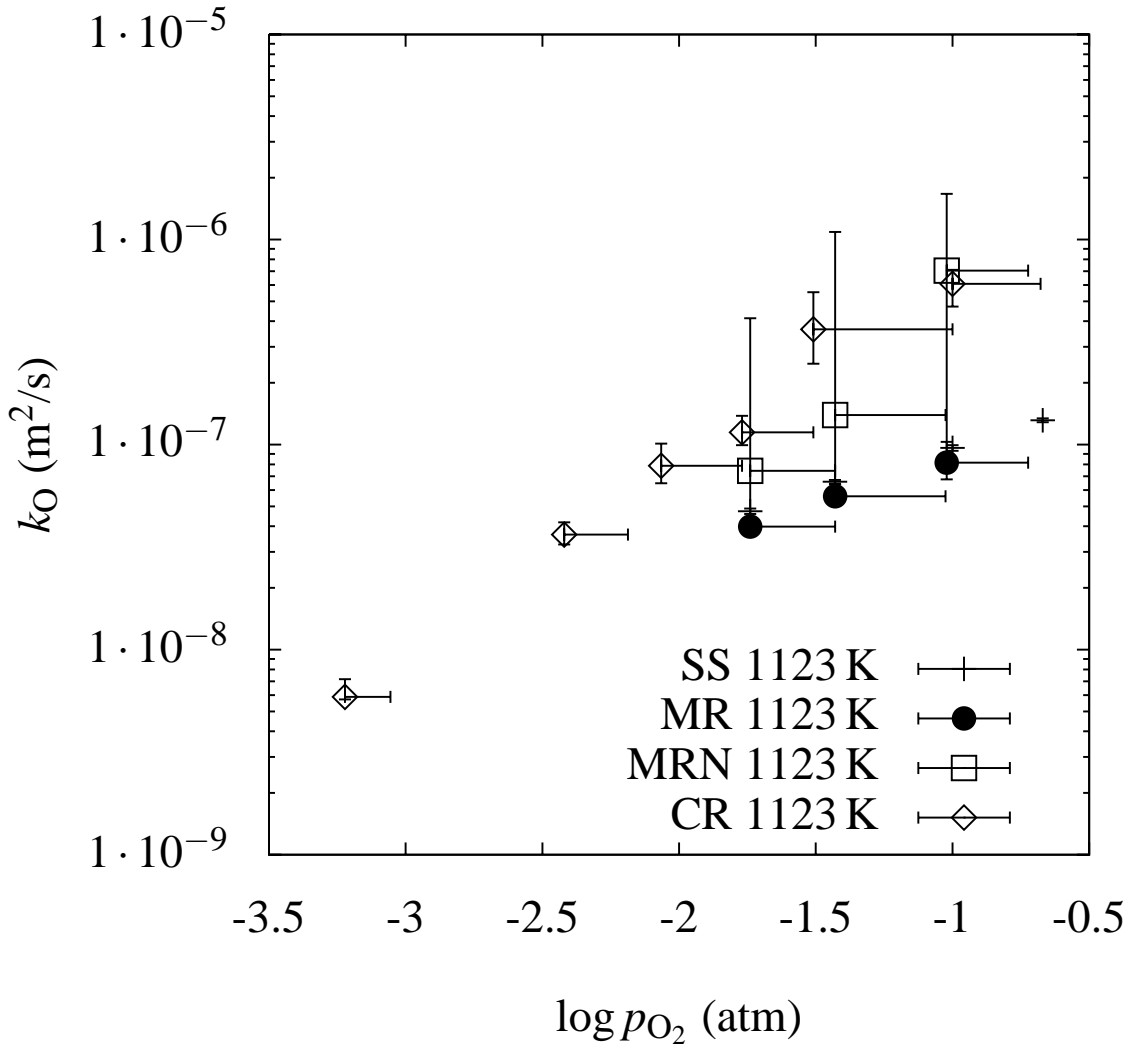


Figure 3.12: k_O calculated from the steady state and the relaxation experiments. MRN is the best fit of the MR experiment, where the probe signal is ignored. The horizontal error bar denotes the p_{O_2} interval of the relaxation, with the symbol at the end p_{O_2} .

To investigate if it is a misinterpretation of the cone signal, that is responsible for the discrepancy between the SS and MR results, and the CR results, the V_{ref} curve of the MR measurements refitted ignoring the probe signal. The results of the MR experiment, where the probe signal is ignored is plotted in Figure 3.12 with the name MRN. It was compared with the other measurements at $T=1123$ K. When the probe signal was removed, the best fit moves and now agrees nicely with the CR values. The error bars also expand significantly as the probe signal is the most direct measure of k_O , and they still overlap the MR error bars.

The measurements taking the probe into account will determine k_O within a narrow confidence interval, as the probe signal is a direct measure of the surface kinetics. Without the probe signal, k_O is not very well determined and even small systematic errors in the fitting of the relaxation can move it. Either the CR measurements are subject to those systematic errors, or the probe signal underestimates k_O .

3.4.4 Errors in modelling the probe signal

The measurements in Figs. 3.10, 3.11 and 3.12 suggest the possibility that k_O is underestimated

when using the probe to measure it. In the SS measurements the $i_{\text{pump}}/V_{\text{probe}}$ relationship is close to linear at all measured p_{O_2} . Any overestimation must therefore have the same linearity.

A probe penetrating too deep into the membrane will probe $\mu_{\text{O}_2}^{\text{MIEC}}$ further into the bulk than expected. A blunt probe will block the flux and alter the $\mu_{\text{O}_2}^{\text{MIEC}}$ profile in the membrane. Both cases result in a larger absolute value of V_{probe} . To detect any penetration of the probe tip, the MR measurements were refitted, where the probe signal was assumed to originate from different depths below the sample surface. A common "best depth" of penetration could, however, not be established for the measurements. The "best depth" seemed to vary systematically with the temperature and p_{O_2} , and is thus dismissed as the origin of the discrepancy between the MR and SS measurements.

Thermovoltages are present in the measurement system, and if a thermovoltage has the same linearity in i_{pump} , it would give a contribution to V_{probe} , which is not easily separated from V_{surface} . Based on the Seebeck coefficient of CG10 measured by Lim *et al.* [40] the probe signal of 0.65 mV would correspond to a temperature difference between the base and the tip of the probe of about 2 K for a 100 Am^{-2} current density measurement at 1273 K and $p_{\text{O}_2} = 0.04 \text{ atm}$. If the voltage response was originating entirely from a temperature gradient, it would have to be current dependent.

Resistive heating of the sample would scale roughly with the surface resistance, but is dismissed as:

- The sample resistance would only generate about 1 Wm^{-2} .
- The contribution to the voltage would be parabolic - not linear - in i_{pump} .

Heating from the endothermic and exothermic reactions on the surface could be linear in i_{pump} . This heating is, however, dismissed as neither the reaction enthalpy nor the Seebeck coefficient varies enough to account for the large span of r_s values.

In conclusion, we attribute the discrepancies between the relaxation techniques and the probe based techniques to systematic errors in the fitting of the transient responses of CR.

3.4.5 Comparison of values to those in the literature

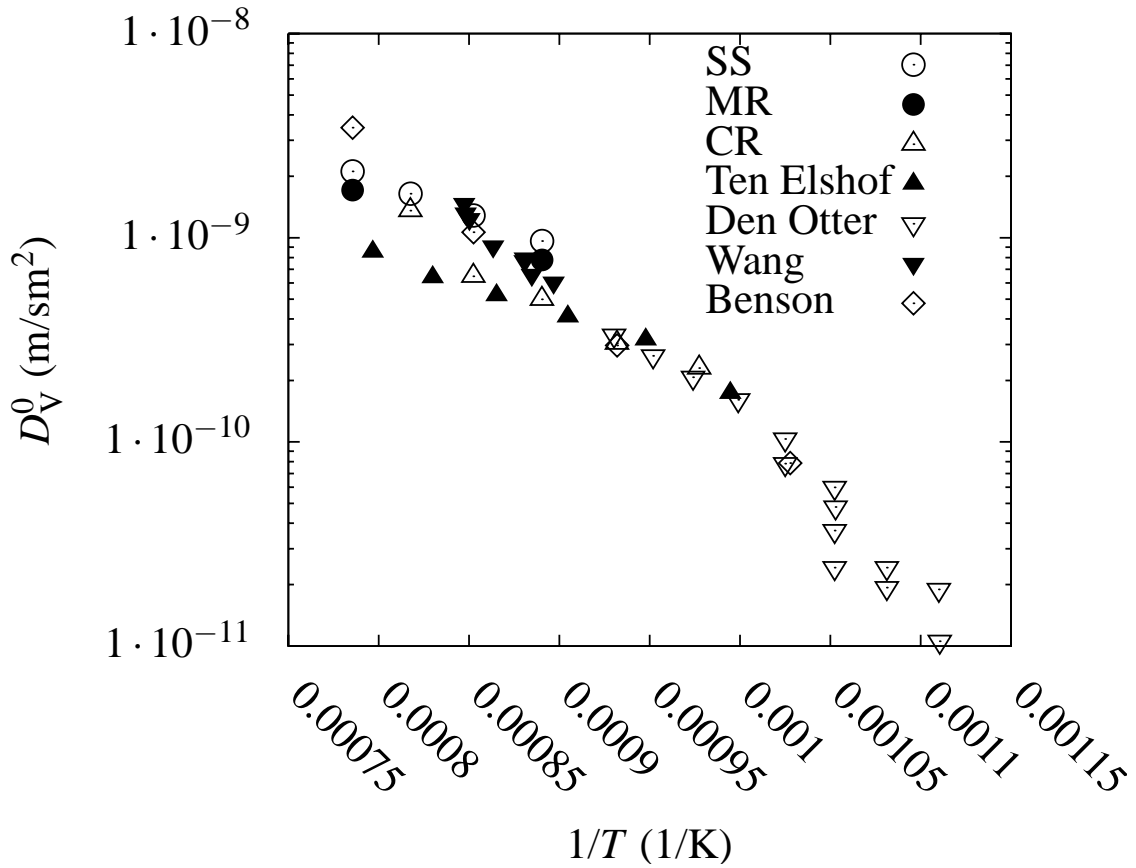


Figure 3.13: Comparison of D_V^0 to values reported in literature and converted to D_V^0 . The values of Ten Elshof [16], Den Otter [39] and Wang [43] were measured using conductivity relaxation while those of Benson [17] were obtained from an isotopic exchange experiment.

The values of D_V^0 found in this study are compared to values reported in the literature in Figure 3.13. The values of D_V^0 from the relaxation data have an activation energy close to that reported in literature. The magnitude of the values derived from SS and MR measurements are, however, about twice those found for CR both in this thesis and in the literature.

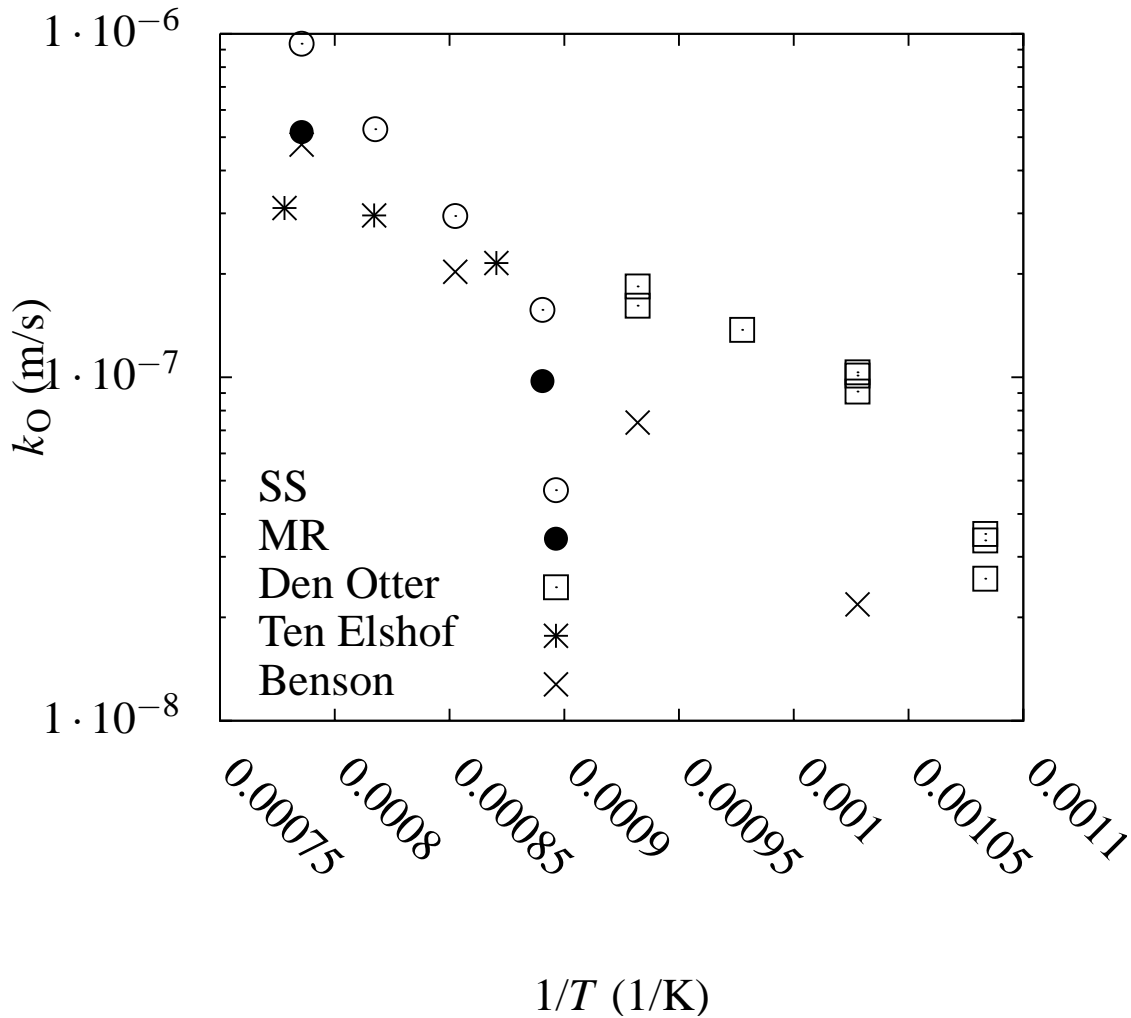


Figure 3.14: Comparison of k_O to values reported in literature and converted to k_O . The values of Ten Elshof [16], Den Otter [39] were measured using conductivity relaxation while those of Benson [17] were obtained from an isotopic exchange experiment.

The values of k_O found in this study are compared to values reported in the literature in Figure 3.14. Both the values of k_O from the relaxation data and from the steady state measurements have an activation energy higher than the CR values by Den Otter and ten Elshof, which is very low at high T . Interestingly, the data reported by Benson, using isotope exchange, show the same high activation energy as the measurements reported in this study. In the measurements of Benson, great care are taken to measure the ^{18}O fraction of the gas, in situ, and the measurements were thus corrected for the reduction in driving force by the ^{16}O leaving the sample.

The conductivity relaxation of Den Otter and ten Elshof do not take the permeation term into account. This reduces the driving force across the surface, and k_O is underestimated. This error grows with the temperature. We therefore propose, that the low activation energy of Den Otter and ten Elshof at high temperature is caused by this.

As the extraction of D_V^0 and k_O from relaxation experiments is notoriously difficult in air where k_O is large, we have not shown our CR results in Fig. 3.14, as they have confidence intervals spanning orders of magnitude.

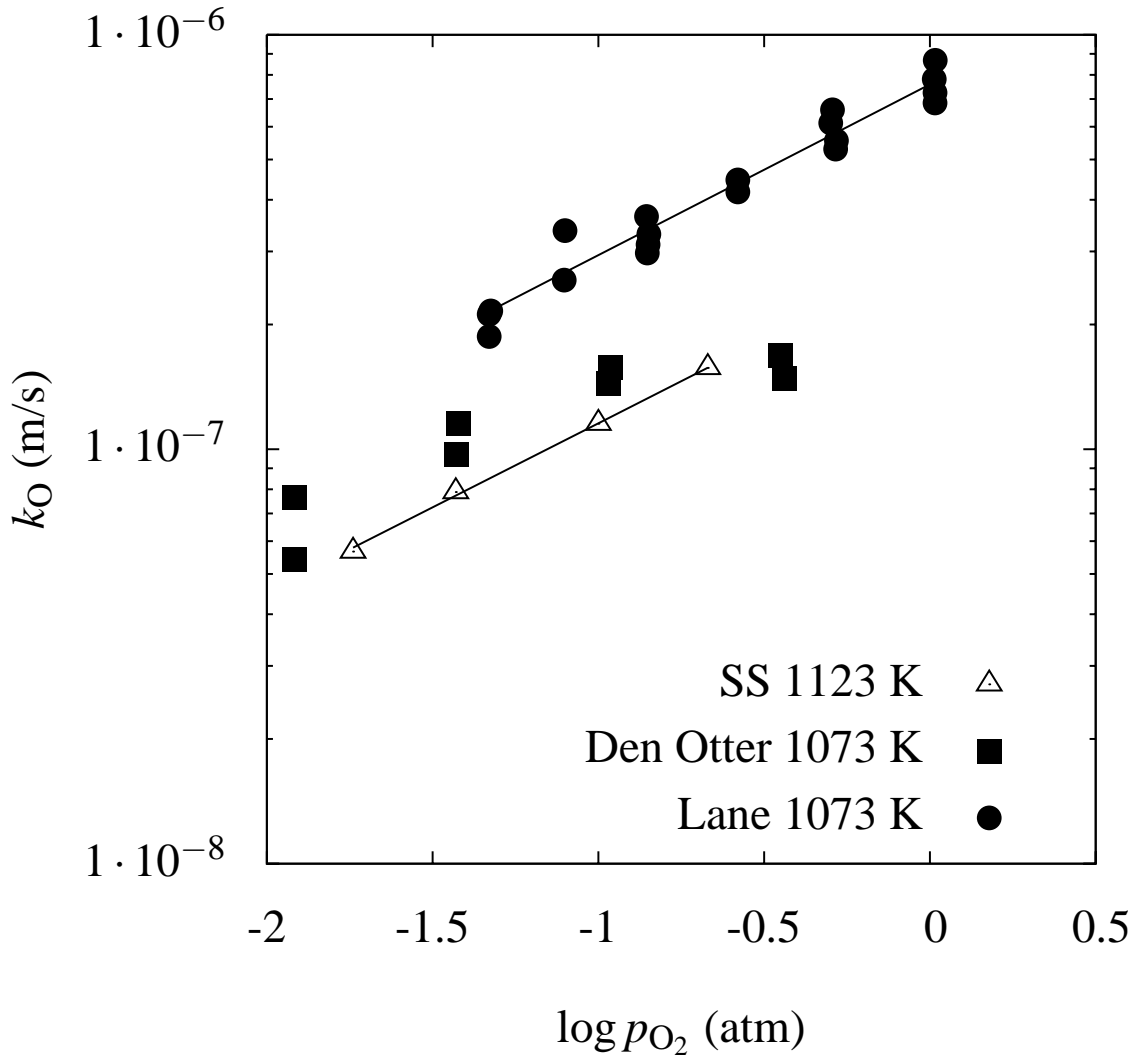


Figure 3.15: Comparison of SS k_O to values reported in literature and converted to k_O as a function of p_{O_2} . The values of Den Otter [39] and Lane [23] were measured using conductivity relaxation.

The values of k_O found in this study using SS are compared to values reported in the literature in Fig. 3.15. The values of Den Otter [39] and Lane [23] were measured using conductivity relaxation. There is excellent agreement on the slope of the results of Lane and this thesis, as they are both 0.42. The slope is equivalent to the reaction order of the surface reaction. The results of Den Otter are also in agreement with the values of this thesis, although they show a levelling out at high p_{O_2} not seen in either the results of Lane or this thesis.

3.5 Conclusion

It was found that the often used approximation of assuming a constant D_{chem} when fitting relaxation data is good for differences in δ less than 0.01 (a factor of 2.5 in p_{O_2} at 1173 K). It was also found that ignoring the effect of the permeation flux on the gas p_{O_2} causes an underestimation up to an order of magnitude when measuring the surface activity.

Analysis of the probe signal dismissed the influence of thermovoltages and shadow effects as insignificant.

It was further found that the electrolyte probe provides a narrower confidence interval for

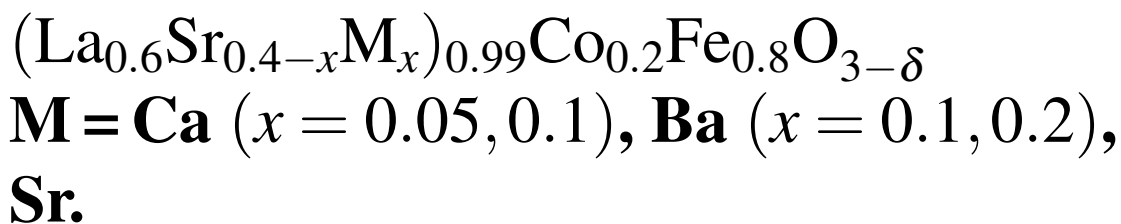
k_O than what can be obtained with conductivity relaxation. It was also shown that steady state measurements are more precise than relaxation measurements.

The values measured in this study as a function of p_{O_2} and T compare favourably to some of the data reported in the literature. The discrepancies found were attributed to the effect of the permeation flux on the gas p_{O_2} not being considered in the literature.

I acknowledge Martin Sjøgaard for providing me with the conductivity relaxation data used in this Chapter.

Chapter 4

Defect Chemistry of



Abstract

This Chapter is the first part of a two part series, where the effects of varying the A-site dopant on the defect chemistry, the reduced diffusion coefficient and the surface catalytic properties of the materials $(\text{La}_{0.6}\text{Sr}_{0.4-x}\text{M}_x)_{0.99}\text{Co}_{0.2}\text{Fe}_{0.8}\text{O}_{3-\delta}$, $M = \text{Sr}, \text{Ca}$ ($x = 0.05, 0.1$), Ba ($x = 0.1, 0.2$) (LSMFC) have been investigated. In part I, the findings on the defect chemistry are reported, while the transport properties are reported in part II (found in Chapter 5). Substitution of Sr^{2+} ions with Ca^{2+} ions (smaller ionic radius) and Ba^{2+} ions (larger ionic radius) strains the crystal structure differently for each composition while keeping the average valence of the cations constant. The Ba^{2+} containing materials show the largest oxygen loss at elevated temperatures, while the purely Sr^{2+} doped material showed the smallest oxygen loss. Some variation in the enthalpies and entropies of oxidation were found among the materials, however, no systematic relation to the dopant amount and type was found. The measured oxygen loss could be modelled with point defect chemistry models.

4.1 Introduction

The materials in the system $(\text{La}_{0.6}\text{Sr}_{0.4-x}\text{M}_x)_{0.99}\text{Co}_{0.2}\text{Fe}_{0.8}\text{O}_{3-\delta}$, $M = \text{Sr}, \text{Ca}$ ($x = 0.05, 0.1$), Ba ($x = 0.1, 0.2$) (LSMFC) are mixed ionic and electronic conductors (MIECs). MIECs are interesting materials for cathodes in solid oxide fuel cells [4, 5]. Other uses of MIECs exist in the field of controlled oxidation, oxygen production, or reactors for partial oxidation of methane to synthesis gas [7, 8]. Current research focuses on identifying materials combining good mechanical, catalytic and oxygen permeation properties [44]. A better understanding of membrane materials can facilitate identification of materials with high thermal stability and oxygen permeability.

In the selected materials, the average valences of the cations are kept constant. The LSMFC materials are thus not as chemically different from each other as, for instance, the series

$\text{La}_{1-x}\text{Sr}_x\text{Co}_{0.2}\text{Fe}_{0.8}\text{O}_{3-\delta}$, ($x = 0.0, 0.2, 0.4$) investigated by Tai *et al.* [38, 45], where the valence of the A site cations is manipulated directly, or the series $\text{La}_{0.6}\text{Sr}_{0.4}\text{Co}_{1-y}\text{Fe}_y\text{O}_{3-\delta}$ ($y = 0, 0.1, 0.25, 0.4, 0.6$) investigated by Lankhorst and ten Elshof [46], where the B site cation is varied between the easily reducible Co and the more stable Fe ions. Substitution of Sr ions with Ca ions (smaller ionic radius) and Ba ions (larger ionic radius) will, however, perturb the crystal structure differently for each composition. The main motivation for this study is to investigate the effects of such a perturbation of the structure on the defect chemistry and the transport properties.

A number of studies have treated the effect of structure on transport properties (see e.g. Cook and Sammells [47], Stevenson *et al.* [22], Tsai *et al.* [48] or Mogensen *et al.* [49, 50]). Common to all these studies are that they report on the ionic conductivity, which is a function of both the concentration of the oxide ion vacancies and the mobility of these vacancies. This Chapter is the first part of a two-Chapter series and reports data from measurements of the oxygen stoichiometry of the LSMCF materials. Chapter 5 reports data from measurements of the transport parameters. The stoichiometry data of this paper is used to distinguish the effects of oxide ion vacancy concentration and the mobility of each ion, when analyzing the transport parameters.

The oxide ion site vacancy concentration is measured using a combination of thermogravimetry (TG), and coulometric titration (CT) in a closed electrochemical cell similar to the one used by Zachau-Christiansen *et al.* [27]. Coulometric titration is used to measure the chemical potential of oxygen in a MIEC, $\mu_{\text{O}_2}^{\text{MIEC}}$, as a function of oxygen pumped, via an oxygen pump, into a sealed chamber with a powder sample. The oxygen content of the sample, can be controlled and measured precisely by the oxygen pump, using a current supply and an amperometer. The oxygen chemical potential can simultaneously be measured using a pair of reference electrodes, thus providing a precise relation between the oxygen stoichiometry and oxygen chemical potential.

To describe the defect chemistry of the materials we use two "chemical picture" models of different complexity. In Model I, the behavior of the overall reaction enthalpy extracted from coulometric titration is predicted by assigning different reaction enthalpies and reaction entropies to the oxidation of Co^{4+} to Co^{3+} and Fe^{4+} to Fe^{3+} ; In Model II, oxidation of Co^{3+} to Co^{2+} is also taken into account.

4.2 Experimental

4.2.1 Sample preparation

LSMCF powders were prepared using the glycine nitrate combustion process [33]. The powders were calcined at 900°C for 12 h, and ball milled using ZrO_2 balls, each weighing 3 g in a 500 ml polyethylene container ($\varnothing = 5$ cm) with ethanol for 24 h at 200 RPM. Shaped samples (diameter 26 mm) were pressed from this powder using uniaxial pressures of 30-70 MPa. These samples were further compressed in an evacuated latex container suspended in water at a pressure up to 325 MPa. The samples were sintered at 1300°C for 12 h (diameter after sintering was 18.5-20 mm). The samples were polished using diamond suspensions with grain sizes down to 1 μm .

4.2.2 X-ray diffraction (XRD)

X-ray diffraction was done with Cu_{k_α} radiation, with a mean wavelength of 1.5406 Å (30 mA/40kV) on a STOE $\theta - \theta$ reflection diffractometer. The energy-dispersive, Peltier cooled Kevex detector was tuned to the Cu_{k_α} energy (8.04 keV with an energy window of 300 eV). The step size was 0.05 degrees, the counting time in each step was 3 s. Horizontal slits were 10 mm, and the vertical slits were 0.8 mm for the primary tube, and 0.3 mm on the detector. Sample rotation was 100 RPM. After the XRD, the sintered samples were crushed to powder for use in TG and CT.

4.2.3 Thermogravimetry (TG)

Powder samples were loaded into a Netzsch TG 439 differential thermobalance. An equal powder volume of alumina was used as the reference material. The powder weights were measured on a Mettler Toledo XS205 scale. Heating curves were performed in an air flow of 100 ml/min at a rate of 2 K/min: 293 K \rightarrow 1273 K \rightarrow 2 h dwell \rightarrow 1273 K \rightarrow 293 K \rightarrow 1273 K \rightarrow 4 h dwell. Hereafter the p_{O_2} was changed by sending, first, 100 ml/min of N_2 gas and, later, a 9% $\text{H}_2/91\%$ N_2 mixture through the thermobalance chamber. The p_{O_2} of the gas mixture was measured using an in-house manufactured YSZ p_{O_2} sensor downstream of the thermobalance. At 1273 K the p_{O_2} in the N_2 gas was 10^{-5} atm, and the p_{O_2} of the 9% $\text{H}_2/91\%$ N_2 mixture was 10^{-19} atm. The temperature was then increased in steps, allowing the sample to equilibrate at each step, until no further mass loss was observed. At $T = 1573$ K the sample weight changed no further.

4.2.4 Coulometric Titration (CT)

Alumina cups with an inner diameter of 9.5 mm and a depth of 15.15 mm giving a volume of $1.07 \cdot 10^{-6} \text{ m}^3$ were used for CT. The cups were dried at a temperature, T , of 573 K and were put into an excicator immediately after removal from the furnace. When the cups had cooled they were weighed on a Mettler Toledo XS205 scale. Each of the crushed powders were filled into a cup, and the cups with powder were dried at $T = 573$ K and put into an excicator immediately after removal from the furnace. The weight of the powders could then be determined as the difference between the weight of the cups without powder and the weight of the cups with powder. The powder weight was about 2.5 g and the cup weight was close to 7.5 g.

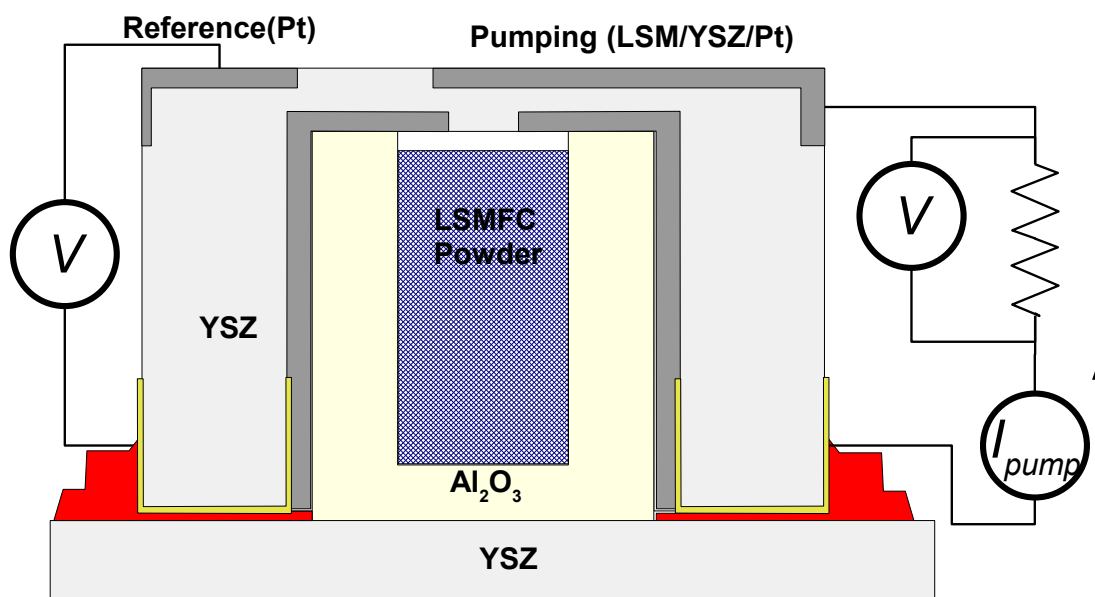


Figure 4.1: Sketch of the sealed electrochemical cell.

The setup for CT is shown in Fig. 4.1. $\text{Y}_{0.16}\text{Zr}_{0.84}\text{O}_{1.92}$ (YSZ) cups were machined with just enough room to contain the alumina cups. A $20 \mu\text{m}$ YSZ/ $\text{La}_{0.75}\text{Sr}_{0.25}\text{MnO}_3$ (LSM) layer for pumping electrodes was spray painted on the inside and outside of the YSZ cups, and sintered at 1373 K. Hand painted porous Pt was used as current collector. Patches of porous Pt (sintered at 1320 K) was also hand painted for reference electrodes. The alumina cups were inserted into the YSZ cups. Gold wires were inserted into grooves in the YSZ cups to obtain contact to the inner

electrodes, through gold paint. The outer electrodes were likewise connected with attached gold wires. Two layers of in-house produced Na_2O : 17.8 mol%, Al_2O_3 : 9.4 mol%, SiO_2 : 72.8 mol% glass tape were attached to the bottom of the YSZ cup for sealing and the assemblies were placed on top of flat YSZ plates. Mechanical pressure was applied from the top and the bottom, and glass paste was applied at the perimeter of the YSZ cup to further strengthen the seal. The setup was slowly heated to 1273 K, with short circuited electrodes and the system equilibrated for several hours.

The majority of the measurements were performed as temperature cycles. Under open circuit conditions, to keep the oxygen content inside the compartment constant, the temperature was lowered to 973 K and back at a rate of 1 K/min, while the voltage between the reference electrodes was continuously recorded. After completion of a temperature cycle, and with the cell at high T , the oxygen content inside the cup was adjusted by pumping oxygen in or out, via the pumping electrodes. The amount of oxygen pumped in or out of the cup was recorded by integrating the current between the pumping electrodes. Then the temperature cycle was repeated. A Keithley 2700 multimeter was used to measure voltage and current between the electrodes. An Instek GPS3030DD power supply was used as a current source when pumping oxide ions between the pumping electrodes. The pumping current was measured as the voltage across an $R \approx 10\ \Omega$ resistor. The exact resistance was measured using a Keithley 580 micro Ω meter.

4.3 Theory

4.3.1 Coulometric titration (CT)

The YSZ cup is an electrochemical cell with a YSZ electrolyte. At the pumping and reference electrodes the following reaction takes place:



The Nernst equation governing the relationship between oxygen chemical potential and cell voltage is:

$$\mu_{\text{O}_2}^{\text{in}} - \mu_{\text{O}_2}^{\text{out}} = RT \ln(p_{\text{O}_2}^{\text{in}}/p_{\text{O}_2}^{\text{out}}) = 4FV_{\text{ref}} \quad (4.2)$$

where T is the temperature, $p_{\text{O}_2}^{\text{in}}$ and $p_{\text{O}_2}^{\text{out}}$ are the oxygen partial pressures inside and outside the cell, $\mu_{\text{O}_2}^{\text{in}}$ and $\mu_{\text{O}_2}^{\text{out}}$ are the oxygen chemical potentials inside and outside the cell, F is the Faraday constant, R is the gas constant and V_{ref} is the voltage between the reference electrodes.

In this study, the gas outside the cell is atmospheric air. The standard chemical potential of oxygen as a function of T , can be calculated using the IUPAC standards for oxygen gas with the pressure $P = p_{\text{O}_2}^{\text{out}} = 0.209\ \text{atm}$ [10]. The chemical potential of oxygen inside the cell, $\mu_{\text{O}_2}^{\text{in}}$ can thus be found from Eq. 4.2 (see also Appendix A):

$$\mu_{\text{O}_2}^{\text{in}} = \mu_{\text{O}_2}^{\ominus}(T, P_{\text{A}}) + RT \ln\left(\frac{p_{\text{O}_2}^{\text{out}}}{P_{\text{A}}}\right) + 4FV_{\text{ref}} \quad (4.3)$$

where $\mu_{\text{O}_2}^{\ominus}(T, P_{\text{A}})$ is the chemical potential of oxygen at the reference pressure $P_{\text{A}} = 10^5\ \text{Pa}$ and the temperature, T . Faraday's equation gives the relationship between pumping current, I , and the oxygen transfer rate J_{O_2} . Four electrons pumped in the external circuit correspond to one oxygen molecule passing between the pumping electrodes:

$$J_{\text{O}_2} = \frac{I}{4F} \quad (4.4)$$

The molar amount, n , of LSMCF in the cup is $n = m/M$ where m is the mass of the powder, and M the molar mass of the perovskite. The change in δ , $\Delta\delta$, during a pumping session lasting from

time t_1 to time t_2 is:

$$\Delta\delta = \frac{2M}{m} \int_{t_1}^{t_2} J_{\text{O}_2}(t) dt = \frac{2M}{m} \int_{t_1}^{t_2} \frac{I(t)}{4F} dt = \frac{M}{2Fm} \int_{t_1}^{t_2} I(t) dt = \frac{M}{2Fm} Q \quad (4.5)$$

where Q is the total charge pumped out of the cell. When the temperature is changed, or when oxygen is pumped out of the cell, the chemical potential of oxygen in the compartment is changed, and the powder will absorb or desorb the oxygen from the gas present inside the sealed cup, changing $\mu_{\text{O}_2}^{\text{gas}}$. This change can then be monitored by the reference electrodes.

For this setup, the oxygen content in the gas inside the cup corresponds to a $\Delta\delta$ of the powder inside the cup of less than 10^{-3} at $p_{\text{O}_2} = 0.21 \cdot 10^5$ Pa and $T = 973$ K. Furthermore the amount of LSM in the cups was about 1/100 times the amount of LSMCF in the cup. The influence of the variation of oxygen stoichiometry of LSM on the measurements can thus be neglected. The amount of oxygen in the gas phase, and in the electrodes inside the cup is thus much smaller than the total amount of oxygen pumped in and out of the cup.

$\mu_{\text{O}_2}^{\text{MIEC}}$ can be written down in terms of the partial molar entropy, S_{Ox} , and partial molar enthalpy, H_{Ox} , of the oxidation).

$$\mu_{\text{O}_2}^{\text{MIEC}} = H_{\text{Ox}} - TS_{\text{Ox}} \quad (4.6)$$

H_{Ox} and S_{Ox} are determined by the crystal environment of the oxide ion sites, and do not directly depend on T . However, both the lattice constant [38, 51] and the valency of the B-site ions are influenced by δ which is T -dependent. To eliminate the influence of δ , the enthalpy and entropy are calculated using T -derivatives at constant δ value.

If the powder and the gas inside the cup is in equilibrium, ($\mu_{\text{O}_2}^{\text{MIEC}} = \mu_{\text{O}_2}^{\text{in}}$), and if we assume that H_{Ox} and S_{Ox} are independent of T , the combination of Eq 4.6 with Eq. 4.3 results in:

$$S_{\text{Ox}} = - \left[\frac{\partial \mu_{\text{O}_2}^{\text{MIEC}}}{\partial T} \right]_{\delta} = - \frac{\partial \mu_{\text{O}_2}^{\ominus}}{\partial T} - R \ln \left(\frac{p_{\text{O}_2}^{\text{out}}}{P_{\text{A}}} \right) - 4F \left[\frac{\partial V_{\text{ref}}}{\partial T} \right]_{\delta} \quad (4.7)$$

and

$$H_{\text{Ox}} = \mu_{\text{O}_2}^{\ominus} + RT \ln \left(\frac{p_{\text{O}_2}^{\text{out}}}{P_{\text{A}}} \right) + 4FV_{\text{ref}} + TS_{\text{Ox}} \quad (4.8)$$

According to the data presented later in this work H_{Ox} and S_{Ox} are indeed independent of T , but do depend on δ .

Most of the measurements were done as temperature cycles at open circuit conditions. As the gas inside the cell only contains a very small oxygen reservoir, δ is constant during such a temperature cycle. This has the advantages, that $\left[\frac{\partial \mu_{\text{O}_2}^{\text{MIEC}}}{\partial T} \right]_{\delta}$ can be easily evaluated, but also that only minute amounts of oxygen need to be exchanged to obtain equilibrium between the gas and the powder, resulting in fast equilibration. The lack of hysteresis (< 3 mV) between the heating and cooling curves, and the independence of the measured values on the ramp rate, confirmed that the equilibration was fast, and that the seal was intact.

4.3.2 Defect chemistry of LSMCF

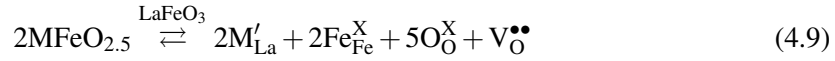
LSMCF has a perovskite structure ABO_3 , where A is a large cation and B a comparably small cation. In simple perovskites, such as LaFeO_3 , the cations on the A (La) and B (Fe) site will have a valency of 3. Table 4.1 summarizes the characteristics of the ions in the LSMCF system. Ionic radii are taken from Shannon [52] and labelled with the Kröger-Vink notation with LaFeO_3 as reference crystal, where both La and Fe have oxidation state 3 and O has oxidation state -2.

LSMCF can be considered $\text{MFeO}_{2.5}$ ($\text{M} = \text{Sr}, \text{Ba}, \text{Ca}$) and LaCoO_3 doped LaFeO_3 . The A-site cations are assumed to have a fixed valency. The incorporation of $\text{MFeO}_{2.5}$ in the lattice can, in

Table 4.1: The ionic species of LSMFC. Ionic radii are from Shannon [52].

Element	molar mass (g/mol)	Valency	site	Coordination Number	ionic radius (Å)
$\text{La}_{\text{La}}^{\text{X}}$	138.905	3	A	12	1.36
Ba'_{La}	137.327	2	A	12	1.61
Ca'_{La}	40.070	2	A	12	1.34
Sr'_{La}	87.62	2	A	12	1.44
Co'_{Fe}	58.933	2	B	6	0.745
$\text{Co}^{\text{X}}_{\text{Fe}}$	58.933	3	B	6	0.61
$\text{Co}^{\bullet}_{\text{Fe}}$	58.933	4	B	6	0.53
Co'_{Fe}	55.845	2	B	6	0.78
$\text{Fe}^{\text{X}}_{\text{Fe}}$	55.845	3	B	6	0.645
$\text{Fe}^{\bullet}_{\text{Fe}}$	55.845	4	B	6	0.585
$\text{O}^{\text{X}}_{\text{O}}$	15.999	-2	O	2	1.35

the Kröger-Vink notation, be written:



To interpret the CT data we will present different models of the defect chemistry. A common requirement is the conservation of A-site species:

$$[\text{La}^{\text{X}}_{\text{La}}] + [\text{Sr}'_{\text{La}}] + [\text{M}'_{\text{La}}] + [\text{V}^{\bullet\bullet}_{\text{La}}] = 1 \quad (4.10)$$

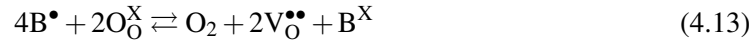
We assume that the B-site is fully occupied: $[\text{B}] = [\text{Fe}] + [\text{Co}] = 1$. For the Co species we then have:

$$[\text{Co}'_{\text{Fe}}] + [\text{Co}^{\text{X}}_{\text{Fe}}] + [\text{Co}^{\bullet}_{\text{Fe}}] = 0.2 \quad (4.11)$$

and for the Fe species:

$$[\text{Fe}'_{\text{Fe}}] + [\text{Fe}^{\text{X}}_{\text{Fe}}] + [\text{Fe}^{\bullet}_{\text{Fe}}] = 0.8 \quad (4.12)$$

We assume that no interstitial sites takes part in the reduction and oxidation of the MIEC. We also assume that the B-site ions Fe and Co are the redox active ions. In the simple model we do not distinguish between them and will use the letter B to denote a Co or Fe ion. Furthermore only the +3 and +4 redox states of the B ions will be taken into account. The overall reaction can be written as:



The associated reaction quotient is:

$$K_{\text{Ox}} = \frac{[\text{B}^{\text{X}}]^4 [\text{V}^{\bullet\bullet}_{\text{O}}]^2 p_{\text{O}_2}}{[\text{B}^{\bullet}]^4 [\text{O}^{\text{X}}_{\text{O}}]^2} \quad (4.14)$$

Charge conservation states:

$$3[\text{V}^{\bullet\bullet}_{\text{La}}] + [\text{Sr}'_{\text{La}}] = 2[\text{V}^{\bullet\bullet}_{\text{O}}] + [\text{B}^{\bullet}] \quad (4.15)$$

$[\text{V}^{\bullet\bullet}_{\text{La}}] = 0.01$ as the LSMCF materials were synthesized with a 1% A-site substoichiometry. As the concentrations on the left side of Eq. 4.15 are constant, the reaction in Eq. 4.13 will balance the charge disparity between electron holes and oxygen vacancies.

Combining Eqs. 4.14 and 4.15 and observing that $[\text{V}^{\bullet\bullet}_{\text{O}}] = \delta$, $[\text{O}^{\text{X}}_{\text{O}}] = 3 - \delta$, $[\text{B}^{\bullet}] = 3(1 - 0.99) + x - 2\delta$ and $\text{B}^{\text{X}} = 1 - [\text{B}^{\bullet}]$ we have:

$$K_{\text{Ox}} = \frac{(1 - 0.03 - x + 2\delta)^4 \delta^2 p_{\text{O}_2}}{(0.03 + x - 2\delta)^4 (3 - \delta)^2} \quad (4.16)$$

The standard Gibbs energy of the reaction in Eq. 4.13, $\Delta G_{\text{ox}}^{\ominus}$ can be written:

$$\Delta G_{\text{ox}}^{\ominus} = \Delta H_{\text{ox}}^{\ominus} - T\Delta S_{\text{ox}}^{\ominus} = -RT \ln K_{\text{Ox}} \quad (4.17)$$

where $\Delta H_{\text{ox}}^{\ominus}$ and $\Delta S_{\text{ox}}^{\ominus}$ are the standard enthalpy and entropy of the oxidation reaction, respectively.

Combining Eqs. 4.2, 4.3, 4.16 and 4.17 we have when equilibrium is established:

$$\mu_{\text{O}_2}^{\text{MIEC}} = \mu_{\text{O}_2}^{\ominus}(T, P_A) + RT \ln \left(\frac{(0.03+x-2\delta)^4(3-\delta)^2}{(1-0.03-x+2\delta)^4\delta^2} \frac{1}{P_A} \right) - \Delta H_{\text{ox}}^{\ominus} + T\Delta S_{\text{ox}}^{\ominus} \quad (4.18)$$

In terms of the partial molar entropy of oxidation we have:

$$S_{\text{Ox}} = - \left[\frac{\partial \mu_{\text{O}_2}^{\text{MIEC}}}{\partial T} \right]_{\delta} = - \frac{\partial \mu_{\text{O}_2}^{\ominus}}{\partial T} - \underbrace{R \ln \left(\frac{(0.03+x-2\delta)^4(3-\delta)^2}{(1-0.03-x+2\delta)^4\delta^2} \frac{1}{P_A} \right)}_{\text{configurational entropy}} - \Delta S_{\text{ox}}^{\ominus} \quad (4.19)$$

Mizusaki *et al.* [53] proposed the name configurational entropy, to the δ dependent term. In terms of the partial molar enthalpy of oxidation we have:

$$H_{\text{Ox}} = \mu_{\text{O}_2}^{\ominus}(T, P_A) - T \frac{\partial \mu_{\text{O}_2}^{\ominus}}{\partial T} - \Delta H_{\text{ox}}^{\ominus} \quad (4.20)$$

Model I

LSMCF has both Fe and Co on the B-site. The oxidation reaction in lanthanum ferrites and lanthanum cobaltites have very different enthalpies and entropies [19, 37]. The different values of K_{Ox} can be taken into account by introducing a redox reaction transfer reaction:



with the associated reaction quotient:

$$K_{\text{mix}} = \frac{[\text{Co}_{\text{Fe}}^{\bullet}][\text{Fe}_{\text{Fe}}^{\text{X}}]}{[\text{Co}_{\text{Fe}}^{\text{X}}][\text{Fe}_{\text{Fe}}^{\bullet}]} \quad (4.22)$$

It is simple to show that:

$$K_{\text{Ox,Co}} = \frac{K_{\text{Ox,Fe}}}{K_{\text{mix}}^4} \Rightarrow \Delta H_{\text{Ox,Co}}^{\ominus} = \Delta H_{\text{Ox,Fe}}^{\ominus} - 4\Delta H_{\text{mix}}^{\ominus}, \quad \Delta S_{\text{Ox,Co}}^{\ominus} = \Delta S_{\text{Ox,Fe}}^{\ominus} - 4\Delta S_{\text{mix}}^{\ominus} \quad (4.23)$$

where $K_{\text{Ox,Co}}$ and $K_{\text{Ox,Fe}}$ are the reaction quotients associated with the reactions found by substituting B in Eq 4.14 with Co and Fe, respectively:

$$K_{\text{Ox,Fe}} = \frac{[\text{Fe}_{\text{Fe}}^{\text{X}}]^4 [\text{V}_{\text{O}}^{\bullet\bullet}]^2 p_{\text{O}_2}}{[\text{Fe}_{\text{Fe}}^{\bullet}]^4 [\text{O}_{\text{O}}^{\text{X}}]^2}, \quad K_{\text{Ox,Co}} = \frac{[\text{Co}_{\text{Fe}}^{\text{X}}]^4 [\text{V}_{\text{O}}^{\bullet\bullet}]^2 p_{\text{O}_2}}{[\text{Co}_{\text{Fe}}^{\bullet}]^4 [\text{O}_{\text{O}}^{\text{X}}]^2} \quad (4.24)$$

Model II

According to Nakamura [54] who investigated $\text{LaCoO}_{3-\delta}$, Co'_{Fe} is also a possible ionic species in the perovskites. It can be taken into account by a electron transfer reaction:



with the reaction quotient:

$$K_{\text{Sch}} = \frac{[\text{Co}_{\text{Fe}}^{\bullet}][\text{Co}'_{\text{Fe}}]}{[\text{Co}_{\text{Fe}}^{\times}]^2} \quad (4.26)$$

Charge conservation now states:

$$3[\text{V}_{\text{La}}'''] + [\text{Sr}'_{\text{La}}] + [\text{Co}'_{\text{Fe}}] = 2[\text{V}_{\text{O}}^{\bullet\bullet}] + [\text{Fe}_{\text{Fe}}^{\bullet}] + [\text{Co}_{\text{Fe}}^{\bullet}] \quad (4.27)$$

This model has also been discussed by Poulsen and Sjøgaard [55].

4.4 Results and discussion

4.4.1 Structure

The X-ray diffractograms recorded at $T=293$ K, of polished samples, are shown in Fig. 4.2, showing single phase perovskites. The detailed view of one peak in Fig. 4.3, shows the shift of peak position associated with different lattice constants.

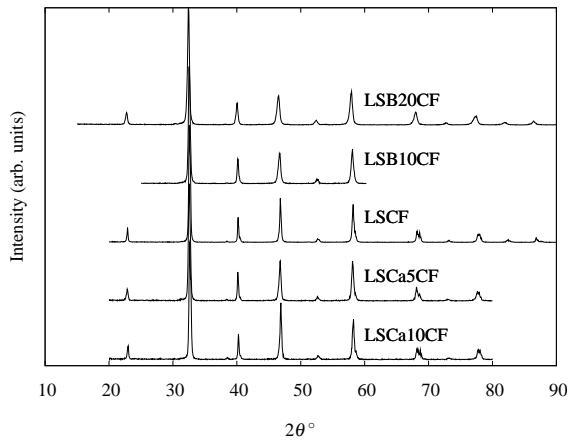


Figure 4.2: X-ray diffractograms of the materials

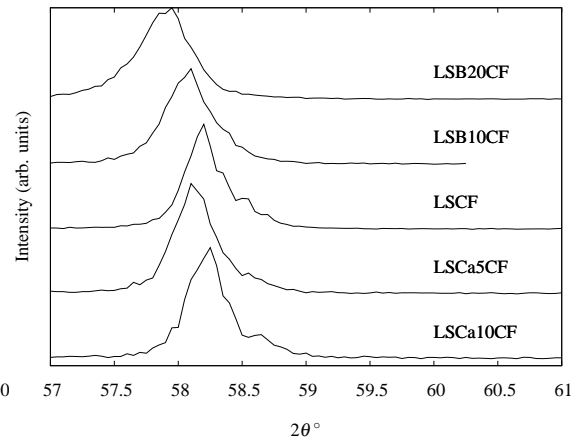


Figure 4.3: X-ray diffractograms of the materials

In Table 4.2 the calculated room temperature characteristics of the powders measured by XRD are tabulated. V_{F} is the volume per formula unit.

There is a clear relation between dopant amount and V_{F} , with the Ba doped materials having the largest V_{F} and the Ca doped materials having the smallest V_{F} as expected. It is however unexpected that V_{F} of LSCF is smaller than V_{F} of LSCa5CF. One explanation could be that the membranes are not completely equilibrated when cooled down. As is shown later in this paper, the value of δ for LSCa5CF is larger than the value of δ for LSCF at high temperature. This difference could be "frozen in" during the cooling phase after membrane sintering, and account for this irregularity in the XRD.

4.4.2 Thermogravimetry (TG)

Total reduction

Table 4.2: Crystal structure at $T = 294 \text{ K}$.

name	Dopant	x	structure	V_F 10^{-30} m^3	a Å	c Å	ρ_{XRD} kg/m^2
LSCF	-	-	Hex.	58.3	5.50	13.38	6310
LSB10CF	Ba	0.1	Cub.	58.9	3.89	3.89	6376
LSB20CF	Ba	0.2	Cub	59.4	3.90	3.90	6481
LSCa5CF	Ca	0.05	Hex	58.7	5.59	13.47	6203
LSCa10CF	Ca	0.1	Hex	58.05	5.49	13.32	6205

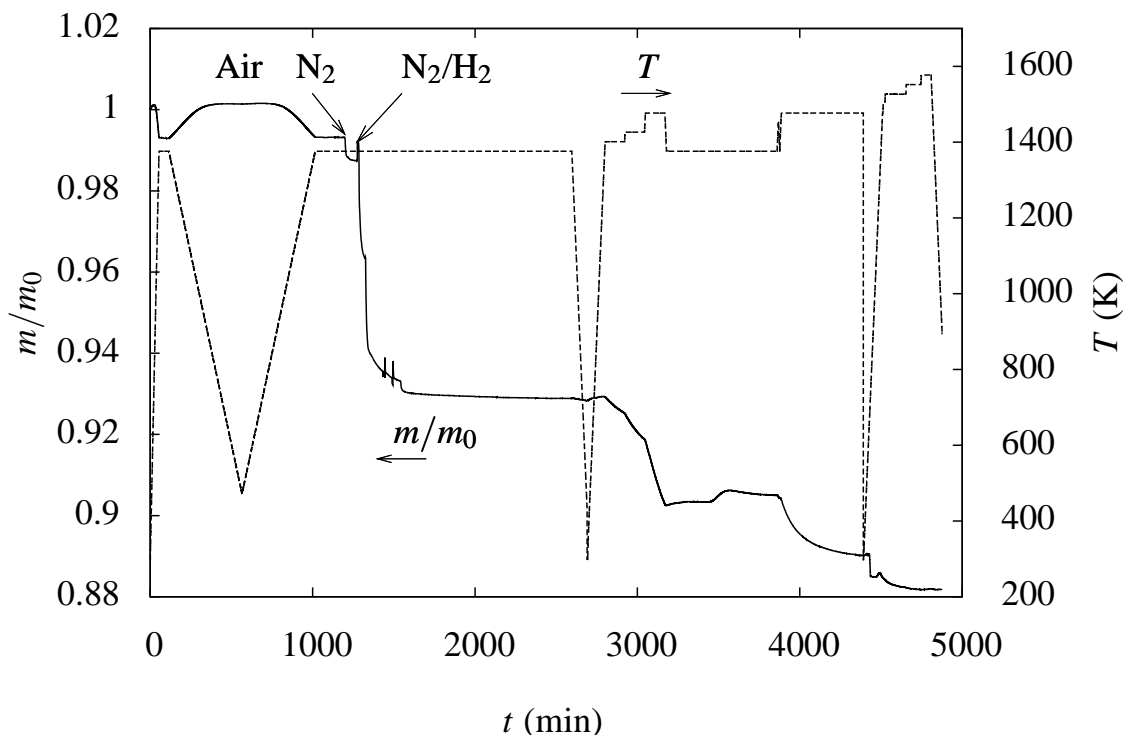


Figure 4.4: T and the normalized mass signal m/m_0 of a TG measurement of LSCF, with a total reduction attempt.

The TG measurements in air and CT measurements only give information about relative differences in δ . TG measurements, in which the powder is reduced in an N_2/H_2 mixture, were performed in order to determine the absolute value of δ . In N_2/H_2 the thermodynamically stable phases are La_2O_3 , SrO , BaO , CaO , Co and Fe . As the oxygen content of these phases are well defined, the oxygen content of the perovskite can be calculated from the mass loss if complete reduction of the powder to equilibrium is achieved.

Figure 4.4 shows the normalized sample mass m/m_0 , m_0 being the initial mass, and T as a functions of time, t , for an exploratory reduction attempt on LSCF. The first heating and cooling sequence until time, $t = 1000 \text{ min}$ is done to equilibrate the powder and remove any moisture and organic residue from the system. This sequence is equivalent to the measurements shown in Fig. 4.5.

At $t = 1192 \text{ min}$ the TG gas is changed to N_2 ($p_{\text{O}_2} \approx 1 \cdot 10^{-5} \text{ atm}$). At $t = 1266 \text{ min}$ the gas is changed to an N_2/H_2 mixture with $p_{\text{O}_2} = 10^{-19} \text{ atm}$ at 1273 K , corresponding to a $p_{\text{H}_2\text{O}} \simeq 4 \cdot 10^{-4} \text{ atm}$. This gas will approximately have $p_{\text{O}_2} = 3 \cdot 10^{-18} \text{ atm}$ at $T = 1373 \text{ K}$ and $p_{\text{O}_2} = 2 \cdot 10^{-16} \text{ atm}$ at $T = 1573 \text{ K}$. In this atmosphere the sample was annealed at 1373 K until $t = 2580 \text{ min}$. After a cooling cycle to room temperature, the sample was taken to 1473 K , where it lost

further mass. The instability during $3150 \text{ min} < t < 3880 \text{ min}$ is attributed to pressure loss in the gas supply. Further heating to 1548 K resulted in rapid equilibration, with no further mass loss when heated to 1573 K. A surprisingly high temperature is required for complete reduction of the perovskite phase. This could be an effect of limitations in the oxygen permeability of the reduced species, that form scales around core phases which are not completely reduced.

Reduction at T up to 1573 K was repeated for all the LSMCF materials. The obtained mass loss corresponds to a room temperature δ_0 of 0 ± 0.02 for all the materials. The precision was estimated from three runs on LSB10CF resulting in calculated values of $\delta = 0.003$, $\delta = 0.022$ and $\delta = -0.01$ at room temperature. The low precision reflects that a change of m/m_0 of 0.01 corresponds to a δ change of 0.14. Given the uncertainty on the value of δ at room temperature, we will, in the following, assume that the room temperature δ 's of all the powders can be represented by the stoichiometric value of 0.

Measurements in air

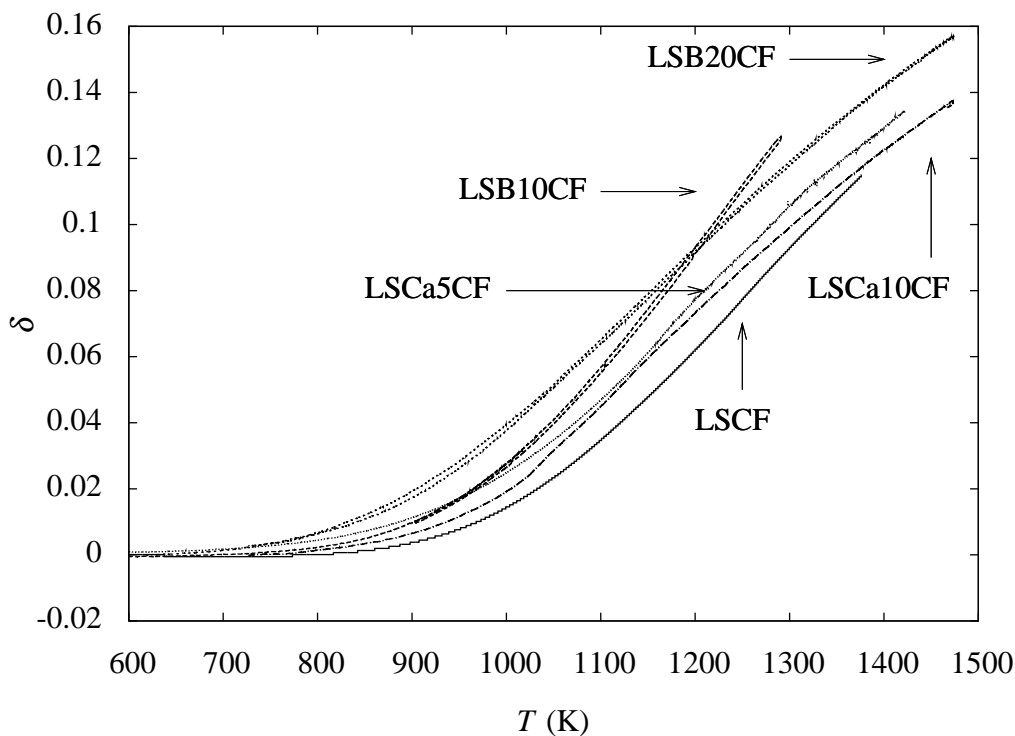


Figure 4.5: δ versus T measured in air using TG.

In Fig. 4.5 δ versus T is shown for the temperature cycles in air. LSCF has the lowest mass loss, while the Ba doped samples have the highest mass loss, in agreement with the findings of Yin and Lin [56]. LSB20CF furthermore starts to lose oxygen at a lower T than the other compositions

4.4.3 CT

To illustrate the data treatment we will present and discuss the partial results for one material, LSB10CF, in detail. The high degree of linearity between δ , T and $\mu_{\text{O}_2}^{\text{MIEC}}$ of LSB10CF is shared by the other LSMCF materials.

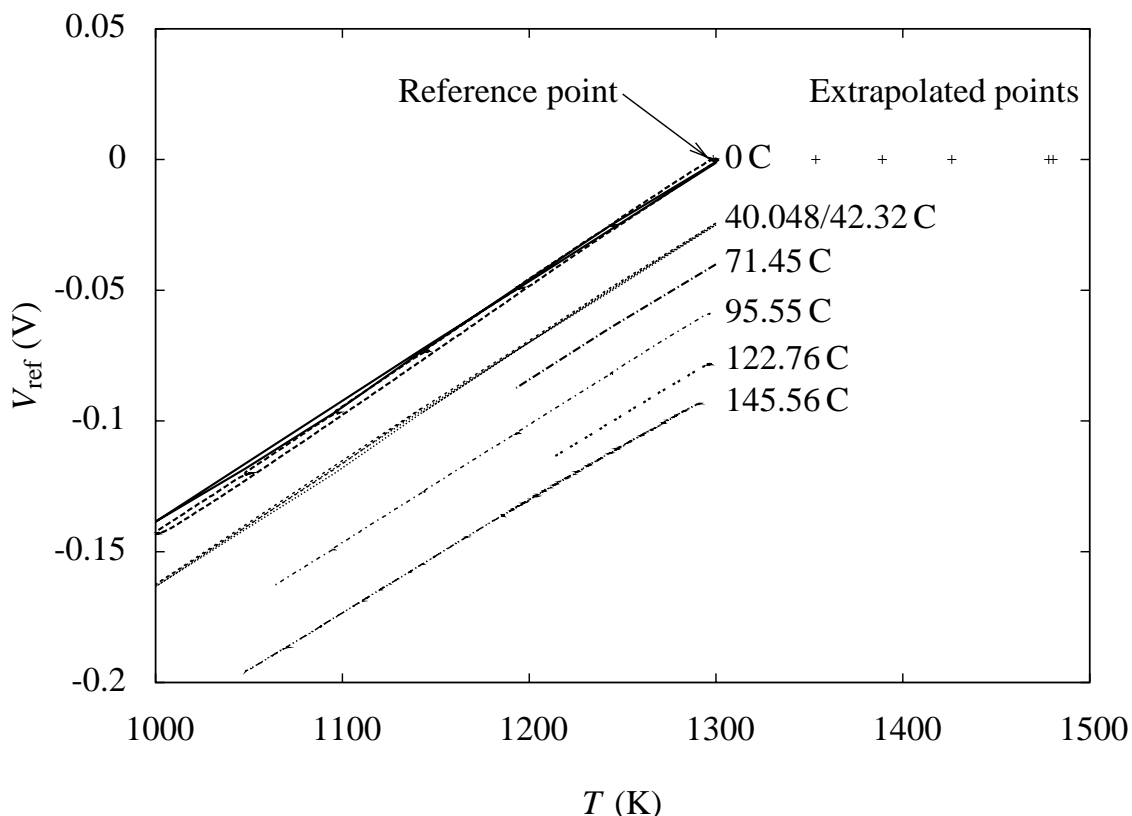


Figure 4.6: V_{ref} as a function of the temperature, when different amounts of charge have been pumped from the compartment. Sample LSB10CF. Q values of 0 C, 40 C, 71 C, 96 C, 123 C and 146 C corresponds to $\Delta\delta$ values of 0, 0.018, 0.031, 0.042, 0.054 and 0.065.

A reference stoichiometry, δ_0 was selected for δ at $T = 1300$ K and $\mu'_{\text{O}_2} - \mu''_{\text{O}_2} = 0$ (i.e. $p_{\text{O}_2}^{\text{in}} = 0.21$ atm). To change δ by $\Delta\delta$, charge was pumped out of the cell in accordance with Eq. 4.5.

In Figure 4.6 the reference voltage as a function of the temperature, when different amounts of charge have been pumped from the compartment, is shown for LSB10CF. Each value of the charge can be converted to a δ difference, $\Delta\delta = Q/(2Fn)$, between the reference value, $\delta(T = 1300 \text{ K}, p_{\text{O}_2} = 0.209)$ and the δ value of the powder after the pumping.

The very low hysteresis between cooling and heating runs, caused by the low drift of the signal and the high precision with which ionic currents can be integrated, is a demonstration of the suitability of CT for stoichiometry determination. The relationship between $\log p_{\text{O}_2}$ (proportional to the voltage) and the temperature is perfectly linear, indicating that H_{ox} and S_{ox} are independent of temperature. This allows us to extrapolate the lines toward $V_{\text{ref}} = 0$, and estimate values for the charge needed to be pumped in order to obtain equilibrium between the powder and a gas of $p_{\text{O}_2} = 0.209$ atm at $T > 1300$ K, providing a basis for comparison with the TG values in air.

We are able to extract H_{ox} and S_{ox} for each line in Fig. 4.6 using Eqs. 4.7 and 4.8.

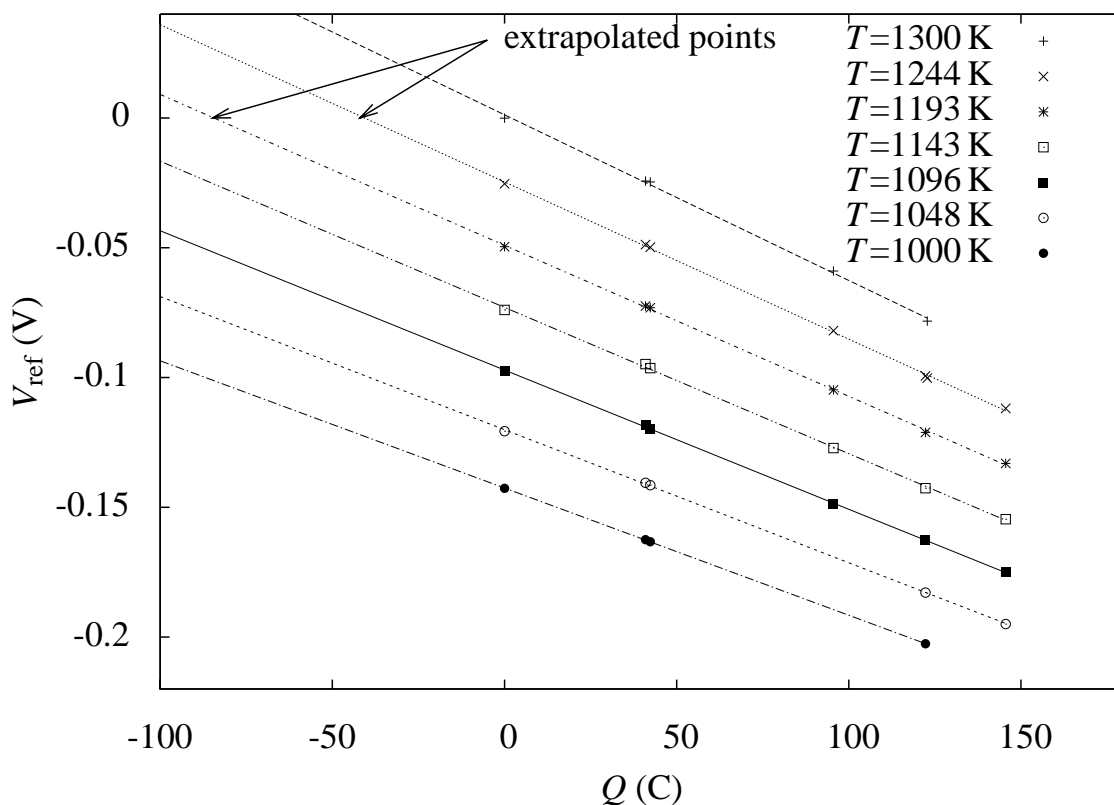


Figure 4.7: The reference voltage as a function of the charge removed from the compartment, at different temperatures. The extrapolations are marked with arrows. Sample LSB10CF.

The reference voltage as a function of the charge pumped from the compartment is shown in Figure 4.7 for sample LSB10CF at different temperatures. The relationship between $\log p_{\text{O}_2}$ (proportional to the voltage) and the charge is linear. This allows us to extrapolate the lines toward $V_{\text{ref}}=0$, and get values for the charge needed to be pumped in order to obtain equilibrium between the powder and a gas of $p_{\text{O}_2} = 0.209$ at $T < 1300\text{K}$, providing a basis for comparison with the TG values in air.

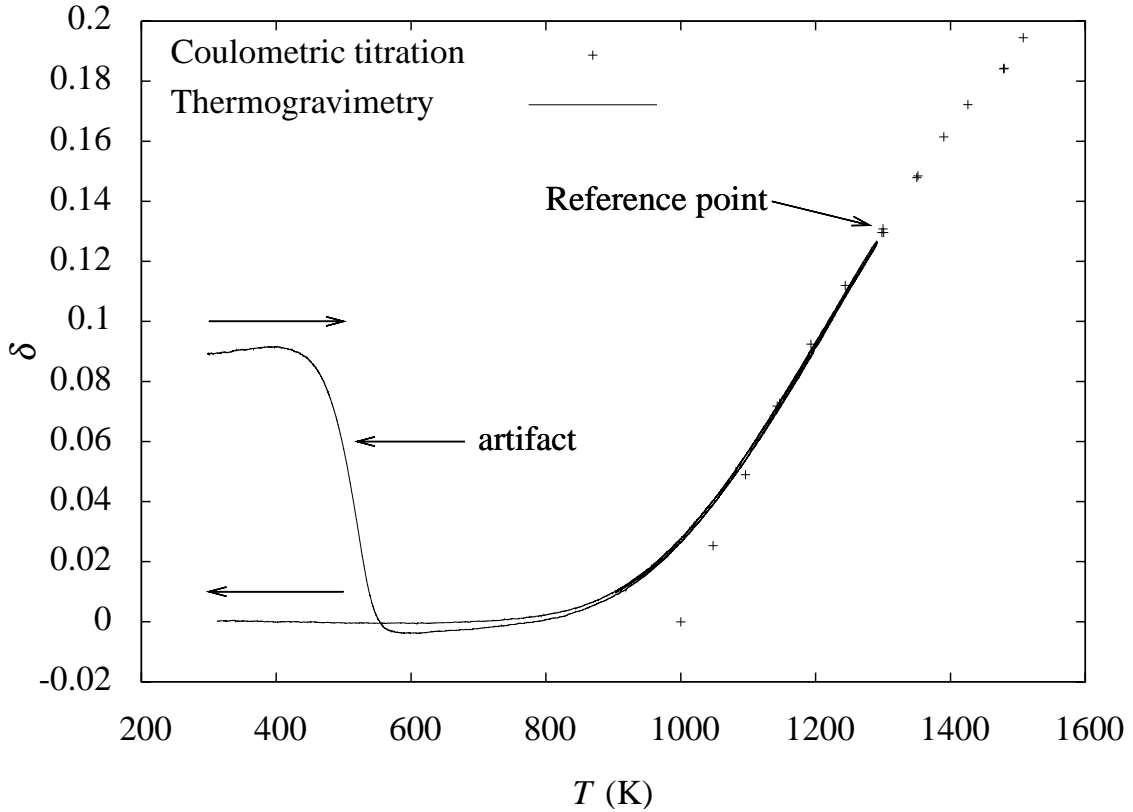


Figure 4.8: Comparison of the values of δ obtained in air using TG and those extrapolated from CT experiments of sample LSB10CF. The plateau at the start of the TG measurement is an artifact possibly due to moist alumina powder in the reference cup.

When performing the CT experiment, the glass seals was observed to be gas permeable until the cup had been annealed for some time at high temperature. This allows the powder to equilibrate with the outside atmosphere, until this sealing is complete. The absolute value of δ at the reference T , δ_0 , can thus not be determined from CT and will, as mentioned, be taken from the TG measurement. Figure 4.8 shows δ as a function of temperature in air obtained using TG measurements (line). The plateau at the initial warm-up phase of the TG measurement is an artifact possibly due to moist alumina powder in the reference cup; the cooldown value at $T = 273$ K is used, which is considered the true $T = 273$ K value of δ . The absolute values of δ from the CT measurement can be calculated from the relative values, $\Delta\delta$, as the absolute value at the chosen reference point ($T = 1300$ K in air), δ_{ref} is known from the TG measurement:

$$\delta = \delta_{\text{ref}} + \Delta\delta = \delta_{\text{ref}} + Q/(2Fn) \quad (4.28)$$

The values of the CT extrapolations from Figures 4.6 and 4.7 are compared to the TG data in Figure 4.8. There is a good agreement on the slope of both datasets around 1300 K. The extrapolated values of the CT data agree with the TG data in the range 1100 K - 1300 K. If the extrapolations are made over large spans in T (i.e. the extrapolated point is far from 1300 K), the accuracy will decline.

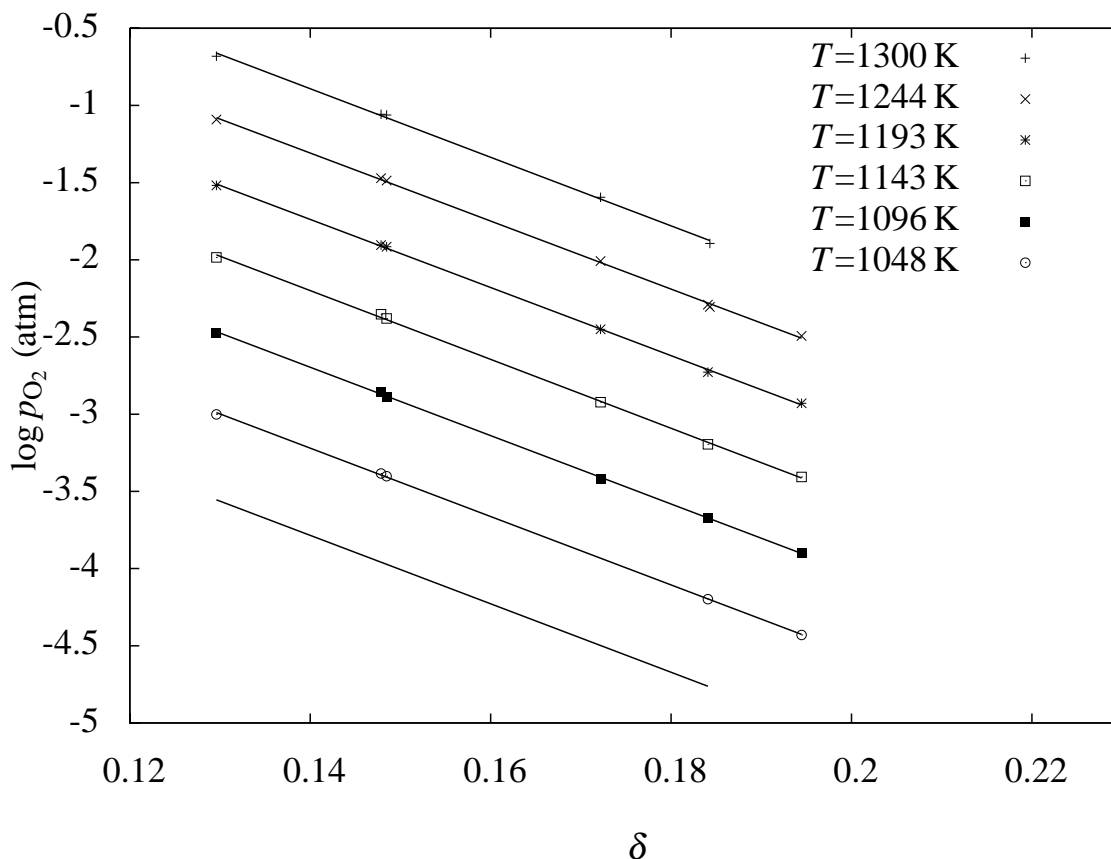


Figure 4.9: $\log p_{\text{O}_2}$ as a function of δ for different temperatures for LSB10CF. Linear fits to the data are shown.

The equilibrium p_{O_2} is shown as a function of δ for different temperatures in Fig 4.9.

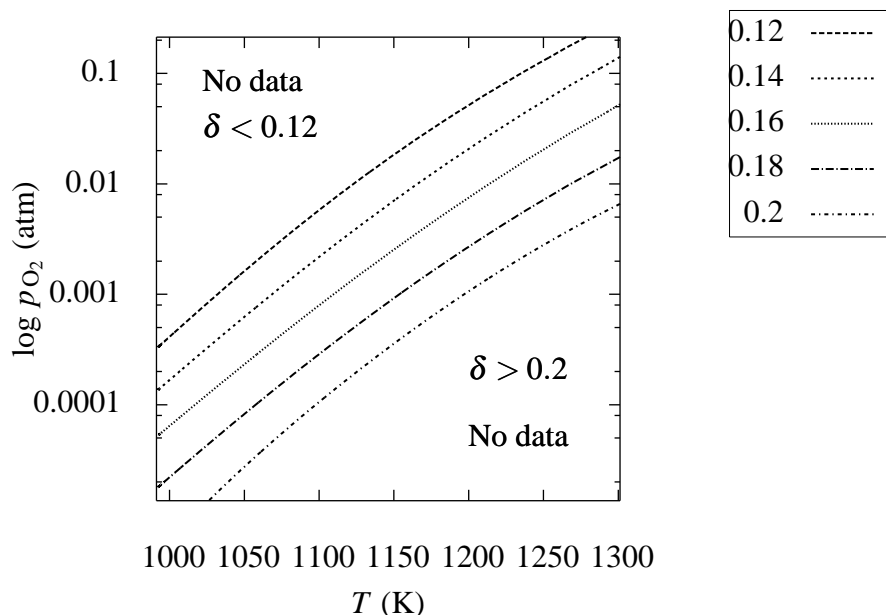


Figure 4.10: Contour plot of δ as a function of $\log p_{\text{O}_2}$ and T for LSB10CF.

The CT measurements are necessarily done in a regime where fast equilibration is possible. The contours of this regime δ as a function of $\log p_{\text{O}_2}$ and T are shown for LSB10CF in Fig. 4.10,

illustrating the area of reliable data. To get data at lower temperatures and high p_{O_2} the reference T could be set at a lower value. A reduction of T will, however, slow the pumping process considerably as the equilibration of the powder and the gas inside the cell is controlled by surface exchange processes in the powder [16, 44] which are thermally activated. The equilibration will also slow down significantly at low p_{O_2} [16, 44], so even at high T , pumping to very low p_{O_2} is time consuming.

4.4.4 p_{O_2} dependence of δ for all materials.

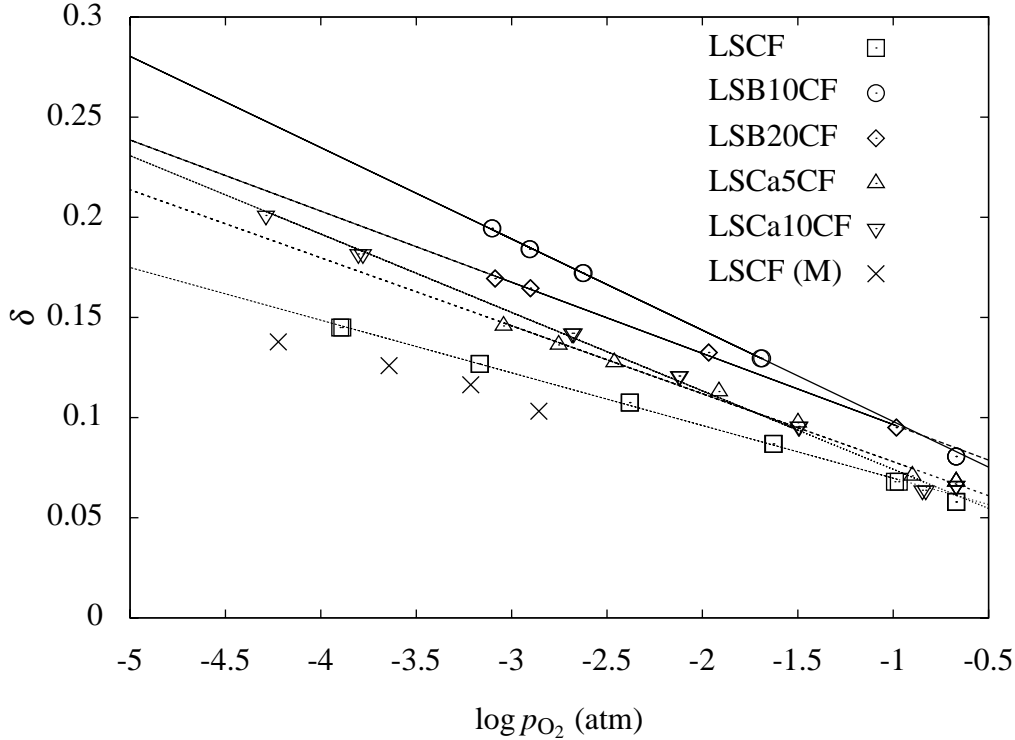


Figure 4.11: Comparison of the p_{O_2} dependence of δ for different materials. $T = 1173 \text{ K}$. $\text{LSCF}(\text{M})$ are values for LSCF obtained by Mantzavinos [57]

A comparison of the p_{O_2} dependence of δ at $T = 1173 \text{ K}$ for different materials is shown in Fig. 4.11. To confirm the results we have compared them to those of LSCF obtained by Mantzavinos [57] in a similar experiment. Good agreement is found.

When the A-site contains Ba, the vacancy concentration is comparably high. When the A-site contains Ca, the vacancy concentration is low, but still higher than LSCF , which is the most redox stable of the compounds. It is furthermore remarkable that, according to Sogaard *et al.* who measured the stoichiometry of $(\text{La}_{0.6}\text{Sr}_{0.4})_{0.99}\text{CoO}_{3-\delta}$ [19] and $(\text{La}_{0.6}\text{Sr}_{0.4})_{0.99}\text{FeO}_{3-\delta}$ [37], the difference between LSCF and LSB10CF is, in this p_{O_2} and temperature range, the same as the difference between $(\text{La}_{0.6}\text{Sr}_{0.4})_{0.99}\text{CoO}_{3-\delta}$ and $(\text{La}_{0.6}\text{Sr}_{0.4})_{0.99}\text{FeO}_{3-\delta}$. A change of 10 % of the A-site cations from the small Sr^{2+} ion to the large Ba^{2+} ion is equivalent to a change of all the B site cations from the reasonably stable Fe to the more reactive Co. The structure thus seems to have an important influence on the defect chemistry.

4.4.5 Low p_{O_2} measurement

A well-sealed cell is capable of reaching very low p_{O_2} through long pumping runs. At $p_{\text{O}_2} < 10^{-4} \text{ atm}$ in an oxygen/nitrogen mixture, the surface exchange for these materials becomes too slow to pump and measure $\mu_{\text{O}_2}^{\text{MIEC}}$ at the same time [44], and only discrete measurement points

after equilibration can be recorded.

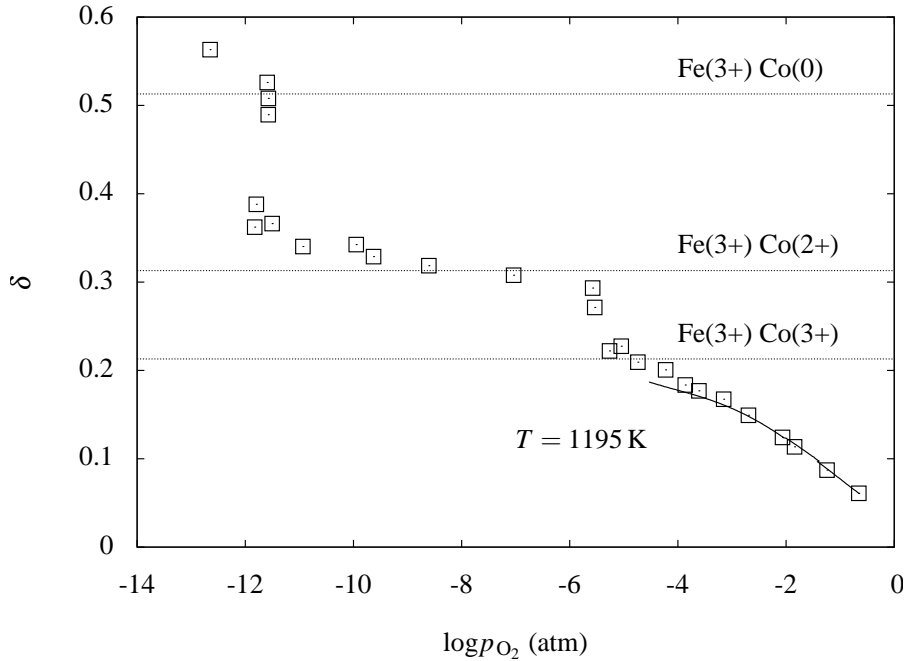


Figure 4.12: δ as a function of p_{O_2} for LSCa10CF. At high p_{O_2} a continuous curve can be recorded while pumping, while measurements at low p_{O_2} require equilibration of the powder and gas inside the cell resulting in point values.

δ is plotted as a function of p_{O_2} for LSCa10CF in Fig. 4.12. The curve is measured while pumping continuously, while the discrete point values are taken after powder equilibration. The points are taken during several pump cycles, and we observe that the behavior is reversible and reproducible.

According to the results of Søgaaard *et al.* [19, 37] at $p_{\text{O}_2} > 10^{-6}$ atm the B-site cations of $(\text{La}_{0.6}\text{Sr}_{0.4})_{0.99}\text{CoO}_{3-\delta}$ and $(\text{La}_{0.6}\text{Sr}_{0.4})_{0.99}\text{FeO}_{3-\delta}$ can have both 4+ and 3+ and, in the case of Co, also 2+, in valency simultaneously. This gives a smooth δ dependence on μ_{O_2} as no phase transitions are involved. As these materials are similar to LSMCF we attribute the curve at $p_{\text{O}_2} > 10^{-6}$ atm to the redox reactions between Co'_{Fe} , Co^{X} and $\text{Co}^{\bullet}_{\text{Fe}}$; and between Fe^{X} and $\text{Fe}^{\bullet}_{\text{Fe}}$.

As the pumping charge directly controls δ it is possible to get equilibrated measurement points at phase transitions. This is much more difficult in other methods, such as TG, where the p_{O_2} of the gas rather than δ is the controlling parameter.

When $0.21 < \delta < 0.3$ at $\log p_{\text{O}_2} = 10^{-6}$ atm, such a phase transition seems to happen, as only a slight change in the chemical potential of oxygen inside the cell was measured, even when δ was changed substantially. If all the Fe and Co cations are in the +3 valence state, $\delta = 0.213$ (if the ratio of A site and B site cations was 1:1, $\delta = 0.2$, however, the ratio of the A and B site cation is 0.99:1 and therefore $\delta = 0.213$). Having all the Fe in the +3 state and all the Co in the +2 state corresponds to $\delta = 0.313$. We thus attribute the step in δ from $\approx 0.21 \rightarrow \approx 0.31$ to the reduction of Co^{X} , and decomposition of the perovskite into several phases, probably CoO , $(\text{La}, \text{Sr}, \text{Ca})_2\text{CoO}_4$ and $(\text{La}, \text{Sr}, \text{Ca})\text{FeO}_3$. Nakamura *et al.* [54] found a similar behavior for LaCoO_3 .

After the perovskite partially decomposes, the meaning of the measured δ changes; instead of referring to the oxygen stoichiometry of a single well known perovskite in the cup, it now refers to the total difference in oxygen content between all the powders in the cup and the stoichiometric reference perovskite originally present in the cup.

At $0.31 < \delta < 0.32$ there is a large change in $\mu_{\text{O}_2}^{\text{MIEC}}$ with little change in δ . We attribute this

to the reluctance of both Co^{2+} [54] and Fe^{3+} [37] to be reduced any further in this p_{O_2} interval.

If all the Fe is Fe^{3+} and all the Co is metallic cobalt (Co^0), δ will be 0.513. At $p_{\text{O}_2} \approx 10^{-12}$ atm a new step between $0.32 < \delta < 0.52$ is thus interpreted as the complete reduction of Co^{2+} to metallic Co(s). This is consistent with the measurements of Nakamura *et al.* [54] on LaCoO_3 .

4.4.6 H_{ox} and S_{ox}

H_{ox} was extracted from the coulometric titration data. The extracted values are shown as a function of δ in Fig. 4.13.

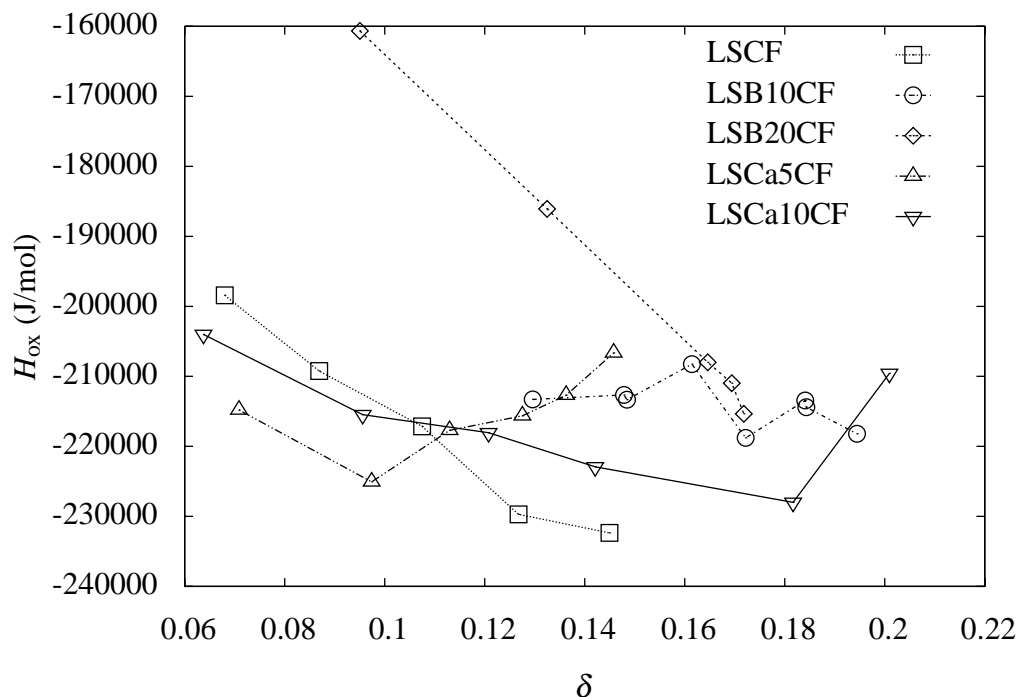


Figure 4.13: H_{ox} as a function of δ . The connecting lines are guides to the eye.

With the exception of LSB20CF and LSCF, the variation of H_{ox} as a function of δ is weak, suggesting a single B-site cation reaction being responsible for the reaction. In the case of LSB20CF and LSCF, the variation suggests that several reactions are simultaneously responsible.

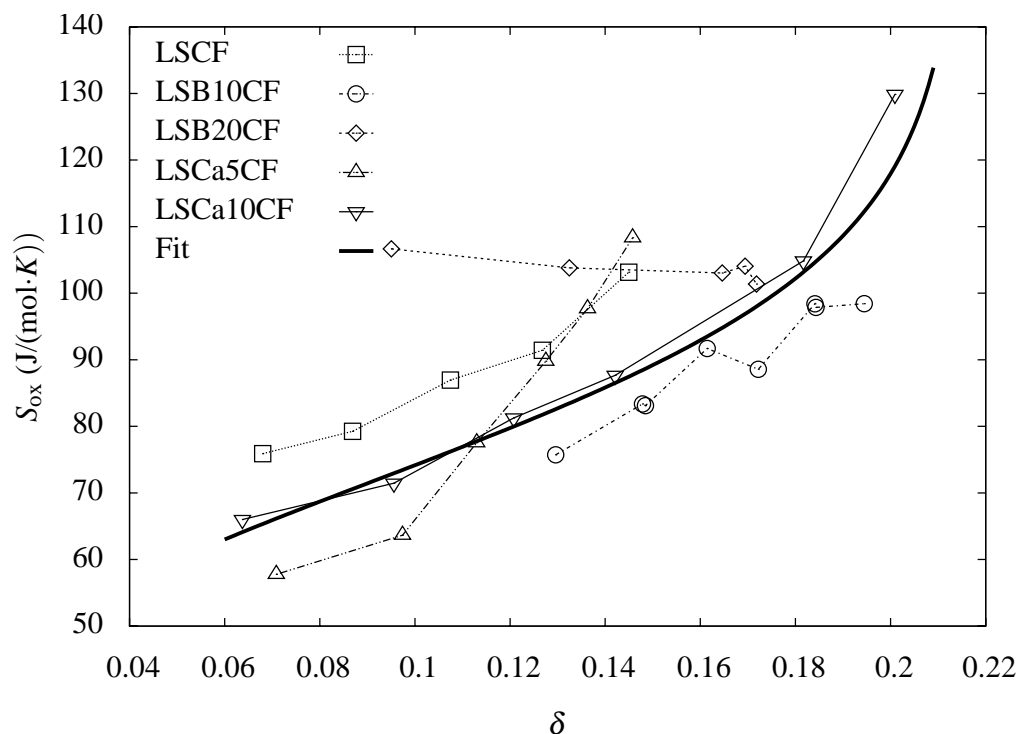


Figure 4.14: S_{ox} as a function of δ for the different materials. A fit to Eq. 4.19 for LSCa10CF has been added. The connecting lines are guides to the eye.

S_{ox} was extracted from the coulometric titration data. The extracted values are shown as a function of δ in Fig. 4.14. A trendline based on Eq. 4.19 can be vertically adjusted to fit the measurement series, with the exception of LSB20CF, that has a S_{ox} independent of δ . The δ dependence of H_{ox} of LSB20CF is also much more pronounced than for the other materials. Apparently, the reduction mechanism is fundamentally different for LSB20CF.

4.4.7 Model fits

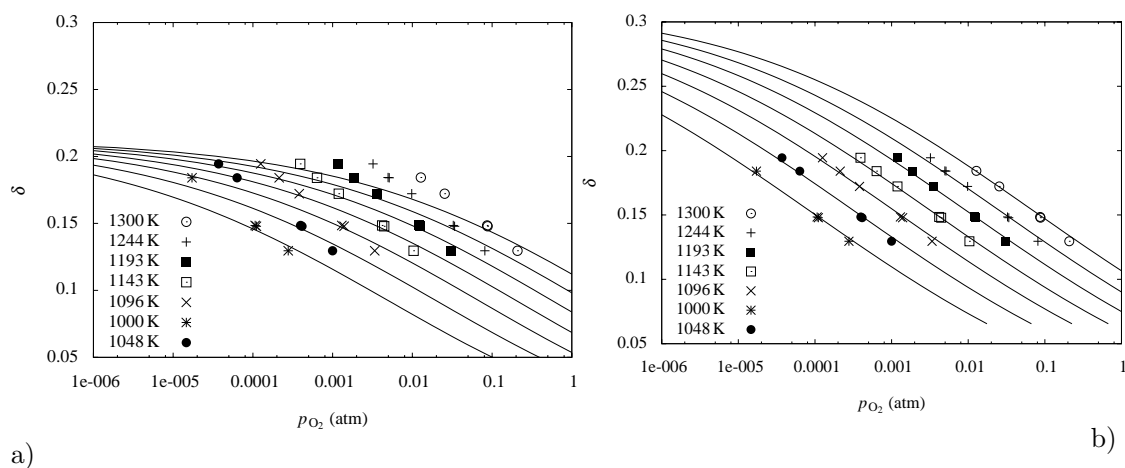


Figure 4.15: a) Fit of LSB10CF to Model I. b) Fit of LSB10CF to Model II

The oxygen nonstoichiometry data for all the materials was fitted to the models described in

Section 4.3.2. An example for LSB10CF, with Model I and Model II is shown in Fig. 4.15a) and Fig. 4.15b), respectively. Model I is not able to reproduce the data at $\delta > 0.15$, as it does not take the reduction into the +2 valence state of the B ions into account. Model I is thus only able to fully reproduce the measurements of LSCF and LSCa5CF, for which $\delta < 0.15$ under all the conditions of measurement. Model II is able to replicate the data precisely for all the materials.

4.4.8 Parameter extraction

The fitting parameters providing the best fit to the measurements, and their confidence intervals, shown below each fitting value, are compared to the measured values of H_{ox} and S_{ox} in Table 4.3 for Model I.

Table 4.3: Fitting parameters of best fit for three of the compositions. Below is shown the parameter value intervals of points resulting in a χ^2 value less than 2.

	Measured			Model I	
	H_{ox} kJ/mol	S_{ox} J/(mol K)	$\ln K_{\text{ox}}$ -	$\ln K_{\text{ox,Co}}$ -	$\ln K_{\text{ox,Fe}}$ -
LSB20CF	-178 -215 ↔ -159	105 102 ↔ 108	-4.4 -	3 -5 ↔ 4	-15 -22 ↔ -12
LSB10CF	-210 -218 ↔ -209	80 78 ↔ 100	-4.5 -	22 0 ↔ 24	-9 -35 ↔ -9
LSCF	-226 -232 ↔ -198	90 76 ↔ 103	-7.5 -	47 20 ↔ 48	24 -20 ↔ 25
LSCa5CF	-216 -225 ↔ -207	84 58 ↔ 108	-5.8 -	66 20 ↔ 96	13 -23 ↔ 19
LSCa10CF	-218 -228 ↔ -204	82 65 ↔ 130	-5.8 -	41 0 ↔ 58	4 -62 ↔ 13

The measured parameters, tabulated in Table 4.3 are the values for $\delta = 0.12$ (See Fig. 4.13 and Fig. 4.14), while the interval tabulated below each value is the spread of these values in the measurements of this study. $\ln K_{\text{ox}}$ is calculated at $T = 1173$ K for $\delta = 0.12$.

Model I was used on all the materials, but only for measurement points with $\delta < 0.15$, as it could not model the data satisfactorily for higher δ values. This, unfortunately, means that the measurements on LSB10CF and LSB20CF are only fitted in a few points, and the precision of the fits of those materials suffers accordingly. On the other hand, one set of $H_{\text{ox,Co}}$, $S_{\text{ox,Co}}$, $H_{\text{ox,Fe}}$, $S_{\text{ox,Fe}}$ values could be used to fit all δ values below 0.15. From this set $K_{\text{ox,Co}}$ and $K_{\text{ox,Fe}}$ was calculated for $T = 1123$ K. The interval tabulated below each value represents the 68% confidence interval based on those fits.

According to Eq. 4.23, K_{ox} should be a convolution of the Co- and Fe-specific reaction constants of Model I, $K_{\text{ox,Co}}$ and $K_{\text{ox,Fe}}$. The fitted values for LSCF, LSCa5CF and LSCa10CF agree with this inside their wide confidence intervals. These measurements can, however, not easily distinguish between a change of valence state of Co or Fe; this is reflected in the wide confidence intervals, where a too large value for Fe is compensated by a too low value for Co. We can thus not, from these fits, extract much knowledge of the balance between oxidation of Co and Fe.

Model II, which has six fitting parameters, has even wider confidence intervals than Model I. It is, however, capable of very high quality fits of the data for all δ values.

Lankhorst and ten Elshof made measurements on LSCF with different ratios of Co to Fe on the B-site. This enabled them to estimate fitting parameters dependent of the Co/Fe ratio, and reduce the number of fitting parameters while maintaining high precision in the replication of their measured data. The model of Lankhorst and ten Elshof could replicate our results,

however, the value of the parameters fixed by Lankhorst and ten Elshof were not valid for our measurements. They needed to be fitted independently, and the resulting confidence intervals were as large as those of Model II.

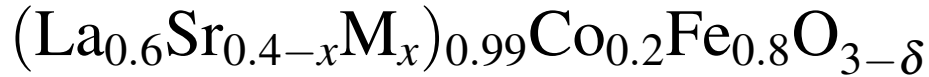
In conclusion it was not possible to model the results with a few well determined fitting parameters applicable to all values of δ . Increasing the model complexity, and the number of fitting parameters, gave excellent reproduction of the measured data, but increased the confidence intervals.

4.5 Conclusions

In this study, the system, $(\text{La}_{0.6}\text{Sr}_{0.4-x}\text{M}_x)_{0.99}\text{Co}_{0.2}\text{Fe}_{0.8}\text{O}_{3-\delta}$, $M = \text{Ca}, \text{Ba}, \text{Sr}$, was investigated using thermogravimetry (TG) and coulometric titration (CT). TG reduction in a N_2/H_2 gas mixture at $T > 1498 \text{ K}$ revealed the absolute oxygen substoichiometry, δ , which was found to be close to 0 at $T = 293 \text{ K}$ for all the materials. TG and CT allowed the relation between δ and the oxygen activity at $T > 873 \text{ K}$ to be measured with high precision. The results of TG and CT were in good agreement. Enthalpies and entropies of oxidation could be extracted for each material. No systematic relation between the sample composition and the thermodynamic properties could be found. Due to the high number of ionic species in these materials, it was impossible to extract detailed knowledge of the redox reactions in the material, from the applied defect chemistry models.

Chapter 5

Oxygen Transport in



M = Ca ($x = 0.05, 0.1$), **Ba** ($x = 0.1, 0.2$),
Sr.

Abstract

This Chapter is the second part of a two part series, where the effects of varying the A-site dopant on the defect chemistry and transport properties of the materials $(\text{La}_{0.6}\text{Sr}_{0.4-x}\text{M}_x)_{0.99}\text{Co}_{0.2}\text{Fe}_{0.8}\text{O}_{3-\delta}$, $M = \text{Sr}, \text{Ca}$ ($x = 0.05, 0.1$), Ba ($x = 0.1, 0.2$) (LSMFC) have been investigated. In part I (Chapter 4), the findings on the defect chemistry were reported, while the oxygen transport properties are reported here in part II. In the investigated material series, the amount of bivalent dopant has been kept constant, while Sr ions have been substituted with Ca ions (smaller ionic radius) or Ba ions (larger ionic radius). The size difference induces different strains into the crystal structure in each composition. The possibility of simple relationships between various crystal strain parameters and the transport properties were analyzed. Oxygen pump controlled permeation experiments and a surface sensitive electrolyte probe were used to extract the permeability and surface resistance, r_s . The highest permeability was found for $(\text{La}_{0.6}\text{Sr}_{0.3}\text{Ca}_{0.1})_{0.99}\text{Co}_{0.2}\text{Fe}_{0.8}\text{O}_{3-\delta}$. The apparent activation energy of the permeability was 78 kJ/mol. The inverse surface resistance, r_s^{-1} , also had an activated behavior with an activation energy close to 180 kJ/mol for most of the materials. A reversible transition to an abnormally low r_s was found in $(\text{La}_{0.6}\text{Sr}_{0.3}\text{Ca}_{0.1})_{0.99}\text{Co}_{0.2}\text{Fe}_{0.8}\text{O}_{3-\delta}$ at $T > 1223$ K.

5.1 Introduction

The materials in the system $(\text{La}_{0.6}\text{Sr}_{0.4-x}\text{M}_x)_{0.99}\text{Co}_{0.2}\text{Fe}_{0.8}\text{O}_{3-\delta}$, $M = \text{Sr}, \text{Ca}$ ($x = 0.05, 0.1$), Ba ($x = 0.1, 0.2$) (LSMFC) are mixed oxide ion and electronic conductors (MIECs). MIECs are being investigated as cathode materials for solid oxide fuel cells [4–6]. Other uses of MIECs exist in the field of controlled oxidation, oxygen production, or reactors for partial oxidation of methane to synthesis gas [7, 8]. Current research focuses on identifying materials combining good mechanical, catalytic and oxygen permeation properties [44]. Detailed knowledge of

the structure, defect chemistry and transport properties of these materials can improve the understanding of membrane materials, and facilitate identification of materials with high thermal stability and oxygen permeability.

The LSMCF materials are derivatives of the perovskite $(\text{La}_{0.6}\text{Sr}_{0.4})_{0.99}\text{Co}_{0.2}\text{Fe}_{0.8}\text{O}_{3-\delta}$ (LSCF) which has been thoroughly characterized in a large number of studies [16, 22, 23, 38, 43, 44, 58], which provide a comprehensive reference for our measurements.

The mechanism of bulk oxygen permeation in these types of materials is the hopping of oxide ions between vacant oxide ion sites in the crystal lattice. Straining the crystal structure changes the energy required for a successful jump. Cook and Sammells [47] proposed that the mobility of oxide ions is dependent on: 1) the bond energy of the oxide ions. 2) the lattice free volume and 3) the critical radius of the saddle point halfway on the path of an oxide ion jump. Mogensen *et al.* [49, 50] found a correlation between the ionic conductivity and the crystal strain in LaBO_3 , B=Mg, Al, Ga, Sc, In. It was quantified by 4) the Goldschmidt factor: $t_{\text{Goldschmidt}} = \frac{r_A+r_O}{\sqrt{2}(r_B+r_O)}$ 5) the difference in A-site ion radius and oxygen ion radius, and, 6) the difference in B-site ion radius and an optimum radius determined by the A and O atoms. All these factors are functions of the crystal structures. Factors 4-6 can be considered as measures of the stress in the crystal lattice, leading Mogensen *et al.* to the conclusion that a stress free lattice is a key parameter determining the oxide ion conductivity in the considered perovskites.

LSCF has a high ionic conductivity, and it is very close to the expected optimum values of the factors 4), 5), and 6). The LSMCF materials were selected in order to vary the A-site ion radius around these optimum values, and thus determine if some of the factors 1)-6) are could account for the bulk diffusion processes. Furthermore, the studied LSMCF materials all have the same average A-site valences of the cations. The LSMCF materials are thus not as chemically different from each other as, for instance, the series $\text{La}_{1-x}\text{Sr}_x\text{Co}_{0.2}\text{Fe}_{0.8}\text{O}_{3-\delta}$, (x = 0.0, 0.2, 0.4) investigated by Tai *et al.* [38, 45], or the series $\text{La}_{0.6}\text{Sr}_{0.4}\text{Co}_{1-y}\text{Fe}_y\text{O}_{3-\delta}$ (y = 0, 0.1, 0.25, 0.4, 0.6) investigated by Lankhorst and ten Elshof [46], where the valence of the A and B site cations are systematically changed. Instead the crystal structure is strained by substitution of Sr ions with Ca ions (smaller ionic radius) and Ba ions (larger ionic radius). While other differences than ionic radii exist between Ca, Sr and Ba, we believe that the effect on the crystal strain would be the most important to the transport properties. Tsai *et al.* [48] investigated $\text{La}_{1-x}\text{A}_x\text{Fe}_{1-y}\text{Co}_y\text{O}_{3-\delta}$, A = Ba, Ca, Sr and found that Ba was the best dopant followed by Ca and finally Sr, with regard to the oxygen permeation flux. Contrary to this, Stevenson *et al.* [22] found that Sr was the better dopant, followed by Ba and Ca in the same system.

Investigation of the coupling of composition and oxygen transport in the LSMCF system requires precise measurements of the oxygen transport parameters of the bulk and the surface, coupled with measurements of the oxygen vacancy concentration. This paper is the second part of a two paper series focusing on the LSMCF system. The first part (Chapter 4) reported data of the measurements of the defect chemistry of the LSMCF materials. Here, in the second part, we report measurements of the transport parameters, and use the measured data from both parts to extract the fundamental parameters of the LSMCF system.

The transport parameters are measured using a setup consisting of a LSMCF membrane, an oxygen pump and an electrolyte probe [44]. The oxygen pump provides a controlled oxygen flux through the membrane, and at the same time measures the oxygen chemical potential difference across the membrane. The electrolyte probe measures the difference in the oxygen chemical potential between the membrane surface and its gas surroundings. This combination provides, as discussed in Chapter 3, precise measurements of the permeation flux and the surface resistance, r_s , which in most other experiment types are heavily correlated under these conditions.

With these data the membrane can be split into a bulk region and two surface regions, all of which are well characterized. We are thus able to extract; 1) the bulk transport parameters; 2) the surface transport parameters and, with the data of Chapter 4, 3) the influence of the defect chemistry and structure on both.

Table 5.1: Membrane properties. Density refers to the geometric density.

Name	M	x	weight (g)	diameter (mm)	thickness (mm)	XRD density (kg/m^3)	density (kg/m^3)	rel. density
LSCF	-	0	4.350	20.3±0.1	2.253±0.005	6280	5965	0.95
LSB10CF	Ba	0.1	5.229	21.1±0.1	2.50±0.01	6382	5982	0.94
LSB20CF	Ba	0.2	4.553	20.7±0.2	2.20±0.02	6483	6134	0.95
LSCa5CF	Ca	0.05	4.1502	20.9±0.1	2.081±0.05	6203	5816	0.94
LSCa10CF	Ca	0.1	4.113	21.45±0.1	1.987±0.05	6140	5645	0.93

5.2 Experimental

5.2.1 Sample preparation

Perovskite powders of composition $(\text{La}_{0.6}\text{Sr}_{0.4-x}\text{M}_x)_{0.99}\text{Co}_{0.2}\text{Fe}_{0.8}\text{O}_{3-\delta}$, $M = \text{Sr}, \text{Ca}$ ($x = 0.05, 0.1$), Ba ($x = 0.1, 0.2$), were prepared by the glycine pyrolysis process [33]. The powders were calcined at 900°C for 12 h, and ball milled using ZrO_2 balls in 500 ml polyethylene containers with ethanol for 24 h at 200 RPM. Flat cylindrically shaped membranes were pressed from these powders using an uniaxial pressure of 30-70 MPa. The membranes were further compressed in an evacuated latex container suspended in water at a hydrostatic pressure of 325 MPa. The samples were sintered at 1250°C - 1350°C for 12-40 hours. The sintered samples were polished with SiC polishing sheets and diamond suspensions (particle size down to 1 μm). The density of each sample was calculated using both the weight of the sample divided by the geometric volume (measured using sliding and micrometer screw gauges), and the archimedean law of displacement, with water as the displaced media. The geometric density was always a bit smaller than the archimedean density. The sintered and polished membrane samples had diameters of 20.3 mm→21.5 mm, and a thickness of 2.0 mm→2.5 mm. Densities of the samples were in the range of 93%→96% of the theoretical density calculated from the XRD and nominal composition.

5.2.2 X-ray diffraction

X-ray diffraction was done with $\text{Cu}_{K\alpha}$ radiation, with a mean wavelength of 1.5406 Å (30 mA/40kV) on a STOE $\theta - \theta$ reflection diffractometer. The energy dispersive, Peltier cooled Kevex detector was tuned to the $\text{Cu}_{K\alpha}$ energy (8.04 keV with an energy window of 300 eV). The step size was 0.05 degrees and the counting time in each step was 5 s. Horizontal slits were 10 mm, and the vertical slits were 0.8 mm for the primary tube, and 0.3 mm on the detector. The sample rotation was 100 RPM.

5.2.3 Membrane and probe measurement

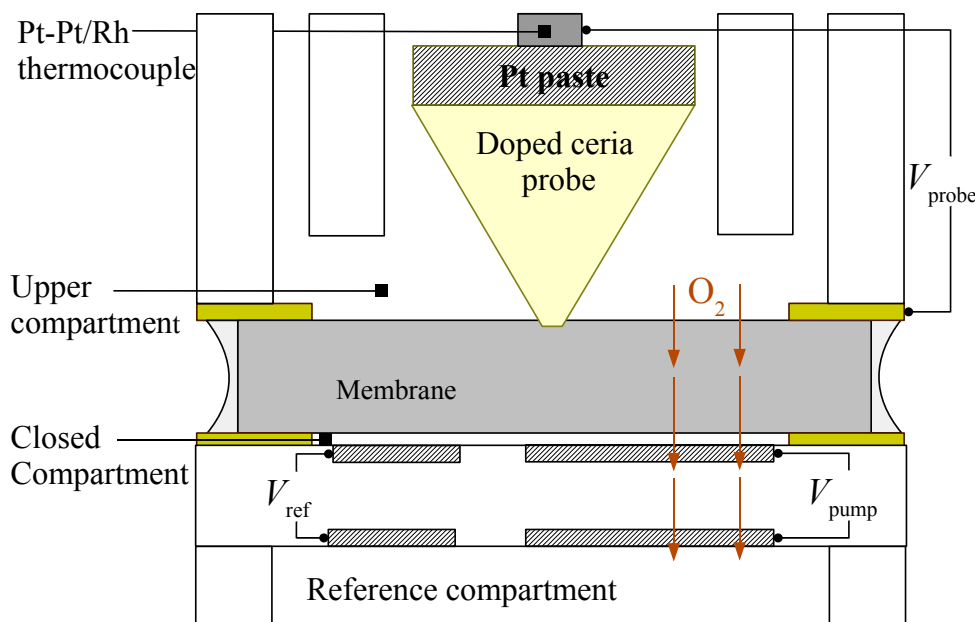


Figure 5.1: *The measurement setup.*

The experimental setup is shown in Figure 5.1. The MIEC membrane is placed between two $300\ \mu\text{m}$ thick gold seal rings. The inner diameter of the gold rings is 14 mm and defines the perimeter of the active surface of the membrane. This arrangement is placed on top of an $\text{Y}_{0.16}\text{Zr}_{0.84}\text{O}_{1.92}$ (YSZ) oxygen pump thus defining the "closed compartment" between the membrane, the gold seal ring and the oxygen pump. Two pairs of electrodes are painted on the oxygen pump. Each pair has one electrode in the closed compartment, and one electrode in the reference compartment, which is flushed with an air flow ($> 2 \cdot 10^{-6}\ \text{m}^3/\text{s}$ ($= 120\ \text{ml}/\text{min}$) at ambient conditions). The *pumping* electrode pair is made of a mixture of porous 50% YSZ+50% $\text{La}_{0.75}\text{Sr}_{0.25}\text{MnO}_3$ (YSZ/LSM) with porous Pt as current collector and is used to pump oxygen in and out of the closed compartment. The *reference* electrode pair is made of porous Pt (sintered "Ferro" Pt paste), and is used to measure the difference in oxygen chemical potential between the closed compartment and the reference compartment. The circumference of the membrane is sealed using Na_2O : 17.8 mol%, Al_2O_3 : 9.4 mol%, SiO_2 : 72.8 mol% glass paste, with a thermal expansion coefficient matching that of YSZ. Above the membrane an alumina cylinder defines an upper compartment. Two concentric alumina pipes terminate in the upper compartment. The inner pipe feeds gas (the "flow gas") to the upper compartment while the outer pipe transports the exhaust gas to a Pt|YSZ|Pt p_{O_2} sensor. The gas flow through the upper compartment is $1.67 \cdot 10^{-6}\ \text{m}^3/\text{s}$ (100 ml/min measured at ambient conditions) of air diluted with N_2 . Inside the inner pipe, a spring loaded thermocouple applies an electrical contact and a downward mechanical force to the Pt electrode on the back of a pointed electrolyte probe, in contact with the membrane surface. All electrical contacts were made using platinum and gold wires. A Solartron 1250/1286 setup was used as a programmable current source with a Keithley 2700 multimeter/data collector. Further details of the setup have been published in [44].

5.3 Defect chemistry and transport properties of LSMCF

In this section, the defect chemistry and transport properties of the investigated materials - LSMCF - are described. The model used to interpret the measurements is also presented.

5.3.1 Defect chemistry

The release and incorporation of oxygen in LSMCF can, in Kröger-Vink notation, be written:



At equilibrium, the chemical potential of oxygen, μ_{O_2} , is the same in the gas and solid phase. This allows us to label the state of the MIEC with the state of the gas with which it is in equilibrium, and vice versa. The chemical potential of oxygen, $\mu_{\text{O}_2}^{\text{MIEC}}$, in a MIEC in equilibrium with a gas with a given chemical potential of oxygen $\mu_{\text{O}_2}^{\text{gas}}$ can then be defined as:

$$\mu_{\text{O}_2}^{\text{MIEC}} = \mu_{\text{O}_2}^{\text{gas}} \quad (5.2)$$

The oxygen chemical potential of a gas, $\mu_{\text{O}_2}^{\text{gas}}$, is a well known function of the oxygen partial pressure and temperature:

$$\mu_{\text{O}_2}^{\text{gas}} = \mu_{\text{O}_2}^\ominus + RT \ln \left(p_{\text{O}_2}^{\text{gas}} / p_{\text{O}_2}^\ominus \right) \quad (5.3)$$

where R is the gas constant and T is the temperature. $p_{\text{O}_2}^{\text{gas}}$ and $p_{\text{O}_2}^\ominus$ are the oxygen partial pressures of the gas and standard gas, respectively. The oxygen chemical potential of the selected standard gas $\mu_{\text{O}_2}^\ominus$ can be calculated using the IUPAC standards [10] (see Appendix A). At a given T , Eq. 5.2 thus allows us to describe the state of the MIEC by a chemical potential of oxygen.

The equilibrium relation between μ_{O_2} and $C_{\text{O}}^{\text{MIEC}}$ has been determined using thermogravimetry and coulometric titration. These measurements were reported in the first paper of this study [59] found in Chapter 4.

5.3.2 Transport properties

In LSMCF, local electroneutrality causes the transport of electrons (e^-) and oxygen ions (O^{2-}) to be coupled. In the absence of external electrical fields, we are free to define the diffusing species in the material as "oxygen", O_2 , consisting of two oxide ions O^{2-} and four electron holes. The least mobile element of O_2 will limit the diffusion of the construct. In LSMCF, the least mobile element is the oxide ions. From the Wagner equation:

$$j_{\text{O}_2} = -\frac{1}{4^2 F^2} \frac{\sigma_e \sigma_{\text{O}}}{\sigma_e + \sigma_{\text{O}}} \nabla \mu_{\text{O}_2}^{\text{MIEC}} = -\frac{1}{4^2 F^2} \Sigma \nabla \mu_{\text{O}_2}^{\text{MIEC}}, \quad \Sigma = \frac{\sigma_e \sigma_{\text{O}}}{\sigma_e + \sigma_{\text{O}}} \quad (5.4)$$

where F is the Faraday constant, j_{O_2} is the oxygen flux, σ_e is the electronic conductivity and σ_{O} is the oxide ion conductivity. Σ is the ambipolar conductivity. For the LSMCF materials, $\sigma_{\text{O}} \ll \sigma_e$ and $\Sigma \simeq \sigma_{\text{O}}$.

As most of the oxide ion sites in the structure are occupied, the diffusion of oxide ions is controlled by the number of oxide ion vacancy sites available. For small vacancy concentrations the transport equation becomes:

$$j_{\text{O}_2} = \frac{\gamma_{\text{V}}}{2} D_{\text{V}}^0 \left(1 - \frac{\delta}{3} \right) \nabla C_{\text{V}}, \quad D_{\text{V}}^0 = \frac{4RT}{C_{\text{V}} \left(1 - \frac{\delta}{3} \right) 4^2 F^2}, \quad \gamma_{\text{V}} = \gamma \frac{C_{\text{V}}}{C_{\text{O}}^{\text{MIEC}}} \quad (5.5)$$

where D_{V}^0 is the reduced diffusion coefficient, C_{V} is the vacancy concentration and γ_{V} is the thermodynamic factor associated with the oxygen vacancies. The term $\left(1 - \frac{\delta}{3} \right)$ is added as a vacancy can not diffuse to a vacant oxide site. We expect a priori that D_{V}^0 is independent of C_{V} apart from second order effects (such as C_{V} influencing the crystal structure or immobilization of vacancies due to ordering). When interpreting our measurements D_{V}^0 will therefore be used as a fitting parameter.

When the surface is brought out of equilibrium with the surrounding atmosphere, a step in μ_{O_2} , $\Delta\mu_{\text{O}_2}$, exists at the surface. Assuming a linear response of the flux to the step in μ_{O_2} we can define a surface exchange coefficient, k , and, keeping the formalism of Eq. 5.4, an area specific surface resistance r_s .

$$j_{\text{O}_2} = -k\Delta\mu_{\text{O}_2} = -\frac{1}{4^2F^2r_s}\Delta\mu_{\text{O}_2} \quad (5.6)$$

5.3.3 Steady state model

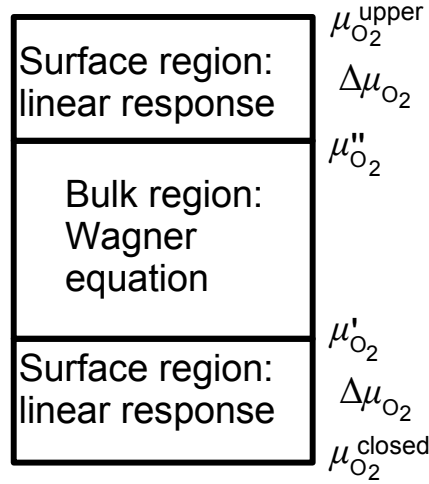


Figure 5.2: Outline of steady state model. $\mu_{\text{O}_2}^{\text{upper}}$ is the μ_{O_2} in the upper compartment, while $\mu_{\text{O}_2}^{\text{lower}}$ is the μ_{O_2} in the lower compartment

To fit data recorded during steady state permeation measurements, a one dimensional numerical model based on the Wagner equation [60] combined with oxygen exchange at the surface is used (Eq. 5.6). The Wagner equation is obtained from integration of Eq. 5.4:

$$j_{\text{O}_2} = -\frac{1}{4^2F^2L} \int_{\mu_{\text{O}_2}'}^{\mu_{\text{O}_2}''} \frac{\sigma_e \sigma_{\text{O}}}{\sigma_e + \sigma_{\text{O}}} d\mu_{\text{O}_2} = -\frac{1}{L} \int_{\mu_{\text{O}_2}'}^{\mu_{\text{O}_2}''} \frac{C_V \left(1 - \frac{\delta}{3}\right)}{4RT} D_V^0 d\mu_{\text{O}_2} \quad (5.7)$$

where μ_{O_2}' and μ_{O_2}'' are the chemical potentials of oxygen of the membrane surfaces. μ_{O_2}' and μ_{O_2}'' differ from the μ_{O_2} of the closed and upper compartment by $\Delta\mu_{\text{O}_2}$ at the surfaces - see Fig. 5.2.

Equations 5.6 and 5.7 are solved simultaneously to extract D_V^0 . Due to the small perturbations it is assumed that $\Delta\mu_{\text{O}_2}$ is the same on both sides of the membrane. Note that for very small differences in μ_{O_2} , $C_V \left(1 - \frac{\delta}{3}\right)$ can be considered constant, and the model can be solved analytically.

The gold seals act as apertures for the surface exchange (see Fig. 5.1) but the membrane cross-section is wider than these apertures, resulting in an overestimation of D_V^0 . D_V^0 can be corrected for this by multiplying with a membrane geometry dependent factor f_c (for the membrane of this study it has a value of 0.92-0.95) [35].

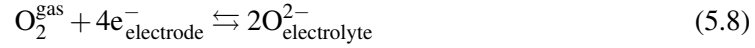
5.4 Measurements using an oxygen pump and an electrochemical probe

The setup used for the electrochemical measurements in this study, and the necessary corrections for nonideal effects have already been discussed extensively. For the full details of the data

treatment we refer to Chapter 2. The basic principles are presented in short form in the following.

5.4.1 Oxygen chemical potential measurement

The basic principle behind both the probe and the oxygen pump is to use oxide conducting electrolytes to measure differences in the chemical potential of oxygen. An oxide ion conducting electrolyte placed between two external phases with different oxygen chemical potential, approaches equilibrium between the oxide or oxygen in the two external phases and the electrolyte surfaces. If the phases are catalytically active electrodes, the electrolyte can be sensitive to the gas phase through the reaction:



The relationship, at equilibrium, between the oxygen activity of the external phases and cell voltage, as measured between electrodes placed on the two interfaces, will then be:

$$\mu'_{\text{O}_2} - \mu''_{\text{O}_2} = 4FV_{\text{electrode}} \quad (5.9)$$

where μ'_{O_2} and μ''_{O_2} are the oxygen chemical potential in each of the external phases, and $V_{\text{electrode}}$ is the voltage between the two electrodes.

5.4.2 The oxygen pump

The YSZ oxygen pump is an electrochemical cell with an YSZ electrolyte. Combining Eqs. 5.3 and 5.9, the Nernst equation governing the relationship between oxygen activity and cell voltage is:

$$p_{\text{O}_2}^{\text{gas}} = p_{\text{O}_2}^{\text{ref}} \cdot \exp\left(\frac{4FV_{\text{ref}}}{RT}\right) \quad (5.10)$$

$p_{\text{O}_2}^{\text{gas}}$ is the oxygen partial pressure of the gas in the closed compartment, $p_{\text{O}_2}^{\text{ref}}$ is the p_{O_2} of the gas in the reference compartment (air in these measurements) and V_{ref} is the voltage between the reference electrodes. As four electrons pumped in the external circuit will correspond to one oxygen molecule passing between the electrodes of the cup the relationship between pumping current and oxygen transfer is:

$$j_{\text{O}_2} = \frac{I_{\text{pump}}}{4F} \quad (5.11)$$

Where I_{pump} is the pumping current.

The area specific conductance, G

In the setup of Fig. 5.1, the ionic current through the membrane in steady state must equal the ionic current through the pump. In general results of permeation experiments are presented as flux versus driving force, but here it is more convenient to express the experimental results as conductance. It is defined as:

$$G = \frac{i_{\text{pump}}}{\Delta V_{\text{Nernst}}}, \quad i_{\text{pump}} = I_{\text{pump}}/A_{\text{MIEC}} \quad (5.12)$$

$$\Delta V_{\text{Nernst}} = V_{\text{closed}} - V_{\text{upper}} = V_{\text{ref}} - V_{\text{ref}}^0 \quad (5.13)$$

where i_{pump} is the area specific current, and A_{MIEC} is the exposed area of the MIEC membrane. ΔV_{Nernst} is the difference in the Nernst voltage between the gas in the upper compartment, V_{upper} , and the gas in the closed compartment, V_{closed} , with the reference compartment gas as a common reference.

The oxygen flux through the membrane changes the p_{O_2} above the membrane [44]. The average Nernst voltage of the gas in the upper compartment, $V_{\text{Nernst}}^{\text{upper}}$ measured versus air is derived in Appendix B as:

$$V_{\text{Nernst}}^{\text{upper}} = \frac{RT}{4F} \left[\ln \left(\frac{p_{\text{O}_2}^{\text{in}}}{p_{\text{O}_2}^{\text{air}}} \right) + \left(\frac{p_{\text{O}_2}^{\text{in}}}{\Delta p_{\text{O}_2}} + 1 \right) \left(\ln \left(\frac{\Delta p_{\text{O}_2}}{p_{\text{O}_2}^{\text{in}}} + 1 \right) - 1 \right) \right] \quad (5.14)$$

$$\Delta p_{\text{O}_2} = \frac{I_{\text{pump}} RT_{\Phi_f}}{4F \Phi_f} \quad (5.15)$$

where T_{Φ_f} is the temperature at which the volume flow is measured. $p_{\text{O}_2}^{\text{in}}$ is the p_{O_2} of the inlet gas, calculated from V_{ref}^0 . When the corrected $V_{\text{Nernst}}^{\text{upper}}$ is used to calculate G this is denoted G_c .

To quantify the p_{O_2} (or μ_{O_2}) dependence at constant T of G_c , we assume a power law dependence:

$$G_c = G_c^0 \left(\frac{p_{\text{O}_2}}{p_{\text{O}_2}^0} \right)^{-n_{G_c}} \quad (5.16)$$

where $p_{\text{O}_2}^0$ and G_c^0 are reference values chosen among the measured data, and n_{G_c} is the power law exponent.

5.4.3 The electrolyte probe

The tip of the electrolyte probe is in ionic and electronic contact with the MIEC membrane; the porous platinum electrode on the other side of the probe resides in the flow gas. Assuming that equilibrium exists between the platinum and the gas and between the probe tip and the MIEC membrane, Eqs. 5.9 and 5.3 state that the probe voltage, V_{probe} , is a direct measure of the difference in μ_{O_2} between the inlet flow gas and the MIEC membrane surface:

$$\Delta \mu_{\text{O}_2} = \mu_{\text{O}_2}^{\text{in}} - \mu_{\text{O}_2}^{\text{MIEC}} = 4F V_{\text{surface}} \quad (5.17)$$

where $\mu_{\text{O}_2}^{\text{in}}$ and $\mu_{\text{O}_2}^{\text{MIEC}}$ are the oxygen chemical potential, of the inlet flow gas, and just inside the MIEC surface, respectively. V_{surface} is the part of the probe voltage, V_{probe} , attributable to the oxygen exchange over the surface. r_s is calculated by combining Eq. 5.6 and Eq. 5.17:

$$r_s = -\frac{\Delta \mu_{\text{O}_2}}{4^2 F^2 j_{\text{O}_2}} \quad (5.18)$$

V_{surface} is not the only contribution to V_{probe} . A few more contributions must be corrected for (see Chapter 2):

$$V_{\text{probe}} = V_{\text{surface}} + V_{\text{grad}} + \sum_i V_i, \quad (5.19)$$

where V_{grad} is the influence of the perturbation flux on the gas p_{O_2} , and $\sum_i V_i$ is the sum of flux independent voltages (thermovoltages, zero point offsets, etc.) present in the system.

r_s is in general strongly p_{O_2} dependent. Assuming a power law, the reaction order n_{r_s} of r_s is defined as:

$$r_s = r_s^0 \left(\frac{p_{\text{O}_2}}{p_{\text{O}_2}^0} \right)^{-n_{r_s}} \quad (5.20)$$

where $p_{\text{O}_2}^0$ and r_s^0 are reference values.

5.5 Results and discussion

The p_{O_2} in the upper compartment was changed by applying different mixtures of air and N_2 . For each gas mixture, several measurements were made, using different values of i_{pump} . The absolute value of i_{pump} was kept low enough to ensure that a linear response of V_{ref} and V_{probe} was observed.

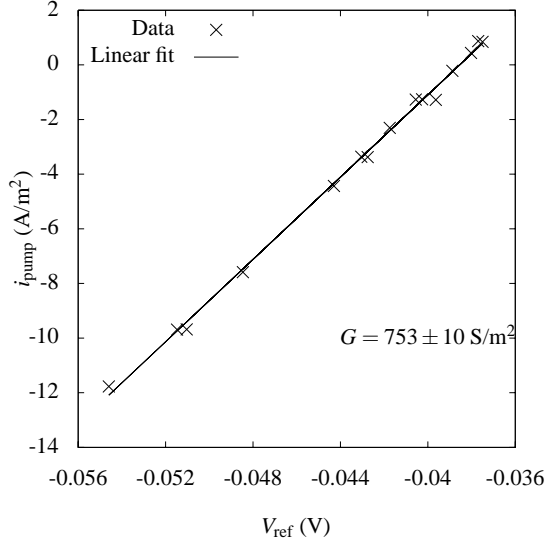


Figure 5.3: i_{pump} as a function of V_{ref} for LSCa5CF. $T=1123$ K, gas 20% air + 80% N_2 .

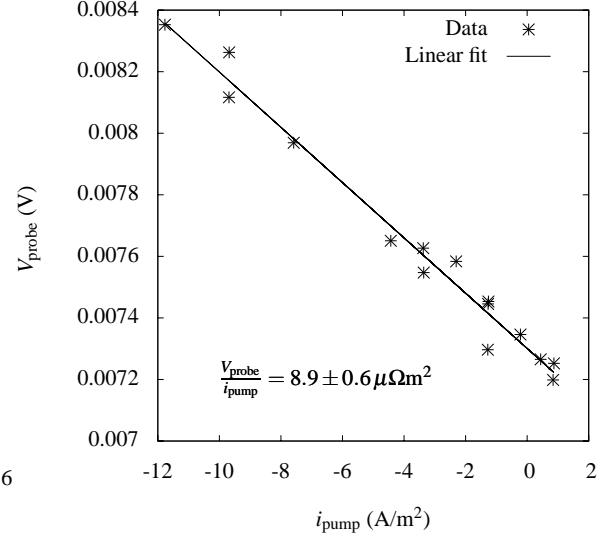


Figure 5.4: V_{probe} as a function of i_{pump} for LSCa5CF. $T=1123$ K, gas 20% air + 80% N_2 .

i_{pump} recorded for LSCa5CF is plotted as a function of the reference voltage at $T=1123$ K in a 4:1 N_2 :air gas mixture (i.e. p_{O_2} about 4 kPa), in Fig. 5.3. There is a linear relation between i_{pump} and V_{ref} . $G = 753 \pm 10 \text{ S/m}^2$ is extracted as the slope of the linear fit. The standard deviation of G is less than 2% of the measured value.

In the same experiment a linear relationship between V_{probe} and i_{pump} is also found. This is shown in Fig. 5.4. Positive values of V_{probe} correspond to μ_{O_2} being lower at the probe tip than at the platinum electrode at the back of the probe. The deviation of V_{probe} from 0 at $i_{\text{pump}} = 0$ is attributed to thermoelectric voltages in the measuring circuit. $\frac{\partial V_{\text{probe}}}{\partial i_{\text{pump}}}$ was extracted as $89 \pm 6 \mu\Omega\text{m}^2$.

In the following, values of r_s and G_c are plotted as a function of the p_{O_2} and T . Each value of r_s and G_c is extracted from a measurement series such as those plotted in Figs. 5.3 and 5.4. The p_{O_2} of the horizontal axis in Figs. 5.3 and 5.4 are the equilibrium p_{O_2} measured at the reference electrodes when $i_{\text{pump}} = 0$. It is equal to the p_{O_2} of the gas mixture led into the upper compartment.

5.5.1 G_c and r_s

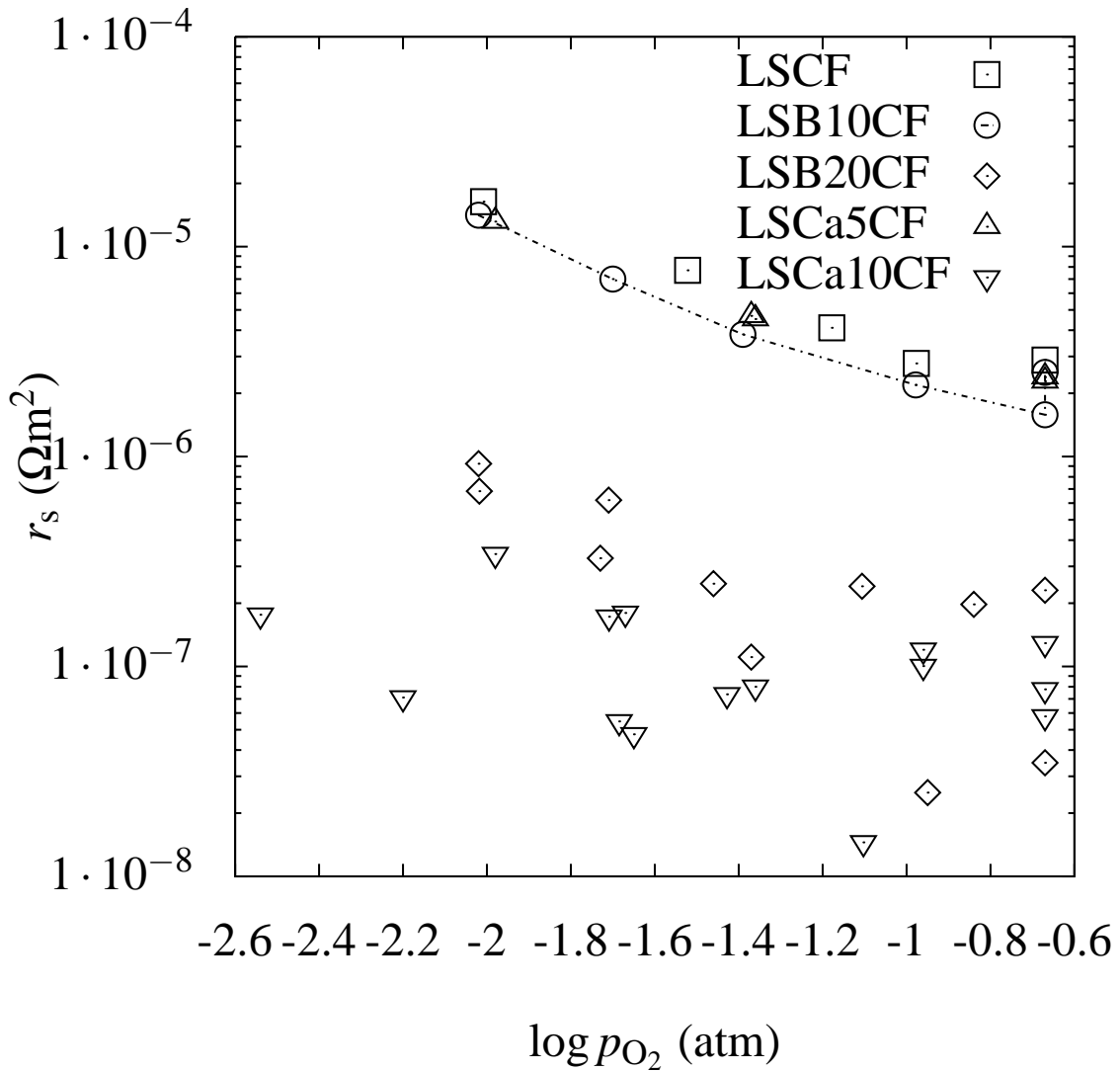


Figure 5.5: r_s as a function of p_{O_2} at $T = 1273 \text{ K}$ for the investigated materials. Connecting lines have been added to LSB10CF as guides to the eye.

The area specific resistance to oxygen permeation of the surface, r_s , can be calculated (Eq. 5.18) from measurements of V_{surface} as a function of j_{O_2} in the linear regime (typically $i_{\text{pump}} < 100 \text{ A/m}^2$). r_s is plotted as a function of the p_{O_2} of the flow gas in the upper compartment at $T = 1273 \text{ K}$ in Fig. 5.5. Error bars have been omitted as the confidence interval of the measurements are smaller than the symbol sizes, except for LSB20CF and LSCa10CF, whose values are low enough to approach the noise limit of the measurement. There is little difference between the p_{O_2} dependence of r_s of LSCF, LSB10CF and LSCa5CF which all have n_{r_s} close to 0.75 (n_{r_s} is proportional to the slope of the data in Fig. 5.5). r_s for LSB20CF and LSCa10CF is an order of magnitude lower than for the other compositions, resulting in large scatter as they are approaching the noise limit of the probe.

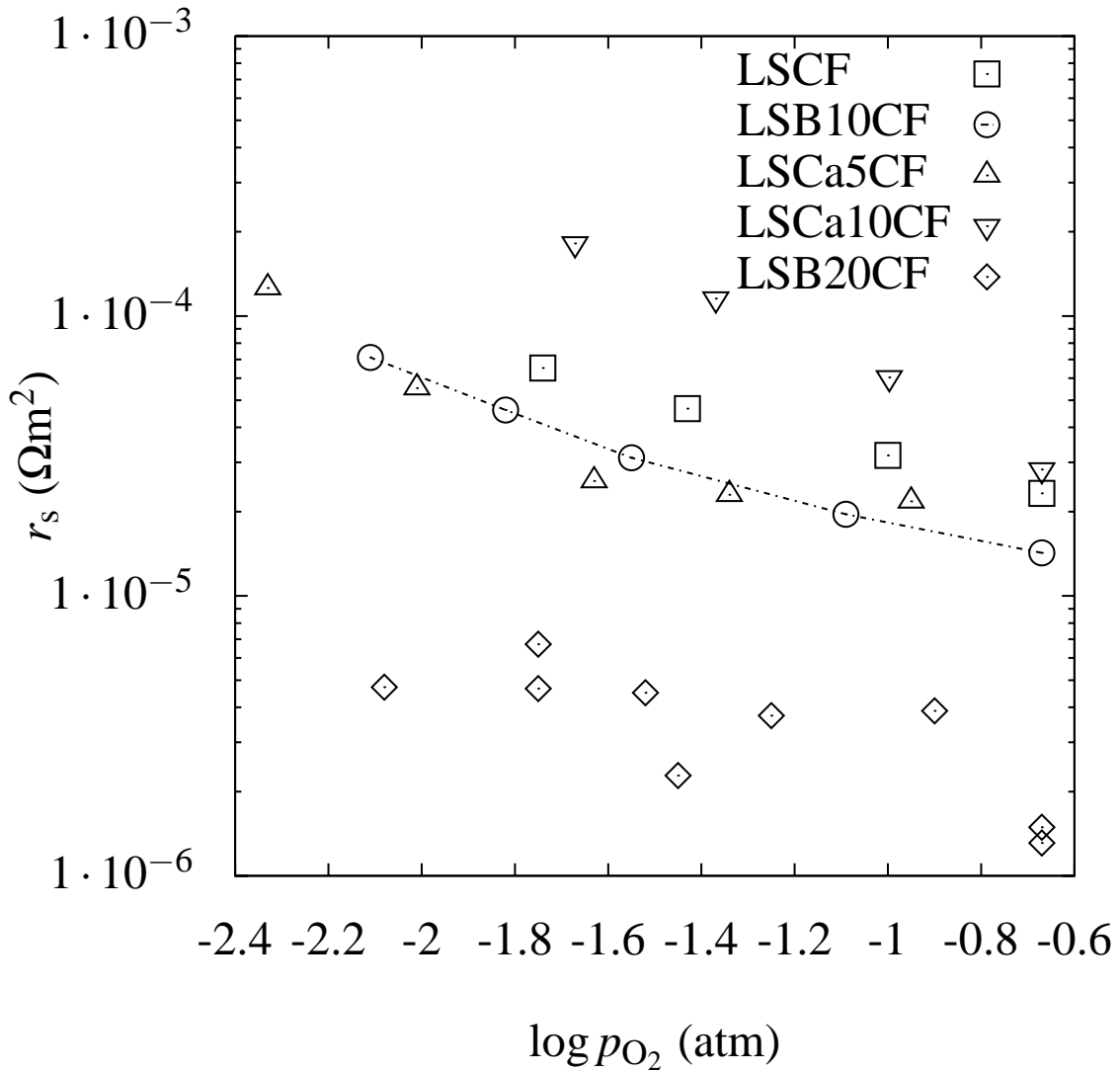


Figure 5.6: r_s as a function of p_{O_2} at $T = 1123$ K. Connecting lines have been added to LSB10CF as guides to the eye.

r_s is shown as a function of p_{O_2} at $T = 1123$ K in Fig. 5.6. Contrary to the measurements at 1273 K, LSCa10CF show the largest r_s of the materials at 1123 K. The power law exponent, n_{r_s} , of LSCa10CF is also considerably higher for $\log p_{\text{O}_2} > -1.6$ (atm) than that of the other materials at this temperature. LSCF, LSB10CF and LSCa5CF have roughly the same r_s and n_{r_s} . r_s of LSB20CF is an order of magnitude lower than r_s of the other materials.

It is a general trend for all the materials that n_{r_s} is higher at 1273 K than at 1123 K.

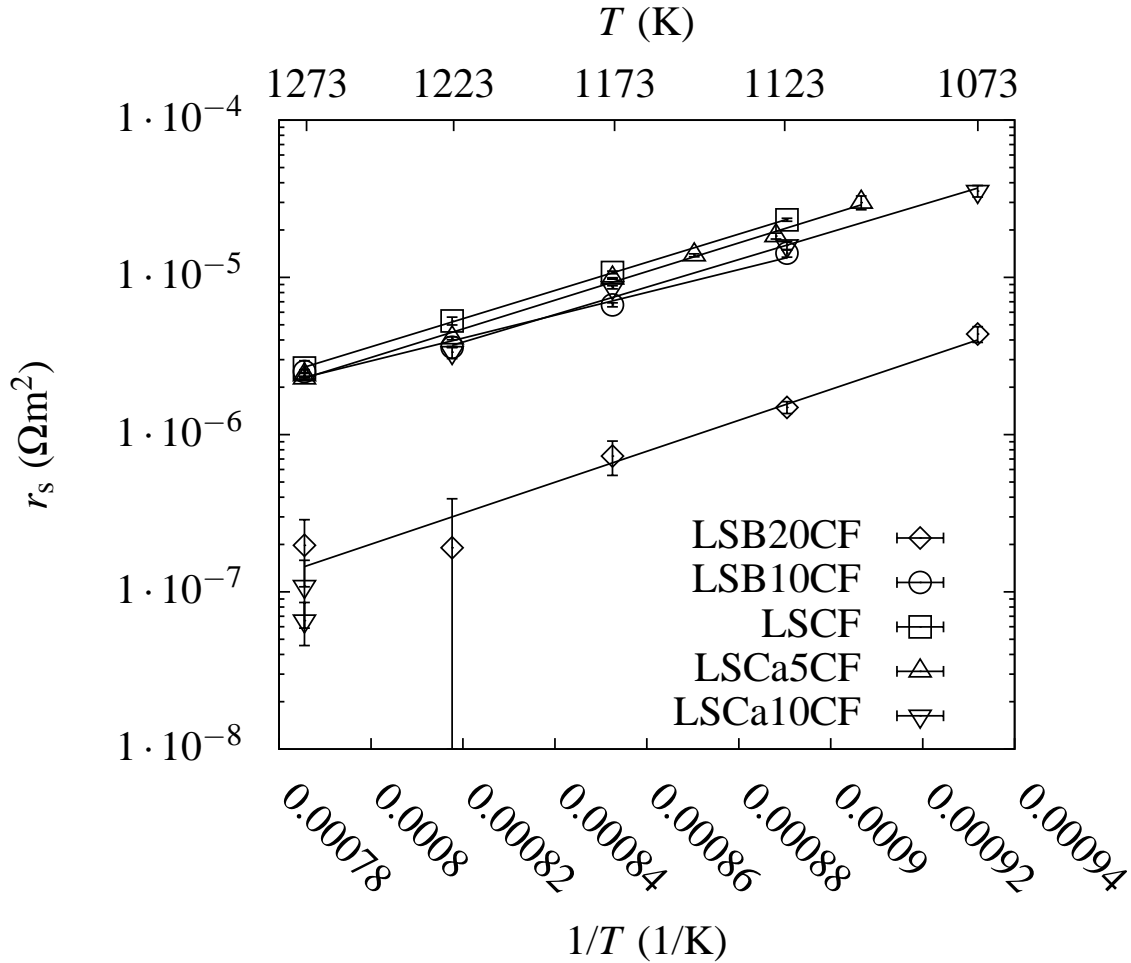


Figure 5.7: r_s as a function of T in air

An Arrhenius plot of r_s as a function of T in air is shown in Fig. 5.7. The activation energies deduced from the plot, $E_a^{r_s}$ are presented in Table 5.3. LSB10CF has the lowest activation energy, $E_a^{r_s}$, at 139 kJ/mol, while the rest of the materials have $E_a^{r_s}$ between 172 kJ/mol and 188 kJ/mol. The error bars found at $r_s < 10^{-6} \Omega\text{m}^2$ signifies that the measurements are approaching the noise limit of the cone. The measurements for $r_s > 10^{-6} \Omega\text{m}^2$ all have error bars smaller than the symbol sizes.

The large change in the surface resistance of LSCa10CF for $T > 1248$ K is reproducible, without hysteresis. The abruptness of the change suggests that a phase change is responsible. LSCa10CF at $T > 1248$ K and LSB20CF at all temperatures has a much smaller r_s than the other materials. The activation energy, however is roughly the same for all materials (except LSCa5CF), suggesting that the reaction mechanism for LSB20CF is the same as for the rest of the materials, but that the pre-exponential term is much larger. LSCa10CF and LSB20CF represent the lowest and highest value of $t_{\text{Goldschmidt}}$ for this series, respectively. Furthermore, LSCa10CF has the low r_s at 1273 K where it has the largest value of δ . The low r_s could thus be associated with instability of the perovskite. No dramatic change of G_c of LSCa10CF was, however, found for $T > 1248$ K, indicating that the effect is exclusively related to the surface. An increased number of active reaction sites in the surface is consistent with a larger pre-exponential term and decreased surface resistance. Possible explanations are chemical effects, i.e. adsorption/desorption of impurities from the carrier gas, or a reversible change in the surface morphology of the MIEC. If the low surface resistance of LSB20CF extends to low temperatures, it is a promising material for SOFC cathodes.

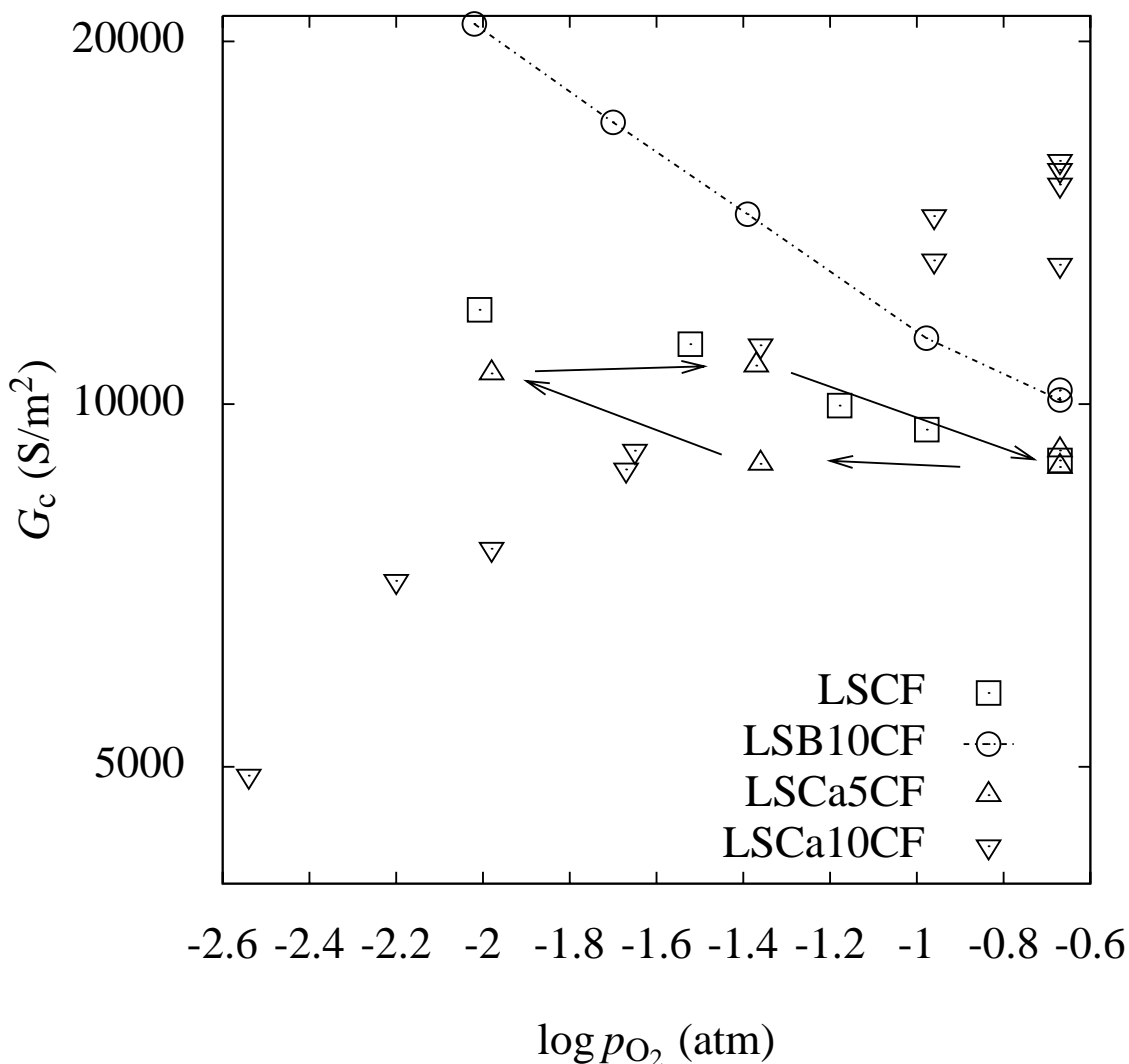


Figure 5.8: G_c as a function of p_{O_2} at $T = 1273$ K. A connecting line has been added to LSB10CF as a guide to the eye

The area specific conductance of the membrane, G_c , can be calculated (Eq. 5.12) from measurements of V_{ref} as a function of j_{O_2} in the linear regime (typically $i_{\text{pump}} < 100 \text{ A}/\text{m}^2$). G_c is shown as a function of p_{O_2} at $T = 1273$ K in Fig. 5.8. The confidence interval of the measurements (i.e. error bars) are smaller than the symbol sizes - the scatter reflects changes of the membrane with time. G_c of LSB10CF is the most p_{O_2} dependent, while G_c of LSCa5CF is the least p_{O_2} dependent. G_c of LSCa5CF shows some hysteresis (illustrated by the arrows in Fig. 5.8), which is assumed to be caused by very slow relaxations in the membrane. Hysteresis spanning an order of magnitude is present in LSB20CF (not plotted in Fig. 5.8). The relaxation responsible for the hysteresis has a characteristic time of about one week. For both LSCa5CF and LSB20CF the measurement order is: high $p_{\text{O}_2} \rightarrow$ low $p_{\text{O}_2} \rightarrow$ high p_{O_2} . The lowest values of G_c are recorded as the p_{O_2} is reduced between each measurement point. No hysteresis is found when the temperature is changed in air, and we conclude that the slow relaxations are triggered by reduction of the membrane. Repeating a reduction cycle after several weeks of measurement reveals a much smaller hysteresis.

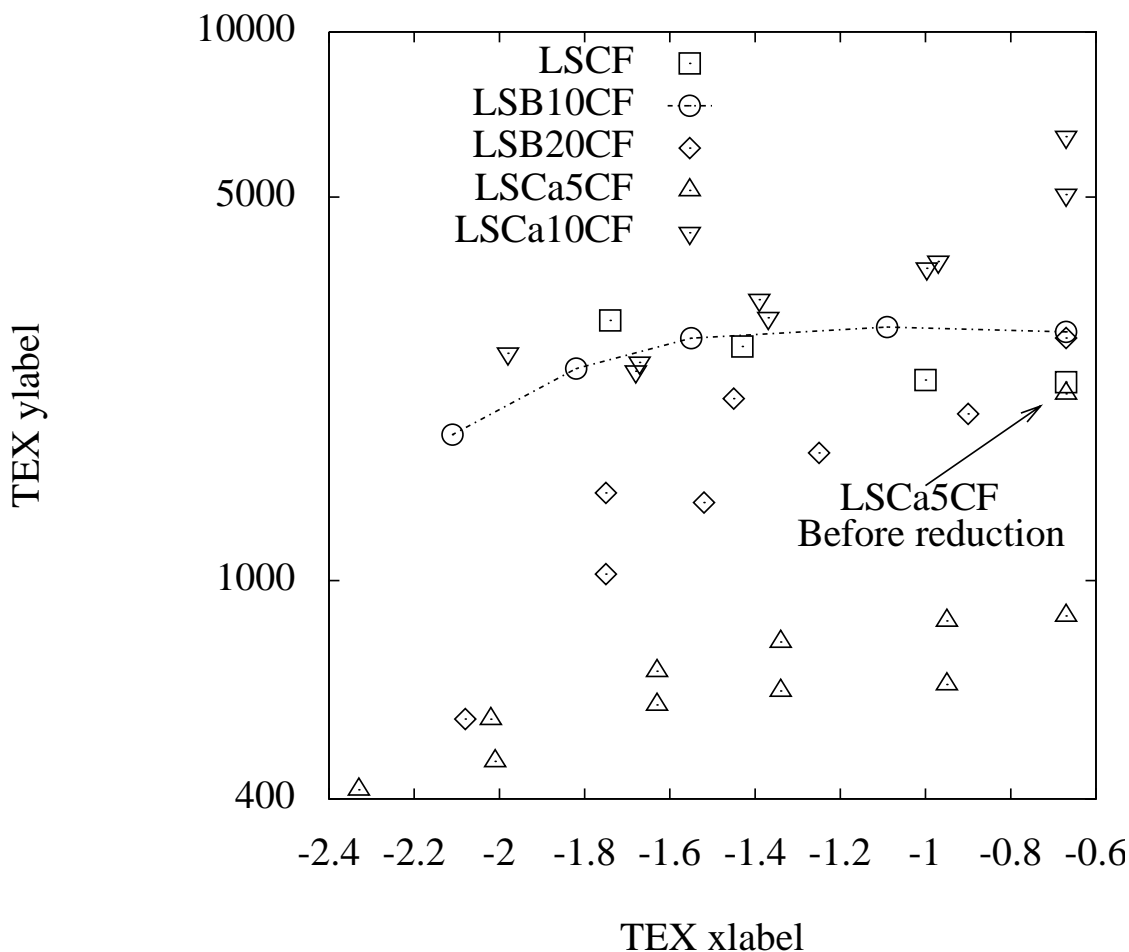


Figure 5.9: G_c as a function of p_{O_2} at $T = 1123$ K. A connecting line have been added to LSB10CF as a guide to the eye

The p_{O_2} dependence of G_c at $T = 1123$ K is shown in Fig. 5.9. The dotted lines are guides to the eye. The hysteresis of LSB20CF is less pronounced than at $T = 1273$ K, and only little hysteresis exist for LSCa5CF.

The series for LSCa5CF was recorded after it had accidentally been exposed to a very high ionic current at $T = 1073$ K (and thus very reducing conditions in the lower compartment). One point in air, ($\log p_{\text{O}_2} = -0.67$, $G_c = 2300$ A/m²) was recorded before this exposure to reducing conditions, and we believe that a large fraction of the lower surface has been deactivated, causing the subsequent low values of G_c . This does not affect the measured r_s as the electrolyte probe measures the r_s on the upper surface of the membrane.

It is interesting that G_c of LSCF tends to increase as p_{O_2} is reduced, while G_c of the other materials decreases. The power law exponents, n_{G_c} , are tabulated in table 5.2.

Table 5.2: Reaction orders

Name	$n_{G_c}^{1273\text{K}}$	$n_{G_c}^{1123\text{K}}$	$n_{r_s}^{1273\text{K}}$	$n_{r_s}^{1123\text{K}}$
LSCF	-0.23	-0.25	0.75	0.41
LSB10CF	-0.53	0.27	0.70	0.48
LSB20CF	-	0.93	0.91	0.38
LSCa5CF	-0.07	0.17	0.74	0.55
LSCa10CF	-	-	0.88	0.71

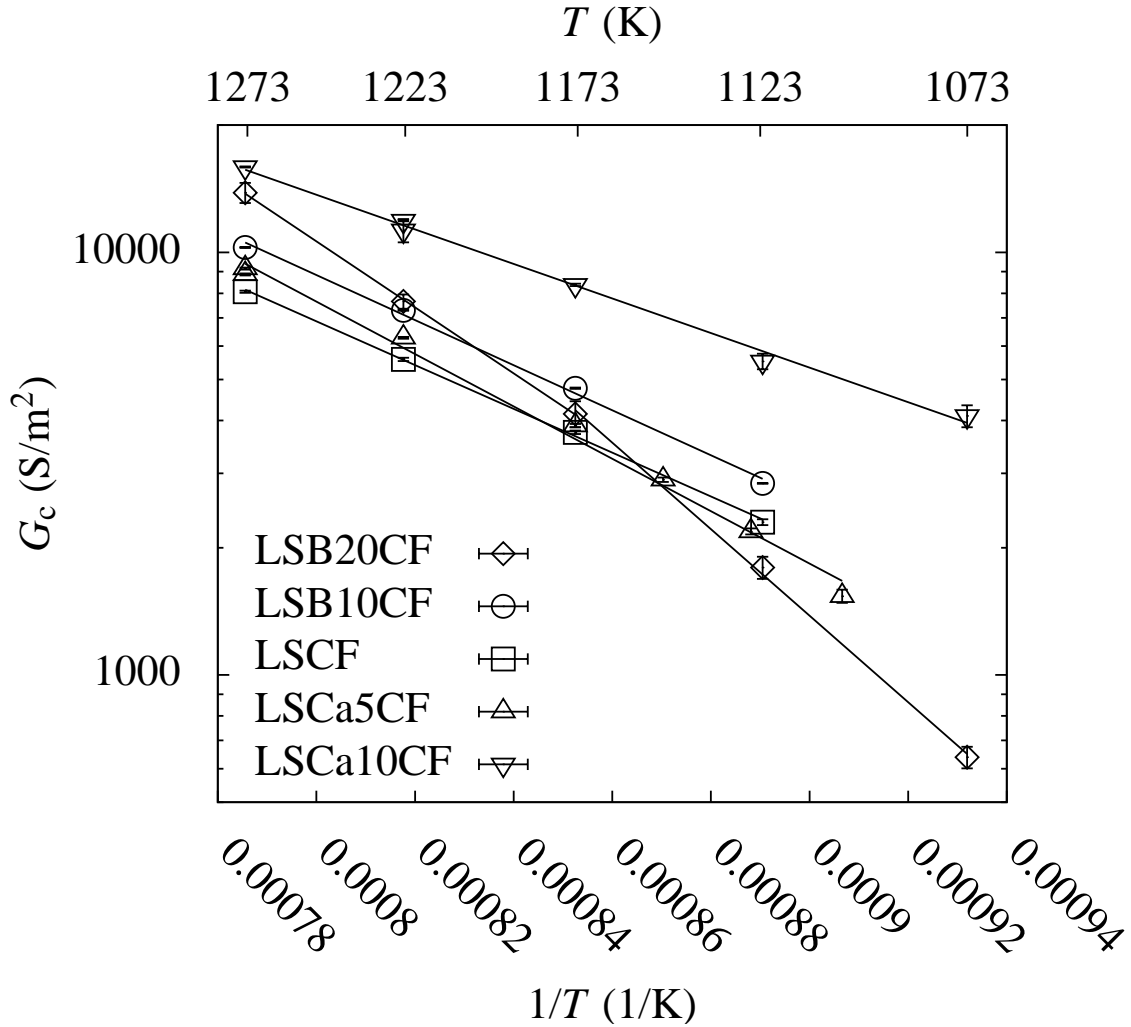


Figure 5.10: G_c as a function of T in air

The temperature dependence of G_c in air is shown in Fig. 5.10. The activation energies, $E_a^{G_c}$, are between 99 kJ/mol and 119 kJ/mol. The only material that does not show an Arrhenius dependence of G_c was LSB20CF which had to be fitted with two Arrhenius curves with large activation energies. LSCa10CF has the highest G_c , and, coupled with a very low activation energy, LSCa10CF is a good candidate material for thick permeation membranes. $E_a^{G_c}$ is tabulated in Table 5.3.

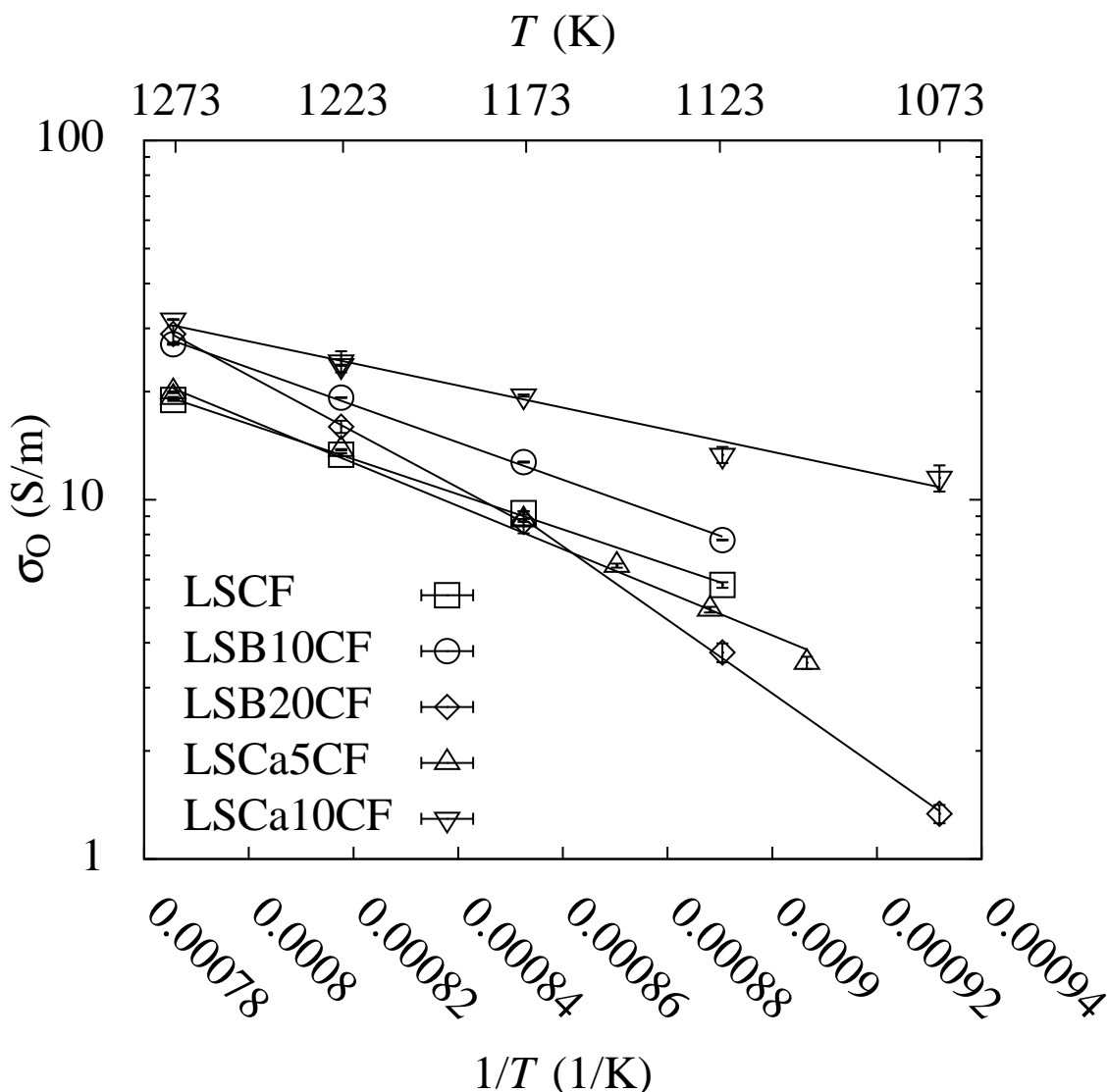


Figure 5.11: σ_{O} of the LSMCF materials.

In the measurements in air, regardless of the material, less than 10% of the total difference in μ_{O_2} across the membrane is found over the two surfaces. The r_s values measured in this experiment, in air, will thus not influence the measured G_c much. When p_{O_2} is 10^{-2} atm, up to 30% of the total difference in μ_{O_2} across the membrane is lost over the two surfaces. Most of the measurements of this study have thus been made in a regime where oxygen permeation is controlled by processes in the bulk of the material and the large differences in r_s of the materials will not necessarily be reflected in G_c . Therefore $\sigma_{\text{O}} \approx LG_c$. A G_c value of 10000 thus corresponds to about 20 S/m for the membranes in this study. σ_{O} is plotted in Fig. 5.11. LSCa10CF stands out with an extraordinarily low activation energy of 59 kJ/mol, suggesting unusually high performance at intermediate temperatures. The low activation energy is mainly caused by a very low activation energy of D_{V}^0 (see Table 5.3).

5.5.2 The reduced diffusion coefficient, D_{V}^0

Most studies in the literature of ionic transport report values of the chemical diffusion coefficient or conductivity of the oxide ions. These parameters include not only the mobility of the individual ion, but also the effect of the number of mobile ions. By focusing on D_{V}^0 we remove the

contribution from the number of mobile ions. D_V^0 is thus a representation of the mobility of the oxide ion vacancies.

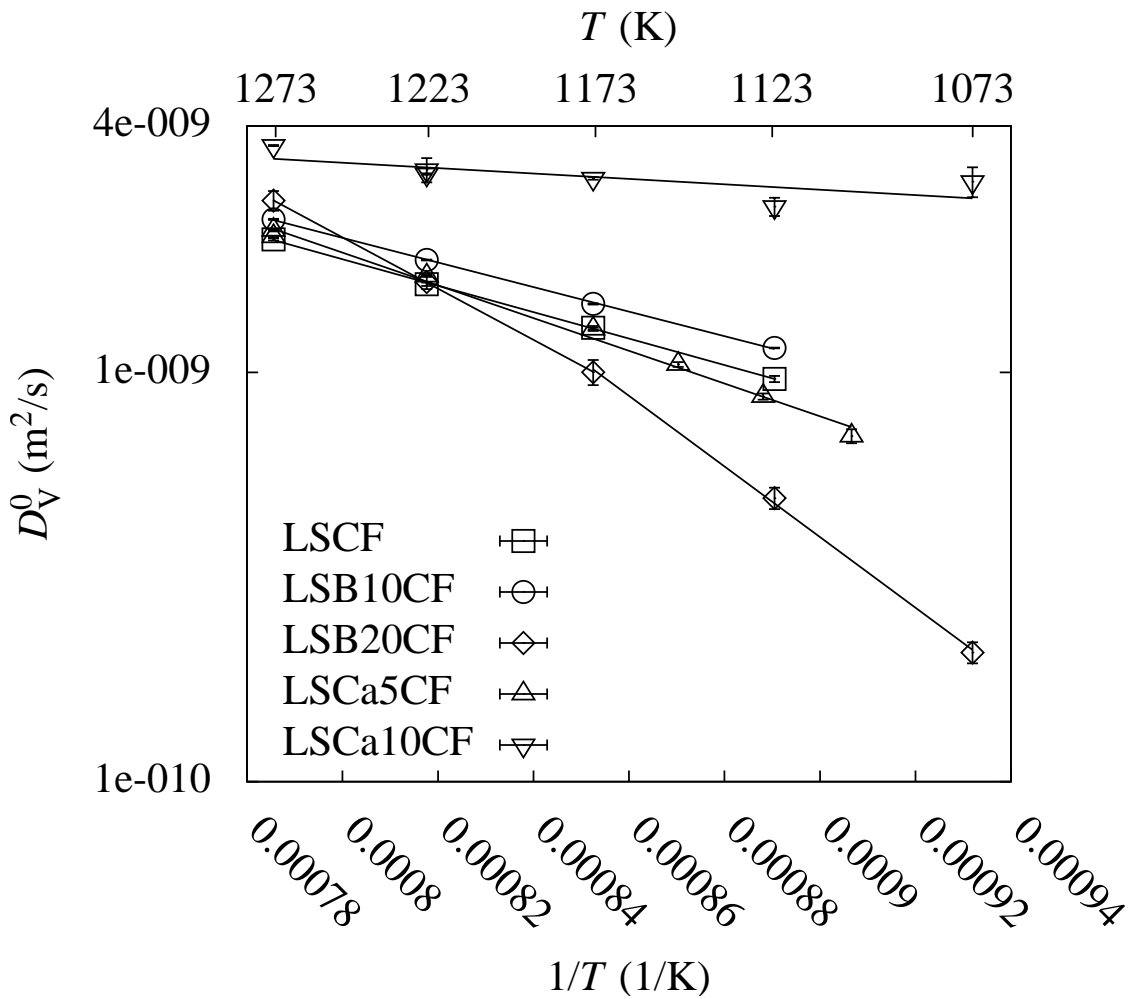


Figure 5.12: Arrhenius plot of D_V^0 .

The temperature dependence of D_V^0 is shown in Fig. 5.13. There is a large variation in D_V^0 ; LSCa10CF has a very low activation energy of the reduced diffusion coefficient and shows promise for a membrane at lower temperatures. The activation energies of D_V^0 , $E_a^{D_V^0}$, extracted from the plot are tabulated in Table 5.3.

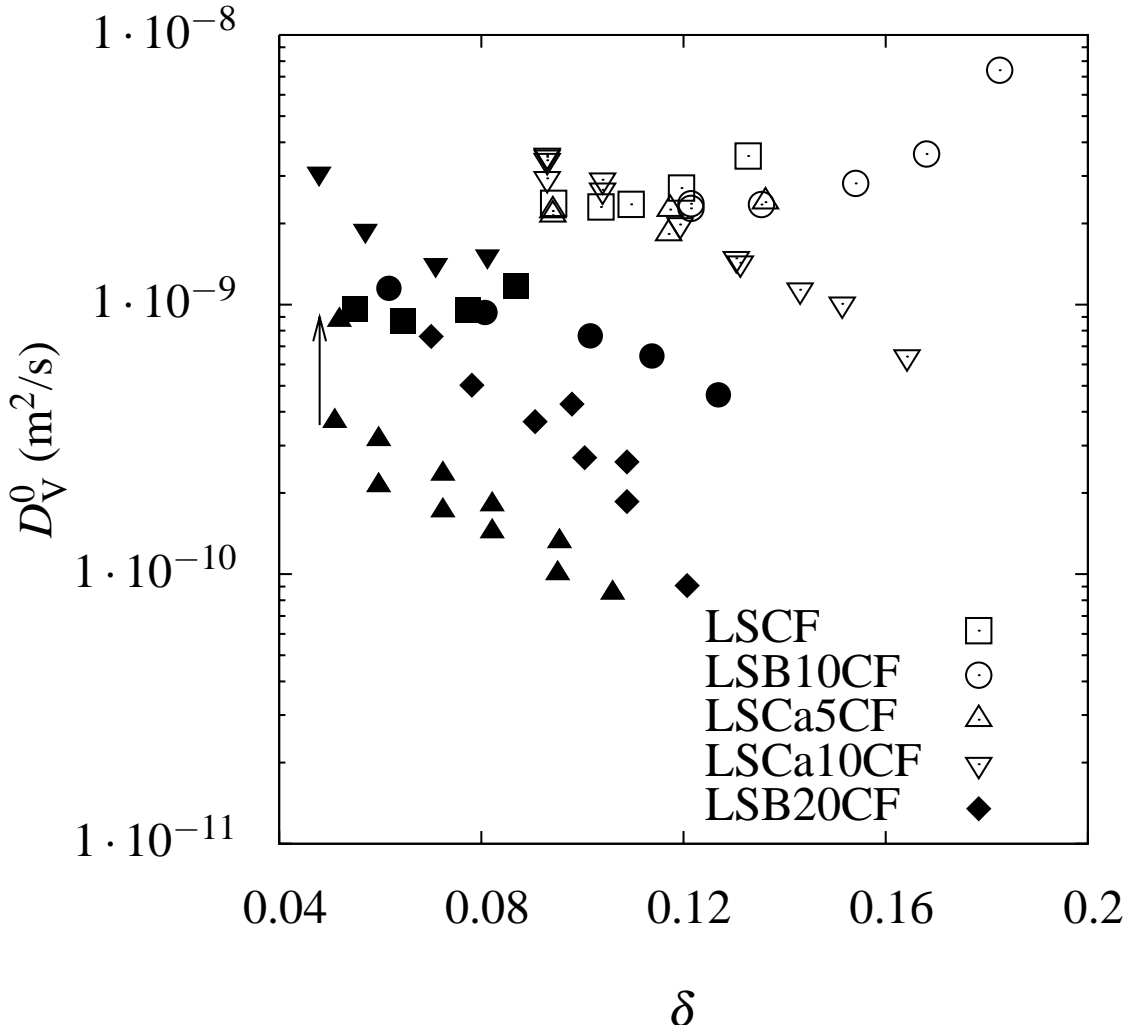


Figure 5.13: D_V^0 as a function of δ at $T = 1273$ K (open symbols) and $T = 1123$ K (filled symbols)

D_V^0 is plotted as a function of δ at $T = 1273$ K (open symbols) and $T = 1123$ K (filled symbols) in Fig. 5.13. The error bars on the individual measurements are smaller than the symbol sizes. The large scatter is attributed to slow changes in the material with a characteristic time of the order of days.

At $T = 1123$ K, we believe that the point at $(\delta = 0.052, D_V^0 = 10^{-9} \text{m}^2/\text{s})$ represents a plausible value of D_V^0 for LSCa5CF. The remaining points of the LSCa5CF material recorded at $T = 1123$ K are underestimated by a factor of 2.5, due to the accidental reduction described in Sec. 5.5.1 and should be moved according to the arrow on the plot. All of the measurements at $T = 1123$ K have decreasing or constant values of D_V^0 , when increasing δ . The absolute value of D_V^0 as a function of δ shows no clear correlation with dopant type or concentration.

At $T = 1273$ K and at low values of δ all the materials have a D_V^0 close to $2 \cdot 10^{-9} \text{m}^2/\text{s}$. Increasing δ values leads to increasing D_V^0 values for LSCF and LSB10CF and reducing D_V^0 values for LSCa5CF and LSCa10CF. There is thus a clear correlation of $\frac{D_V^0}{\delta}$ and the dopant type and amount at $T = 1273$ K.

As mentioned in the introduction, correlations between the ionic conductivity and the crystal strain gauged by 1) the Goldschmidt factor: $t_{\text{Goldschmidt}} = \frac{r_A + r_O}{\sqrt{2}(r_B + r_O)}$ and 2) the difference in B-site radius and an optimum matching radius of 0.64 \AA , 3) the bond energy of the oxide ions, 4) the lattice free volume and 5) the critical radius of the saddle point halfway on the path of an oxide ion jump were expected. Using the data of the unit cell parameter dependence on p_{O_2} and T , we

Table 5.3: Activation energies of the different transport parameters.

Name	Activation energies				
	$E_a^{G_c}$ kJ/mol	$E_a^{r_s}$ kJ/mol	$E_a^{\sigma_o}$ kJ/mol	$E_a^{D_v^0}$ kJ/mol	E_a^δ kJ/mol
LSCF	99	172	94	62	66
LSB10CF	102	139	99	57	55
LSB20CF	195/149	188	195/149	165/120	40
LSCa5CF	119	174	115	76	56
LSCa10CF	78	179	59	13	60

have calculated all these parameters and plotted D_V^0 as a function of them in Appendix C. There is, however, no consistent correlation between D_V^0 and these parameters which can explain the observed data. This suggests that two or more effects are competing when determining D_V^0 .

We propose that the decrease in D_V^0 with increased δ found at $T = 1123$ K is caused by increased vacancy ordering or trapping. At $T = 1273$ K, this effect is overcome by thermal vibrations, and controls D_V^0 to a lesser degree. We further propose that an increase in δ changes some unknown mobility determining structural parameter. This behavior can be shown to apply to the Goldschmidt factor, critical radius, or the matching radius. If LSCF and LSB10CF, due to their large average A-site ion radius, are on one side of the optimum (and thus move closer to the optimum when δ is increased), and the Ca containing materials are on the other side of the optimum (and thus move further away from the optimum when δ is increased) this proposal is consistent with the measured data. The data are, however, insufficient to decisively confirm these proposals.

5.5.3 Parameter importance

As the previous sections have shown, the conductance of a MIEC membrane is dependent on several parameters. The activation energies of the conductance, $E_a^{G_c}$, the surface resistance, $E_a^{r_s}$, the ionic conductivity, $E_a^{\sigma_o}$, the reduced diffusion coefficient, $E_a^{D_v^0}$, and the substoichiometry, E_a^δ , are listed in Table 5.3. All the values are given for measurements in air. There is a clear coupling between the activation energies, $E_a^{\sigma_o} \approx E_a^{G_c}$ which we would expect from bulk controlled materials. The one exception is LSCa10CF, as it, due to its high σ_O is partially limited by the surface resistance. Furthermore $E_a^{\sigma_o} \approx E_a^\delta + E_a^{D_v^0}$ reflecting that $\sigma_O \propto D_V^0 \delta$ as expected from theoretical considerations. With the exceptions of LSB20CF and LSCa10CF we also observe that $E_a^\delta \approx E_a^{D_v^0}$ which leads to the conclusion that *the vacancy concentration and mobility are equally important to the temperature dependence of the ionic conductance*. As $E_a^{r_s} > E_a^\delta + E_a^{D_v^0}$ we can also conclude, that *while the membranes are bulk controlled in air at the measured temperatures, they become surface reaction limited at lower temperatures*.

In Table 5.4, values of several of the measured parameters are shown measured at $T = 1123$ K at $p_{O_2} = 0.21$ atm and $p_{O_2} = 0.016$ atm (in brackets). The parameter f_B in this table is defined as:

$$f_B = \frac{\mu_{O_2}^{\text{upper}} - \mu_{O_2}^{\text{lower}} - 2\Delta\mu_{O_2}}{\mu_{O_2}^{\text{upper}} - \mu_{O_2}^{\text{lower}}} \quad (5.21)$$

i.e., the fraction of the total μ_{O_2} difference across the membrane lost in the bulk (see Fig. 5.2). The lower f_B is, the more important is the surface resistance in determining G_c . As G_c , f_B is not a material parameter, but a parameter specific to a membrane, as a change in geometry can change f_B .

The decrease in f_B shows that the surface resistance, r_s , becomes more important when

Table 5.4: Material parameters at $T = 1123 \text{ K}$. Values not enclosed in brackets were measured at $p_{\text{O}_2} = 0.21 \text{ atm}$. Values enclosed in brackets were measured at $p_{\text{O}_2} = 0.016 \text{ atm}$.

Name	Values at $T = 1123 \text{ K}$ in at $p_{\text{O}_2} = 0.21 (0.016) \text{ atm}$					
	G_c kS/m ²	r_s $\mu\Omega\text{m}^2$	D_V^0 $10^{-10}\text{m}^2/\text{s}$	δ -	σ_{O} S/m	f_B -
LSCF	2.3 (2.1)	23 (65)	9.7 (11.2)	0.041 (0.087)	5.8 (11)	0.89 (0.69)
LSB10CF	2.9 (2.5)	14 (46)	12 (6.4)	0.063 (0.11)	7.7 (7.8)	0.91 (0.77)
LSB20CF	2.7 (1.0)	1.5 (6.7)	5 (1.9)	0.072 (0.11)	3.8 (2.2)	1.00 (0.98)
LSCa5CF	2.2	22	8.5	0.053	4.9	0.92
LSCa10CF	5.1 (2.5)	16 (150)	25 (15)	0.052 (0.087)	14 (13)	0.82 (0.35)

determining G_c if the membrane is in a reduced atmosphere. This is also evident from the much larger r_s in reducing atmospheres. At $p_{\text{O}_2} = 0.21 \text{ atm}$ the membranes are quite close to being independent of r_s , with the exception of LSCa10CF, due to its high σ_{O} . If we extrapolate towards $p_{\text{O}_2} > 0.21 \text{ atm}$ - the working regime of pressurized oxygen separation membranes - the main effect is that both r_s and D_V^0 decreases. This has the most impact on LSCa10CF, as it has most to gain from a decrease in r_s . LSCa10CF is thus the primary candidate for a pressurized oxygen separation membrane among the studied materials.

The ionic conductivity, σ_{O} , is enhanced for LSCF under reducing conditions. From the values of δ and D_V^0 , we see that this enhancement is mainly due to an increase in δ . The other materials also have this increase in δ , but for them, it is offset by a decrease in D_V^0 . Except for LSCF we therefore have that the p_{O_2} -dependence of both D_V^0 and δ is important when determining the p_{O_2} -dependence of σ_{O} . LSCF thus takes a special role at this temperature, but we must remark that at $T = 1273 \text{ K}$, the D_V^0 of both LSCF and LSB10CF are enhanced at reducing conditions.

5.5.4 Large perturbations

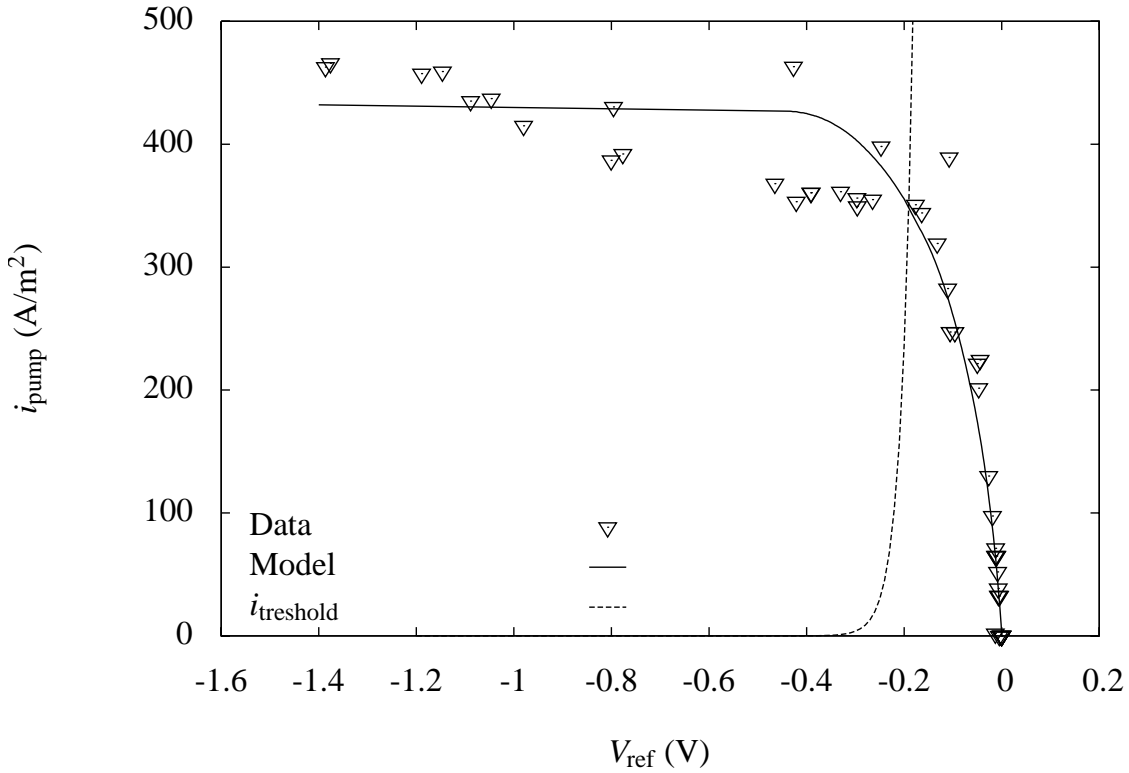


Figure 5.14: Permeation measurement on LSCa10CF with large pumping currents as a function of V_{ref} .

A measurement with LSCa10CF with large i_{pump} was performed. The gas led into the upper compartment was air. The measurement is plotted in Fig. 5.14. We see that when $V_{\text{ref}} < -0.4$ V, corresponding to $p_{\text{O}_2} = 10^{-8}$ atm, the flux levels off. The considerable scatter at high i_{pump} is attributed to the membrane being operated in a regime where the Co^{3+} cations are being reduced to Co^{2+} cations and creating secondary phases (see Chapter 4).

Due to the steady state conditions all oxygen transported through the membrane is also transported across the closed compartment. The transport is governed by Ficks law of diffusion, and a gradient in the molecular oxygen concentration is needed to support it. At $p_{\text{O}_2} > 10^{-5}$ atm this gradient is minute, and the closed compartment can be considered homogenous. When the p_{O_2} in the closed compartment becomes low, however, the gradients becomes significant, and V_{ref} no longer measures the true p_{O_2} in the gas just outside the membrane surface. The $i_{\text{threshold}}$ curve is the calculated maximum current obtainable before gas gradients in the closed compartment become significant:

$$i_{\text{threshold}} = D \frac{\Delta C_{\text{O}_2}}{L_{\text{closed}}} \quad (5.22)$$

where D is the gas diffusion coefficient, C_{O_2} is the concentration of O_2 molecules in the gas, and L_{closed} is the width of the closed compartment (300 μm). The calculation is based on the gas diffusion coefficients of Reid, Prausnitz and Polling [36]. The current is calculated assuming a p_{O_2} at the pump electrodes of 0, and a p_{O_2} just outside the membrane surface equal to that measured by the reference electrodes. When the measured current exceeds that of the i_{max} curve, we conclude that, in order to support the gas transport from the membrane to the pumping electrodes, the p_{O_2} just outside the membrane surface is larger than the p_{O_2} measured by the reference electrodes. In other words, the transport starts to be affected by finite diffusion rate in the gas.

A model calculation of a large permeation current using the data obtained from the measurements at small permeation are also shown in Fig. 5.14. They have been inserted into Eq. 5.6 and Eq. 5.7. The surface resistances have been applied based on the $\mu_{\text{O}_2}^{\text{MIEC}}$ of the respective surfaces - not the μ_{O_2} of the gas just outside the surface. No fitting was applied. Excellent agreement is, not surprisingly, found at low pumping currents. Furthermore the model successfully predicts the levelling off of the flux, as the surface resistance on the low p_{O_2} side increases. When $V_{\text{ref}} < -0.4 \text{ V}$, corresponding to $p_{\text{O}_2} = 10^{-8} \text{ atm}$, the $\mu_{\text{O}_2}^{\text{MIEC}}$ in the low p_{O_2} surface is almost independent of V_{ref} , and have a value equal to that of a gas with $p_{\text{O}_2} \approx 0.003 \text{ atm}$. Applying a lower μ_{O_2} to the gas in the closed compartment does not increase the current, as the low p_{O_2} surface resistance increases fast enough to compensate.

Both gas diffusion limitations and surface resistances predict that the flux should increase with increasing $\Delta\mu_{\text{O}_2}$, but should approach a limiting flux when the p_{O_2} of the closed compartment is less than $p_{\text{O}_2} = 10^{-8} \text{ atm}$. This is indeed observed, but we cannot distinguish which of the two limiting factors is responsible for the maximum flux.

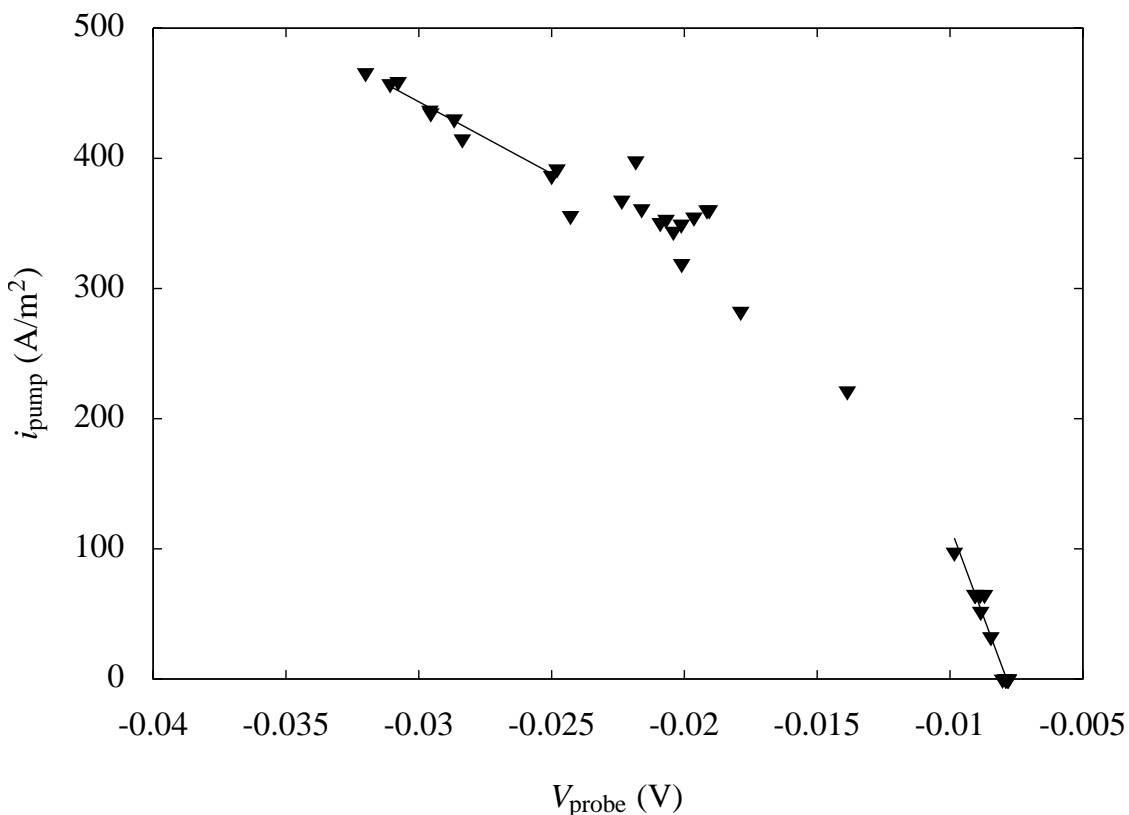


Figure 5.15: Permeation current measurement on *LSCa10CF* with large pumping currents as a function of V_{probe} .

The pumping current as a function of V_{probe} is plotted in Fig. 5.15. Two regimes exist: the low pumping current regime where the steep curve gradient indicates a low r_s and the high pumping current regime, where the less steep curve gradient indicates a higher r_s . There is a gradual change of the curvature between the two regimes indicating a change of r_s by a factor of 4, reasonably consistent with the measurements in Fig. 5.6 if the p_{O_2} of the surface and not the gas is assumed to decide r_s ($V_{\text{probe}} = -0.04 \text{ V}$ corresponds to a $\log p_{\text{O}_2}$ of -1.4). Note that the absolute values of V_{probe} are much smaller than the absolute values of V_{ref} shown in Fig. 5.14. This is consistent with the assumption that most of the driving force is spent by gas diffusion in the closed compartment or by the surface resistance on the membrane surface in the closed compartment.

5.5.5 Evaluation of measurements

The slow relaxation phenomena, as well as the vulnerability to reducing conditions, requires careful consideration of the history of the sample, when evaluating the measurements. In this study we have removed numerous measurements, which were not reproducible. There seems to be some effect of the history of the sample, and we believe that reducing the ambient p_{O_2} triggers slow relaxations in the membrane. These relaxations have a time constant on the order of a week or more. A borderline example of this is found in Fig. 5.9 for LSB20CF, where a considerable hysteresis is found. Changes in temperature do not seem to trigger hysteresis. While this removal will bias the results, the remaining data is considered far more trustworthy.

It is noteworthy that the only measurements in this study for which the data scatter originates from precision limits of the measurement method is the r_s measurements of LSCa10CF at $T=1273$ K and the r_s measurements of LSB20CF. Any other scatter is much larger than the error bars of the individual measurements and originate from the slow relaxation phenomena in the membranes.

It is also noteworthy that, although we have tested several LSCF membranes for reference, the measured values of r_s and σ_{O} of the initial test measurement at 1273 K and $p_{\text{O}_2} = 0.21$ atm is within 5%. The discrepancy of measurements between individual, but similar, membranes are thus far smaller than some of the discrepancies observed between measurements on the same membrane, before and after a gentle reduction.

The reason for these slow relaxations can be many. They do, however, seem to be localized to the bulk, as the measurements of r_s do not show any significant hysteresis. Structural changes, cation diffusion and impurity segregation are possible explanations.

The cone and pump method is a very precise method, but also a cumbersome and time demanding method. The many relaxation phenomena present in the materials, to some degree, removes the advantage of the precision when discussing the bulk transport in the materials. As a tool for analyzing the surface exchange processes, where relaxations are apparently much faster, the precision of the electrolyte probe makes the cone and probe method attractive.

5.5.6 Comparison with literature

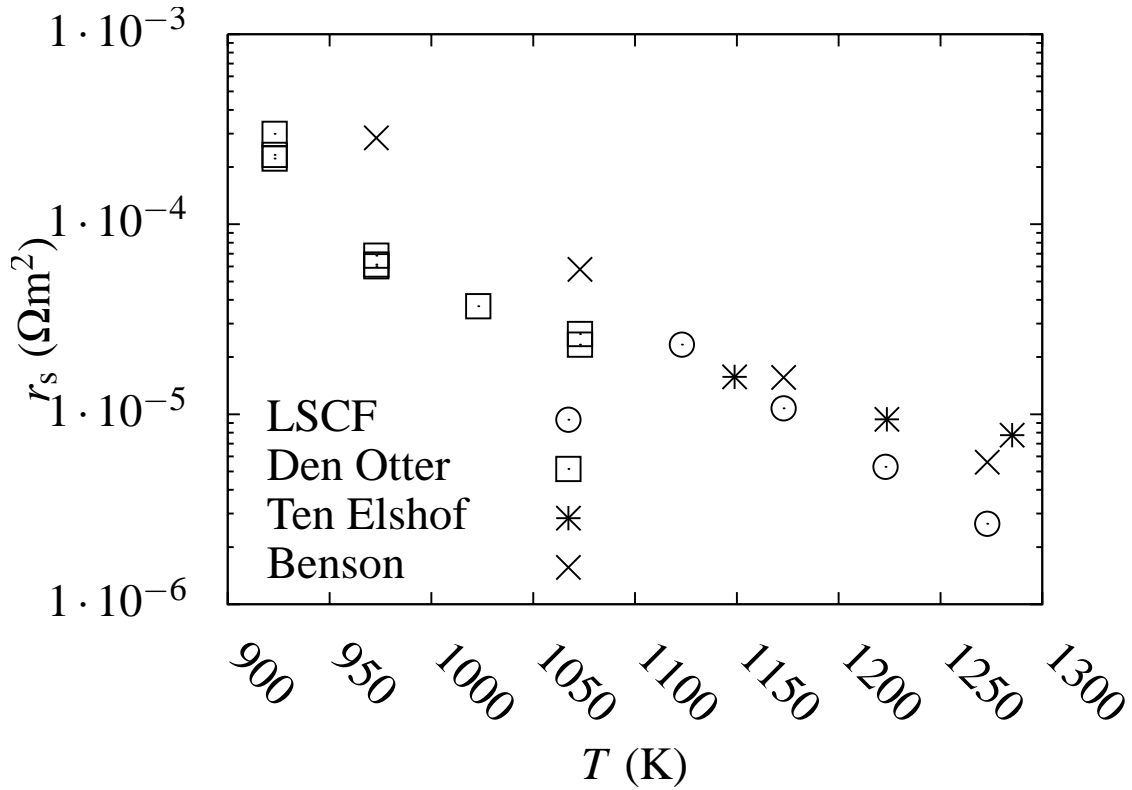


Figure 5.16: Comparison of r_s with values reported in literature. The values of ten Elshof *et al.* [16], Den Otter *et al.* [39] were measured using conductivity relaxation while those of Benson [17] were obtained from an isotopic exchange experiment.

The values of r_s found in this study are compared to values reported in the literature in Fig. 5.16. The values of ten Elshof *et al.* [16] and Den Otter *et al.* [39] were measured using conductivity relaxation while those of Benson [17] were obtained from an isotopic exchange experiment. The measurements of Den Otter *et al.* and ten Elshof *et al.* do not take the Δp_{O_2} calculated in Eq. 5.14 into account, thus ignoring the mixing of the flow gas and the oxygen flux out of their sample. This explains the discrepancy between their results and those of this study. There is thus a reasonably good agreement between the values of this study and those of the literature.

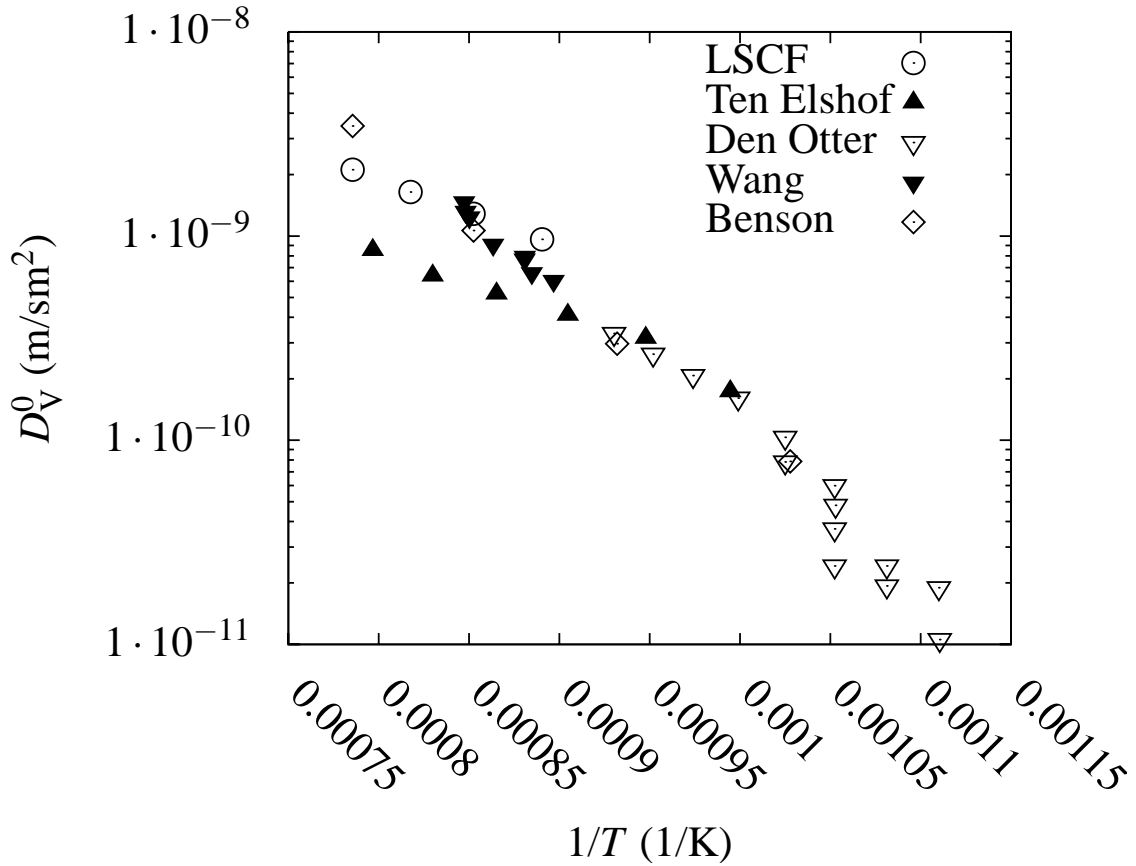


Figure 5.17: Comparison of D_V^0 with values reported in literature and converted to D_V^0 . The values of ten Elshof *et al.* [16], Den Otter *et al.* [39] and Wang *et al.* [43] were measured using conductivity relaxation while those of Benson *et al.* [17] were obtained from an isotopic exchange experiment.

The values of D_V^0 found in this study are compared to values reported in the literature in Figure 5.17. The values of ten Elshof *et al.* [16], Den Otter *et al.* [39] and Wang *et al.* [43] were measured using conductivity relaxation while those of Benson *et al.* [17] were obtained from an isotopic exchange experiment. There is some variation in the activation energies of D_V^0 , but there is reasonable agreement between the absolute values of D_V^0 .

Tsai *et al.* [48] and Stevenson *et al.* [22] measured permeation rates for perovskites with compositions close to the compositions of this study. From this, they calculated an ionic conductivity, σ_O , at $T = 1123$ K and an activation energy, $E_A^{\sigma_O}$, as tabulated in Table 5.5. The materials investigated by Tsai *et al.* and Stevenson *et al.* are $\text{La}_{0.1-i}\text{M}_{0.1-j}\text{Co}_{0.2}\text{Fe}_{0.8}\text{O}_{3-\delta}$ and are labelled as LMCFij28. Tsai *et al.* measured the permeation between air and He atmospheres. Their low values of σ_O compared to the ones of this study can probably be attributed to the very slow surface exchange in the oxygen starved He atmosphere. If that is the case, then the relatively high σ_O of LBCF4628 is really a sign of a comparably fast r_s on the He side of the membrane. This apparent effect of a high Ba content is consistent with the low r_s of LSB20CF measured in this study. Stevenson *et al.* measured the permeation between air and N_2 atmospheres. Contrary to the results of Tsai *et al.*, Stevenson *et al.* measured the highest ionic conductivity in the Sr containing samples. In conclusion, neither this study nor the literature reveals a simple relation between A-site composition and permeability.

Table 5.5: Comparison of values measured in this study with values from the literature.

	Material	σ_{O} (S/m)	$E_{\text{A}}^{\sigma_{\text{O}}}$ (kJ/mol)
This study	LSB20CF	3.6	150
	LSB10CF	7.9	100
	LSCF	5.9	94
	LSCa5CF	4.8	114
	LSCa10CF	13	68
Tsai <i>et al.</i> [48]	LBCF4628	7.9	72
	LCCF4628	1.3	95
	LSCF4628	0.75	105
Stevenson <i>et al.</i> [22]	LBCF6428	0.5	158
	LBCF4628	2.2	87
	LSCF6428	13	125
	LSCF4628	26	92
	LCCF4628	2.2	68

5.6 Conclusions

In this study, single phase perovskite MIEC membranes of the composition $(\text{La}_{0.6}\text{Sr}_{0.4-x}\text{M}_x)_{0.99}\text{Co}_{0.2}\text{Fe}_{0.8}\text{O}_{3-\delta}$, $M = \text{Sr}, \text{Ca}$ ($x = 0.05, 0.1$), Ba ($x = 0.1, 0.2$) were investigated using measurements of oxygen pump controlled permeation fluxes and a surface sensitive electrolyte probe.

The surface resistance, r_s , had an Arrhenius behavior with an activation energy close to 180 kJ/mol for all materials except LSBa10CF. All the materials experienced an increase in r_s as the p_{O_2} was lowered. The conductance, G_c , of the materials showed that the overall permeability had an Arrhenius behavior with an activation energy close to 110 kJ/mol for all materials except G_c of LSBa20CF who had an activation energy of more than 149 kJ/mol, and G_c of LSCa10CF which had an activation energy of 78 kJ/mol.

It was found that the reduced diffusion coefficient, D_V^0 and δ were equally important to the p_{O_2} and T dependence of the ionic conductance σ_{O} of the membranes. It was also found that the membranes were limited by bulk transport at high temperature and p_{O_2} , while they were limited by the surface resistance at low temperature and p_{O_2} .

In air, LSCa10CF had the highest permeability coupled with a low activation energy. In air, LSB20CF had the lowest r_s , an order of magnitude less than the other materials. For $T > 1248$ K, there was a reduction in the r_s of LSCa10CF to the level of r_s of LSB20CF. The two abnormally small r_s were proposed to originate from stress in the perovskite structure.

The values recorded in the linear regime could be used to model a measurement with a large i_{pump} , with excellent agreement. A maximum pumping current was found.

A consistent relation between the transport properties and any structural parameter could not be proven.

Chapter 6

Defect chemistry of $(\text{Ba}_{0.5}\text{Sr}_{0.5})_{0.99}\text{Co}_{0.8}\text{Fe}_{0.2}\text{O}_{3-\delta}$

Abstract

The defect chemistry of $(\text{Ba}_{0.5}\text{Sr}_{0.5})_{0.99}\text{Co}_{0.8}\text{Fe}_{0.2}\text{O}_{3-\delta}$ was investigated using coulometric titration (CT), thermogravimetry (TG) and X-ray Absorption Near Edge Structure (XANES). Values of the oxygen substoichiometry, δ , of more than 0.5 were measured with CT and TG. The dependence of δ on the temperature and oxygen partial pressure was discussed and compared with literature data. XANES measurements were performed on $(\text{Ba}_{0.5}\text{Sr}_{0.5})_{0.99}\text{Co}_{0.8}\text{Fe}_{0.2}\text{O}_{3-\delta}$ powder compacts. Co and Fe sp-transitions were investigated. Line broadening of the Co sp-transition was observed when heating the sample in an He atmosphere. No line broadening was observed for the Fe sp-transition. When heating in an air atmosphere, neither the Co nor the Fe sp-transition showed any line broadening.

6.1 Introduction

In 2004 Shao and Haile [61] reported extraordinary performance of solid oxide fuel cells (SOFCs) with the perovskite cathode material $\text{Ba}_{0.5}\text{Sr}_{0.5}\text{Co}_{0.8}\text{Fe}_{0.2}\text{O}_{3-\delta}$ (BSCF). The electrode area specific resistances reported at temperatures lower than 873 K were considered a major breakthrough for SOFCs working in the intermediate temperature range (673 K - 873 K). Most perovskites will adopt the brownmillerite structure when δ exceeds 0.5. In 2006, McIntosh *et al.* [62, 63] showed that BSCF retained its perovskite structure even when δ exceeds 0.5. In 2007 Chen *et al.* [64, 65] made permeation experiments where the ionic conductivity was more than twice as big as the ionic conductivity of $(\text{La}_{0.6}\text{Sr}_{0.4})_{0.99}\text{Co}_{0.2}\text{Fe}_{0.8}\text{O}_{3-\delta}$ (LSCF) data presented in Chapter 2 of this thesis. In this study we present new measurements made with coulometric titration (CT) and thermogravimetry (TG) and compare them with the literature data. Furthermore, we study BSCF using X-ray Absorption Near Edge Structure (XANES) at low temperatures to establish which cation is reduced during heating.

6.2 Experimental

6.2.1 Sample preparation

BSCF powder was prepared using the glycine nitrate combustion process [33]. The powder was calcined at 1100°C for 12 h, and ball milled using ZrO_2 balls, each weighing 3 g in a 500 ml polyethylene container ($\varnothing = 5$ cm) with ethanol for 24 h at 200 RPM.

6.2.2 Thermogravimetry and coulometric titration

The experimental procedures of the coulometric titration (CT) and thermogravimetric (TG) measurements in air are identical to those described in Chapter 4. They are summarized below.

A known amount of BSCF powder was placed in a closed yttria stabilized zirconia (YSZ) electrochemical cell placed inside a furnace. The chemical potential of oxygen in the cup could be gauged by the voltage, V_{ref} , measured between a pair of porous platinum reference electrodes placed on the inside and outside of the cell. The oxygen content could be varied by pumping current between a pair of porous platinum pumping electrodes placed on the inside and outside of the cell. The cell was sealed with glass paste, and electrical contacts to a Keithley 2400 multimeter and an Instek GPS3030DD power supply were made with gold and platinum wires.

TG measurements were performed with a SEIKO differential TGA, with an adjustable gas flow. Gas with $p_{\text{O}_2} < 0.21$ atm was produced by mixing N_2 and air gas. The reference weight was a mixture of gold and alumina powder, adjusted to give the same powder density and weight as the BSCF powder. The p_{O_2} was measured using an in-house fabricated YSZ p_{O_2} monitor with platinum electrodes operated at 1273 K.

6.2.3 XANES

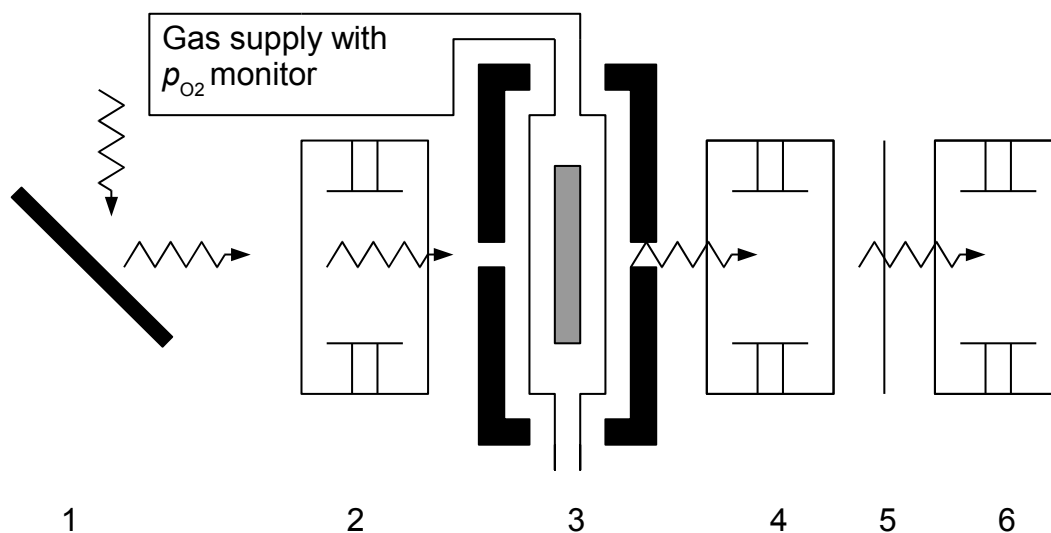


Figure 6.1: The XANES setup. (1) Motor controlled diffraction crystal. (2,4,6) Chambers containing thin Ar gas and capacitor plates. (3) Oven containing the sample. The oven has a gas supply with a p_{O_2} monitor. (5) Reference foil.

The XANES (X-ray Absorption Near Edge Structure) experiment consists of three chambers arranged along a synchrotron beamline as shown in Fig. 6.1. Each of the chambers contains thin Ar gas. In the beamline between the first and second chamber an oven with a maximum temperature of 773 K is placed. The oven is gas tight and gas (air or helium) can be fed to

it in these experiments at 50 ml/min. The oxygen partial pressure is measured by a zirconia p_{O_2} monitor operating at 1273 K downstream of the oven. Using air, the partial pressure was 0.21 atm, while using helium yielded an oxygen partial pressure of $5.2 \cdot 10^{-4}$ atm. In the oven, a thin disc of sample, pressed from the powder to be analyzed mixed with alumina powder, resides in the center of the beamline. In the beamline between the second and third chamber, a reference foil consisting of the target element (in this case Co) is placed. Diffracted monochromatic x-rays are directed through the chambers. Whenever the beam passes through a chamber it will ionize the molecules of the thin gas in the chamber. The resulting charged particles are then captured by capacitor plates, and the current between the plates is measured by a Keithley amperometer. When comparing the current intensities between the two chambers, the absorption intensity I of the intermittent matter can be quantified as $I = \ln \frac{i_0}{i_1}$. Scanning the photon energy of the X-rays can therefore yield an absorption spectrum of a sample. The energies chosen for this experiment are the resonant sp-transition energy of Co. When Co is in a crystal, this transition energy is perturbed. The perturbation strength depends on the oxidation state of Co. The absorption spectrum thus yields information about the chemical conditions of Co in the sample.

6.3 Theory

6.3.1 Coulometric Titration (CT)

The theory used to treat the data presented in this Chapter is identical to that described in Chapter 4.

The chemical potential of a MIEC, $\mu_{\text{O}_2}^{\text{MIEC}}$, can be written down in terms of the partial molar entropy S_{ox} and partial molar enthalpy H_{ox} of the total oxidation reaction.

$$\mu_{\text{O}_2}^{\text{MIEC}} = H_{\text{ox}} - TS_{\text{ox}} \quad (6.1)$$

Assuming that the values of H_{ox} and S_{ox} are invariant with temperature, we see that there are a temperature dependence of $\mu_{\text{O}_2}^{\text{MIEC}}$. In coulometric titration, the temperature can be varied while keeping a constant amount of oxygen inside the closed electrochemical cell containing the sample. The $\mu_{\text{O}_2}^{\text{MIEC}}$ changes with the temperature, and can be recorded as it equilibrates with the chemical potential of the gas also present in the cup, which is measurable using a set of reference electrodes.

The p_{O_2} can be measured by the voltage of the reference electrodes:

$$p_{\text{O}_2} = p'_{\text{O}_2} \exp\left(\frac{4FV_{\text{ref}}}{RT}\right) \quad (6.2)$$

where p'_{O_2} is the p_{O_2} of the atmosphere outside the cup, R is the gas constant and T the temperature.

The H_{ox} and S_{ox} values are furthermore dependent on the δ value of the MIEC. In coulometric titration, oxygen can be electrochemically pumped in and out of the closed electrochemical cell. The correspondence between the pumped charge, Q , and the change in oxygen stoichiometry, $\Delta\delta$, can be written:

$$\Delta\delta = \frac{M}{2Fm}Q \quad (6.3)$$

where M is the molar mass of the powder, m is the mass of the powder, and F is Faradays constant.

In conclusion CT allows us to map the δ - p_{O_2} relationship of a MIEC in a number of different temperatures and p_{O_2} -ranges.

6.4 Results and Discussion

6.4.1 Coulometric Titration (CT)

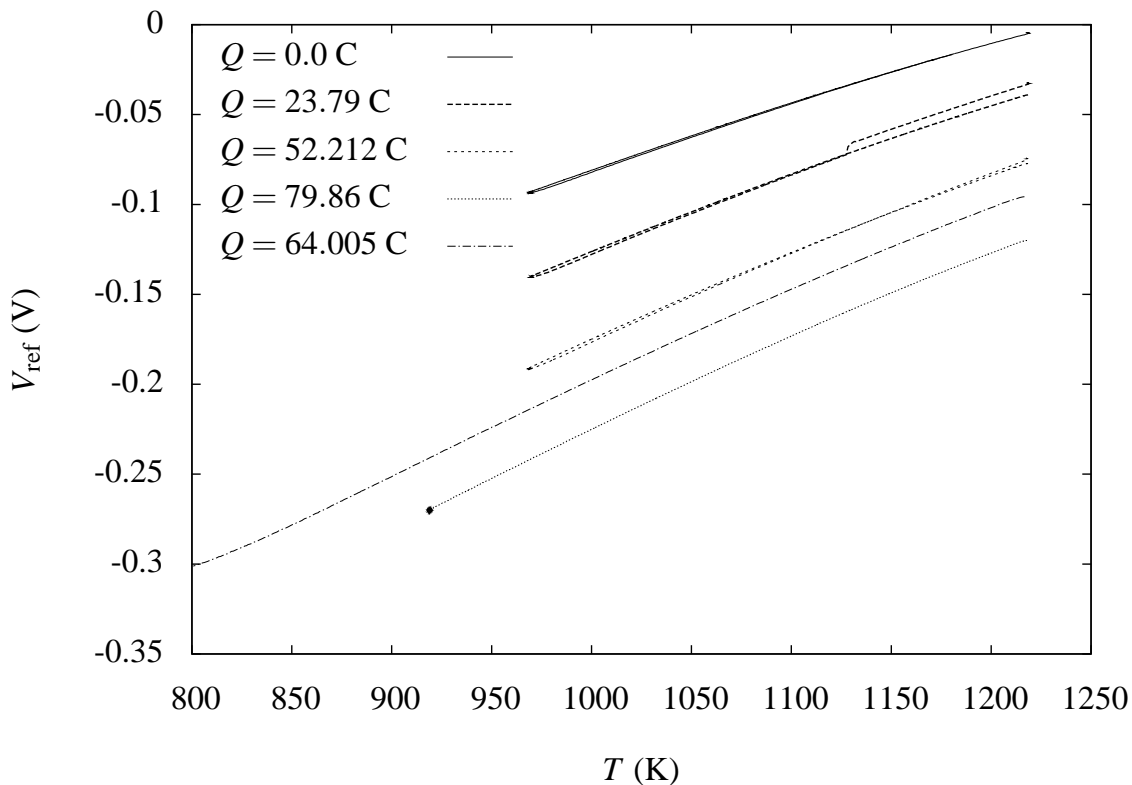


Figure 6.2: V_{ref} recorded as a function of T .

V_{ref} recorded as a function of T is shown in Fig. 6.2. No hysteresis is seen except for the temperature cycle of $Q = 23.79 \text{ C}$, which experiences a small leak at the end of the cycle. At the end of the cycle of $Q = 79.86 \text{ C}$, the system was kept at constant T for 16 h. No leak was detectable.

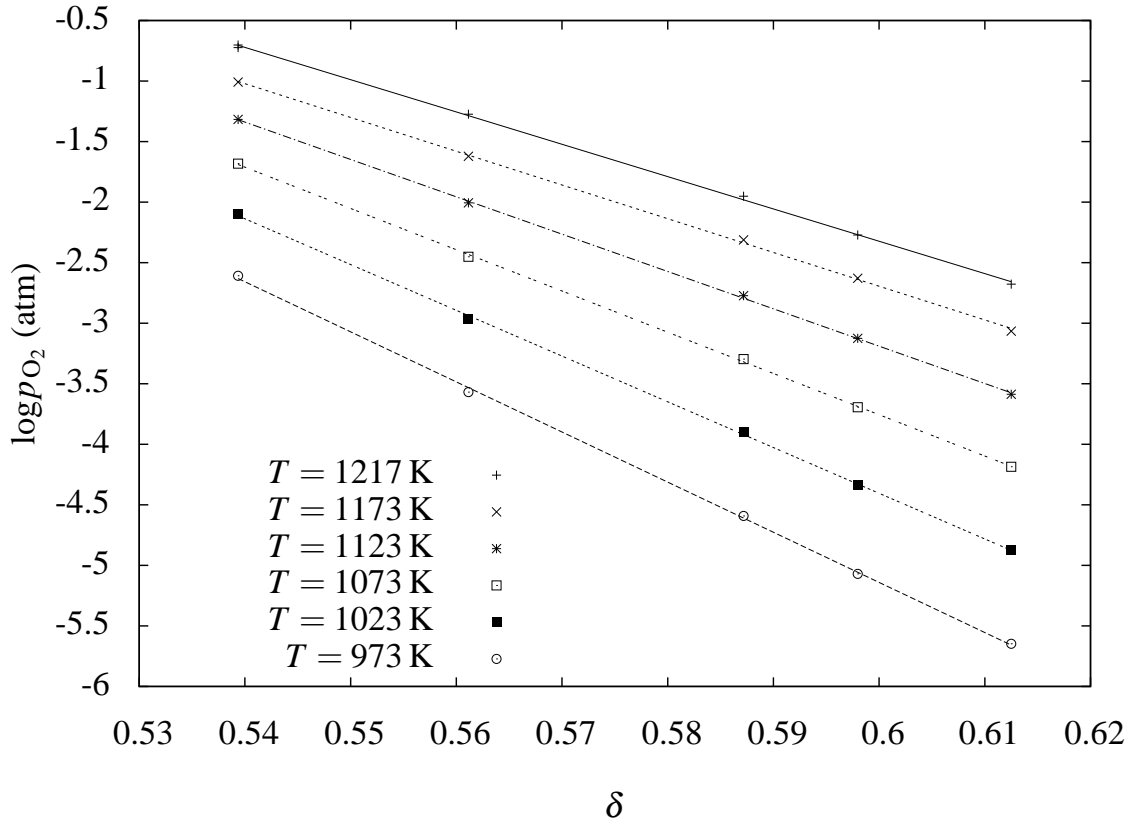


Figure 6.3: $\log p_{\text{O}_2}$ as a function of δ

The absolute value of δ is calculated as $\delta = \delta_0 + \Delta\delta$, where δ_0 is the value measured using TG at $T = 1217 \text{ K}$. The data of Fig 6.2 is replotted with $\log p_{\text{O}_2}$ as a function of δ in Fig. 6.3. The thermodynamic factor, $\gamma = \frac{1}{2} \frac{d \ln p_{\text{O}_2}}{d \ln C_{\text{O}}^{\text{MIEC}}}$, has a strong temperature dependence compared to the LSMFC materials (see Chapter 4). The low deviation of the data from the linear fits show that no δ dependence of γ is observed in the measured interval.

6.4.2 Thermogravimetry (TG)

The sample was heated to $T = 1218 \text{ K}$ in Air. As is the case with the LSMFC materials investigated in Chapter 4, a change of atmosphere to 9% $\text{H}_2 + 91\% \text{N}_2$, and heating to 1573 K is assumed to reduce the sample to Fe, Co, BaO and SrO. From the weight difference, δ at 1218 K, was calculated to be 0.53(2).

Post reduction X-ray diffraction analysis showed a quantity of hydrates and oxides as exposure to ambient atmosphere quickly oxidizes and moisten the powders. Extra sample mass from hydrates and oxides result in an overestimation of δ . We, however, believe that the hydration happens after the sample is cooled, and that the sample is completely reduced to Fe, Co, BaO and SrO at 1573 K. Further reduction of BaO or SrO to metallic Ba or Sr is not considered realistic.

With a new sample in the TG setup, the sample was heated to 1273 K and annealed. It was then cooled to 900 K, and the atmosphere was changed using different mixtures of N_2 and air. This was repeated for 1001 K, 1098 K, 1195 K, and 1288 K.

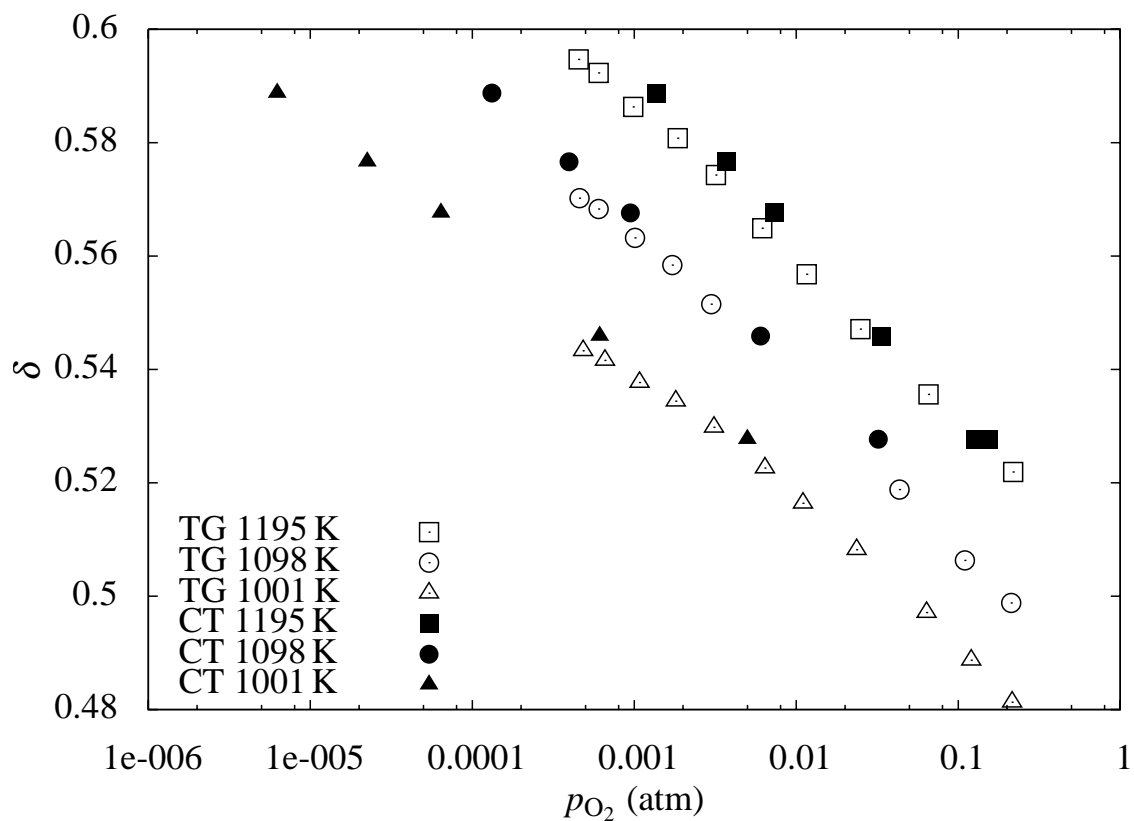


Figure 6.4: δ calculated from TG data together with CT data.

The δ values calculated from thermogravimetric data are compared with interpolated CT data in Fig. 6.4. There is good agreement between CT data and TG data, both regarding the T dependence and the p_{O_2} dependence of δ .

6.4.3 Comparison with literature

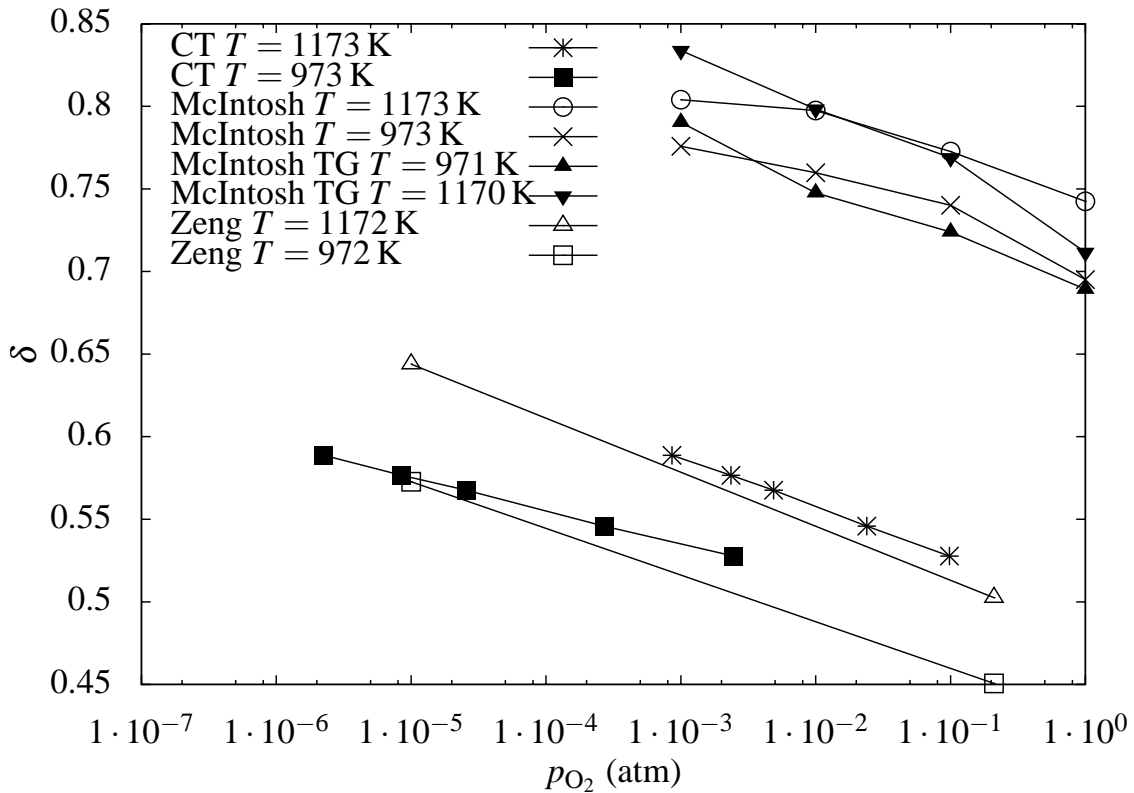


Figure 6.5: The measured stoichiometry data compared with literature data. CT are the values of this study, McIntosh are values from McIntosh *et al.* [62, 63] and Zeng are results from Zeng *et al.* [65]

The measured stoichiometry data are compared with literature data in Fig. 6.5.

Zeng *et al.* [65] measured the absolute stoichiometry at room temperature using iodometric titration. TG measurements were done in air and N_2 (we estimate the p_{O_2} of the N_2 gas to be 10^{-5} atm).

The results of Zeng *et al.* agree well with the results of this study. The absolute values of δ of the two experiments are almost identical, and they are obtained using two very different measurement methods. The p_{O_2} dependence of δ agrees well, considering the uncertainty of the values of Zeng *et al.* where we have basically guessed the p_{O_2} of the measurements in N_2 , and where the gradient is calculated from two separate TG runs with considerable scatter.

McIntosh *et al.* [62, 63] measured the absolute stoichiometry of BSCF using the same approach as in this study (reduction in 10% H_2 + 90% N_2 albeit at $T=1273$ K). δ values were obtained using neutron diffraction, and TG. McIntosh reported that the perovskite structure remained stable, even at δ values approaching 0.8; this is equivalent to more than one out of four oxide ion sites being vacant.

$\gamma = \frac{\partial \ln p_{\text{O}_2}^{\text{eq, gas}}}{2 \partial \ln C_{\text{O}}^{\text{MIEC}}}$ of the CT measurements of this study agrees well with the TG values of McIntosh *et al.*. The neutron diffraction determined values of McIntosh *et al.*, however, show a curvature in γ not seen in the TG or CT measurements of the three groups.

McIntosh *et al.* measures higher absolute values of δ than in this study, despite that the absolute value is established using a similar method as in this study. If the A-site substoichiometry of the BSCF of this study, resulted in the creation of 0.01 Co_2O_3 this meant that δ of this study was overestimated by 0.015. Neither this, nor a possible incomplete reduction can thus account for the discrepancy which suggest an underestimation of the δ reported in this study.

Despite the scatter of the results of the different groups, McIntosh *et al.* have established that BSCF, remarkably, retains its perovskite structure, despite that Zeng *et al.*, McIntosh *et al.* and this study all report oxygen stoichiometries lower than 2.5, where one would expect that a phase transition to the brownmillerite structure occurs.

6.4.4 XANES

Figure 6.6 shows the $I = \ln \frac{i_0}{i_1}$ spectrum of a $(\text{Ba}_{0.5}\text{Sr}_{0.5})_{0.99}\text{Co}_{0.8}\text{Fe}_{0.2}\text{O}_{3-\delta}$ sample. In order to exploit this spectrum it must first be calibrated and normalized.

As there is a certain amount of drift in the motors controlling the monochromatizer, they need to be calibrated during each run. The calibration is performed using the absorption spectrum of the reference foil. As the sp-transition in the foil is constant between each measurement, it can be used to calibrate the energy. The calibration energy is defined as the steepest point in the main step. This is found by finding the maximum value of the derivative of the intensity. This is done, as can be seen in Figure 6.7, using a polynomial fit due to the large noise levels.

In addition to the resonant Co absorptions, there are other contributions to the absorption spectrum. These contributions are dependent on the photon energy. Furthermore, the intensity of the beam decreases with time. To extract the contribution from the sp transition, the other components are considered a linear function of the photon energy. They are estimated by fitting to first degree polynomials the spectrum below and above the resonant energy. Furthermore, for convenience, the spectrum is normalized by defining the unit of absorption as the energy difference between the two polynomials. The converted spectrum can be seen in Figure 6.8.

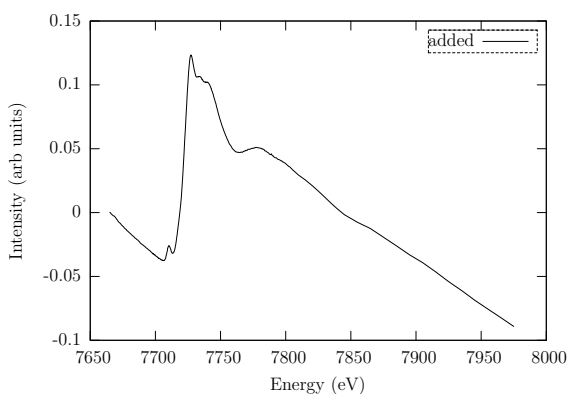


Figure 6.6: XANES spectrum of the BSCF sample.

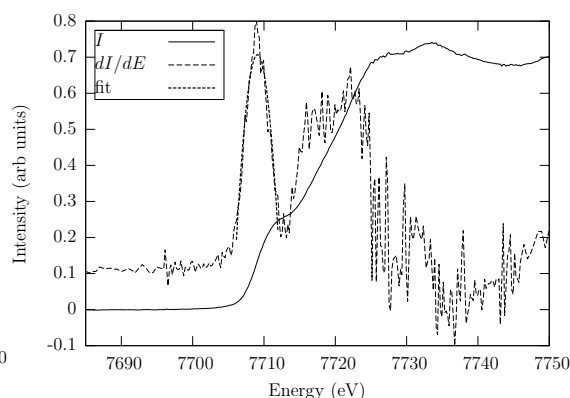


Figure 6.7: XANES of the reference Co foil, together with the first energy derivative of the signal

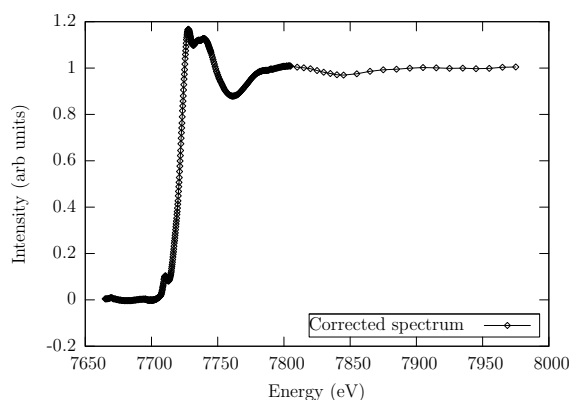


Figure 6.8: The background corrected spectrum.

The calibrated and normalized spectrum is then analyzed. Two positions are found:

- The edge position E_{edge} . This position is defined, as in the reference foil spectrum, as the point of maximum slope on the edge. A second degree polynomial fit to the first derivative is used to find the position.
- The energy at maximum absorbance E_{max} . The point is found by fitting a Gaussian to the area around the maximum.

In figure 6.9 the energy at maximum absorbance E_{max} is shown during a temperature run. The ramp when going up in temperature is 2 K/min, while the ramp going down in temperature is 6 K/min for the air sample and 3 K/min for the sample in He. No difference in E_{max} is seen apart from the scatter.

In Figure 6.10 the quantity $E_{\text{max}} - E_{\text{edge}}$ is plotted. This is a measure of the linewidth of the resonant absorption. A broad linewidth signifies that a larger number of transitions are possible. In this case it is interpreted as the existence of ions in several different oxidation states. As can be seen, the sample in air is rather unaffected by a temperature increase. This is contrary to the sample in helium which shows a significant increase in linewidth at higher temperatures. This indicates a change of the oxidation number of a fraction of the Co ions in the sample, consistent with the sample expelling oxygen and creating charged vacancies. As E_{max} is fixed, this means that E_{edge} decreases when the temperature rises, reflecting a reduction of Co^{3+} . The hysteresis is expected as the surface exchange and diffusion coefficient of oxygen in the sample should be quite low at these temperatures.

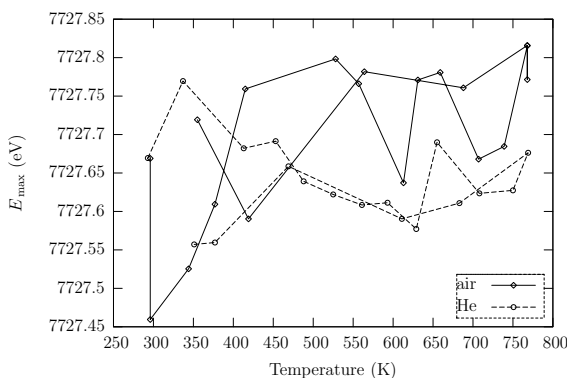


Figure 6.9: Position of maximum peak in spectra

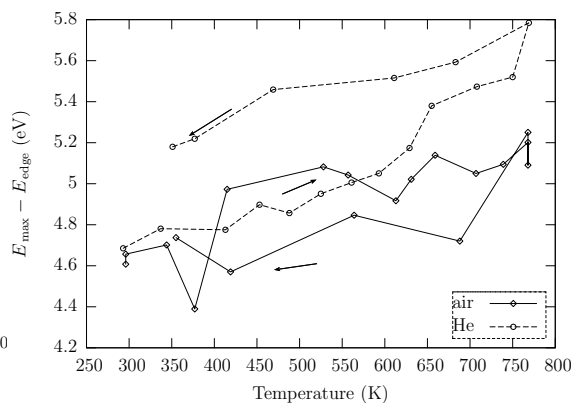


Figure 6.10: Difference in position between maximum peak and edge in spectra

The Fe spectra are harder to fit, but no significant change is seen (peak and max energies differ by less than 0.3 eV between RT and 500°C - well within the confidence interval).

6.5 Conclusion

The defect chemistry of $(\text{Ba}_{0.5}\text{Sr}_{0.5})_{0.99}\text{Co}_{0.8}\text{Fe}_{0.2}\text{O}_{3-\delta}$ was investigated using coulometric titration (CT) and thermogravimetry (TG). Values of δ from CT and TG were in good agreement with each other and with the results of Zeng *et al.* [65]. Values of the oxygen substoichiometry, δ of more than 0.5 were measured, under conditions where McIntosh *et al.* [62, 63] reports a perovskite structure. Measurements of the thermodynamic factor, γ , were also in agreement with TG values reported by McIntosh *et al.*

XANES measurements showed a significant line broadening of the sp-transition energy of a sample of $(\text{Ba}_{0.5}\text{Sr}_{0.5})_{0.99}\text{Co}_{0.8}\text{Fe}_{0.2}\text{O}_{3-\delta}$, when the sample is exposed to a reducing gas and

heated. If the sample is heated in air, no effect is seen. No line broadening was observed for the Fe sp-transition.

Chapter 7

Assesment of doped Ceria as electrolyte

Abstract

A model describing the performance of a fuel cell based on 10 mole% gadolinia doped ceria, $\text{Ce}_{0.9}\text{Gd}_{0.1}\text{O}_{1.95-x}$ (CG10), has been formulated. The total electrical conductivity of CG10 was measured under strongly reducing conditions in the temperature range of 753 K to 948 K. Oxygen permeation experiments were carried out to measure the leak current through a ceria electrolyte. The results of the measurements are compared with predictions of the formulated model. Furthermore, the response of a fuel cell to changing operating conditions such as external load, temperature, electrode polarization resistances and defect chemistry is investigated using the model. It is found that the maximum achievable efficiency of a CG10 based fuel cell is increased when, a) the temperature is decreased, when b) the thickness is increased, or when c) the cathode polarization resistance is decreased. In certain circumstances the efficiency can also be increased by an increase of the anode polarization resistance. Finally, the efficiency is reduced if the vacancy formation enthalpy is decreased to the level of fine-grained CG10. The performance of a CG10 based fuel cell is evaluated by comparing it with a state of the art zirconia based fuel cell. At 873 K, the efficiency of a fuel cell with a 10 μm CG10 electrolyte was limited to 0.74. The power output of the CG10 cell at this efficiency is, however, four times larger than the zirconia based cell at the same efficiency. This is due to the much lower cathode polarization resistance of $(\text{La}_{0.6}\text{Sr}_{0.4})_z\text{Co}_{0.2}\text{Fe}_{0.8}\text{O}_{3-\delta}$ -CG10 (LSCF-CG10) cathodes on CG10 compared to the $(\text{La}_{0.75}\text{Sr}_{0.25})_{0.95}\text{MnO}_3$ (LSM) cathodes on stabilized zirconia.

7.1 Introduction

Doped ceria $\text{Ce}_{1-y}\text{Re}_y\text{O}_{2-y/2-x}$, $\text{Re}=\text{Gd,Sm}$, $y<0.4$, is a well known class of fast oxide ion conductors. Despite being an electronic conductor when exposed to reducing conditions and high temperatures [66], doped ceria has attracted renewed attention as an electrolyte in solid oxide fuel cells (SOFCs). Doped ceria has advantages over conventional zirconia oxide based electrolytes in several areas such as higher ionic conduction at low temperature [67] and better chemical compatibility with new high performance cathode materials such as $\text{La}_x\text{Sr}_{1-x}\text{Co}_y\text{Fe}_{1-y}\text{O}_{3-\delta}$ [68–70]. The degree to which doped ceria is a mixed ionic and electronic conductor (MIEC) varies with dopant level, temperature and oxide activity. High leak current densities may be deduced from reports on SOFCs with a ceria based electrolyte [71–73], in which OCV values below 900 mV were observed at temperatures as low as 725 K using 97% H_2 +3% H_2O fuel gas

mixtures. Recently, however, ceria based cells with high performance have been demonstrated [74].

The ionic transport through an imperfect electrolyte such as CG10 depends on several factors many of which are interdependent. For instance, the vacancy concentration profile across the electrolyte affects the leak current which affects the electrode polarization, which again affects the vacancy concentration profile. These intimate relations complicate both the interpretation of measured data and the identification of key areas in which to focus research [75]. Modelling of the ionic and electronic transport of the MIEC can provide better understanding of the phenomena involved in the transport. The literature contains several model studies of MIEC electrolytes and fuel cells [2, 76–80].

This study considers a model of a cell with a $\text{Ce}_{0.9}\text{Gd}_{0.1}\text{O}_{1.95-x}$ (CG10) electrolyte. To validate this model, measurements of the total conductivity of CG10 under strongly reducing conditions and of the oxygen leakage through a CG10 disc are also presented. Validation is performed by comparison of the model results with measurement data reported in the literature. Individual model parameters are varied one at a time from a common reference state, and the impact on cell performance is evaluated. The parameters varied are; the external load resistor, the temperature, the oxide ion vacancy formation enthalpy, the electrode polarization resistances and the thickness of the electrolyte. Finally, a comparison with a state of the art doped zirconia electrolyte based cell is made. The treatment includes conditions where CG10 is an electrolyte and conditions where it shows a significant electronic conductivity. Nevertheless, the CG10 layer between the electrodes will be referred to as the "electrolyte" for ease of reading, even when it shows mixed conduction.

7.2 Theory and model description

7.2.1 Defect chemistry of $\text{Ce}_{0.9}\text{Gd}_{0.1}\text{O}_{1.95-x}$ (CG10)

In CG10, oxide ion vacancies are created by the partial substitution of Ce^{4+} with Gd^{3+} . Written in the Kröger-Vink notation, the reaction is:



At high p_{O_2} , oxide ion vacancy formation by substitution contributes only ionic charge carriers.

Oxide ion vacancies can also be created as oxide ions interact with the gas-phase oxygen at the surfaces.



Reducing the oxide activity in the material creates both electronic charge carriers (Ce'_{Ce}) and ionic charge carriers ($\text{V}_{\text{O}}^{\bullet\bullet}$) according to equation 7.2.

The oxide ion vacancy concentration of an oxide material is related to the oxygen partial pressure of a gas with which the material is in equilibrium. In equilibrium, the chemical potentials of the oxide and the gas are equal:

$$\Delta H(x) - T\Delta S(x) = \mu_{\text{O}_2}^0(T) + RT \ln p_{\text{O}_2} \quad (7.3)$$

x is the number of oxide ions per formula unit who were removed from the lattice by reduction of the stoichiometric oxide ($\text{Ce}_{0.9}\text{Gd}_{0.1}\text{O}_{1.95}$ in the case of CG10). $\Delta H(x)$ and $\Delta S(x)$ are the x dependent partial molar enthalpy and entropy associated with the reaction in Eq. 7.2. $\mu_{\text{O}_2}^0(T)$ is the standard chemical potential of oxygen. T is the temperature in K and R is the gas constant. Ignoring the temperature dependence of the chemical potential of oxygen in a gas the relation

can be rewritten:

$$\ln p_{\text{O}_2} = \frac{\Delta H(x)}{RT} - \frac{\Delta S(x)}{R} \quad (7.4)$$

If $\Delta H(x)$ and $\Delta S(x)$ are known, then x , and with it both the electronic and ionic charge carrier concentrations can be calculated with Eq. 7.4.

7.2.2 Ambipolar transport model

Overview

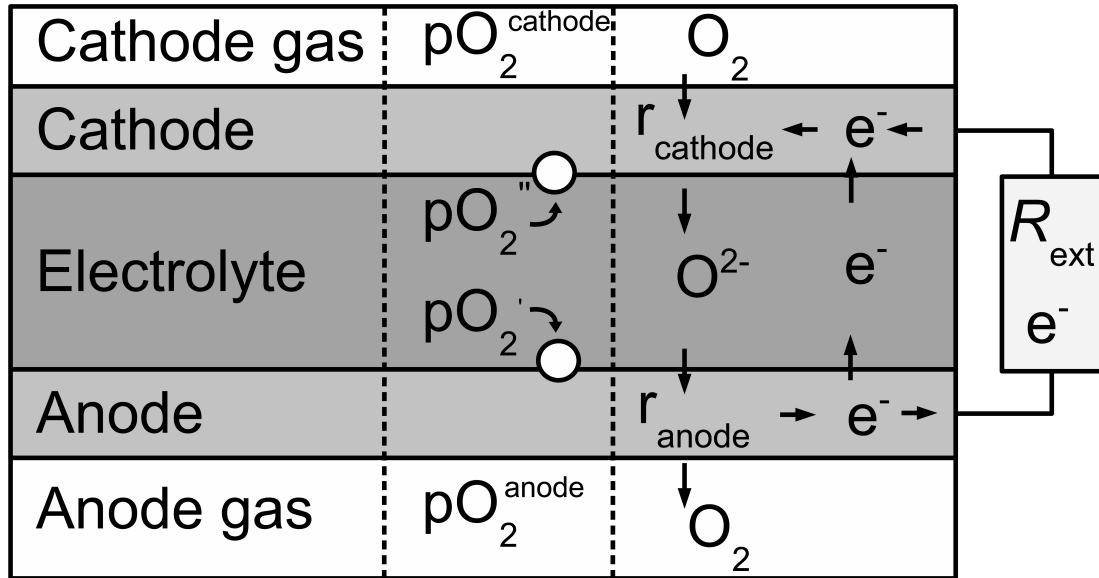


Figure 7.1: The cell considered in the model. The left column shows the name of the cell parts. The middle column marks the p_{O_2} labels through the cell. The right column shows the current circuit of the cell.

The model used in this paper is outlined in Figure 7.1. At the cathode, oxygen molecules from the cathode gas dissociate, absorb electrons and diffuse into the electrolyte as ions. This process is represented with a cathode polarization resistance, r_{cathode} . The oxide ions are then transported through the electrolyte to the anode. At the anode, the oxide ions are transformed to oxygen molecules in the anode gas, shedding electrons in the process. This process is represented with an anode polarization resistance r_{anode} . The electrons are transferred back to the cathode through either the external resistance or as leak current in the electrolyte.

Transport in the electrolyte

The transport in the electrolyte is treated using the model published by Näfe [76]. This is a one dimensional model of a MIEC membrane placed in an oxygen potential gradient. It is necessary to treat CG10 as a MIEC as it can have a significant electronic leak current. The model of Näfe is, as the Wagner model [34], constructed from the following requirements: 1) Local and global charge balance. 2) Current balance of the ionic, electronic and external (electronic) currents and 3) The difference of the electrochemical potential of electrons must equal FU between the electrodes, U being the voltage difference and F Faradays number. Contrary to the Wagner model, the electrolyte in the model of Näfe can be connected with a parallel external

resistance r_{ext} . In the case of a homogenous current density through the electrolyte, r_{ext} can be expressed as $r_{\text{ext}} = \frac{L}{\sigma_{\text{ext}}A}$ where L is the electrolyte width, A is the electrolyte area and σ_{ext} is the conductance of a load resistor of the same geometry as the electrolyte. Using the model of Näfe and rearranging the formulae the internal electronic current density, i_e can be calculated as:

$$i_e = -\frac{RT}{z_e z_i F N_O L} \int_{\ln p_{O_2}}^{\ln p_{O_2}^*} \frac{\sigma_e \sigma_i}{\sigma_i + (\sigma_e + \sigma_{\text{ext}})} d(\ln p_{O_2}) \quad (7.5)$$

where z_i and z_e are the charges of the ionic species and electrons in units of e , F is Faradays constant, N_O is the number of atoms per molecule in the gas phase (2 for oxygen). σ_i and σ_e are the x dependent conductivities of electrons and ions in the electrolyte. The internal electronic current density is often referred to as the leak current density.

The oxide ion current density can be written [76]:

$$i_i = -\frac{RT}{z_i N_O F L} \int_{\ln p_{O_2}}^{\ln p_{O_2}^*} \frac{\sigma_i (\sigma_e + \sigma_{\text{ext}})}{\sigma_i + (\sigma_e + \sigma_{\text{ext}})} d(\ln p_{O_2}) \quad (7.6)$$

The quantity $\frac{\sigma_i (\sigma_e + \sigma_{\text{ext}})}{\sigma_i + (\sigma_e + \sigma_{\text{ext}})}$ which has the dimension of a conductivity, but refers to the entire system, including the load resistor, is abbreviated by Σ . As can be seen the essence of the approach of Näfe is to treat the external electronic current density as if a second type of electron was running in the electrolyte.

The gradient of the electrochemical potential of the electrons, $\nabla \eta_e$, can be calculated as [76]:

$$\nabla \eta_e = -\frac{1}{z_i N_O} \frac{\sigma_i}{\sigma_i + (\sigma_e + \sigma_{\text{ext}})} \nabla \mu_{O_2} \quad (7.7)$$

In the case of electrodes with equal electron chemical potentials, the voltage U can be calculated by integration of Eq. 7.7. This integration reduces to the Nernst equation when $(\sigma_e + \sigma_{\text{ext}}) = 0$. This model (Eqs. 7.5-7.7) is used in this study to calculate the ionic and electronic current densities in the electrolyte, as well as the electric potential difference between the electrodes. The p_{O_2} boundaries of the integrations are dependent on the p_{O_2} of the surrounding gas and the polarization of the electrodes.

Electrode polarization resistance

The electrode kinetics are modelled as two extra layers of matter with finite resistance on each side of the electrolyte. This electrode polarization resistance represents the summation of processes which transforms an oxygen molecule from the surrounding gas to two oxide ions and four electrons in the MIEC. For simplicity, linear electrode kinetics and no resistance dependence on the various concentrations in neither the gas phase nor electrode are considered when modelling the electrodes. The ionic current density through the electrode layer can then be written:

$$i_i = \frac{1}{z_i F N_O} \frac{1}{r_{\text{electrode}}} \Delta(RT \ln p_{O_2}) \quad (7.8)$$

where $r_{\text{electrode}}$ is the electrode polarization resistance. The cell is divided into discrete segments (100 bulk segments + 2 electrode segments) with each segment labelled with a p_{O_2} . Equations 7.5 through 7.8 are solved under the requirement of a constant oxide ion current, constant electron current and constant external electron current density for all the segments. The p_{O_2} on the fuel and air side provides the boundary conditions.

7.2.3 Power density and efficiency

In order to characterize the cell performance, three characteristic quantities are calculated:

- The power density of the fuel cell (p) is defined as the power dissipated in the external resistor. It is calculated as:

$$p = i_{\text{ext}}U \quad (7.9)$$

where U is the voltage between the electrodes and i_{ext} is the current density in the external resistor.

- The efficiency, η , is defined as the product of the ratio of the cell voltage to the Nernst voltage, $\frac{U}{U_{\text{Nernst}}}$ and the ratio of the external current density to the ionic current density, $\frac{i_{\text{ext}}}{i_i}$.

$$\eta = \frac{U}{U_{\text{Nernst}}} \frac{i_{\text{ext}}}{i_i} \quad (7.10)$$

The efficiency is a normalized measure of the energy dissipated in the load resistor per oxygen molecule transferred from the cathode gas to the anode gas. An efficiency of 1 corresponds to a perfect electrolyte running at the Nernst voltage.

Using Kirchoffs law of current balance, U can be written in terms of U_{Nernst} , the current density and the resistances:

$$U = U_{\text{Nernst}} - (r_{\text{anode}} + r_{\text{cathode}} + r_{\text{ion}})(i_{\text{ext}} + i_e) \quad (7.11)$$

where $r_{\text{ion}} = \int_{\text{electrolyte}} \frac{1}{\sigma_i}$. Combining equations 7.11 and 7.10, the efficiency can be expressed as a function of resistances. The following substitutions are necessary: $r_e = U/i_e$, $i_i = i_{\text{ext}} + i_e$ and $r_{\text{ext}} = U/i_{\text{ext}}$.

$$\eta = \frac{1}{1 + (r_{\text{anode}} + r_{\text{cathode}} + r_{\text{ion}}) \left(\frac{1}{r_{\text{ext}}} + \frac{1}{r_e} \right)} \cdot \frac{1}{1 + \frac{r_{\text{ext}}}{r_e}} \quad (7.12)$$

The first factor is the voltage efficiency and the second factor is the faradaic efficiency. One of the important parameters in the following analysis is the maximum possible efficiency η_{max} . To find η_{max} , r_{ext} is adjusted while the temperature, electrode polarization resistances and gas mixtures are kept constant.

7.2.4 Reference cell

During this model study a number of different cells are investigated. In this section a reference cell is defined. The cell parameters are summarized in Table 7.1. If the cells deviate from the reference cell it is explicitly stated in the text.

Mogensen *et al.* [66] have evaluated values of $\Delta H(x)$ and $\Delta S(x)$ reported by several research groups. In this model study, the ΔH and ΔS reported by Wang *et al.* [81] are used.

Wang *et al.* [82] have also reported values of the temperature dependent mobilities of the ionic and electronic charge carriers in CG10. These values are used in this model study and are given in the table below. Wang *et al.* describes the large activation energy of $\mu_e T$ as abnormal, possibly due to defect association at high temperature. In this study it will nevertheless be assumed that the activation energy is correct. For simplicity, the mobilities are assumed to be independent of the concentration of vacancies.

The polarization resistance measured on a composite yttrium doped zirconia and nickel (Ni-YSZ) electrode in a hydrogen/water mixture are used for the anode polarization resistance. The used value of the resistance has not been published explicitly, but can be rationalized from the work of Primdahl and Mogensen [83] and Barfod *et al.* [84]. Only the temperature dependence is taken into account. As Ni-CG10 electrodes would be expected to be the best choice for a

CG10 electrolyte, it is assumed that it is possible to fabricate anodes of Ni-CG10 which are as good as the Ni-YSZ electrodes reported.

The cathode polarization resistance that was reported by W. Wang [68] for a $(\text{La}_{0.6}\text{Sr}_{0.4})_z\text{Co}_{0.2}\text{Fe}_{0.8}\text{O}_{3-\delta}$ -CG10 (LSCF-CG10) composite cathode in air is used.

Table 7.1: Reference cell parameters

Temperature:	873 K
ΔH and ΔS	see Wang <i>et al.</i> [82]
Anode gas:	50% H_2O + 50% H_2 $p_{\text{O}_2} = 10^{-23.9}$ atm at 873 K
Cathode p_{O_2} :	Air $p_{\text{O}_2} = 0.209$ atm at 873 K
L :	10 μm
r_{ext}	varied parameter
r_{anode} :	$1.3 \cdot 10^{-9} \Omega\text{m}^2 \cdot \exp\left(\frac{77 \frac{\text{kJ}}{\text{mol}}}{RT}\right)$ [83, 84] ($5.33 \cdot 10^{-5} \Omega\text{m}^2$ at 873 K)
r_{cathode} :	$2.5 \cdot 10^{-12} \Omega\text{m}^2 \cdot \exp\left(\frac{116 \frac{\text{kJ}}{\text{mol}}}{RT}\right)$ [68] ($2.15 \cdot 10^{-5} \Omega\text{m}^2$ at 873 K)
μ_i	$\mu_i T = 0.02925 \exp\left(-65.18 \frac{\text{kJ}}{\text{mol}} / RT\right) \frac{\text{m}^2}{\text{Vs}}$ [81]
μ_e	$\mu_e T = 0.8433 \exp\left(-76.81 \frac{\text{kJ}}{\text{mol}} / RT\right) \frac{\text{m}^2}{\text{Vs}}$ [81]

7.3 Experimental

7.3.1 Total conductivity measurements

CGO10 powder from Rhodia was pressed isostatically into a pellet. The pellet was sintered at 1773 K for 2 h standing on 8YSZ tape. The pellet was cut to a bar (2x3x5 mm) and ground to having parallel sides. Before measuring the conductivity, Pt-paste was applied as electrodes and the samples were heat-treated at 1273 K for $\frac{1}{2}$ h.

The conductivity was measured by pseudo 4-point (using 4-wires connecting 2 electrodes) [85] impedance spectroscopy using a computer controlled HIOKI 3522-50 LCR HiTESTER using the frequency range: 1 MHz - 46 Hz. The impedance was measured at reducing conditions at temperatures between 753 K and 948 K and in air between 403 K and 1273 K.

7.3.2 Oxygen permeation experiments

The oxygen permeation rates were measured on a sample of tapecast CGO10 of thickness 210 μm , produced by ECN Netherlands, equipped with an anode of NiO/CGO10 and a cathode of $(\text{La}_{0.6}\text{Sr}_{0.4})_{0.9}\text{Co}_{0.2}\text{Fe}_{0.8}\text{O}_3/\text{Ce}_{0.9}\text{Gd}_{0.1}\text{O}_2$ (LSCF/CGO10). The sample was sealed on to an Al_2O_3 tube using a ring of tapecast, powdered glass with a softening point of ca. 880 K. The arrangement is shown in Figure 7.2. The sample was exposed to dry flowing mixtures of N_2/H_2 on the inner compartment, and air on the outer. The water vapour concentration in the N_2/H_2 exhaust was monitored using a dewpoint meter (type *Dewlux*, MCM Ltd, England) and, from this and the known gas flowrate (20 N ml/min), the internal short circuit currents in the CGO were calculated via Faraday's law. The currents were converted to current densities using the geometric area of the cell, namely 0.28 cm^2 . Measurements were performed at 823, 873 and 923 K.

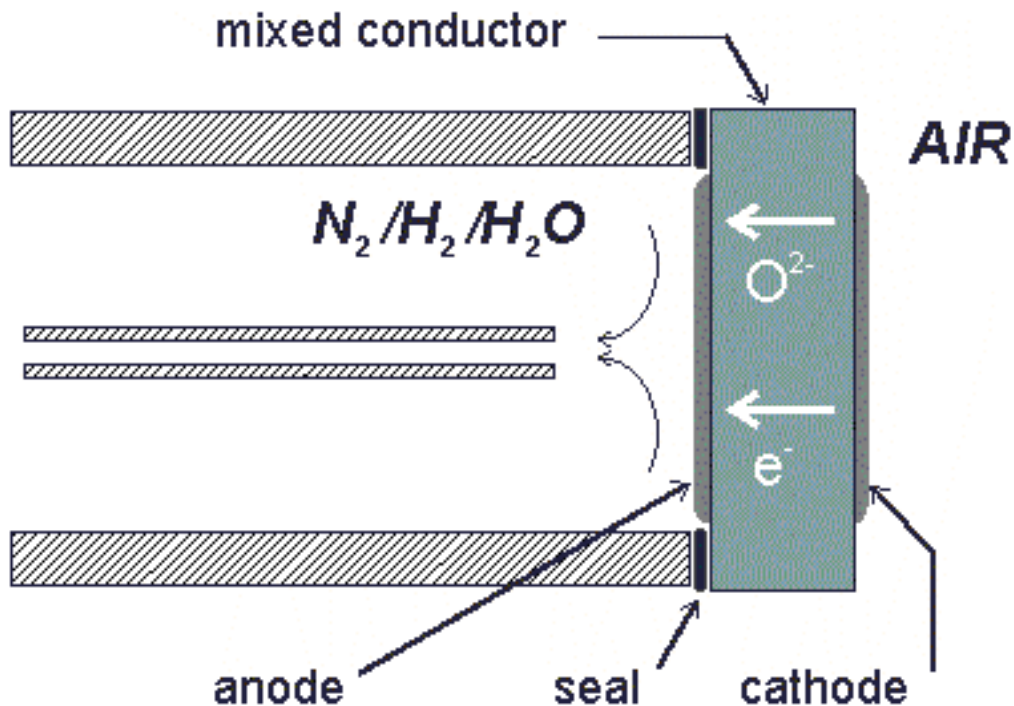


Figure 7.2: Measurement setup of the permeation flux measurement.

7.4 Model validation

7.4.1 CG10 conductivity

The relation between x and p_{O_2} used in the model, is calculated using the enthalpy and entropy of formation of oxide ion vacancies, as well as electron and ion mobility data (see Section 7.2.4). To evaluate these data, comparisons of the measured and model-derived data of the total conductivity of bulk CG10 have been made.

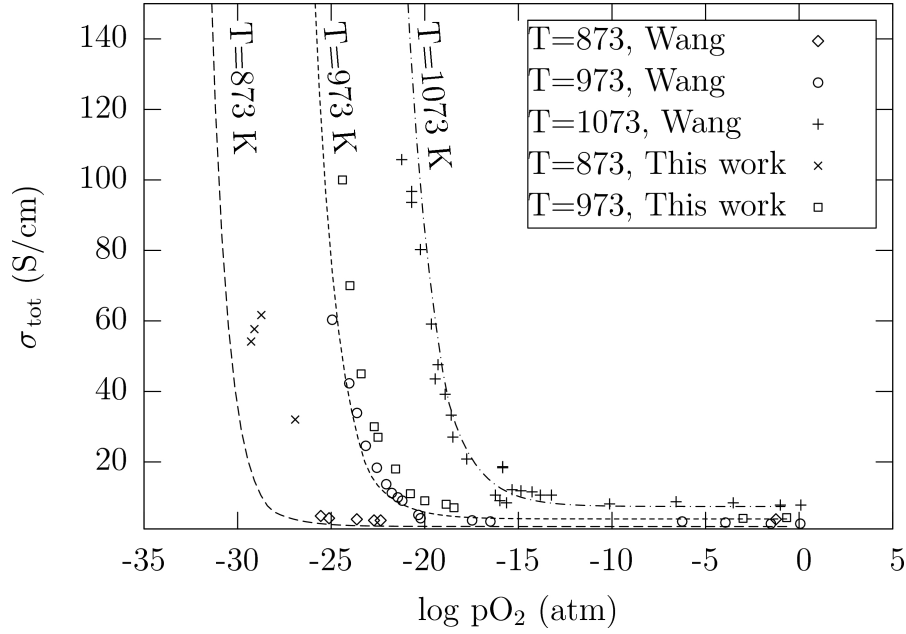


Figure 7.3: Total conductivity of CG10 plotted as a function of p_{O_2} . The figure contains data reported by Wang *et al.* [82] (points) and measurements (points) and model calculations (lines) from this work.

There is good agreement between the total conductivity plots of the model and the experimental data reported by Wang *et al.* [82] shown in Figure 7.3. This is not surprising, as both the mobility data and the thermodynamic data used in the model was reported by Wang *et al.*

The measurement data of this work are in fair agreement with those of Wang *et al.* [82] at 873 K. Discrepancies can be attributed to differences in the conditions of the measurements in this work and those of Wang *et al.*. At 873 K, Wang *et al.* do not have many measurements under strongly reducing conditions, and a small deviation between model and experiments is observed. The measurements indicate that the p_{O_2} range, at which the electronic conductivity exceeds the ionic conductivity, is underestimated in the modelling. It should therefore be noted that the model values might underestimate the leak current.

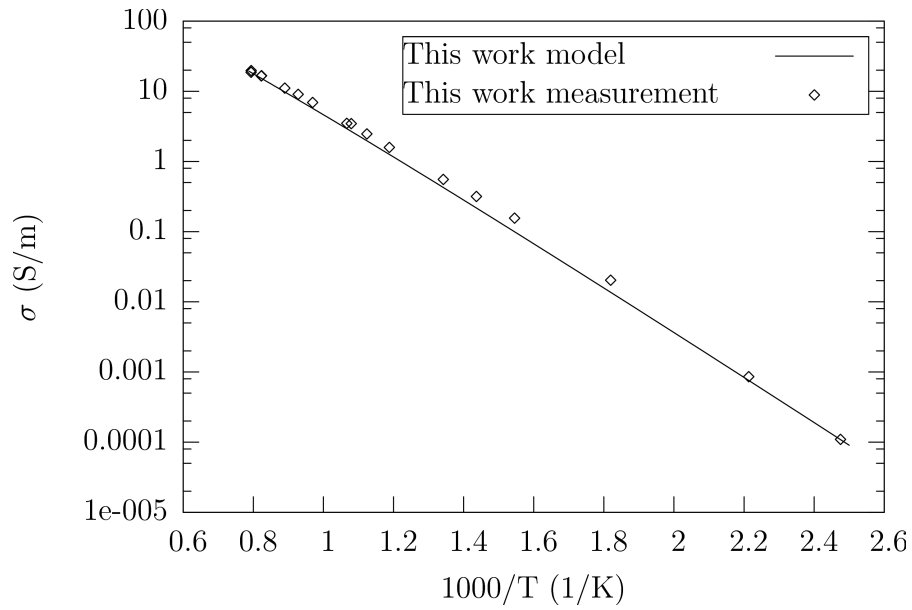


Figure 7.4: Total conductivity in air as a function of temperature. Measured data of this work (points) are compared with calculated data of the model (line). To calculate the total conductivity the model uses data reported by Wang *et al* [81, 82].

An Arrhenius plot of total conductivity data measured in this work and model calculated total conductivity data is displayed in Figure 7.4. There is good agreement between the measured and model derived data. This suggests that the data reported by Wang *et al.* used for calculating the vacancy concentration and conductivities in the model describes the total conductivity in the high p_{O_2} regime well.

7.4.2 Leak current through a CG10 disk

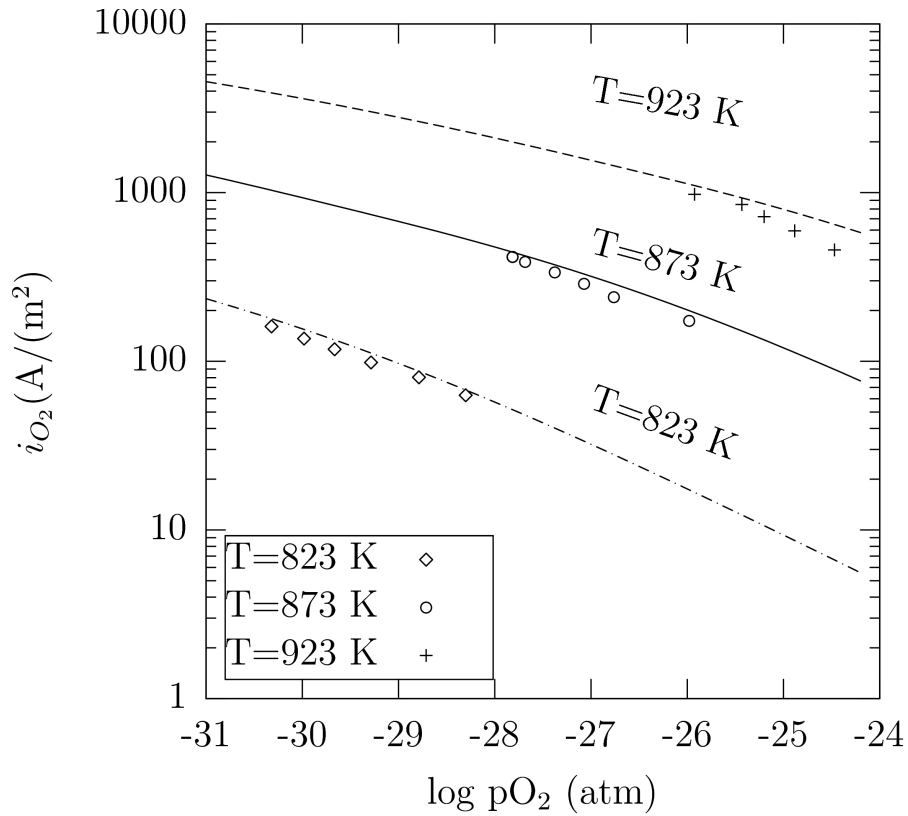


Figure 7.5: Leak current density in a 210 μm thick CG10 electrolyte as a function of p_{O_2} and temperature. Measurements of this work (points) are compared to model calculations (lines). To calculate the total conductivity the model uses data reported by Wang et al. [81, 82] for the electrolyte, and data reported by Wang and Mogensen et al. [68] for the cathode. The anode is based on values of Primdahl and Mogensen [83] and Barfod et al. [84].

Leak current density data obtained by oxygen permeation measurements on a 210 μm CG10 disk are compared with model data in Figure 7.5. The discrepancy between measured and model derived values is in the range of 14-40% of the measured values. This is reasonable, when considering the precision of the model input data, the intrinsic deviations of real systems from model behavior and the precision of the measured data.

7.4.3 Cell characteristics

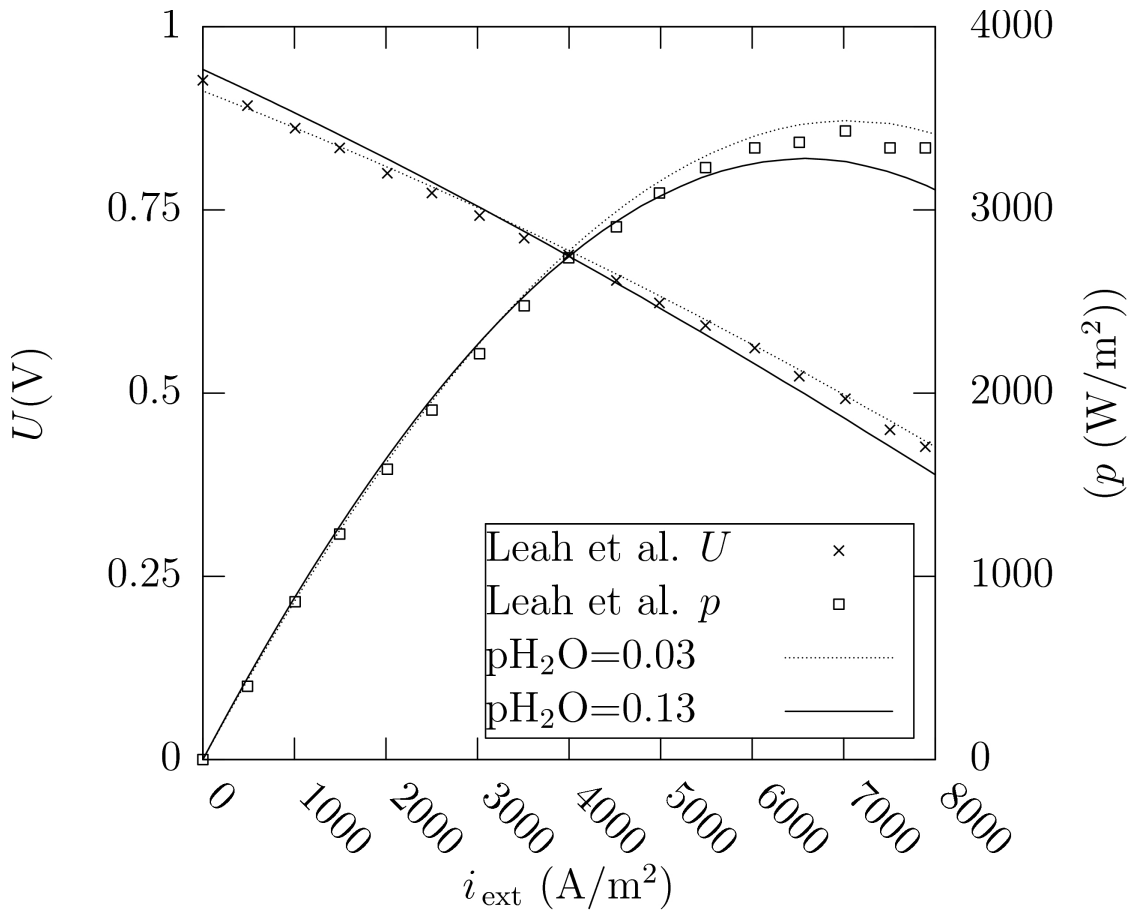


Figure 7.6: Cell voltage and power density of a loaded fuel cell. The discrete points are measurements reported by Leah [2] on a CG10 based fuel cell with $15 \mu\text{m}$ thick CG10 electrolyte at 873 K. The anode gas used by Leah was $97\% \text{H}_2 + 3\% \text{H}_2\text{O}$. The lines are model calculated values of an equivalent cell. The model cell uses $r_{\text{cathode}} = 5.5 \cdot 10^{-5} \Omega\text{m}^2$ and $r_{\text{anode}} = 2.0 \cdot 10^{-5} \Omega\text{m}^2$. The electrolyte is modelled using the data of Wang et al. [81, 82]. The two lines represent measurements with an anode gas of $97\% \text{H}_2 + 3\% \text{H}_2\text{O}$ and $87\% \text{H}_2 + 13\% \text{H}_2\text{O}$, respectively.

Leah *et al.* [2] have experimentally characterized the electrical performance of a CG10 based fuel cell at 873 K. The CG10 electrolyte was $15 \mu\text{m}$ thick. The fuel gas was $97\% \text{H}_2 + 3\% \text{H}_2\text{O}$, and the cathode gas was air. The data of Leah is shown in Figure 7.6 with two curves calculated from the model outlined in Section 7.2. One set is with a $97\% \text{H}_2 + 3\% \text{H}_2\text{O}$ gas mixture which should be valid at low currents. The other is with $87\% \text{H}_2 + 13\% \text{H}_2\text{O}$ gas mixture which should be valid at about 8000 A/m^2 considering the gas flows used by Leah *et al.* [2]. In order to get good agreement between the model curves and Leah's data, the anode polarization resistance used in the model has been changed from the reference case value of $5.33 \cdot 10^{-5} \Omega\text{m}^2$ to $2.0 \cdot 10^{-5} \Omega\text{m}^2$. The cathode polarization resistance has been changed from the reference case value of $2.15 \cdot 10^{-5} \Omega\text{m}^2$ to $5.5 \cdot 10^{-5} \Omega\text{m}^2$. Adjusting the electrode polarization resistances in this manner makes the model data and the measured data agree.

The agreement in performance of the model cell and of the real cells suggests that the model is capable of simulating the characteristic features of a cell based on a CG10 MIEC electrolyte. The agreement also suggests that the reference case values used in this study are close (within a factor of 3 for the electrodes) to a set of values which will reproduce the cell characteristics as

reported by Leah *et al.*

7.5 Modelling results and discussion

7.5.1 Ionic and electronic conductivity

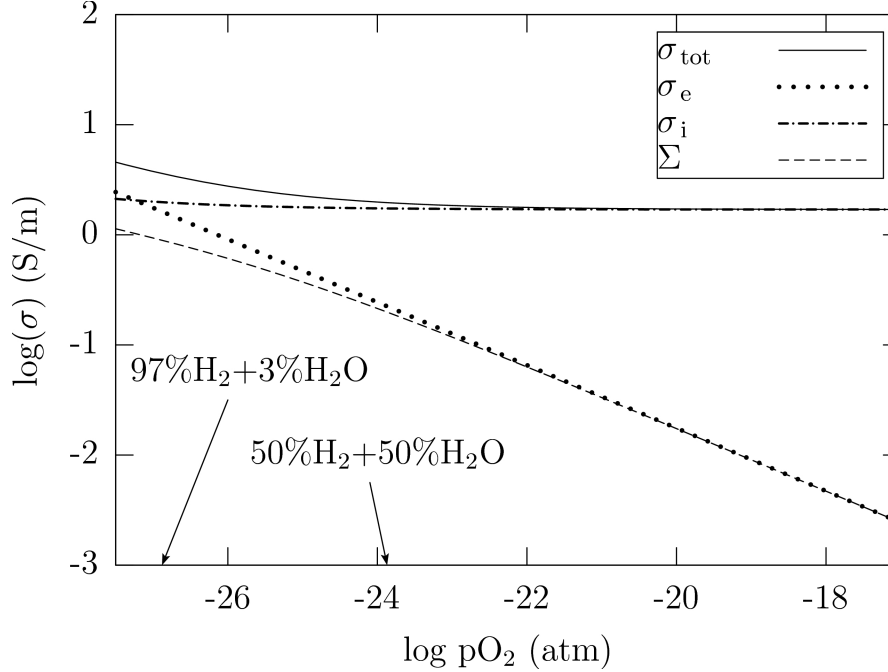


Figure 7.7: Conductivities as a function of surrounding atmosphere. $T=873$ K. Σ , as defined in eq. 7.6 is plotted for OCV, i.e. $\sigma_{\text{ext}} = 0$.

The model-calculated p_{O_2} dependence of the ionic and electronic conductivity at $T=873$ K is shown in Figure 7.7. In the high p_{O_2} regime the ionic conductivity is almost independent of p_{O_2} , as the contribution to the oxide charge carrier concentration from the redox reaction (Eq. 7.2) is small. For the same reason the electronic conductivity is very small compared to the ionic conductivity at p_{O_2} higher than 10^{-23} atm. Therefore, the electronic conductivity determines Σ . At a p_{O_2} of about $10^{-27.5}$ atm, the electronic and ionic conductivities are equal in magnitude, and at p_{O_2} less than 10^{-30} atm, the ionic conductivity is much smaller than the electronic conductivity. In this regime, Σ is therefore determined by the ionic conductivity.

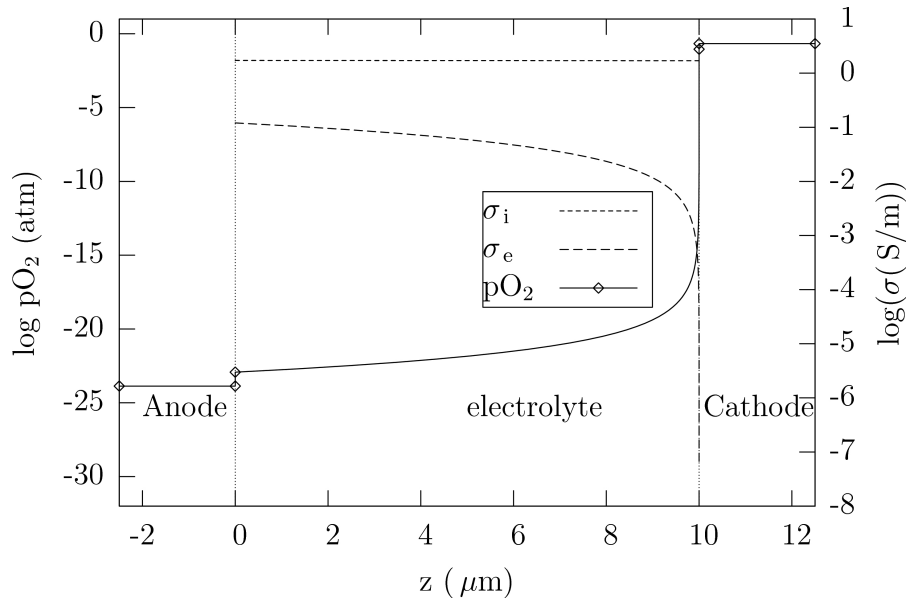
7.5.2 p_{O_2} profile through the cell under open circuit and loaded conditions


Figure 7.8: Conductivities and p_{O_2} profile of a cell. $T=873$ K. Open circuit conditions. The anode gas is 50% $H_2O + 50\%H_2$. Thickness is $10 \mu m$. Arrows point to the appropriate axis.

The p_{O_2} profile and the ionic and electronic conductivity profiles across a cell in open circuit conditions are plotted in Figure 7.8. The voltage between the electrodes is 0.942 V, which is smaller than the Nernst voltage of 1.004 V. This voltage reduction is due to the electrode polarization caused by the leak current. The ionic conductivity is nearly constant throughout the electrolyte, while the electronic conductivity becomes very small close to the cathode. The p_{O_2} experiences a small jump at each interface, due to the electrode polarization.

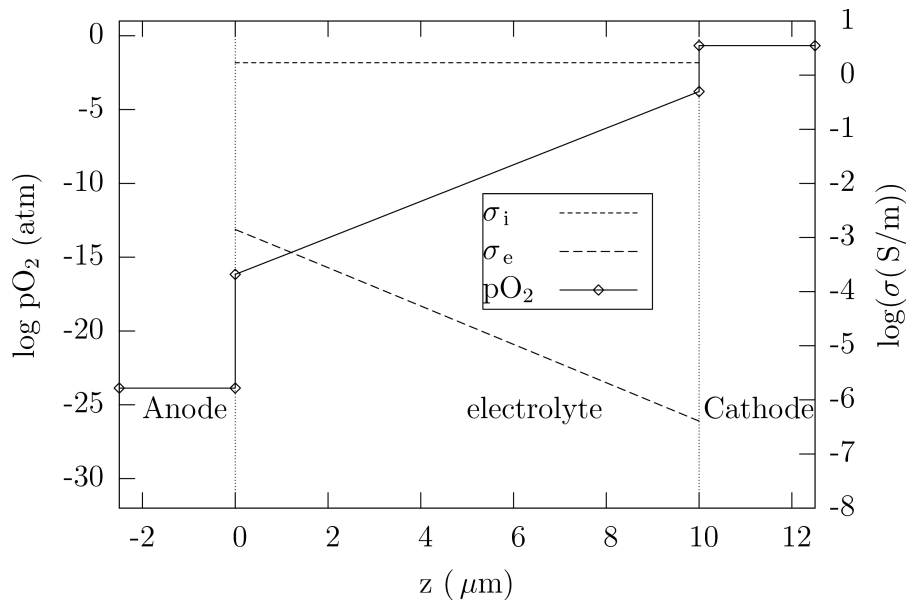


Figure 7.9: Conductivities and p_{O_2} as a function of position. $T=873$ K. An external load resistance of $r_{ext} = 8 \cdot 10^{-5} \Omega m^2$ has been connected. The anode gas is 50% $H_2O + 50\%H_2$. Thickness is $10 \mu m$.

The p_{O_2} and the ionic and electronic conductivity are plotted in Figure 7.9 as a function of the

position in the cell with an applied external load resistance of $8 \cdot 10^{-5} \Omega \text{m}^2$. This is the load resistance which provides the largest power, p , possible under these operating conditions. The voltage between the electrodes is 0.56 V. When loaded the increased Σ increases the ionic current density. The larger ionic current density increases the electrode polarization. This has the interesting effect of fixing the electrolyte at a p_{O_2} between 10^{-16} and 10^{-5} atm. In this regime the electronic conductivity is very low compared to the ionic conductivity. In effect, the CG10 electrolyte has become a much better electrolyte than at OCV. This shielding of the electrolyte from the reducing conditions of the anode gas will be referred to as the anode shielding effect.

7.5.3 The coupling of leak current density and efficiency

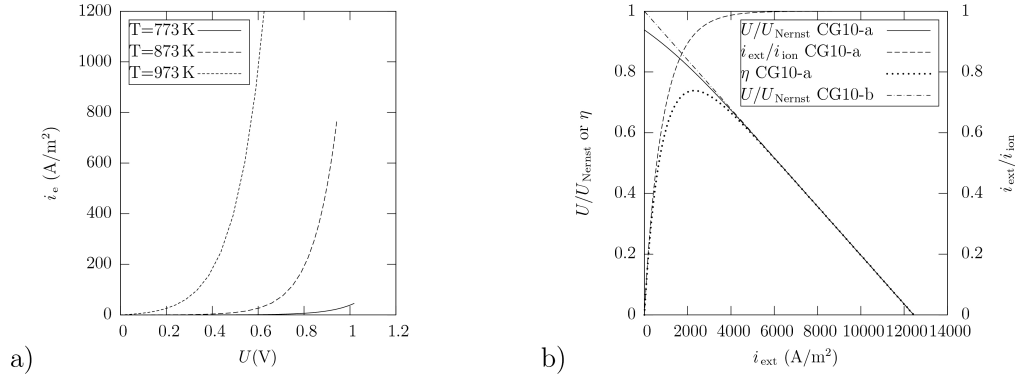


Figure 7.10: **a** Electronic leak current density as a function of temperature and cell voltage. $T=873$ K. $L=10 \mu\text{m}$. The anode gas is 50% $\text{H}_2\text{O} + 50\% \text{H}_2$. **b** Faradaic efficiency, voltage efficiency and η of a reference cell (CG10-a) plotted as a functions of i_{ext} . For comparison, the voltage efficiency of a perfect CG10 electrolyte (CG10-b) is also plotted. $T=873$ K. $L=10 \mu\text{m}$. The anode gas is 50% $\text{H}_2\text{O} + 50\% \text{H}_2$.

The leak electronic current density, i_e , is strongly dependent on the operation voltage of the cell. This is illustrated in Figure 7.10a, where the leak current density at different temperatures is plotted as a function of the cell voltage. The reduction of cell voltage from open circuit conditions is executed by reducing the external resistance to allow i_{ext} to increase. It is interesting that it is not only the fraction of electrons that runs through the electrolyte which gets reduced when current is allowed to run in the external resistor. It is also the absolute electronic leak current density that is reduced. As temperature is decreased, only a moderate decrease of voltage is required in order to reduce the electronic leak current density to insignificant levels.

The efficiency, $\eta = \frac{U}{U_{\text{Nernst}}} \frac{i_{\text{ext}}}{i_i}$ and its two factors are plotted in Figure 7.10b as a functions of i_{ext} . CG10-a denotes a CG10 MIEC while CG10-b denotes a perfect CG10 electrolyte (i.e. the electron mobility has been set to nil). Under open circuit conditions, the entire electronic current runs as a leak current through the electrolyte (the situation shown in Figure 7.8). This gives a faradaic efficiency of nil. At high current densities the electronic current runs in the external circuit (the situation shown in Figure 7.8). This gives a faradaic efficiency of 1. The deviation from U_{Nernst} of U can be divided into two terms according to Eq. 7.11. The term proportional to i_{ext} is the load term and the term proportional to i_e is the leak term. The leak term is the difference between the voltage of CG10-a and CG10-b. The load term is the difference between the Nernst voltage and the voltage of CG10-b and is a consequence of the external current. For the reference set of parameters, current densities below 500 A/m^2 make the leak term the largest term. At current densities exceeding 500 A/m^2 , the load term is the largest term.

The efficiency of a CG10 cell is at very low current densities determined by the leak current density dominance of the electronic current density (i.e. $\frac{i_{\text{ext}}}{i_i}$ very low) and to some degree by the leak current density term of the voltage efficiency. At high current densities, the CG10 layer

shows electrolytic behavior, and the efficiency is determined exclusively by the load term of the voltage deviation. This load term is also found in perfect electrolytes. CG10 thus performs as a perfect electrolyte at high current densities.

7.5.4 Temperature dependence of performance

The mobilities of the ions and the electrons, the cathode and anode polarization resistances and the charge carrier concentrations are all thermally activated and all affect the oxide stoichiometry and transport parameters of a CG10 based cell. The ionic flux through a loaded cell are enhanced with increasing temperature, due to these activated processes. The temperature dependence of the efficiency of the cell will however depend on whether the ionic or the leak current density gets the largest enhancement from the increase in temperature.

The efficiency is plotted as a function of the power density at different operation temperatures in Figure 7.11a. The highest power density is found at the highest temperature, due to the increase in ionic conductivity and decrease in polarization resistance, while the highest efficiency is found at low temperature due to the lower concentration and mobility of electronic charge carriers.

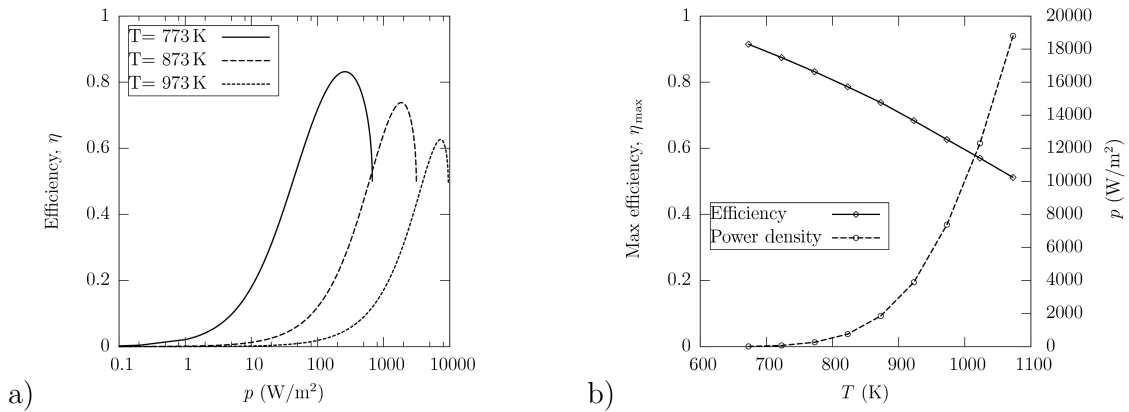


Figure 7.11: *a)* Efficiency as a function of power density and temperature. $L=10 \mu\text{m}$. The anode gas is 50% $\text{H}_2\text{O} + 50\% \text{H}_2$. *b)* η_{max} and power density at η_{max} as a function of temperature. $L=10 \mu\text{m}$. The anode gas is 50% $\text{H}_2\text{O} + 50\% \text{H}_2$.

η_{max} and the power density at η_{max} is plotted in Figure 7.11b. Increasing the temperature causes an almost linear decrease in efficiency. The activation enthalpy of electronic charge carrier formation (Eq. 7.2) is around 450 kJ/mol and the activation energy of the electron mobility is about 75 kJ/mol giving a total activation energy in excess of 500 kJ/mol. This is much larger than the activation energies of both the electrode polarization resistances and the ionic conductivity (who are all less than 120 kJ/mol). r_e thus has the strongest temperature dependence of the resistances in Eq. 7.12. As r_e decreases when the temperature increases, the efficiency will also decrease as the voltage efficiency drops. As the ionic mobility and the electrode polarization resistances are thermally activated processes, the power increases with temperature. At sufficiently high temperatures, however, the reduction of the voltage efficiency will reduce the power of the cell as the cell short circuits internally. This is in contrast to what is observed in cells with perfect electrolytes.

7.5.5 Effects of anode polarization

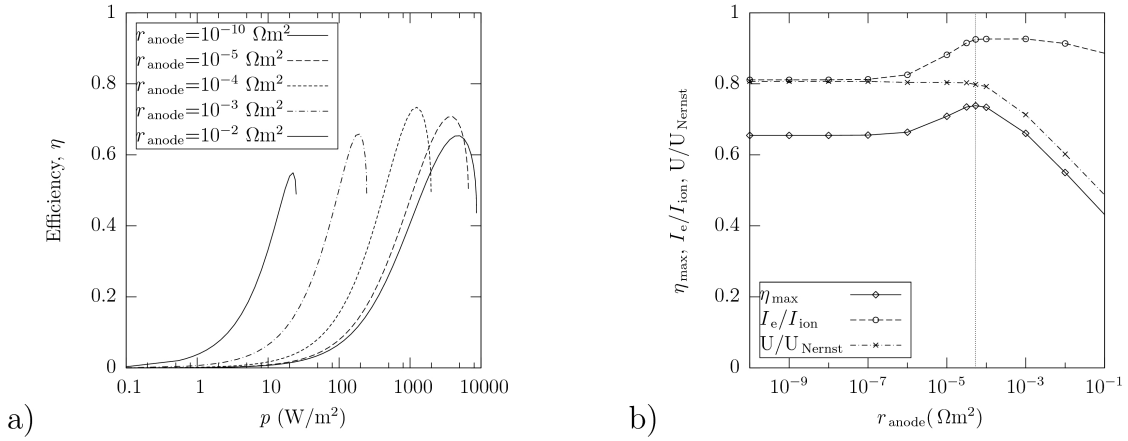


Figure 7.12: **a)** Efficiency as a function of power density and anode polarization resistance. $T=873 \text{ K}$. $L=10 \mu\text{m}$. The anode gas is $50\% \text{ H}_2\text{O} + 50\% \text{ H}_2$. **b)** Maximum efficiency, η_{max} , faradaic efficiency i_{ext}/i_i at η_{max} and voltage efficiency at U/U_{Nernst} η_{max} . $T=873 \text{ K}$. $L=10 \mu\text{m}$. The anode gas is $50\% \text{ H}_2\text{O} + 50\% \text{ H}_2$. The vertical line marks the reference cell anode polarization resistance.

In section 7.5.2 it was shown that when a load is applied, the anode polarization shields the electrolyte from the reducing anode gas. The electrolyte is thus not reduced as much as it would be under open circuit conditions, and due to the resulting very low electronic carrier density, the CG10 electrolyte is transformed into a true electrolyte. An anode polarization resistance of sufficient magnitude is required to effectively shield the electrolyte. Increasing the anode polarization resistance, however, will limit the oxide current density.

Figure 7.12a shows the efficiency as a function of the power density for a range of anode polarization resistances. For large anode polarization resistances the power density is reduced by the polarization loss at the anode. At small anode polarization resistances the power density reaches its maximum, but the efficiency suffers as the electronic conductivity of the electrolyte is high due to a weak anode shielding effect.

η_{max} , the faradaic efficiency at η_{max} and the voltage efficiency at η_{max} are plotted as a function of the anode polarization resistance in Figure 7.12b. The anode resistance of the reference case (marked by the vertical dotted line) in Figure 7.12b is quite close to the resistance where η_{max} (75 %) is achieved. A further reduction of the polarization resistance would result in poorer η_{max} (66%). This is a noteworthy result, as it means that the anode resistance can in fact become too low. This is even more important when using a fuel gas of lower p_{O_2} or when increasing the temperature of the cell.

To explain the shape of the curves in Figure 7.12b, one must realize that the polarization resistance does not necessarily affect the *maximum* efficiency, η_{max} , of a cell (even though it will reduce the efficiency at some loads). For instance a cell with a perfect electrolyte are able to reach an efficiency of 1 (see eq. 7.12) regardless of polarization resistance, in the limit of $i_{\text{ext}} \rightarrow 0$.

Equation 7.12 shows the dependence of the efficiency on the different resistances of the cell. If one keeps in mind the dependence of r_e on r_{anode} through the anode shielding effect, the anode resistance dependence of the efficiency can be analyzed.

When the anode polarization resistance is less than $1 \cdot 10^{-7} \Omega\text{m}^2$, the system is insensitive to changes of r_{anode} as it is small enough neither to influence either the voltage efficiency nor to impose any anode shielding effect.

When $1 \cdot 10^{-7} \Omega\text{m}^2 < r_{\text{anode}} < 5 \cdot 10^{-5} \Omega\text{m}^2$, the anode shielding effect increases r_e signifi-

cantly. This leads to an increase in the faradaic efficiency. r_{anode} is, in this regime, of the same order of magnitude or less than $r_{\text{cathode}} + r_{\text{ion}}$. The detrimental effect on the voltage efficiency of an increase in r_{anode} is thus diluted by $r_{\text{cathode}} + r_{\text{ion}}$. Therefore, the benefits of the shielding effect on both the faradaic and the voltage efficiency will give a net increase in efficiency when r_{anode} is increased.

When $r_{\text{anode}} > 5 \cdot 10^{-5} \Omega\text{m}^2$, r_{anode} severely limits the ion current density. The anode shielding effect thus benefits less in this regime from an increase of r_{anode} as the anode polarization is the product of r_{anode} and i_1 . Furthermore, r_{anode} is now larger than $r_{\text{cathode}} + r_{\text{ion}}$, and the voltage efficiency is thus very sensitive to r_{anode} . The net effect is that the voltage efficiency is reduced when r_{anode} is increased.

When r_{anode} becomes very large, r_{ext} will have to be of the same order as r_{anode} in order to keep up the voltage efficiency. At the same time, it is not beneficial for r_{ext} to be much larger than r_e as the faradaic efficiency will decrease. It turns out that to get η_{max} when increasing r_{anode} , it is necessary to increase r_{ext} a bit faster than r_e is increased, and as a result i_{ext}/i_1 is decreased for very large values of r_{anode} .

7.5.6 Effects of cathode polarization

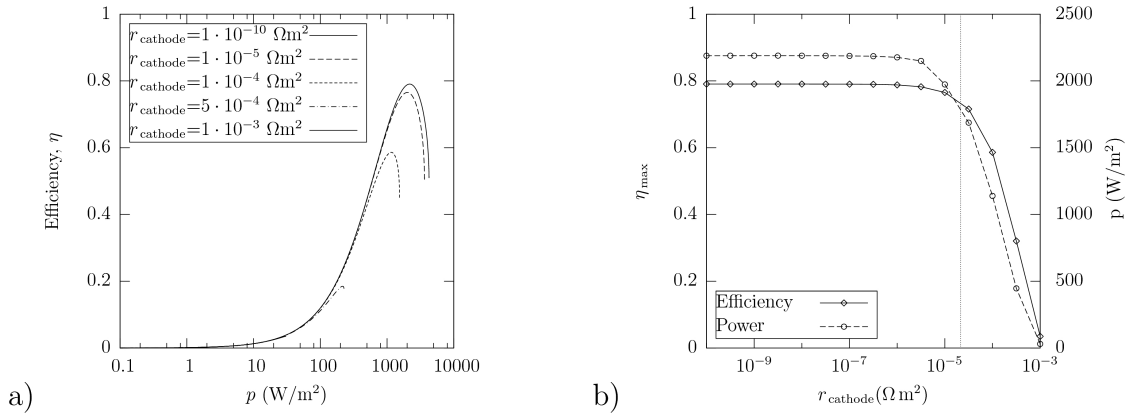


Figure 7.13: *a)* Efficiency as a function of power density and cathode polarization resistance. $T=873 \text{ K}$. $L=10 \mu\text{m}$. The anode gas is $50\% \text{ H}_2\text{O} + 50\% \text{ H}_2$. *b)* η_{max} and power density at maximum efficiency as a function of the cathode resistance. The vertical line marks the reference cell cathode polarization resistance. $T=873 \text{ K}$. $L=10 \mu\text{m}$. The anode gas is $50\% \text{ H}_2\text{O} + 50\% \text{ H}_2$.

The efficiency as a function of the power density of a cell when using different cathode polarization resistances is shown in Figure 7.13a. Contrary to a high r_{anode} , a high r_{cathode} will shield the electrolyte from high p_{O_2} . This reduces the electrolyte and decreases r_e . This is the cathode shielding effect. Contrary to the anode shielding effect, the cathode shielding effect is detrimental to the electrolyte performance. The impact of the cathode shielding effect is, however, smaller than the anode shielding effect, as the high p_{O_2} parts of the electrolyte have lower electronic conductivity than the low p_{O_2} parts, and thus contribute less to the integral in Eq. 7.5. Eq. 7.12 states that the combination of a large r_{cathode} and a small r_e decreases both the faradaic and the voltage efficiency as can be seen in Figure 7.13b. At $r_{\text{cathode}} < 10^{-7} \Omega\text{m}^2$, the detrimental effect of the cathode polarization resistance becomes insignificant. A decrease of the cathode polarization resistance from the current state (vertical dotted line), however, increases both power density and efficiency.

7.5.7 Effects of the electrode polarization distribution

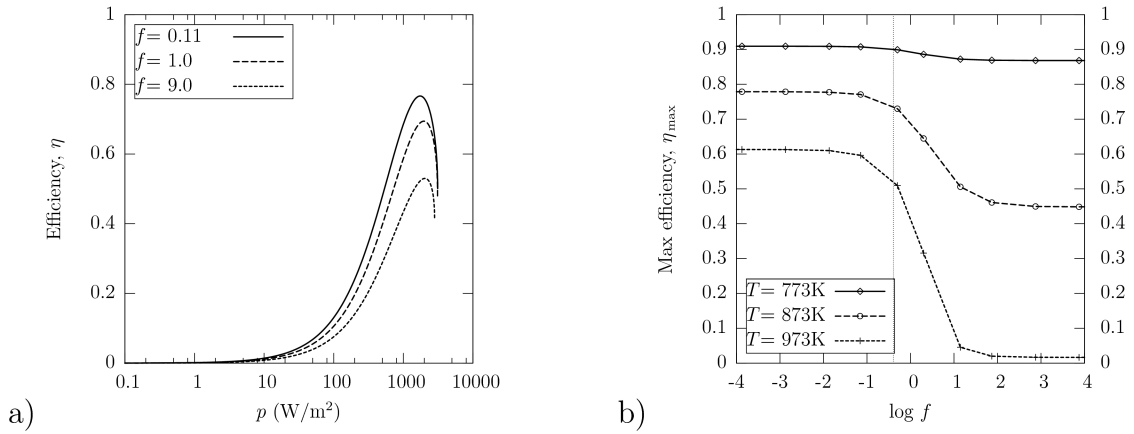


Figure 7.14: **a)** Efficiency as a function of power density and values of $f = \frac{r_{\text{cathode}}}{r_{\text{anode}}}$. $r_{\text{anode}} + r_{\text{cathode}} = 7.5 \cdot 10^{-5} \Omega\text{m}^2$. $T = 873\text{ K}$. $L = 10\ \mu\text{m}$. The anode gas is 50% $\text{H}_2\text{O} + 50\% \text{H}_2$. **b)** η_{\max} as a function of $f = \frac{r_{\text{cathode}}}{r_{\text{anode}}}$ and temperature. The vertical dotted line marks the reference cell. $T = 873\text{ K}$. $L = 10\ \mu\text{m}$. The anode gas is 50% $\text{H}_2\text{O} + 50\% \text{H}_2$.

When large ionic current densities are flowing through a CG10 based cell for a given set of parameter values, Figure 7.9 suggests that a significant p_{O_2} gradient is found across the electrodes. In the previous paragraphs it was shown that the cathode and the anode polarization resistances influence the performance of the cell in part by their polarization loss, and in part by the anode and cathode shielding effects.

The efficiency as a function of the power density in the external resistor is plotted in Figure 7.14a for a range of cathode to anode polarization resistance ratios, f . The total electrode polarization resistance ($r_{\text{cathode}} + r_{\text{anode}}$) was kept constant, and the ratio of cathode to anode polarization resistance (f) was varied.

Figure 7.14b states that at large values of f a low efficiency and power density is achieved while at small values of f a high efficiency and power density is achieved. As the total electrode polarization resistance is constant, this is entirely an effect of the p_{O_2} in which the electrolyte is operating, which is determined by the distribution of the electrode polarization between the cathode and the anode. Furthermore, as sensitivity of r_e to the p_{O_2} is dependent on the operating temperature, the anode and cathode shielding becomes much more critical at high temperatures. At 773 K the efficiency could be changed from 87% to 91% while keeping the total polarization resistance constant. At 973 K the efficiency could be changed from 18% to 62% while keeping the total polarization resistance constant. The temperature dependence reflects the larger significance of the shielding effects due to easier reduction of the electrolyte at high temperatures.

7.5.8 Thickness dependence

One way to increase the ionic current densities through a cell is to reduce the thickness of the electrolyte. This reduces the electrolyte resistance of ions, but also of leak electrons.

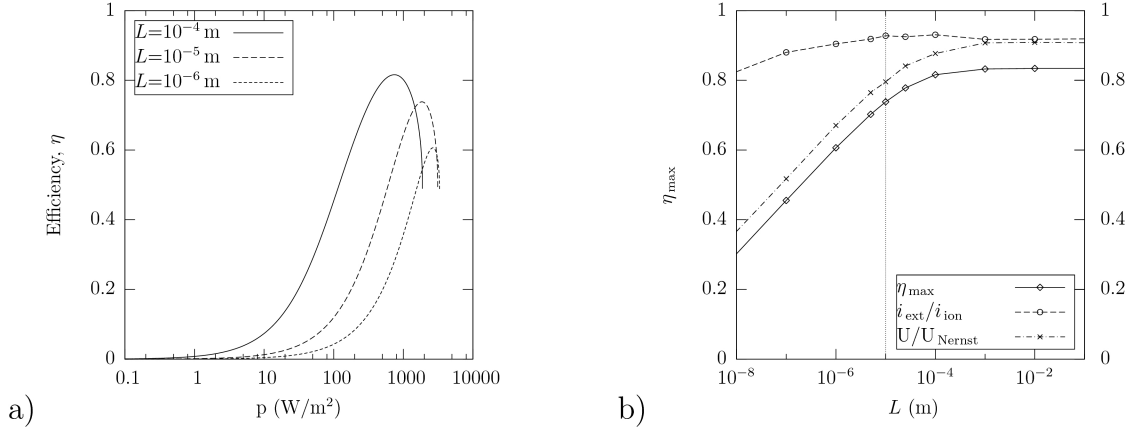


Figure 7.15: **a)** Efficiency as a function of power density and electrolyte thickness, L . $T=873$ K. The anode gas is 50% $\text{H}_2\text{O} + 50\%\text{H}_2$. **b)** Plot of the η_{max} , the faradaic efficiency at η_{max} and the voltage efficiency at η_{max} as a function of the thickness, L , of the CG10 electrolyte. $T=873$ K. The anode gas is 50% $\text{H}_2\text{O} + 50\%\text{H}_2$.

The efficiency is plotted as a function of the power density for three different values of electrolyte thickness in Figure 7.15a. Making electrolytes thinner than $10\ \mu\text{m}$ yields a small increase of power density at the expense of a considerable reduction of η_{max} .

η_{max} , the faradaic efficiency and the voltage efficiency are plotted as a function of the electrolyte thickness L in Figure 7.15b. A reduction of the electrolyte thickness reduces the ionic resistance of the electrolyte. At thicknesses larger than 10^{-5} m any thickness reduction therefore leads to increased ionic current density and so to larger electrode polarizations. This will in turn increase the anode and cathode shielding effects and decrease σ_e . As r_e is proportional to both L and σ_e^{-1} , the anode shielding effect ensures that r_e actually increases a bit as L is decreased. When L becomes less than 10^{-5} m, the increase in current density levels off, as most of the cell resistance is located at the electrodes. Therefore, below this thickness σ_e is constant as the anode polarization has reached its maximum, and when L is shrunk, r_e will decrease. As Eq. 7.12 states, this will have a detrimental effect on both the voltage and the faradaic efficiency.

It seems that little effort should be put into creating electrolytes thinner than $10\ \mu\text{m}$, as this has a detrimental effect on performance.

7.5.9 Nanocrystalline CG10 electrolytes and the importance of the vacancy formation enthalpy

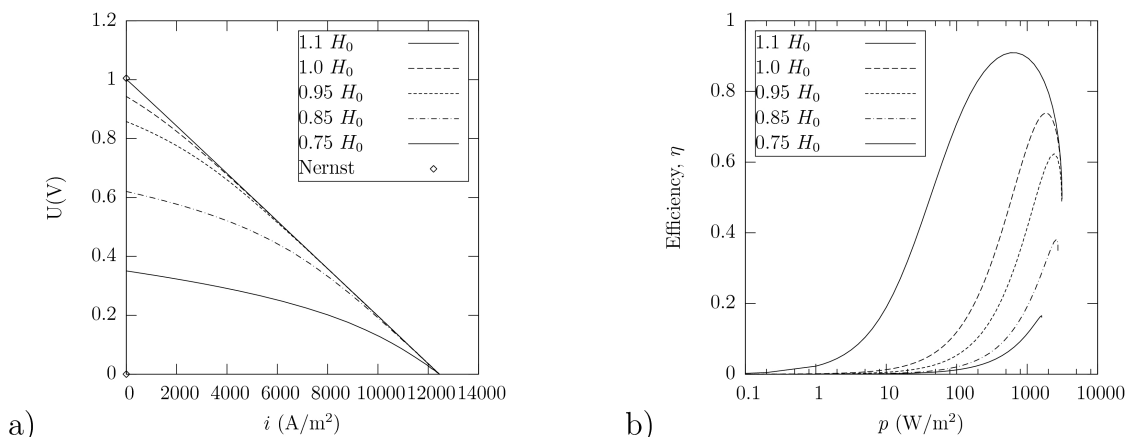


Figure 7.16: **a)** IV plot of the external resistor. Plots are for CG10 and CG10 with modified vacancy formation enthalpies. The labels state the enthalpies as a function of the bulk enthalpy H_0 . $T=873$ K. $L=10$ μm . The anode gas is 50% $\text{H}_2\text{O} + 50\%\text{H}_2$. **b)** Efficiency as a function of power density and vacancy formation enthalpy. Plots are for CG10 and CG10 with modified vacancy formation enthalpies. The labels state the enthalpies as a function of the bulk enthalpy H_0 . $T=873$ K. $L=10$ μm . The anode gas is 50% $\text{H}_2\text{O} + 50\%\text{H}_2$.

Suzuki *et al.* [86] have investigated the effects of grain size on the defect chemistry of doped and undoped ceria. They found that fine grained samples of CG20, CG10 and pure ceria have a significantly lower vacancy formation enthalpy than coarse grained samples. The low enthalpy of the fine grained samples is caused by their larger concentration of grain boundaries, which are believed to be easily reduced. The lower vacancy formation enthalpy of fine grained samples creates more electronic charge carriers for a given p_{O_2} and temperature than a large grained sample. For each gadoleia concentration, Suzuki *et al.* found a threshold diameter (less than 20 nm). This threshold diameter decreases as the Gadoleia content increases. Chiang *et al.* [87, 88] found that the enthalpy of oxide ion vacancy formation in pure ceria with grains of 10 nm in diameter was half that of the bulk, resulting in an electronic conduction 10^4 times larger than that of bulk ceria. In the heavily doped composition of $\text{Ce}_{0.74}\text{Gd}_{0.26}\text{O}_{1.87-x}$ (CG26) Chiang found no increase in electronic conductivity with grain diameters as low as 10 nm compared to coarse grained samples, in accordance with the findings of Suzuki *et al.*. While a very high gadoleia content prevents reduction of the grain boundary, a high dopant content decreases the ionic conductivity dramatically due to trapping of the ionic charge carriers [66].

Calculated IV curves of a cell based on a 10 μm thick CG10 electrolyte using different oxide ion vacancy formation enthalpies are plotted in Figure 7.16a. An enthalpy reduction of 5% of the reference value H_0 results in a reduction of 10% of the open circuit voltage. At higher fluxes, the difference of the reference case and the cases with reduced oxide ion vacancy formation enthalpy is reduced. A 10% increase in enthalpy gives an open circuit voltage close to the Nernst voltage (marked by a circle on the U axis).

η is plotted as a function of the power density produced using different oxide ion vacancy formation enthalpies in Figure 7.16b. Both the efficiency and the power density are strongly dependent on the enthalpy of oxide ion vacancy formation. The extra ionic charge carriers created by lowering ΔH have no beneficial effect as they are very few compared to those created by gadoleia substitution of ceria.

The performance of a cell is very sensitive to the vacancy formation enthalpy. A ten percent increase in the oxide ion vacancy formation enthalpy gives a performance quite superior

to a normal CG10 cell. A CG10 fuel cell manufactured with small grains though is unlikely to perform well. Fine grained CG10 electrolytes with correspondingly low vacancy formation enthalpy could on the other hand find applications as oxygen separation membranes, especially at elevated temperatures, due to their high σ_i .

7.5.10 Comparison with state of the art zirconia based electrolytes.

If CG10 should be successful as an electrolyte in a fuel cell, it must compare well with other candidate electrolytes. For comparison the electrolyte $Zr_{0.79}Ce_{0.01}Sc_{0.20}O_{1.9}$ (ZrScCe) with ionic conductivities reported in Mogensen *et al.* [75] is used. The electronic conduction in ZrScCe is assumed to be nil. The anode polarization resistance is assumed to be equivalent to that of the CG10 cells. State of the art zirconia based cells have inferior cathodes compared with their ceria based counterparts. W. Wang *et al.* [51] has reported the performance of a $(La_{0.75}Sr_{0.25})_{0.95}MnO_3$ (LSM) cathode for zirconia based cells with the following temperature dependent polarization resistance:

$$r_{\text{Cathode}} = 1.40 \cdot 10^{-11} \Omega \text{m}^2 \cdot \exp\left(\frac{122086 \frac{\text{J}}{\text{mol}}}{RT}\right) \quad (7.13)$$

At 873 K this cathode polarization resistance is roughly eight times larger than the one used for the CG10 cell.

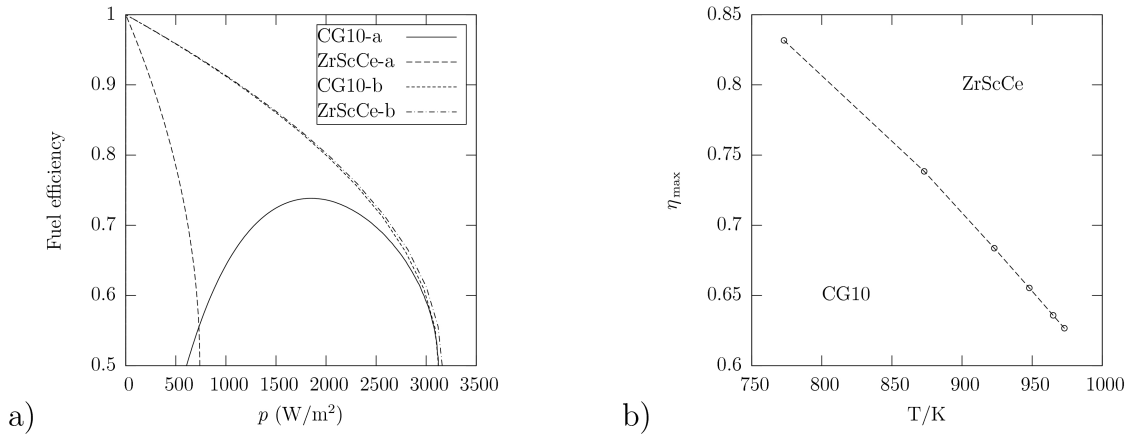


Figure 7.17: *a)* Efficiency as a function of power density. CG10-a is CG10. ZrScCe-a is ZrScCe with its usual cathode. ZrScCe-b is ZrScCe with a cathode comparable with the CG10 cell electrodes. CG10-b is CG10 with the electronic conduction set to nil. $T=873$ K. $L=10$ μm . The anode gas is 50% $\text{H}_2\text{O} + 50\% \text{H}_2$. *b)* Plot of the η_{max} of the CG10 electrolyte. $L=10$ μm . The anode gas is 50% $\text{H}_2\text{O} + 50\% \text{H}_2$.

The efficiency as a function of the power density is shown in Figure 7.17a for different cells. Comparing ZrScCe-a (ZrScCe with its usual cathode resistance) and ZrScCe-b (ZrScCe with the CG10 cathode resistance) it is clear that the cells are very sensitive to the cathode resistance, as decreasing the cathode resistance eight-fold increases the power density five-fold.

ZrScCe-b and CG10-b (CG10 where the electronic conduction is set to nil) are nearly identical as their ionic conductance is similar.

Comparing CG10-a (normal CG10) and CG10-b, they are identical at the point of maximum power density output. At lower power they diverge as the leak current density begins to build up in CG10-a which reaches an η_{max} value of 0.73.

Comparing CG10-a with ZrScCe-b these points still stand. If cathodes comparable to the ones available for CG10 were developed for ZrScCe cells, the ZrScCe cell surpasses the performance of the CG10 cells at temperatures higher than 873 K. Simulations at 773 K (not shown)

show that at lower temperatures CG10 cells will have an advantage over ZrScCe cells at high power density due to a larger ionic conductivity at low temperatures, even when similar electrodes are used.

At a given efficiency CG10-a can provide about four times the power density that ZrScCe-a can provide. When approaching open circuit conditions CG10 reaches its η_{\max} of 0.74, and if higher efficiencies are required, CG10 is not an option.

The power density of a CG10 cell is substantially higher than that of a zirconia cell even when operating at the maximum efficiency of the CG10 cell. The important parameter when deciding between a CG10 and a zirconia cell is thus what efficiency is required of the cell, and at what temperature the cell is required to operate. The η_{\max} obtainable with a CG10 electrolyte as a function of temperature is plotted in Figure 7.17b. If the efficiency requirements of a cell are in the bottom left part of the plot, CG10 should be chosen for the electrolyte as it supports higher power densities. If the efficiency requirements are in the top right part of the plot, ZrScCe should be chosen as CG10 is not able to reach adequate efficiencies.

One of the arguments for selecting a CG10 electrolyte over a zirconia based electrolyte is that the leak current density is small when the cell is strongly polarized and has a large ionic current density. This is the region where the performance curves of CG10-a and CG10-b converge in Figure 7.17. That argument is not good as the efficiency at this point has been driven down to about 0.6 by polarization losses. At the point of η_{\max} , the leak current density is actually about 8% of the ionic current density.

7.6 Discussion

7.6.1 Possibilities of improving cells based on CG10 electrolytes

The amount of resources which should be spent on enhancing the performance of a specific part of a CG10 fuel cell is related to the importance of this part to the performance of the whole cell. Estimating the important parts is not trivial, due to the many related phenomena taking place. What limits the performance under one set of conditions might be irrelevant in another set of conditions. Even the term "performance" is not uniquely defined. Due to the load term of the voltage efficiency, the operation conditions even of fuel cells with a perfect electrolyte will always be a tradeoff between power density and efficiency.

Case 1: High power density applications

The cost of running a fuel cell power plant contains contributions from both the capital cost of the power plant, and the cost of fuel. In the case that the capital and associated depreciation costs are large compared to the fuel costs, a high power density is preferable to a high efficiency. A high power density will also be advantageous when size-limited systems demand a certain power density, for use for instance in vehicles or portable electronics.

Changing the temperature and the external resistance are ways to quickly increase the power density of a cell. In the longer term, the components of the cell could be improved. About 20% more power could be extracted without any loss of efficiency if the cathode polarization resistance was eliminated. 5 times more power could be extracted if the anode resistance was eliminated with only a small loss of efficiency. Reducing the electrolyte thickness would potentially increase the power density about 20%. Because the power density limiting parameter is the anode resistance, only a modest benefit of reducing the thickness or the cathode resistance is found. If the anode resistance was eliminated it would again be more feasible to reduce the other parameters. At some point, however, the faradaic efficiency is so low that the power density will suffer, and no further power enhancement could be realized. This is in contrast to cells based on

perfect electrolytes, which in the case of an infinitely thin electrolyte with perfect electrodes, as far as the mathematics is concerned, should support an infinitely high power density.

Case 2: High efficiency applications

If the production cost of a fuel cell power plant is sufficiently low compared to the fuel cost, a high efficiency becomes vital. This is the case in larger power plants with long lifetimes.

The anode polarization resistance of the reference cell is actually at its optimum. This optimum could, however, move towards lower values of anode resistance, if future advances reduced the resistance of other parts of the cell, allowing a higher current density. Eliminating the cathode polarization resistance would increase the maximum efficiency from 74% to 79%.

Increasing the thickness from 10 μm to 100 μm would increase the efficiency from 74% to 82%. The same increase in efficiency would be found by reducing the temperature to 773 K. The power density, would be reduced to 40% of the reference case value by increasing the thickness. The power density however would be reduced to 14% of the reference case value by reducing the temperature from 873 K to 773 K. Increasing the efficiency by increasing the electrolyte thickness would thus reduce the power density less than a decrease in temperature.

A good choice would therefore be to increase the thickness of the cell, and reduce the cathode resistance. Further optimizations would be achieved by lowering of the temperature and adjustment of the anode polarization resistance.

Finally, Matsui *et al.* [79] reported that increasing the p_{O_2} of the fuel gas increases the efficiency of doped ceria cells. Doped ceria cells could be placed downstream from zirconia based cells and only be exposed to fuel with large water content to prevent reduction of the CG10 electrolyte.

Case 3: low temperature

One of the principal parameters of SOFC cells is their lifetime. By reducing the operating temperature the lifetime can be significantly increased if temperature activated ageing processes are important. As the electronic conductivity is strongly temperature activated, it will lose significance as the temperature is reduced. Furthermore, as the electrode polarization resistance is more temperature dependent than the ionic conductivity, a reduction of temperature would mean that both the efficiency and the power density become limited by the electrode polarization resistances. As the anode shielding effect is less important with a low electronic conductivity, it becomes vital to decrease the electrode polarization resistances. This is doubly important as high electrode polarizations can be at least as detrimental to cell performance at high temperature [89, 90].

7.6.2 Considerations of CG10 or zirconia

Compared to conventional "perfect" electrolytes such as zirconia, the lower cathode polarization resistance is the main advantage of CG10. This allows CG10 to have a significantly higher power density than zirconia electrolyte based cells. Another advantage is a higher ionic conductivity below 873 K. The disadvantages include a maximum efficiency and a lower limit to the thickness of the electrolyte due to the electronic leak current density.

The reference CG10 electrolyte based cell is able to support higher power densities than state of the art zirconia based cells. Furthermore, if the power density is increased beyond the point of η_{max} , the efficiency will actually approach that of zirconia based cells. In this case, CG10 is the better choice for the electrolyte. The requirements for power density could also be so high that the temperature has to be increased to support them. A large temperature increase will make zirconia based cells the best choice, in part because the cathode performance matters less at high temperature, and in part because of CG10 being easily reduced at high temperature.

The reference CG10 cells have a limit to their maximum efficiency. When the required efficiency exceeds this limit, zirconia based cells are required. If, on the other hand, it is possible to optimize the CG10 cells to meet the required efficiency, CG10 should be considered as electrolyte. CG10 has the advantage of a higher power density compared to zirconia cells at equal efficiency especially at $T < 873$ K. Among the drawbacks are a narrow power density range at which the CG10 cell operates close to η_{\max} . A cell with a perfect electrolyte will, in periods of low power consumption, be able to reduce fuel consumption by increasing the load resistor, and gain efficiency. These good part load characteristics are not shared by CG10 based cells. A CG10 cell will, if the load resistor is increased, reduce its efficiency, and will thus not reduce its fuel consumption as much as a perfect electrolyte would. Reducing the temperature would be an alternative way to reduce fuel consumption in a CG10 cell, but although the efficiency is increased, frequent temperature cycles will possibly have a detrimental effect on the cell lifetime.

Future situation

The above discussion centers around the reference CG10 cell, which is based on the state of the art technology of late 2005. Future developments could change the situation significantly. If better cathodes for zirconia based cells were developed, much of the advantage of CG10 cells would disappear. At the moment the possibility of adding a doped ceria layer on top of the zirconia electrolyte to support better cathodes is being investigated. If these good cathodes can be realized for zirconia based cells, they are able to provide nearly the same power densities as CG10 cells even below 873 K, while maintaining higher efficiencies. So far, however, the progress has been limited [91–93].

7.7 Conclusions

A model combining established defect chemistry and ambipolar transport theory has been applied to a fuel cell based on a CG10 electrolyte. The model is able to reproduce measurements made of total conductivity of CG10 and permeation flux of a CG10 cell. It was found that CG10 can become a good electrolyte when loaded such that a large ionic current is running through it. The efficiency of a CG10 cell can be enhanced by using a thicker electrolyte layer, lowering the temperature, and a low cathode polarization resistance. Reducing the enthalpy of oxide ion vacancy formation should be avoided as it decreases the efficiency. Compared to zirconia based cells, CG10 cells support higher fluxes at a given efficiency, but are limited in their maximum efficiency. This makes CG10 based cells a valid alternative to zirconia based cells in applications where operation at temperatures below 873 K or high power density is required.

Chapter 8

Model study of a gadolinia doped ceria membrane

Abstract

In this section the feasibility of creating a 10% gadolinia doped ceria ($\text{Ce}_{0.9}\text{Gd}_{0.1}\text{O}_{1.95}$ or CG10) mixed ionic and electronic conductor (MIEC) oxygen separation membrane for use in syngas production is evaluated.

8.1 Introduction

Ceria (CeO_2) is a fluorite type MIEC which, contrary to the perovskites considered in other parts of this thesis, is stable in very low p_{O_2} and high T . Ceria will expel oxygen creating both ionic charge carriers (oxide ion vacancies) and electronic charge carriers (localized hopping electrons) at low p_{O_2} and high T :



The concentrations of these charge carriers are quite low, and undoped ceria has low electronic and ionic conductivity. Doping with valence-III materials, such as Gd or Sm, creates oxide ion vacancies, enabling oxygen transport through the material:



As the extra electron on Gd'_{Ce} is tightly bound, no mobile electrons are created. Doping like this will thus shift the balance of ceria from a predominantly electron conducting MIEC to a predominantly ion conducting MIEC. In fact, at sufficiently low temperatures (below 873 K) and large dopant levels ($[\text{V}_\text{O}^{\bullet\bullet}] - \frac{1}{2}[\text{Gd}'_{\text{Ce}}] \ll [\text{V}_\text{O}^{\bullet\bullet}]$), doped ceria can be considered an electrolyte for many purposes.

According to Eq. 1.6, the flux is proportional to the ambipolar conductivity, Σ :

$$\Sigma = \frac{\sigma_e \sigma_\text{O}}{\sigma_e + \sigma_\text{O}} \quad (8.3)$$

If $\sigma_e \gg \sigma_\text{O}$, transport is controlled by σ_O and vice versa.

As σ_e has a larger activation energy than σ_O , a temperature increase shifts the balance of doped ceria back towards an electron conducting MIEC. As the electronic mobility is much larger than the oxygen ion mobility, this is also the case when increasing $[V_{O}^{\bullet\bullet}]$ and Ce'_{Ce} through reduction.

At high T , where σ_e starts to rise, doped ceria becomes interesting as a potential material for a syngas membrane. The potential of a ceria membrane is the topic of this study. A target oxygen current density of 20.000 A/m^2 ($= 2 \text{ A/cm}^2$) has been set as a success criteria. A tubular setup is assumed, where the initial CH_4 gas will increase its oxygen content as the gas moves along the MIEC tube. It is further assumed that the maximum oxygen to methane ratio in such an experiment is 1:2, i.e., the stoichiometric ratio of the syngas reaction:



The modelling is done under optimum conditions, i.e., state of the art cathode and anode materials have been applied to each side of the membrane, for optimum catalytic performance. The characteristics of these materials, as well as the bulk conductivity values and the modelling procedure can all be found in Chapter 7. As a syngas membrane, lacks the external circuits of a fuel cell, all the modelling is done with an open circuit.

8.2 Gas equilibria

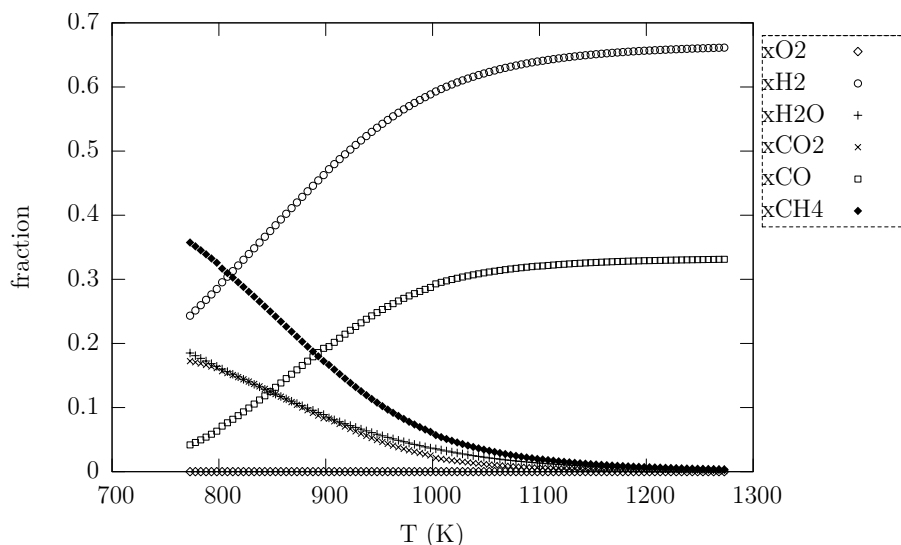


Figure 8.1: Partial pressures of a syngas mixture as a function of temperature

In Figure 8.1 the equilibrium partial pressures of the different gas mixtures present in a syngas mixture are shown as a function of temperature at a pressure of 1 atm. To ensure the stability of the gas, the membrane should be operated above 973 K. In the following, the equilibrium p_{O_2} of the gas is assumed when calculating the oxygen chemical potential on the low- p_{O_2} side.

8.3 Ceria and the alternatives

Fluorite and perovskite materials offer a number of candidates for good membrane materials. In this section, we rationalize the selection of doped ceria for membrane material. Table 8.1 tabulates the oxygen ion conductivity, σ_O , of some of these materials as well as the p_{O_2} of

Table 8.1: Properties of membrane candidate materials.

	$\sigma_{\text{O}}(\text{S/m}), 1073 \text{ K}$	$\sigma_{\text{O}}(\text{S/m}), 1273 \text{ K}$	$p_{\text{O}_2} (\text{atm})$
$\text{La}_{0.6}\text{Sr}_{0.4}\text{FeO}_{3-\delta}$	1 [37]	20 [37]	10^{-17} (1273 K) 10^{-14} (1473 K) [54]
$\text{La}_{0.6}\text{Sr}_{0.4}\text{Co}_{0.2}\text{Fe}_{0.8}\text{O}_{3-\delta}$	4 [44]	20 [44]	10^{-7} (1273 K) [54]
$\text{La}_{0.6}\text{Sr}_{0.4}\text{CoO}_{3-\delta}$	6 [19]	40 [19]	10^{-7} (1273 K) [54]
$\text{Ba}_{0.5}\text{Sr}_{0.5}\text{FeO}_{3-\delta}$	> 4 [64]	> 8 [64]	10^{-7} (1273 K) [54]
$\text{Ba}_{0.5}\text{Sr}_{0.5}\text{Co}_{0.8}\text{Fe}_{0.2}\text{O}_{3-\delta}$	> 27 [64]	> 47 [64]	10^{-7} (1273 K) [54]
$\text{Ce}_{0.9}\text{Gd}_{0.1}\text{O}_{1.95-\delta}$	6 [81]	16 [81]	-
$\text{Ce}_{0.8}\text{Gd}_{0.2}\text{O}_{1.9-\delta}$	6 [81], 20 [94]	16 [81], 25 [94]	-
$\text{Ce}_{0.8}\text{Pr}_{0.2}\text{O}_{1.9-\delta}$	7 [95]	18 [95]	-
$\text{Y}_{0.16}\text{Zr}_{0.84}\text{O}_{1.92}$		10 [94]	-

decomposition in the operating temperature range of an oxygen separation membrane.

The p_{O_2} of decomposition is estimated as the p_{O_2} of decomposition of LaCoO_3 for the Co containing perovskites, and the p_{O_2} of decomposition of LaFeO_3 for the Fe containing perovskites. The rest of the materials are stable in the obtainable p_{O_2} range.

$\text{Ce}_{0.9}\text{Gd}_{0.1}\text{O}_{1.95-\delta}$ and $\text{Ce}_{0.8}\text{Gd}_{0.2}\text{O}_{1.9-\delta}$ are at high p_{O_2} limited by their electronic conductivity, σ_{e} which is extremely low. Doping with Pr introduces some electronic conductivity to make performance equivalent to that of $\text{La}_{0.6}\text{Sr}_{0.4}\text{Co}_{0.2}\text{Fe}_{0.8}\text{O}_{3-\delta}$. For syngas production, $\text{Ce}_{0.9}\text{Gd}_{0.1}\text{O}_{1.95-\delta}$ and $\text{Ce}_{0.8}\text{Gd}_{0.2}\text{O}_{1.9-\delta}$ are in a reduced state with a high σ_{e} , and the performance will be determined partly by σ_{e} and partly by σ_{O} .

YSZ is not a candidate for a simple membrane material, as its electronic conductivity is very low.

We evaluate that for syngas production, stability dictates that $\text{La}_{0.6}\text{Sr}_{0.4}\text{FeO}_{3-\delta}$, $\text{Ce}_{0.9}\text{Gd}_{0.1}\text{O}_{1.95-\delta}$ and $\text{Ce}_{0.8}\text{Gd}_{0.2}\text{O}_{1.9-\delta}$ are the only usable materials.

For oxygen separation (i.e. high p_{O_2} applications) the perovskites can be used while CeO_2 needs to be doped with Pr to be usable.

8.4 Electronic or ionic conductivity.

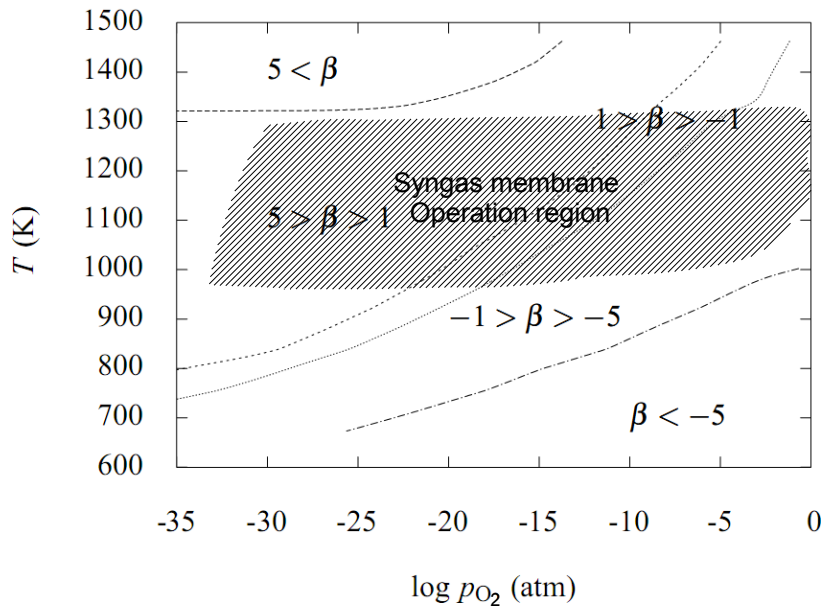


Figure 8.2: Contour plot of $\beta = \log \frac{\sigma_e}{\sigma_o}$ as a function of p_{O_2} and temperature for CG10. The typical operation region of a syngas membrane has been shaded.

In Fig. 8.2, a contour plot of $\beta = \log \frac{\sigma_e}{\sigma_o}$ for CG10 is shown. When $\beta < -1$, σ_e is limiting the transport, while $\beta > 1$ means that σ_o is limiting the transport. The typical syngas membrane operation regime has been shaded in Fig. 8.2. A CG10 membrane for syngas production works in a mixed regime where both σ_e and σ_o have to be taken into account.

8.5 Effect of membrane thickness

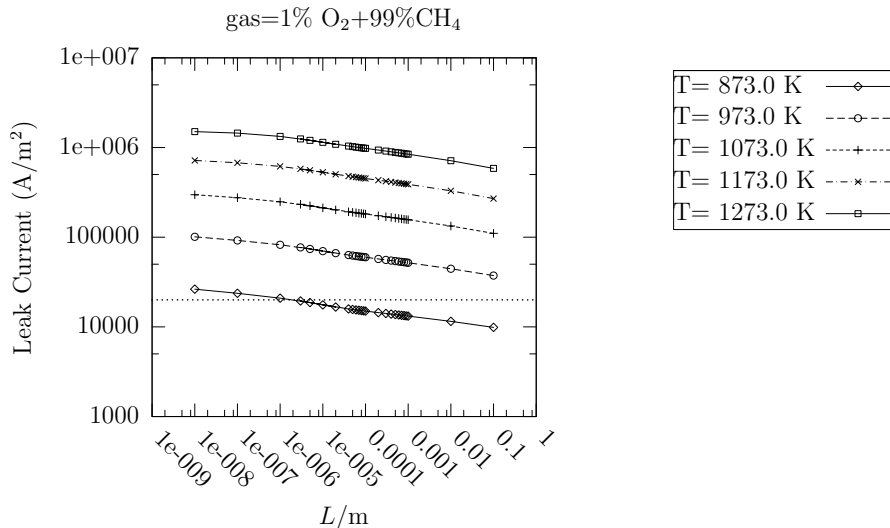


Figure 8.3: Open circuit leak current at different temperatures and thicknesses. The reducing gas is 1% O₂+ 99% CH₄. Dotted line shows $20000 \text{ A/m}^2 = 2 \text{ A/cm}^2$. The membranes are electrode limited due to nearly complete reduction.

In Figure 8.3 the simulated oxygen ion permeation current is shown as a function of membrane thickness and temperature. A strongly reducing gas mixture of 1% O₂+ 99% CH₄ is used (which is a mixture of mainly CH₄, CO, and H₂O at elevated temperatures), which corresponds to a point very close to the gas inlet position. The CG10 is quite reduced, so the electronic conductivity is high. Most of the driving force is thus spent over the surfaces resulting in surface limited transport with a weak thickness dependence. Fluxes at temperatures above 973 K are exceeding the target flux of 20000 A/m².

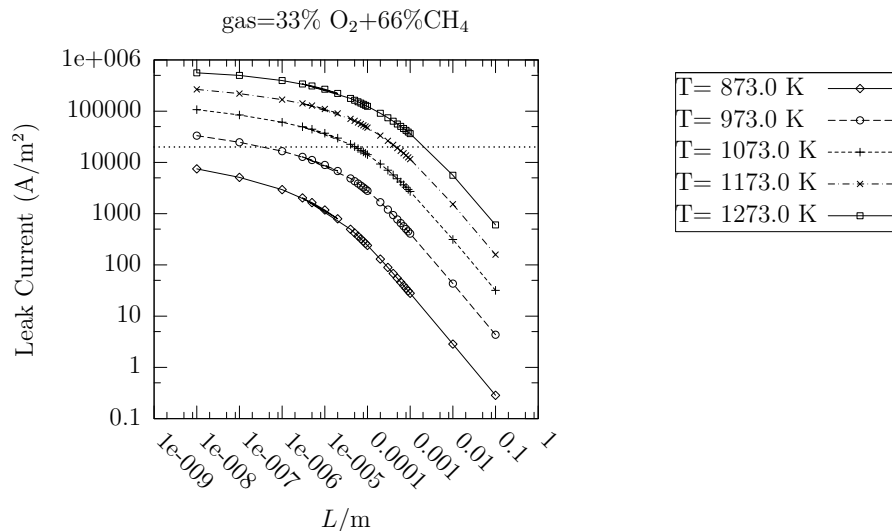


Figure 8.4: Open circuit leak current at different temperatures and thicknesses. The reducing gas is 33% O₂+ 67% CH₄. Dotted line shows 20000 A/m² = 2 A/cm². At large thicknesses, the leak is limited by the bulk electron conductivity. At small thicknesses the leak is limited by the surface exchange

Further away from the inlet, oxygen permeating through the membrane has increased the oxygen content of the reducing gas. In Figure 8.4 the simulated oxygen ion permeation current as a function of membrane thickness and temperature is shown. The gas mixture of 33% O₂+ 67% CH₄ (which becomes stoichiometric syngas at elevated temperatures) corresponds to a point close to the end of the membrane tube. This is where the lowest flux is seen as the CG10 will not have a very large electron conductivity. As can be seen, membrane thicknesses below 1 μm are required if a high flux is to be achieved below 973 K. At 1073 K and above high fluxes are obtained, even with thick membranes.

8.6 Thin films with small grain size

In a thin film, prepared with sputtering techniques, it is often possible to reduce the grain size of the film. It has been shown that the oxygen partial molar enthalpy is dependent on the grain size of doped ceria. For very small grain sizes enthalpy reductions of 50% [96] have been reported.

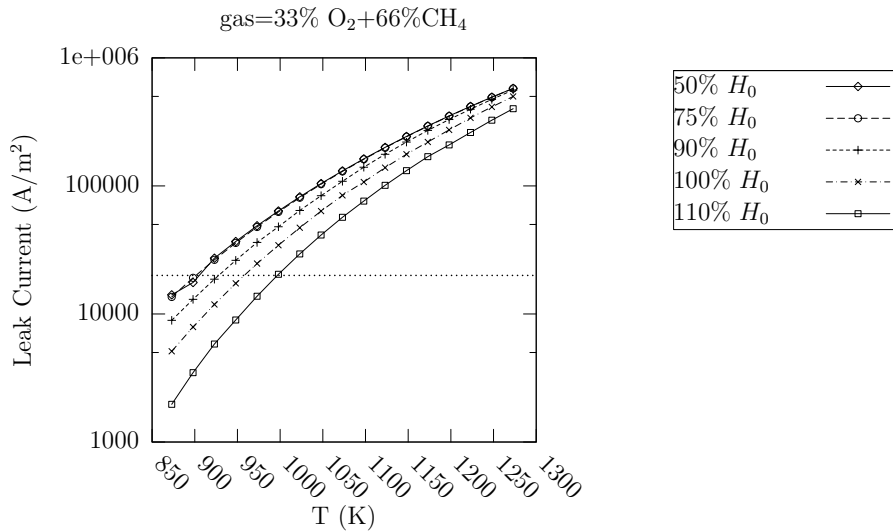


Figure 8.5: Thin film simulation. $L=100\text{nm}$.

The flux through a 100 nm thin film membrane as a function of temperature and partial molar enthalpy of the total oxidation reaction, H_{ox} (as fraction of the bulk partial molar enthalpy of the total oxidation reaction H_0) is plotted in Figure 8.5. With enthalpies below 75% H_0 the membrane is surface controlled, and further reduction of H_{ox} will have no effect. High fluxes can be maintained at temperatures as low as 873 K, if the enthalpy can be reduced below 75% H_0

8.7 Pr doped Ceria

Gadolinia doped ceria has high electronic resistance at high p_{O_2} , making it less efficient as a membrane material. Introduction of electronic conductivity by replacing Gd with Pr is evaluated in this section. The purpose is not to precisely evaluate the feasibility of using $\text{Ce}_{0.8}\text{Pr}_{0.2}\text{O}_{1.9\pm\delta}$ (CP20) specifically, but rather to evaluate the effect of Pr doping in general. Thus a pseudo-CP20 material is constructed, using σ_{O} measured by Wang *et al.* [81, 82] for $\text{Ce}_{0.8}\text{Gd}_{0.2}\text{O}_{1.9\pm\delta}$ (CG20) combined with σ_{e} measurements.

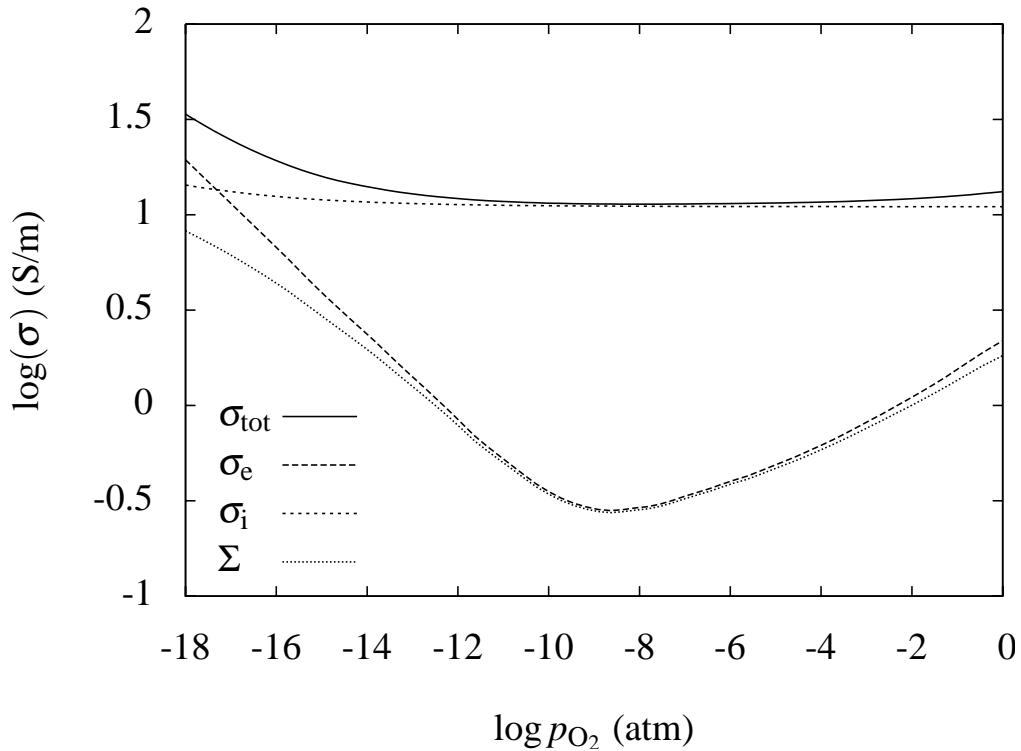


Figure 8.6: σ_o , σ_e and the ambipolar conductivity, Σ as a function of p_{O_2} at 1123 K for CP20

σ_o , σ_e and the ambipolar conductivity, Σ , are plotted as a function of p_{O_2} at 1123 K for CP20 in Figure 8.6. The jump in σ_e at $p_{O_2} = 10^{-6}$ atm is an artifact of the measured data. As it is in the low conductivity regime, it will not affect the simulations. Σ closely follows σ_e as $\sigma_e \ll \sigma_o$. The rise in Σ at high p_{O_2} is caused by p-type conductivity.

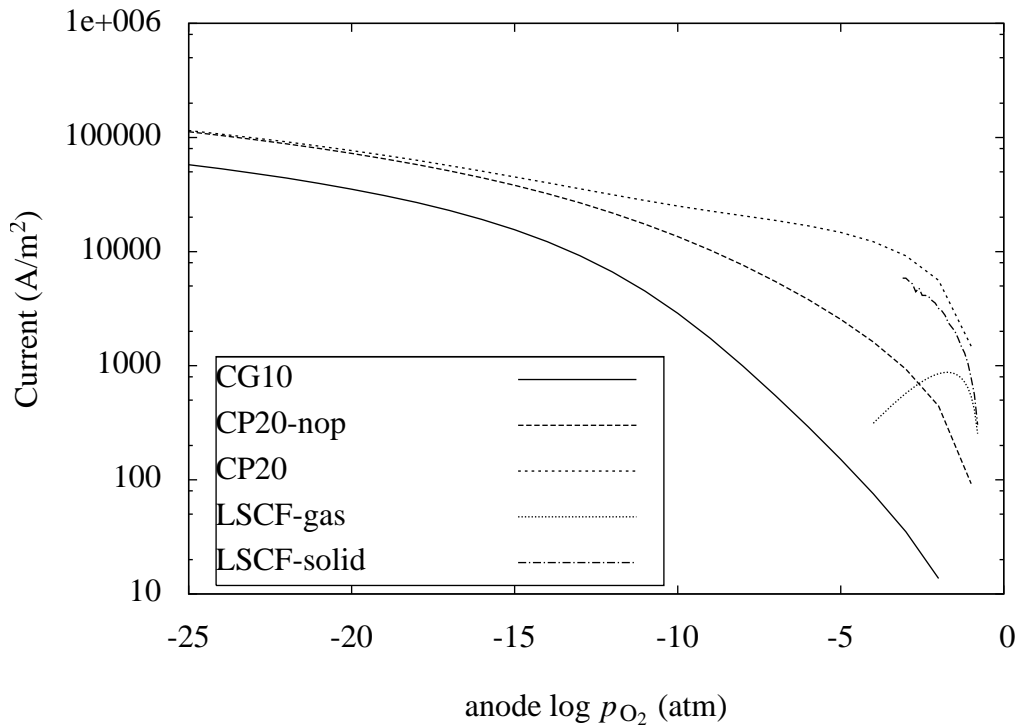


Figure 8.7: The flux through 10 μm thick membranes of different compositions at $T = 1123$ K as a function of the p_{O_2} at the syngas side.

The flux through 10 μm thick membranes of different compositions at $T = 1123\text{ K}$ is shown in Figure 8.7 as a function of the p_{O_2} at the anode side. CP20-nop is a membrane with the stoichiometry of CP20, but with the p-type conductivity set to 0. CG10, CP20-nop and CP20 have surface resistances representing the anode and cathode materials reported in section 7. LSCF-gas and LSCF-solid is for $(\text{La}_{0.6}\text{Sr}_{0.4})_{0.99}\text{Co}_{0.2}\text{Fe}_{0.8}\text{O}_{3-\delta}$ (LSCF) membranes with conductivities and surface resistances as measured in Chapter 2. LSCF-gas assumes that the surface exchange rate is determined by the oxygen chemical potential, μ_{O_2} , in the gas phase. LSCF-surf assumes that the surface exchange rate is determined by the μ_{O_2} in the MIEC surface. The performance of CP20 is comparable to the LSCF materials and superior to CG10 and CP20-nop at high anode p_{O_2} . In this regime, the whole membrane is oxidized, and the high performance of CP20 is attributable to its p-type conductivity. At low anode p_{O_2} the performance of CP20 is the same as that of CP20-nop, and thus the p-type doping has no effect.

It is remarkable that the p-type conductivity becomes irrelevant when the reducing gas has a $p_{\text{O}_2} < 10^{-15}\text{ atm}$, despite that one of the membrane sides is in direct contact with air. The reason can be read directly from the Wagner equation (rewritten for simplicity):

$$j_{\text{O}_2} \propto \int_{p_{\text{O}_2}^{\text{cathode}}}^{p_{\text{O}_2}^{\text{anode}}} \Sigma d \log p_{\text{O}_2} \quad (8.5)$$

The membranes can be divided in sections defined by the $\log p_{\text{O}_2}$ at the section limits. If the difference in $\log p_{\text{O}_2}$ between the borders of each section is the same for all sections, sections with large Σ will add more to the integral than those with small Σ . The Wagner equation reflects that doubling the conductivity is more advantageous in sections of high Σ than in sections of low Σ . The reason is that the low Σ section requires a large gradient in μ_{O_2} (equivalent to $\ln p_{\text{O}_2}$) to transport ions. In membranes with differences of orders of magnitude between the highest Σ and lowest Σ , this means that the width of the low Σ sections is inversely proportional to their Σ . The resistance of a low Σ section, $r = L/\Sigma$, where the L is the section width, is thus independent of Σ . The only addition to the resistance when Σ is reduced in this section, originates from the reduction of L , which means that other sections have to fill the extra space. This matters little as L for the low Σ sections is very low. This is illustrated in Fig 7.8.

8.8 Conclusions

- Syngas at atmospheric pressure is not stable below a temperature of 973 K and this temperature represents the lower limit of the operation temperature of a membrane for syngas production.
- CG10 syngas production membranes work in a regime where both electronic and ionic conductivity affects the flux.
- Ionic currents above 20000 A/m² are possible if the membrane thickness is 1 μm or less and $T > 973\text{ K}$.
- Reducing the enthalpy of oxidation will increase performance.
- Introducing p-type conductivity allows ceria based membranes to work as oxygen separation membranes at high T .

I thank Christodoulos Chartzichristodoulou for the σ_e data of CP20.

Chapter 9

Recommendations for further work.

In this Chapter a few recommendations for further investigation based on the findings of this thesis is stated.

- Further confirmation of the measurements of the electrolyte probe described in Chapters 2, 3 and 5 is needed. A combination of the conductivity relaxation setup and an electrolyte probe, performing relaxation measurements on a MIEC bar in the surface controlled domain, would yield two simultaneous measures of the surface resistance, r_s . For a MIEC bar made from LSMCF, measurement temperatures below 1073 K would be preferable, as the permeation term when calculating the p_{O_2} will be small. Using probes of different point sharpness will give insight into shadowing effects.

A combined conductivity relaxation and electrolyte probe measurement on a thin film MIEC could provide further information about the difference in surface resistance of bulk and thin film samples, such as that reported by Mosleh *et al.* (to be published).

- Reproduction of the abnormally low surface resistance, r_s , of LSCa10CF at $T > 1223$ K and LSB20CF at all measured temperatures is needed, preferably using a setup not relying on an electrolyte probe. Conductivity relaxation will, however, need extremely careful experiments to resolve the surface exchange at high temperatures.
- X-ray absorption near edge structure (XANES) measurements could be carried out at higher temperatures than the 773 K of the measurements in Chapter 6, and be applied to the LSMCF materials also. Knowledge about the temperatures and p_{O_2} where the individual cation species change valency could strengthen the analysis in Chapters 4 and 6.
- Measurements of the ionic conductivity of LSCa10CF at low temperatures could confirm whether the low activation energy measured in Chapter 5 results in unusually high ionic conductivity at intermediate temperatures ($773 \text{ K} < T < 973 \text{ K}$). This would make LSCa10CF an excellent ionic conductor for a composite cathode in intermediate temperature fuel cells.
- Production and testing of a LSCa10CF cathode for fuel cells operating in the range $T < 1273$ K should be feasible, as it is potentially superior to the standard LSCF cathode with regard to both ionic conductivity and surface resistance.
- Studies of the structural strength and stability of LSCa10CF at high p_{O_2} should be initiated, as it is an excellent candidate for an oxygen separation membrane for pure oxygen production.
- Production of a LSB15CF membrane could result in a membrane with the combination of the low r_s of LSB20CF and the good transport properties of LSB10CF. LSCa15CF and

LSCa20CF membranes would likewise be candidates for membranes with ionic conductivities comparable to that of LSCa10CF, but with the temperature range of the abnormally low r_s observed at 1273 K extended to lower temperatures.

- Further research into the spread of literature values of BSCF stoichiometry measurements are needed. A high temperature coulometric titration experiment, where complete reduction of the sample is obtained, could give yet another measure of the absolute stoichiometry, but care would have to be taken in order to seal the cell, as the long reaction times will make even small leaks critical.
- The coupling of the reduced diffusion coefficient to properties of the crystal structures, which was the objective of Chapters 4 and 5 failed. Part of the answer to that failure could be in the selection of the LSMCF series for this study. The materials contains up to six atomic species, and while Ba, Sr and Ca behaves similarly in many ways, they may be quite different in other ways. More importantly, the stability of Co containing materials, even at the relatively high p_{O_2} of these measurements is questionable, and adds another complication. Making similar measurements on the simpler $(Sr_{1-x}M_x)_{0.99}FeO_{3-\delta}$, M = Ca, Ba, Sr, series could yield a simpler analysis framework.

Bibliography

- [1] Paul N. Dyer, Robin E. Richards, Steven L. Russek, and Dale M. Taylor. Ion transport membrane technology for oxygen separation and syngas production. *Solid State Ionics*, 134:21–33, 2000.
- [2] R.T. Leah, N.P. Brandon, and P. Aguiar. Modelling of cells, stacks and systems based around metal-supported planar IT-SOFC cells with CGO electrolytes operating at 500-600°C. *Journal of Power Sources*, 145:336–352, 2005.
- [3] J. B. Hansen, J. Pålsson, J. U. Nielsen, N. Christiansen, E. Ramschak, M. Schüssler, and P. Preeninger. Successful testing of a sofc stack for mobile apu applications. *Fuel Cell Seminar, Palm Springs, California*, 2005.
- [4] P.J. Gellings and H.J.M. Bouwmeester. *The CRC Handbook of Solid State Electrochemistry*. CRC Press, 1997.
- [5] Stephen J. Skinner and John A. Kilner. Oxygen ion conductors. *Mater. Today* , 6:30–37, 2003.
- [6] S.P. Jiang and W. Wang. Novel structured mixed ionic and electronic conducting cathodes of solid oxide fuel cells. *Solid State Ionics*, 176:1351–1357, 2005.
- [7] Peter Vang Hendriksen, Peter Halvor Larsen, Mogens Mogensen, Finn Willy Poulsen, and Kjell Wiik. Prospects and problems of dense oxygen permeable membranes. *Catal. Today* , 56:283–295, 2000.
- [8] Henny J. M. Bouwmeester. Dense ceramic membranes for methane conversion. *Catal. Today* , 82:141–150, 2003.
- [9] Avner Rothschild and Harry L.Tuller. Gas sensors: New materials and processing approaches. *Journal of Electroceramics*, 17(2-4):1005–1012, 2006.
- [10] W. Wagner and K. M. de Reuck. Oxygen. *IUPAC International Tables of the Fluid State*, 9, 1987.
- [11] Joachim Maier. On the correlation of macroscopic and microscopic rate constants in solid state chemistry. *Solid State Ionics*, 112:197–228, 1998.
- [12] R.J.D. Tilley. *Principles and Applications of Chemical Defects*. Stanley Thornes (publishers) Ltd., 1998.
- [13] S. Kim, Y.L. Yang, A.J. Jacobson, and B. Abeles. Oxygen surface exchange in mixed ionic electronic conductor membranes. *Solid State Ionics* , 121:31–36, 1999.
- [14] S. Carter, A. Selcuk, R. J. Chater, J. Kajda, J. A. Kilner, and B. C. H. Steele. Oxygen transport in selected nonstoichiometric perovskite-structure oxides. *Solid State Ionics*, 53-56:597–605, 1992.

- [15] Isamu Yasuda and Tomoji Hikita. Precise determination of the chemical diffusion coefficient of calcium-doped lanthanum chromites by means of electrical conductivity relaxation. *Journal of the Electrochemical Society*, 141:1268–1273, 1994.
- [16] J.E. ten Elshof, M.H.R. Lankhorst, and H.J.M. Bouwmeester. Chemical diffusion and oxygen exchange of $\text{La}_{0.6}\text{Sr}_{0.4}\text{Co}_{0.2}\text{Fe}_{0.8}\text{O}_{3-\delta}$. *Solid State Ionics*, 99:15–22, 1997.
- [17] S. J. Benson, R. J. Chater, and J. A. Kilner. Oxygen diffusion and surface exchange in the mixed conducting perovskite $\text{La}_{0.6}\text{Sr}_{0.4}\text{Fe}_{0.8}\text{Co}_{0.2}\text{O}_{3-\delta}$. *Proc. - Electrochem. Soc.*, 97-24:596–609, 1999.
- [18] J.A. Lane and J.A. Kilner. Measuring oxygen diffusion and oxygen surface exchange by conductivity relaxation. *Solid State Ionics*, 136-137:997–1001, 2000.
- [19] Martin Sjøgaard, Peter Vang Hendriksen, Mogens Mogensen, Finn Willy Poulsen, and Eivind Skou. Oxygen nonstoichiometry and transport properties of strontium substituted lanthanum cobaltite. *Solid State Ionics*, 177:3285–3296, 2006.
- [20] P.R. Bevington and D.K. Robinson. *Data reduction and error analysis for the physical sciences*. McGraw-Hill Education, NY(US), 3rd edition, 2003.
- [21] J.E. ten Elshof, H.J.M. Bouwmeester, and H. Verweij. Oxygen transport through $\text{La}_{1-x}\text{Sr}_x\text{FeO}_{3-\delta}$ membranes. i. permeation in air/he gradients. *Solid State Ionics*, 81:97–109, 1995.
- [22] J.W. Stevenson, T.R. Armstrong, R.D. Carnheim, L.R. Pederson, and W.J. Weber. Electrochemical properties of mixed conducting perovskites $\text{La}_{1-x}\text{M}_x\text{Co}_{1-y}\text{Fe}_y\text{O}_{3-\delta}$ (m=sr, ba, ca). *J. Electrochem. Soc.*, 143:2722–2729, 1996.
- [23] J.A. Lane, S.J. Benson, D. Waller, and J.A. Kilner. Oxygen transport in $\text{La}_{0.6}\text{Sr}_{0.4}\text{Co}_{0.2}\text{Fe}_{0.8}\text{O}_{3-\delta}$. *Solid State Ionics*, 121:201–208, 1999.
- [24] Martijn Lankhorst. *Thermodynamic and Transport Properties of Mixed Ionic-Electronic Conducting Perovskite-type Oxides*. PhD thesis, Universiteit Twente, Enschede, 1997.
- [25] Martin Sjøgaard, Peter V. Hendriksen, and Finn Willy Poulsen. Determination of transport and catalytic properties of mixed ionic and electronic conductors using transient responses. *Proceedings of the 26th Risø International Symposium on Materials Science*, 1:355–362, 2005.
- [26] Yuemei L. Yang, A. J. Jacobsen, C. L. Chen, G. P. Luo, K. D. Ross, and C. W. Chu. Oxygen exchange kinetics on a highly oriented $\text{La}_{0.5}\text{Sr}_{0.5}\text{CoO}_{3-\delta}$ thin film prepared by pulsed-laser deposition. *Appl. Phys. Lett.*, 79(6):776–778, 2001.
- [27] B. Zachau-Christiansen, T. Jacobsen, and S. Skaarup. Electrochemical determination of oxygen stoichiometry and entropy in oxides. *Solid State Ionics*, 86-88:725–731, 1996.
- [28] A. Belzner, T. M. Gür, and R. A. Huggins. Measurement of the chemical diffusion coefficient of oxygen in mixed conductors by a solid state electrochemical method. *Solid State Ionics*, 40-41:535–538, 1990.
- [29] Stefan Diethelm. *Electrochemical Characterization of Oxygen Transport and Nonstoichiometry in Mixed Conducting Perovskite-Type Oxides*. PhD thesis, Lausanne EPFL, 2001.
- [30] Doh-Kwon Lee and Han-Il Yoo. Electrochemical determination of the oxygen permeability of $\text{La}_{1-x}\text{Ca}_x\text{CrO}_{3-\delta}$ ($x = 0.27$). *J. Electrochem. Soc.*, 147:2835–2843, 2000.

- [31] J. Fouletier, P. Fabry, and M. Kleitz. Electrochemical semipermeability and the electrode microsystem in solid oxide electrolyte cells. *J. Electrochem. Soc.* , 123:204, 1976.
- [32] H.-D. Wiemhöfer, H.-G. Bredes, U. Nigge, and W. Zipprich. Studies of ionic transport and oxygen exchange on oxide materials for electrochemical gas sensors. *Solid State Ionics*, 150:63–77, 2002.
- [33] L. A. Chick, G. L. Maupin, L. R. Pederson, D. E. McCready, and J. L. Bates. Redox effects in self-sustaining combustion synthesis of oxide ceramic powders. *Mat. Res. Soc. Symp. Proc.*, 249:159–164, 1992.
- [34] C. Wagner and W. Schottky. Beitrag zur Theorie des Anlaufsvorganges. *Z. Phys. Chem. B* 11, 11, 1930.
- [35] J. Crank. *The Mathematics of Diffusion*. Oxford University Press, 1975.
- [36] Robert C. Reid, John M. Prausnitz, and Bruce E. Polling. *The Properties of Gases and Liquids*. McGraw-Hill, Inc, 1987.
- [37] Martin Søgaaard, Peter Vang Hendriksen, and Mogens Mogensen. Oxygen nonstoichiometry and transport properties of strontium substituted lanthanum ferrite. *J. Solid State Chem* , 180:1489–1503, 2007.
- [38] L-W. Tai, M.M. Nasrallah, H. U. Anderson, D.M. Sparlin, and S.R. Sehlin. Structure and electrical properties of $\text{La}_x\text{Sr}_{1-x}\text{Co}_{1-y}\text{Fe}_y$ part 2. the system $\text{La}_{1-x}\text{Sr}_x\text{Co}_{0.2}\text{Fe}_{0.8}$. *Solid State Ionics*, 76:273–283, 1995.
- [39] M.W. den Otter. *A study of OXYGEN TRANSPORT in mixed conducting oxides using isotopic exchange and conductivity relaxation*. PhD thesis, Universiteit Twente, Enschede, 2000.
- [40] Hyung-Tae Lim and Anil V. Virkar. Thermoelectric power of gd-doped $\text{ce}_{0.1}\text{ce}_{0.9}\text{o}_{2-\delta}$ (gdc10): Measurements on porous samples. *J. Power Sources* , 161:676–684, 2006.
- [41] Isamu Yasuda and Masakazu Hishinuma. Electrical conductivity and chemical diffusion coefficient of strontium-doped lanthanum manganites. *Journal of Solid State Chemistry*, 123:382–390, 1996.
- [42] Chang-Rock Song and Han Ill Yoo. Chemical diffusivity of $\text{BaTiO}_{3-\delta}$. *Solid State Ionics*, 124:289–299, 1999.
- [43] S. Wang, P.A.W. van der Heide, C. Chavez, A.J. Jacobson, and S.B. Adler. An electrical conductivity relaxation study of $\text{La}_{0.6}\text{Sr}_{0.4}\text{Fe}_{0.8}\text{Co}_{0.2}\text{O}_{3-\delta}$. *Solid State Ionics*, 156:201–208, 2003.
- [44] Bjarke Dalslet, Martin Søgaaard, and Peter Vang Hendriksen. Determination of oxygen transport properties from flux and driving force measurements using an oxygen pump and an electrolyte probe. *J. Electrochem. Soc.* , 154(12), 2007.
- [45] L-W. Tai, M.M. Nasrallah, and H. U. Anderson. Thermochemical stability, electrical conductivity, and seebeck coefficient of Sr-doped $\text{LaCo}_{0.2}\text{Fe}_{0.8}\text{O}_{3-\delta}$. *Journal of Solid State Chemistry*, 118:117–124, 1995.
- [46] M. H. R. Lankhorst and J. E. ten Elshof. Thermodynamic quantities and defect structure of $\text{La}_{0.6}\text{Sr}_{0.4}\text{Co}_{1-y}\text{Fe}_y\text{O}_{3-\delta}$ ($y = 0 - 0.6$) from high-temperature coulometric titration experiments. *Journal of Solid State Chemistry*, 130:302–310, 1997.

- [47] Ronald L. Cook and Anthony F. Sammels. On the systematic selection of perovskite solid electrolytes for intermediate temperature fuel cells. *Solid State Ionics*, 45:311–321, 1991.
- [48] C.Y. Tsai, A.G. Dixon, Y.H. Ma, W.R. Moser, and M.R. Pascucci. Dense perovskite, $\text{La}_{1-x}\text{A}_x\text{Fe}_{1-y}\text{Co}_y\text{O}_{3-\delta}$ (A = Ba, Sr, Ca), membrane synthesis, applications, and characterization. *J. Electrochem. Soc.*, 81:1437, 1998.
- [49] Mogens Mogensen, Dorthe Lybye, Nikolaos Bonanos, and Peter V. Hendriksen. Oxide ion transport in solid oxide fuel cells. *Advances in Science and Technology*, 29:1261–1272, 2000.
- [50] M. Mogensen, D. Lybye, N. Bonanos, P.V. Hendriksen, and F.W. Poulsen. Factors controlling the oxide ion conductivity of fluorite and perovskite structured oxides. *Solid State Ionics*, 174:279–286, 2004.
- [51] W.G. Wang, R. Barfod, P.H. Larsen, K. Kammer, J. Bentzen, P.V. Hendriksen, and M. Mogensen. Improvement of LSM cathode for high power density SOFC. *SOFC VIII (Paris) proceedings*, page 400, 2003.
- [52] R. D. Shannon. Revised effective ionic radii and systematic studies of interatomic distances in halides and chalcogenides. *Acta Crystallographica*, A32:751–767, 1976.
- [53] Junichiro Mizusaki, Shigeru Yamauchi, Kazuo Fueki, and Akira Ishikawa. Nonstoichiometry of the perovskite-type oxide $\text{La}_{1-x}\text{Sr}_x\text{CrO}_{3-\delta}$. *Solid State Ionics*, 12:119–124, 1984.
- [54] Tetsuro Nakamura, G. Petzow, and L. J. Gauckler. Stability of the perovskite phase LaBO_3 (B = V, Cr, Mn, Fe, Co, Ni) in reducing atmosphere i. experimental results. *Materials Research Bulletin*, 14:649–659, 1979.
- [55] Finn Willy Poulsen and Martin Søggaard. Defect chemistry modelling of complex soft materials. *Proc. 5. th. European SOFC Forum*, 2002.
- [56] Qinghua Yin and Y. S. Lin. Effect of dopant addition on oxygen sorption properties of La – Sr – Co – Fe – O perovskite type oxide. *Adsorption*, 12(5-6):329–338, 2006.
- [57] Dionissios Mantzavinos, Anne Hartley, Ian S. Metcalfe, and Mortaza Sahibzada. Oxygen stoichiometries in $\text{La}_{1-x}\text{Sr}_x\text{Co}_{1-y}\text{Fe}_y\text{O}_{3-\delta}$ perovskites at reduced oxygen partial pressures. *Solid State Ionics*, 134:103–109, 2000.
- [58] S.P. Scott, D. Mantzavinos, A. Hartley, M. Sahibzada, and I.S. Metcalfe. Reactivity of lscf perovskites. *Solid State Ionics*, 152-153:777–781, 2002.
- [59] Bjarke Dalslet, Martin Søggaard, and Peter Vang Hendriksen. Defect chemistry and oxygen transport of $(\text{La}_{0.6}\text{Sr}_{0.4-x}\text{M}_x)_{0.99}\text{Co}_{0.2}\text{Fe}_{0.8}\text{O}_{3-\delta}$, $m = \text{ca}$ ($x = 0.05, 0.1$), ba ($x = 0.1, 0.2$), sr , part i: Defect chemistry. *to be published*, 2008.
- [60] C. Wagner. Equations for transport in solid oxides and sulfides of transition metals. *Prog. Solid State Chem.*, 10:3–16, 1975.
- [61] Zongping Shao and Sossina M. Haile. A high-performance cathode for the next generation of solid-oxide fuel cells. *Nature*, 43:170–173, 2004.
- [62] Steven McIntosh, Jaap F. Vente, Wim G. Haije, Dave H. A. Blank, and Henny J. M. Bouwmeester. Structure and oxygen stoichiometry of $\text{SrCo}_{0.8}\text{Fe}_{0.2}\text{O}_{3-\delta}$ and $\text{Ba}_{0.5}\text{Sr}_{0.5}\text{Co}_{0.8}\text{Fe}_{0.2}\text{O}_{3-\delta}$. *Solid State Ionics*, 177:1737–1742, 2006.

- [63] Steven McIntosh, Jaap F. Vente, Wim. G. Haije, Dave H. A. Blank, and Henny J. M. Bouwmeester. Oxygen stoichiometry and chemical expansion of $\text{Ba}_{0.5}\text{Sr}_{0.5}\text{Co}_{0.8}\text{Fe}_{0.2}\text{O}_{3-\delta}$ measured by in situ neutron diffraction. *Chem. Mater.*, 18:2187–2193, 2006.
- [64] Zhihao Chen, Ran Ran, Wei Zhou, Zongping Shao, and Shaomin Liu. Assessment of $\text{Ba}_{0.5}\text{Sr}_{0.5}\text{Co}_{1-y}\text{Fe}_y\text{O}_{3-\delta}$ ($y=0.0-1.0$) for prospective application as cathode for it-sofcs or oxygen permeating membrane. *Electrochimica Acta*, 52:7343–7351, 2007.
- [65] Pingying Zeng, Zhihao Chen, Wei Zhou, Hongxia Gu, Zongping Shao, and Shaomin Liu. Re-evaluation of $\text{Ba}_{0.5}\text{Sr}_{0.5}\text{Co}_{0.8}\text{Fe}_{0.2}\text{O}_{3-\delta}$ perovskite as oxygen semi-permeable membrane. *Journal of Membrane Science*, 291:148–156, 2007.
- [66] Mogens Mogensen, Nigel M. Sammes, and Geoff A. Tompsett. Physical, chemical and electrochemical properties of pure and doped ceria. *Solid State Ionics*, 129:63–94, 2000.
- [67] Hideaki Inaba and Hiroaki Tagawa. Ceria based solid electrolytes. *Solid State Ionics*, 83:1–16, 1996.
- [68] Wei Guo Wang and Mogens Mogensen. High-performance lanthanum-ferrite-based cathode for SOFC. *Solid State Ionics*, 176:457–462, 2005.
- [69] Xingyan Xu, Changrong Xia, Guoliang Xiao, and Dingkun Peng. Fabrication and performance of functionally graded cathodes for it-sofcs based on doped ceria electrolytes. *Solid State Ionics*, 176:1513–1520, 2005.
- [70] Zhonghe Bi, Mojie Cheng, Yonglai Dong, Hejin Wu, Yunchuan She, and Baolian Yi. Electrochemical evaluation of $\text{La}_{0.6}\text{Sr}_{0.4}\text{CoO}_3 - \text{La}_{0.45}\text{Ce}_{0.55}\text{O}_2$ composite cathodes for anode-supported $\text{La}_{0.45}\text{Ce}_{0.55}\text{O}_2 - \text{La}_{0.9}\text{Sr}_{0.1}\text{Ga}_{0.8}\text{Mg}_{0.2}\text{O}_{2.85}$ bilayer electrolyte solid oxide fuel cells. *Solid State Ionics*, 176:655–661, 2005.
- [71] Changrong Xia, Fanglin Chen, , and Meilin Liu. Reduced-temperature solid oxide fuel cells fabricated by screen printing. *Electrochemical Solid-State Letters*, 4:A52–A54, 2001.
- [72] Takashi Hibino, Atsuko Hashimoto, Kazuyo Asano, Masaya Yano, Masanori Suzuki, and Mitsuru Sano. An intermediate-temperature solid oxide fuel cell providing higher performance with hydrocarbons than with hydrogen. *Electrochemical and Solid-State Letters*, 5:A242–A244, 2002.
- [73] Shaowu Zha, Ashley Moore, Harry Abernathy, and Meilin Liu. Gdc-based low-temperature sofcs powered by hydrocarbon fuels. *Journal of the Electrochemical Society*, 151:A1128–A1133, 2004.
- [74] P. Attryde, A. Baker, S. Baron, A. Blake, N. P. Brandon, D. Corcoran, D. Cumming, A. Duckett, K. El-Koury, D. Haigh, M. Harrington, C. Kidd, R. Leah, G. Lewis, C. Matthews, N. Maynard, T. McColm, A. Selcuk, M. Schmidt, R. Trezona, and L. Verdugo. Stacks and systems based around metal supported SOFCs operating at 500-600c. *SOFC IX (Quebec) proceedings*, pages 113–123, 2005.
- [75] Mogens Mogensen, D. Lybye, K. Kammer, and N. Bonanos. Ceria revisited: Electrolyte or electrode material? *SOFC IX (Quebec) proceedings*, 2005.
- [76] J. Näfe. Solid electrolyte galvanic cell under load. *Journal of Applied Electrochemistry*, 31:1235–1241, 2001.
- [77] I. Riess, M. Gödickemeier, and L.J. Gauckler. Characterization of solid oxide fuel cells based on solid electrolytes or mixed ionic electronic conductors. *Solid State Ionics*, 90:91–104, 1996.

- [78] B. C. H. Steele. Appraisal of $\text{Ce}_{1-y}\text{Gd}_y\text{O}_{2-y/2}$ electrolytes for IT-SOFC operation at 500°C . *Solid State Ionics*, 129:95–110, 2000.
- [79] Toshiaki Matsui, Minoru Inaba, Atsushi Mineshige, and Zempachi Ogumi. Electrochemical properties of ceria-based oxides for use in intermediate-temperature SOFCs. *Solid State Ionics*, 176:647–654, 2005.
- [80] Anil V. Virkar. Theoretical analysis of the role of interfaces in transport through oxygen ion and electron conducting membranes. *Journal of Power Sources*, 147:8–31, 2005.
- [81] Shaorong Wanga, Hideaki Inaba, Hiroaki Tagawa, Masayuki Dokiya, and Takuya Hashimoto. Nonstoichiometry of $\text{Ce}_{0.9}\text{Gd}_{0.1}\text{O}_{1.95-x}$. *Solid State Ionics*, 107:73–79, 1998.
- [82] Shaorong Wang, Takehisa Kobayashi, Masayuki Dokiya, and Takuya Hashimoto. Electrical and ionic conductivity of gd-doped ceria. *Journal of The Electrochemical Society*, 147:3606–3609, 2000.
- [83] S. Primdahl and M. Mogensen. Limitations in the hydrogen oxidation rate on ni/ysz anodes. *Proceedings. 6. International symposium on solid oxide fuel cells (SOFC 6)*, PV 99-19:530–540, 1999.
- [84] R. Barfod, M. Mogensen, T. Klemensø, A. Hagen, Y.-L. Liu, and P.V. Hendriksen. Detailed characterization of anode supported sofc by impedance spectroscopy. *Proceedings of the 9th International symposium on solid oxide fuel cells (SOFC IX)*, volume PV 2005-07:524–533, 2005.
- [85] C. C. Appel, N. Bonanos, A. Horsewell, and S. Linderoth. Ageing behaviour of zirconia stabilised by yttria and manganese oxide. *Journal of Materials Science*, 36:4493–4501, 2001.
- [86] Toshio Suzuki, Igor Kosacki, and Harlan U. Anderson. Defect and mixed conductivity in nanocrystalline doped cerium oxide. *Journal of the American Ceramic Society*, 85:1492–1498, 2002.
- [87] Y.-M. Chiang, E. B. Lavik, I. Kosacki, H. L. Tuller, and J. Y. Ying. Defect and transport properties of nanocrystalline CeO_{2-x} . *Applied Physics Letters*, 69:185–187, 1996.
- [88] Y.-M. Chiang, E. B. Lavik, and D. A. Blom. Defect thermodynamics and electrical properties of nanocrystalline oxides: Pure and doped CeO_2 . *Nanostructured Materials*, 9:633–642, 1997.
- [89] A. Hagen, R. Barfod, P.V. Hendriksen, Y.-L. Liu, and S. Ramousse. Degradation of anode supported sofc as a function of temperature and current load. *J. Electrochem. Soc.*, 154:A1165–A1171, 2006.
- [90] Søren Koch, Peter Vang Hendriksen, Mogens Mogensen, Yi-Lin Liu, Nico Dekker, Bert Rietveld, Bert de Haart, and Frank Tietz. Solid oxide fuel cell performance under severe operating conditions. *Fuel Cells*, 6:130–136, 2006.
- [91] Yoshio Matsuzaki and Isamu Yasuda. Electrochemical properties of reduced-temperature sofc with mixed ionic-electronic conductors in electrodes and/or interlayers. *Solid State Ionics*, 152-153:463–468, 2002.
- [92] Tuong Lan Nguyen, Kenichi Kobayashi, Takeo Honda, Youko Iimura, Ken Kato, Akira Neghisi, Ken Nozaki, Fabrizio Tappero, Kazuya Sasaki, Hiroshi Shirahama, Kenichiro Ota, Masayuki Dokiya, and Tohru Kato. Preparation and evaluation of doped ceria interlayer on

- supported stabilized zirconia electrolyte sofc's by wet ceramic processes. *Solid State Ionics*, 174:163–174, 2004.
- [93] Mitsunobu Shiono, Kenichi Kobayashi, Tuong Lan Nguyen, Kan Hosoda, Toru Kato, Kenichiro Ota, and Masayuki Dokiya. Effect of CeO₂ interlayer on ZrO₂ electrolyte/La(Sr)CoO₃ cathode for low-temperature sofc's. *Solid State Ionics*, 170:1–7, 2004.
- [94] N.M. Sammes and Zhihong Cai. Ionic conductivity of ceria/yttria stabilized zirconia electrolyte materials. *Solid State Ionics*, 100:39–44, 1997.
- [95] D.P. Fagg, J.R. Frade, V.V. Kharton, and I.P. Marozau. The defect chemistry of Ce(Pr,Zr)O_{2-δ}. *Journal of Solid State Chemistry*, 179:1469–1477, 2006.
- [96] Jennifer L.M. Rupp and Ludwig J. Gauckler. Microstructures and electrical conductivity of nanocrystalline ceria-based thin films. *Solid State Ionics*, 177:2513–2518, 2006.

Appendix

A Chemical Potential of Oxygen in the Gas Phase

The following equations and values are all taken from "Oxygen International Thermodynamic Tables Of The Fluid State - 9" [10].

The entropy, $S^{\text{id}}(T)$, and the enthalpy, $H^{\text{id}}(T)$, of an ideal gas at the temperature, T and the pressure $P_A = 1$ atm can be found from the equations below:

$$S^{\text{id}}(T, P_A) = R \left[-\frac{2n_1}{3} \left(\frac{T}{K}\right)^{-\frac{3}{2}} + n_2 \ln\left(\frac{T}{K}\right) + \frac{n_3}{2} \left(\frac{T}{K}\right)^2 + n_4 \left(\frac{ue^u}{e^u - 1} - \ln(e^u - 1)\right) + n_5 \left(\frac{\frac{2}{3}\eta e^{-\eta}}{1 + \frac{2}{3}e^{-\eta}} + \ln\left(1 + \frac{2}{3}e^{-\eta}\right)\right) \right]_{298.15\text{K}}^T + 205.146 \text{ J mol}^{-1} \text{ K}^{-1} \quad (\text{A.1})$$

$$H^{\text{id}}(T, P_A) = R(1(\text{K})) \left[-2n_1 \left(\frac{T}{K}\right)^{-\frac{1}{2}} + n_2 \frac{T}{K} + \frac{n_3}{3} \left(\frac{T}{K}\right)^3 + n_4 \frac{u\left(\frac{T}{K}\right)}{e^u - 1} - n_5 \frac{\eta\left(\frac{T}{K}\right)}{1 + \frac{2}{3}e^{-\eta}} \right]_{298.15\text{K}}^T \quad (\text{A.2})$$

In the above equations $u = n_6/T$ and $\eta = n_7/T$ and the values of $n_1, n_2, n_3, n_4, n_5, n_6$ and n_7 can be found in Table A.1.

Using these formulas the entropy and the enthalpy is determined at a temperature T . The term $205.146 \text{ J mol}^{-1} \text{ K}^{-1}$ (in Equation A.1) originates from the entropy difference between the state of the ideal crystal at 0 K and that of the ideal gas at (298.15 K, 0.1 MPa).

The chemical potential of oxygen in the gas phase is then calculated as

$$\mu_{\text{O}_2} = \mu_{\text{O}_2}^{\ominus} + RT \ln\left(\frac{P}{P_A}\right) \quad (\text{A.3})$$

Table A.1: Values of n_i to be used in Equation A.1 and Equation A.2.

n_1	1.06778
n_2	3.50042
n_3	0.166961×10^{-7}
n_4	1.01258
n_5	0.944365
n_6	2242.45 K
n_7	11580.4 K

where

$$\mu_{\text{O}_2}^{\ominus} = H^{\text{id}}(T, P_A) - TS^{\text{id}}(T, P_A) \quad (\text{A.4})$$

B Derivation of the average driving force above the membrane

When a molar flow of oxygen, J_{O_2} [mol s⁻¹], passes through the membrane it will change the p_{O_2} in the upper compartment:

$$p_{\text{O}_2} = p_{\text{O}_2}^{\text{in}} + \frac{J_{\text{O}_2}}{J_{\text{N}_2/\text{O}_2} + J_{\text{O}_2}} \approx p_{\text{O}_2}^{\text{in}} + \frac{J_{\text{O}_2}RT\Phi_f}{P\Phi_f} \quad (\text{B.5})$$

where $J_{\text{N}_2/\text{O}_2}$ is the molar flow of the nitrogen/air mixture, led from the external gas supply through the tubes into the upper compartment. P is the absolute pressure, Φ_f is the volume flow, and T_{Φ_f} is the T where the volume flow is measured.

The gas flow enters the upper compartment above the center of the membrane and moves towards the periphery. The p_{O_2} above the center of the membrane will thus be close to the p_{O_2} of the gas entering the chamber, while the p_{O_2} of the gas at the periphery will be close to the p_{O_2} of the gas leaving the chamber. $V_{\text{Nernst}}^{\text{upper}}$ will thus depend on the distance from the center of the membrane, r :

$$V_{\text{Nernst}}^{\text{upper}}(r) = \frac{RT}{4F} \ln \left(\frac{p_{\text{O}_2}^{\text{in}} + \frac{J_{\text{O}_2}(r)RT\Phi_f}{P\Phi_f}}{p_{\text{O}_2}^{\text{ref}}} \right) \quad (\text{B.6})$$

where $J_{\text{O}_2}(r)$ is the amount of oxygen passing through the membrane inside a circle with radius r . $J_{\text{O}_2}(r)$ is a fraction of J_{O_2} :

$$J_{\text{O}_2}(r) = \int_0^r J_{\text{O}_2} \frac{2\pi r'}{\pi r_0} dr' = \frac{r^2}{r_0^2} J_{\text{O}_2} \quad (\text{B.7})$$

where r_0 is the total exposed membrane surface. The average $V_{\text{Nernst}}^{\text{upper}}$ on the surface is:

$$V_{\text{Nernst}}^{\text{upper}} = \frac{1}{\pi r_0^2} \int_0^{r_0} V_{\text{Nernst}}^{\text{upper}}(r) \cdot 2\pi r dr \quad (\text{B.8})$$

which leads to Eq. 2.22.

C Correlation of D_V^0 with structural parameters

In Chapter 5, a number of material parameters are mentioned, which are speculated to dictate the transport of oxide ions. Here, plots are shown of the relevant parameters.

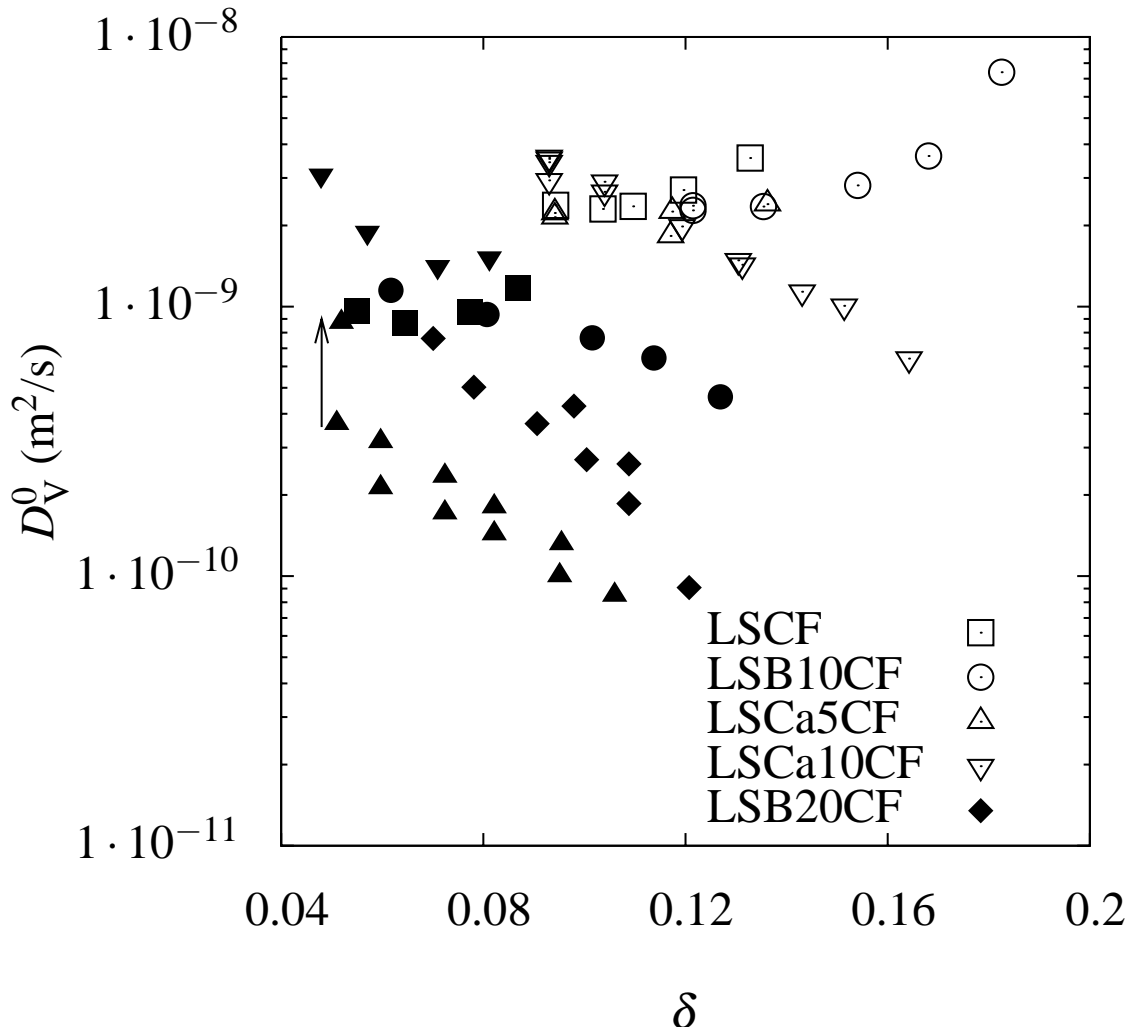


Figure B.1: D_V^0 as a function of δ . Filled symbols are measurements at $T = 1123 \text{ K}$; open symbols are measurements at $T = 1123 \text{ K}$

In the vacancy diluted regime, no influence of the oxygen substoichiometry, δ on D_V^0 is expected. The oxygen substoichiometry of the LSMCF materials (0.04-0.2) are however large enough that the dilution criteria is not necessarily satisfied. Then it is expected that ordering and trapping of ionic defects will begin to limit D_V^0 as δ is increased. Figure B.1 plots D_V^0 as a function of δ . No unique correlation between the values of δ and D_V^0 is seen.

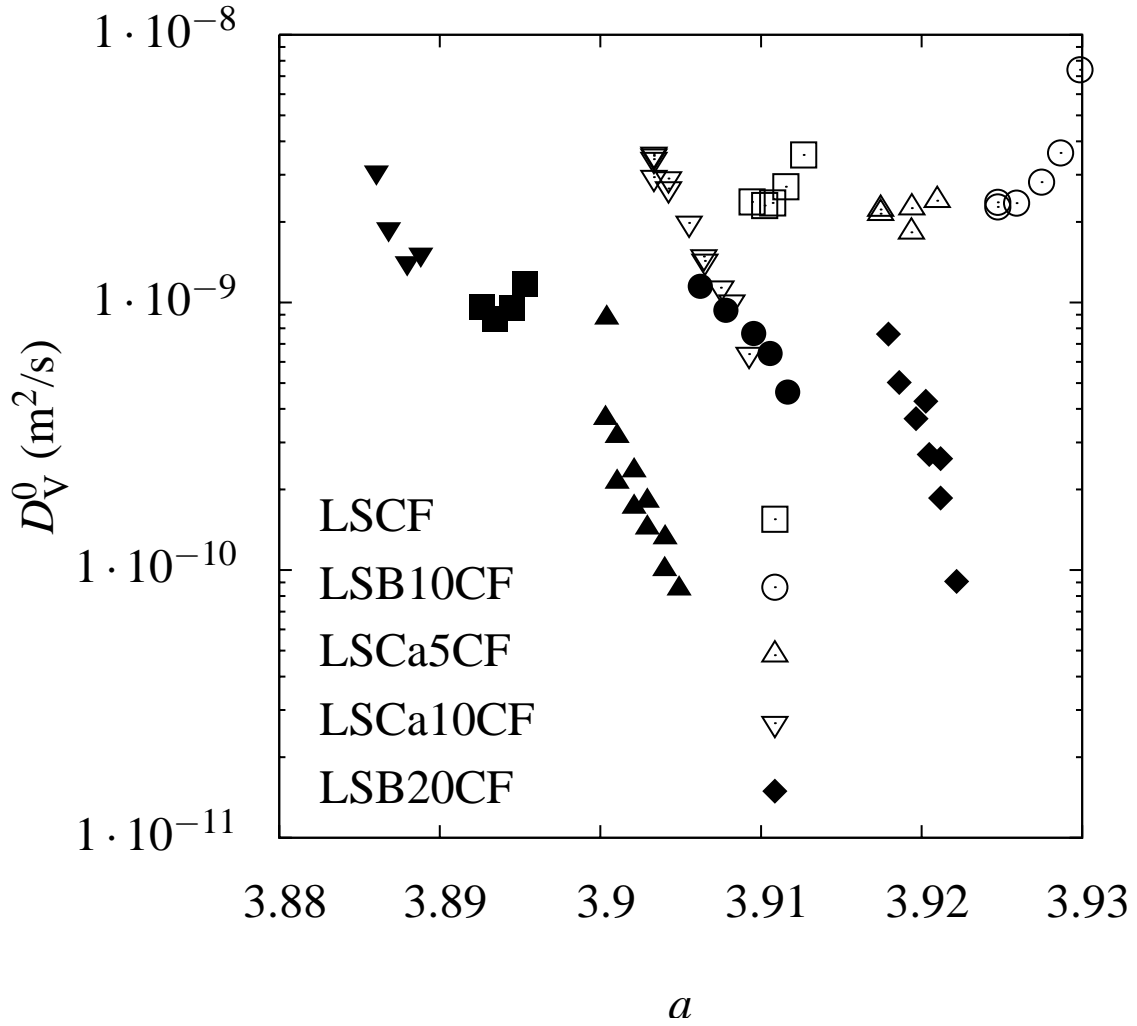


Figure B.2: D_V^0 as a function of the pseudo-cubic lattice constant a . Filled symbols are measurements at $T = 1123\text{ K}$; open symbols are measurements at $T = 1123\text{ K}$

When jumping between the oxide sites oxide ions need to overcome the repulsion of the neighbouring cations. The pseudo-cubic lattice constant $a = V_F^{1/3}$, where V_F is the volume of the perovskite formula unit, is a measure of how open the crystal structure is. Figure B.2 plots D_V^0 as a function of the pseudo-cubic lattice constant $a = V_F^{1/3}$. No unique correlation between the values of a and D_V^0 is seen.

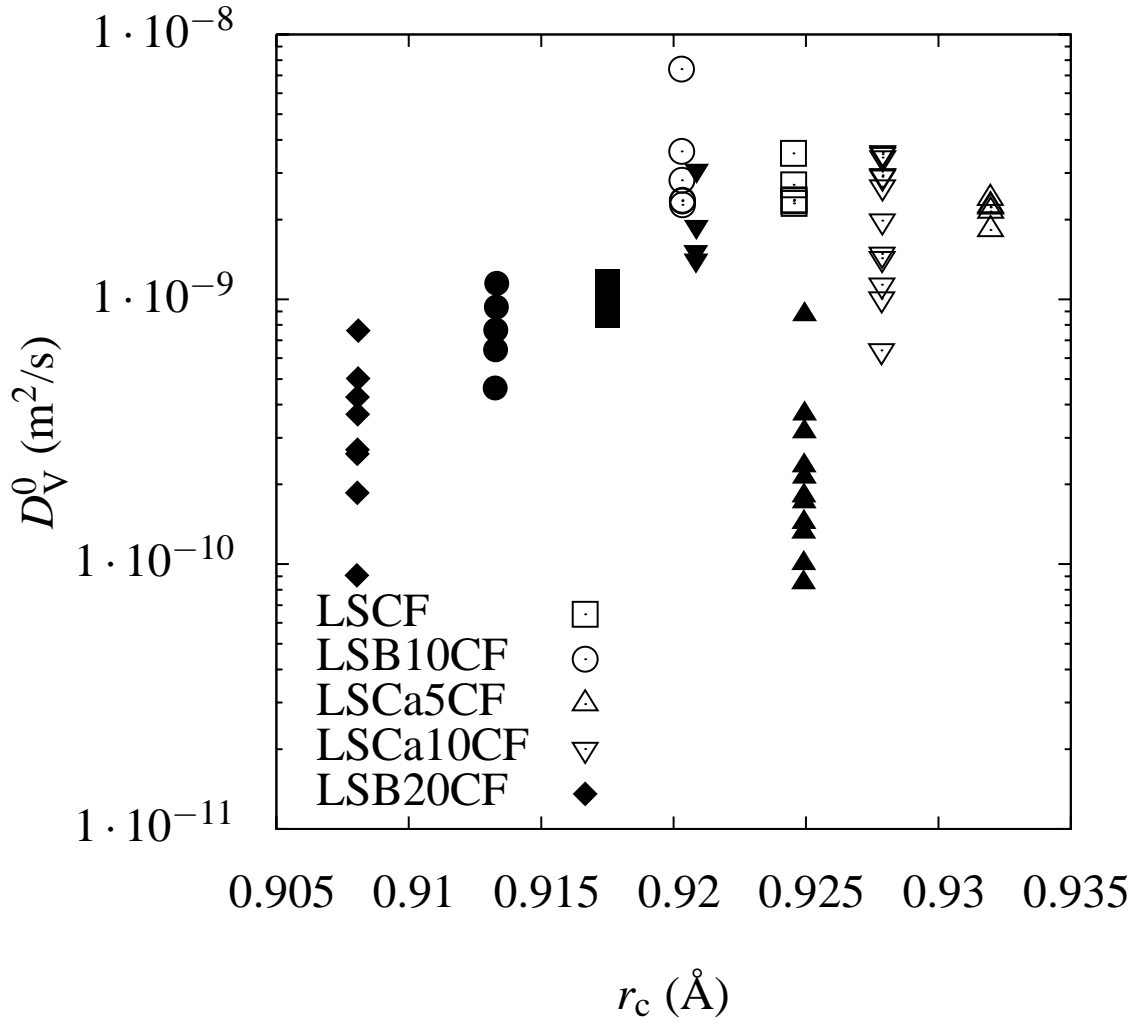


Figure B.3: D_V^0 as a function of the critical radius of oxygen ion jumps. Filled symbols are measurements at $T = 1123\text{ K}$; open symbols are measurements at $T = 1123\text{ K}$

Another measure of the ease with which the oxide ions can jump from one site to another, is the radius of the saddle point halfway between the sites, where the gap is at its narrowest. The critical radius, r_c , is defined as:

$$r_c = \frac{r_A^2 + \frac{4}{3}a^2 - \sqrt{2}ar_B + r_B^2}{2r_A + \sqrt{2}a - 2r_B} \quad (\text{C.9})$$

where r_A and r_B is the ionic radius of the A and B cations respectively. D_V^0 as a function of the critical radius of oxygen ion jumps is plotted in Fig B.3. No direct correlation between the values of r_c and D_V^0 is seen.

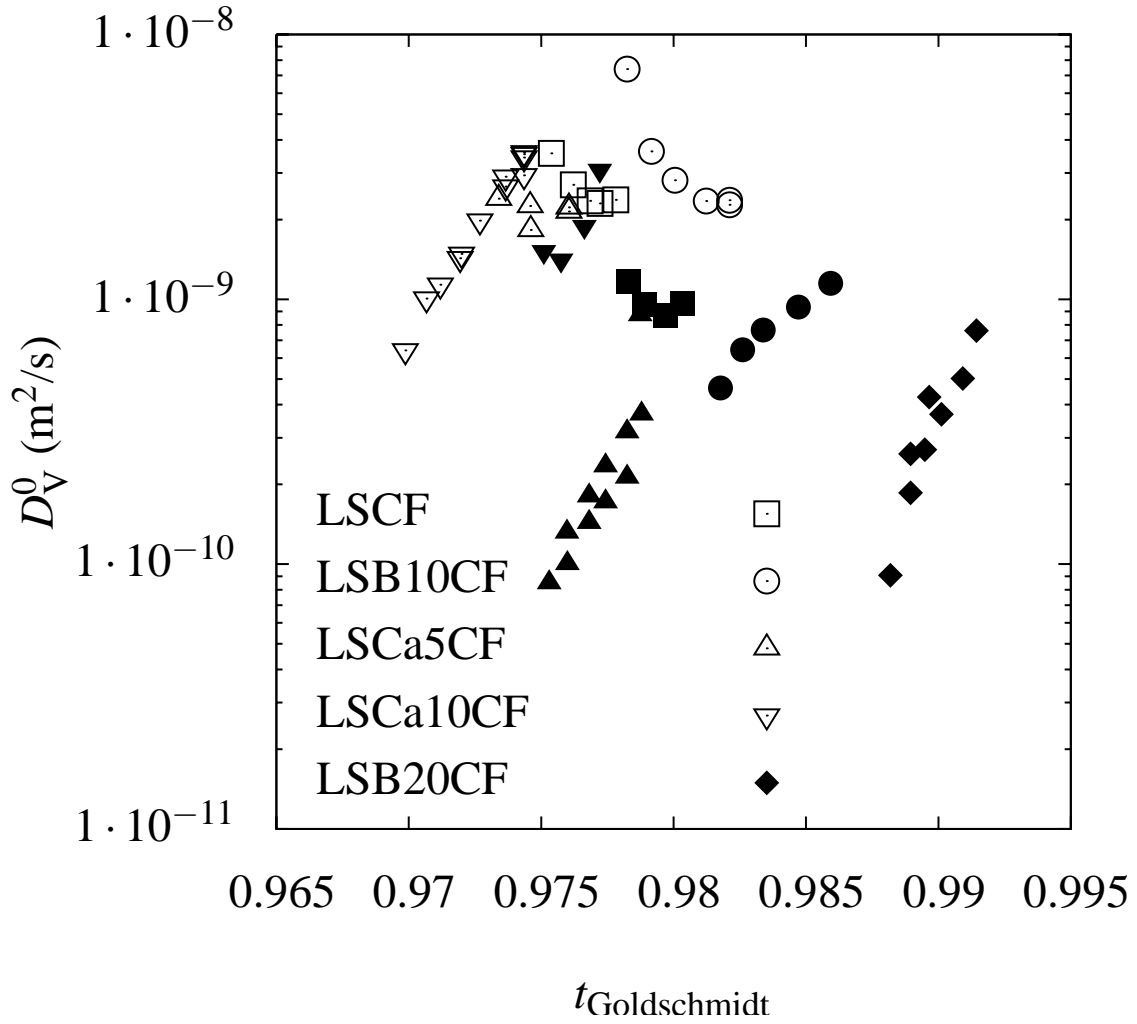


Figure B.4: D_V^0 as a function of the Goldschmidt factor. Filled symbols are measurements at $T = 1123 \text{ K}$; open symbols are measurements at $T = 1123 \text{ K}$

D_V^0 as a function of the Goldschmidt factor, $t_{\text{Goldschmidt}} = \frac{r_A + r_O}{\sqrt{2}(r_B + r_O)}$, where r_A, r_B, r_O are the average ionic radii of the A, B and O site ions, is plotted in Fig B.4. The Goldschmidt factor is a measure of the strain of the perovskite lattice - a Goldschmidt factor deviating from 1, means that the size of the A and B cations and the oxygen ions are mismatched compared to the perovskite lattice. A Goldschmidt factor close to 1 thus means that the lattice is under the least possible strain. No direct correlation between the values of $t_{\text{Goldschmidt}}$ and D_V^0 is seen.

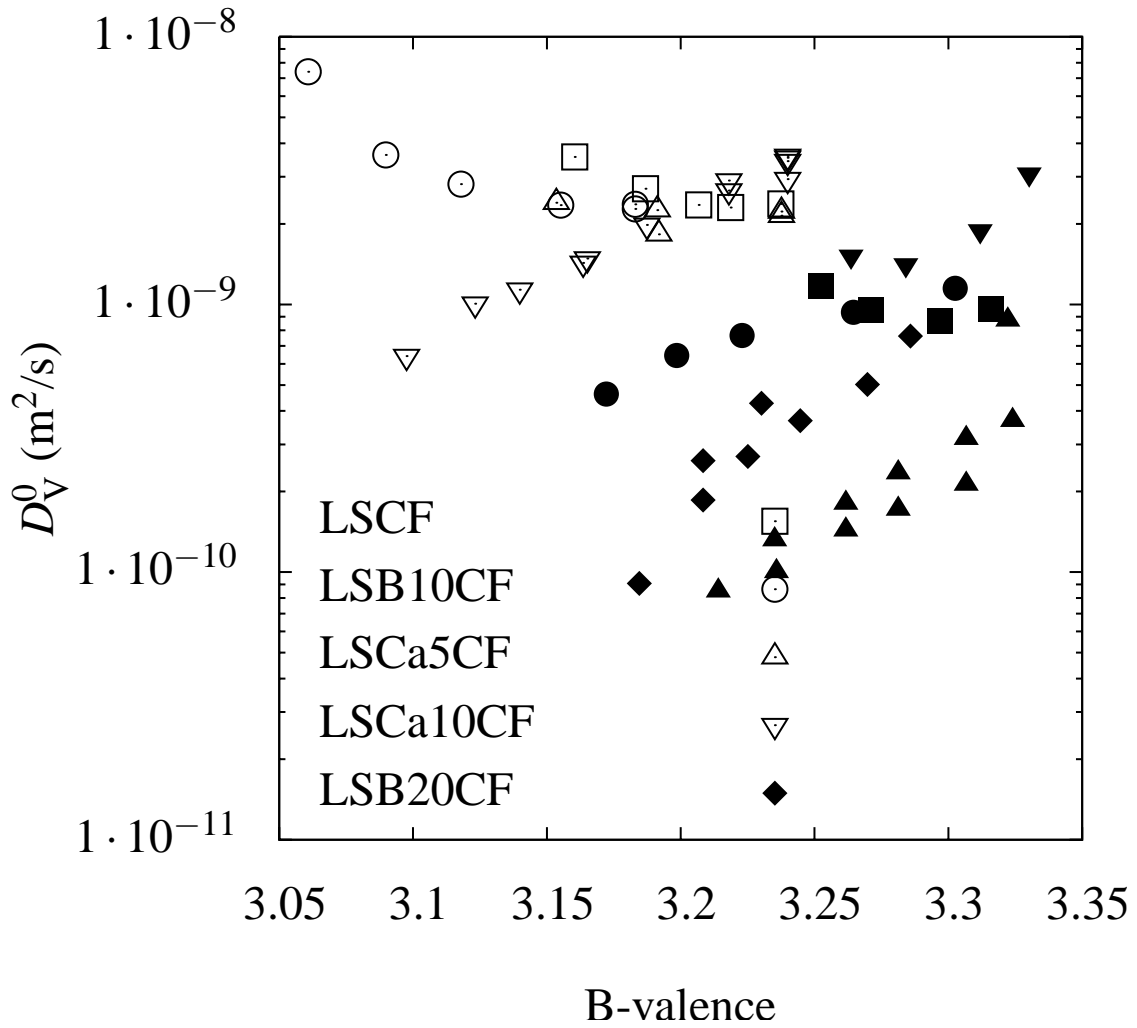


Figure B.5: D_V^0 as a function of the average valency of the B-site cations. Filled symbols are measurements at $T = 1123 \text{ K}$; open symbols are measurements at $T = 1123 \text{ K}$

Another element determining the potential energy well is the ionization of the cations. D_V^0 as a function of the average valency of the B-site cations is plotted in Figure B.5. No direct correlation between the values of the B-valence and D_V^0 is seen.

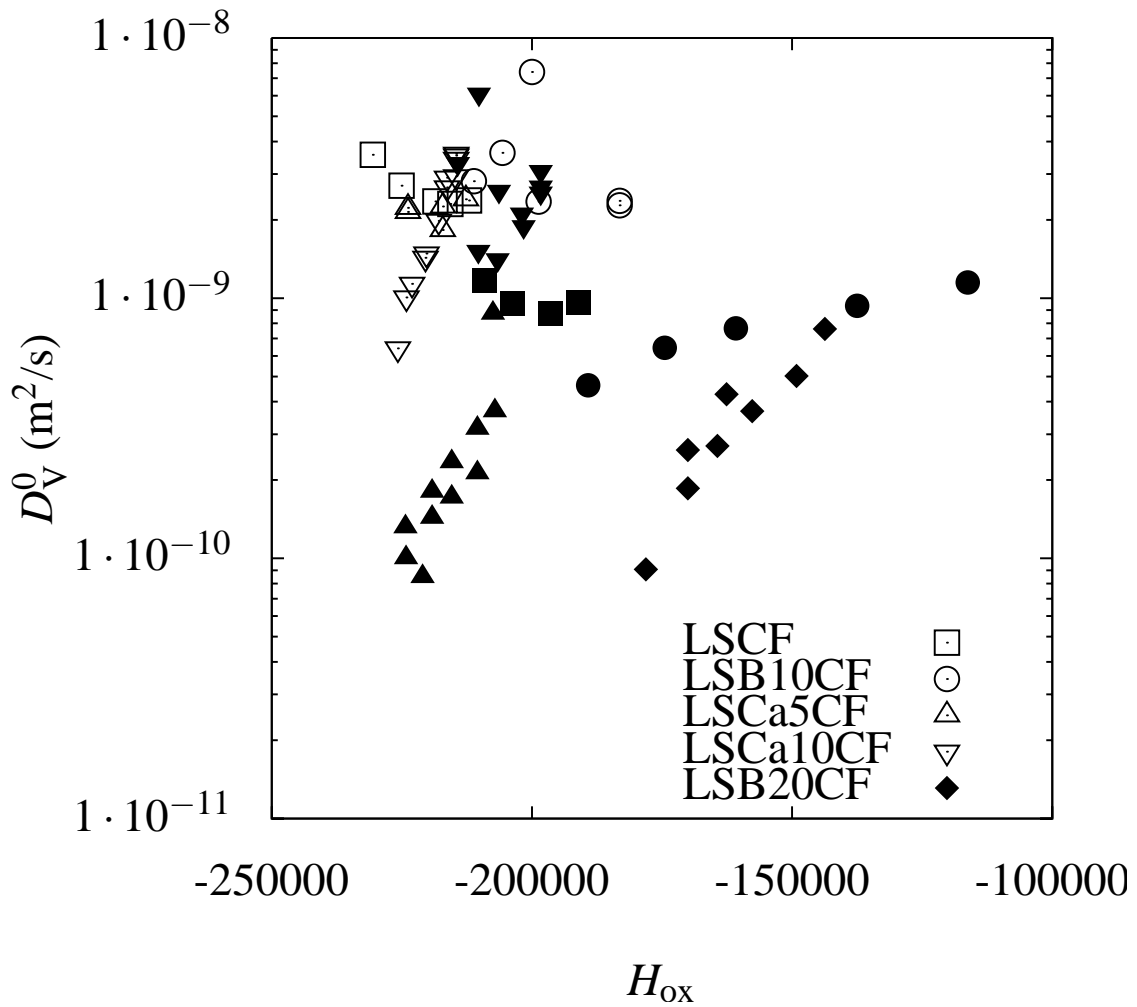


Figure B.6: D_V^0 as a function of the oxide vacancy creation enthalpy. Filled symbols are measurements at $T = 1123$ K; open symbols are measurements at $T = 1123$ K

The partial molar enthalpy of reduction of the perovskite can also influence D_V^0 , as the jumping process involves a reduction and an oxidation process. D_V^0 as a function of the oxide vacancy creation enthalpy measured in Chapter 4, is plotted in Fig. B.6. No direct correlation between the values of H_{OX} and D_V^0 is seen.

Curriculum Vitae

Bjarke Thomas Dalslet
Born october 3rd 1979
Master of Science in Engineering

Theklavej 29A, st.th.
2400 Kbh. NV
Danmark

Bjarkehingrumme@hotmail.com

- Timeline

1995 Graduated Public school, Ganløse skole

1998 Graduated high school, Stenløse Gymnasium

1999 Conscripted soldier, Royal Danish Marines, "Bevogtning & nærforsvar (BON)"
Flådestation Korsør

2004 Graduated as Cand. polyt. (civil engineer / master of science in technical physics)
Technical University of Denmark (DTU)

2004-2007 Employed as PhD. student, University of Twente (NED) / Fuel Cells and Solid State
Chemistry Department, Risø National Laboratory, DTU.

2007-... Employed as Post Doc, magnetic biosensors, Department of Micro and Nanotech-
nology (MIC), DTU.

- Publications

- **Surface exchange rates of mixed conductors determined by local pO_2 probing**
Dalslet, B.; Søgaard, M.; Hendriksen, P.V.
Proceedings 26.Risø international symposium on materials science, Risø (DK), 4-8
Sep 2005
- **Assessment of doped ceria as electrolyte**
Dalslet, B.; Blennow, P.; Hendriksen, P.V.; Bonanos, N.; Lybye, D.; Mogensen, M.
J. Solid State Electrochem., 2006, v. 10 p. 547-561
- **Determination of Oxygen Transport Properties from Flux and Driving Force
Measurements Using an Oxygen Pump and an Electrolyte Probe**
Dalslet, B.; Søgaard, M.; Hendriksen, P.V.
J. Electrochem. Soc. , 2007, v. 154 n. 12

- Patents

- **Cheap thin film oxygen membranes**
Hendriksen, P.V.; Mogensen, M; Dalslet, B; Wang, W.G.
European Patent Office No. 07017098

Acknowledgements

I would like to thank the following people:

- Dr. Peter Vang Hendriksen for his tireless supervision, ambition and enthusiasm, elevating this thesis.
- Dr. H.J.M. Bouwmeester for his time, suggestions, affirmations and advice.
- Dr. Martin Søggaard, for advice, help and much more of his time than could reasonably be expected.
- Most of the people at the Solid State Chemistry Department of Risø National Laboratory for help and advice, and for making life so much more fun both inside and outside the lab. And for all the cake.
- My family, for support, and for accepting my absence.